

SELF-CHANNELISATION AND ROLL WAVES IN DRY GRANULAR FLOWS

A THESIS SUBMITTED TO THE UNIVERSITY OF MANCHESTER
FOR THE DEGREE OF DOCTOR OF PHILOSOPHY
IN THE FACULTY OF SCIENCE AND ENGINEERING
SCHOOL OF NATURAL SCIENCES

2020

Francisco M. Rocha

Department of Mathematics

Contents

Abstract	7
Declaration	8
Copyright Statement	9
Acknowledgements	10
Contributions	12
1 Introduction	15
1.1 Granular materials	15
1.2 Granular rheology	18
1.3 Depth-averaged avalanche models	24
1.4 Particle size segregation	30
1.5 What's next? – Thesis structure	34
2 Deriving the governing equations of motion	37
2.1 Depth-averaged viscous theory in one dimension	37
2.1.1 Equating the problem	37
2.1.2 Free-surface boundary conditions	40
2.1.3 Non-dimensionalisation	41
2.1.4 Vertical pressure, stress and velocity profiles	42
2.1.5 Depth-averaged mass and momentum equations	44
2.1.6 Adding a depth-averaged viscous-like dissipation	47
2.1.7 The basal friction law	49
2.2 Two-dimensional depth-averaged $\mu(I)$ -rheology	53

2.3	Depth-averaged segregation equation	55
3	Self-channelisation and levee formation in monodisperse granular flows	60
4	Granular fingering on a cone	125
5	The kinematics of bidisperse granular roll waves	150
6	Conclusion	201

Word count 48,312

List of Figures

1.1	Examples of granular materials. Starting from the top left, the first figure shows a collection of different alimentary grains (taken from Flavor 2017), then moving to the right a collection of pharmaceutical pills. In the second row, on the left an image of Saturn’s rings (photo credit: NASA), and on the right a debris flow on the Moon (image taken from Kokelaar <i>et al.</i> 2017). At the bottom row the first is a photo of a slush avalanche in the region of central Svalbard, Norway (Eckerstorfer & Christiansen, 2012), whilst bottom right displays a discharge of a corn silo.	16
1.2	Granular materials in different states of matter. In (a) acting like a solid in the form a sand sculpture (photo credit: Monllar 2011), whilst (b) shows a dense liquid-like granular flow on a desert sand dune in Erg Chebbi, Morocco (Barale, 2015) and (c) a dust storm, example of a granular gas, in Golmud, China (photo credit: Shepherd <i>et al.</i> 2016). In panel (d) is shown a zoomed-in image of steel beads being poured in a pile showing all three regimes in the same experiment (Forterre & Pouliquen, 2008).	17
1.3	Schematic illustration of (a) the macroscopic time scale $1/\dot{\gamma}$ for a particle in the upper layer to cross a particle underneath and (b) the microscopic characteristic time $d/\sqrt{p/\rho^*}$ for the upper-layer particle to snap into a hole of size proportional to the grain diameter d	19

1.4	(a) Schematic representation of a simple shear experiment, where the material is confined in between two rough plates by a confining pressure p , and the top plate is sheared with a shear stress τ leading to a shear rate $\dot{\gamma}$. (b) Typical behaviour of the coefficient of friction μ with the inertial number I . The friction coefficient reaches a finite value when I goes to zero, whilst it asymptotes a constant μ_2 when $I \rightarrow \infty$	21
1.5	Examples of dense granular flows with solid- and liquid-like regimes coexisting. Panels (a) and (b) show a rotating drum in which near the free surface the material behaves like a liquid whereas the bulk move in solid-body rotation with the drum, behaving like a solid (image from Gray & Ancey 2011). (b) When a pile of mustard seed is tilted above the angle of repose, an avalanche is triggered at the surface, whilst deeper grains are not in motion (image from Jaeger <i>et al.</i> 1996). Panel (d) shows a lab experiment of a self-channelised flow, where the flow spontaneously solidify creating the lateral static boundaries (solid-like) at each side of the confined liquid-like flow (image from Rocha <i>et al.</i> 2019).	23
1.6	Figure adapted from Pouliquen (1999a), showing the flow rule for steady uniform flows of spherical glass beads. The Froude number Fr , which is the ration between depth-averaged speed \bar{u} to the speed of surface gravity waves, is a linear function of the flow thickness h . Pouliquen (1999a) has shown that the deposit thickness $h_{stop}(\zeta)$ is the appropriate scaling to obtain a collapse of the data.	26
1.7	Figure adapted from Pouliquen & Forterre (2002), illustrating the experiment performed to obtain $\zeta_{stop}(h)$ and $\zeta_{start}(h)$. These functions can be used to characterise a non-monotonic basal friction law that incorporates frictional hysteresis.	27
1.8	Coefficient of basal friction μ_b as a function of the Froude number Fr for different flow thickness h as proposed by (a) Pouliquen & Forterre (2002) and (b) Edwards <i>et al.</i> (2019). Blue dots represent the maximum static friction and the blue region in (b) indicates the hysteretic region between the minimum obeying the dynamic law and the maximum static.	28

1.9	Examples of segregation patterns. (a) Petal-like fingers formed in a rotating drum (taken from Zuriguel <i>et al.</i> (2006)), (b) stratified pattern generated by modulated granular flows (taken from Lueptow <i>et al.</i> (2017)), (c) segregation-induced fingering (taken from Gray <i>et al.</i> (2015)) and (d) segregation pattern formed by a flow down a granular heap (taken from Thomas (2000)).	31
2.1	Schematic representation of the avalanche. The chute is inclined at an angle ζ to the horizontal and the material flows above the basal topography which is defined by the function $b(x, t)$ with velocity field $\mathbf{u}(x, z, t)$. The free surface of the flow is described by $s(x, t)$ which leads to the definition of the thickness of the avalanche $h(x, t) = s(x, t) - b(x, t)$.	38
2.2	Schematic representation of the avalanche. An inverse graded configuration is assumed for the whole flow with an upper layer of large particles between $l(x, t)$ and the free surface $s(x, t)$. The finer grains flows in the middle between the basal topography $b(x)$ and $l(x, t)$. The thickness of flow is defined as $h(x, t) = s(x, t) - b(x)$ whilst the layer of small particles is $\eta(x, t) = l(x, t) - b(x)$ thick. The chute is inclined at an angle ζ to the horizontal, \mathbf{g} is the gravitational acceleration and $\mathbf{u}(x, z, t)$ the velocity field of the material.	55

The University of Manchester

Francisco M. Rocha

Doctor of Philosophy

Self-channelisation and Roll Waves in Dry Granular Flows

April 15, 2020

Dense granular flows are observed in a wide range of natural phenomena, such as debris flows, snow avalanches and dense pyroclastic flows, to small-scale chute flows that are used extensively in industry. Understanding the underlying physics of such systems is of great importance to avoid waste and essential for developing hazard mitigation strategies. In this thesis, two processes are investigated: Self-channelisation in monodisperse flows and the effect of particle size segregation on the kinematics of granular roll waves. Firstly, we consider the problem of self-channelisation that occurs when a monodisperse granular material is supplied onto an inclined rough plane with a constant injection rate and, as the front propagates downstream, the edges of the flow spontaneously solidify to form static levees, confining a central flowing channel. A viscous depth-averaged avalanche model is used to show that two physical mechanisms are crucial to uniquely select the equilibrium state and quantitatively predict the self-channelisation process, namely frictional hysteresis and depth-averaged lateral viscous dissipation. Importantly, it is shown that the steady configuration is governed by a well-defined force balance, which implies that the width of leveed channels is not necessarily set by the granular front. Time-dependent simulations are performed to investigate the transient evolution towards the equilibrium state, as well as how the system transitions to an unsteady avalanching regime as the mass flux is reduced. We proceed by investigating a monodisperse granular flow over a rough conical surface. Small-scale experiments show that down the cone the granular material spreads, thins and slows down until the interface splits, generating a beautiful fingering pattern, in which each individual finger has the morphology of a self-channelised flow. Numerical solutions of the depth-averaged model are used to predict the position at which the interface breaks, as well as the number of fully developed fingers, demonstrating that granular fingering is possible in monodisperse flows due to the hysteretic nature of the particulate media. The second problem addressed in this thesis regards the formation of roll waves in bidisperse granular avalanches. This is investigated through experiments with two different-sized spherical beads confined between rigid glass sidewalls. Using a depth-averaged segregation model, we construct travelling-wave solutions for the bulk flow and show that different regimes are possible for the particle concentration profile. Time-dependent simulations qualitatively recover the experiments, showing that a concertina-like effect results in a higher concentration of larger and more friction particles at the wave crests. Both phenomena here studied can lead to a significant increase in the destructive potential of large-scale flows and, therefore, our results may be particularly relevant in the geophysical context.

Declaration

No portion of the work referred to in the thesis has been submitted in support of an application for another degree or qualification of this or any other university or other institute of learning.

Copyright Statement

- i.** The author of this thesis (including any appendices and/or schedules to this thesis) owns certain copyright or related rights in it (the “Copyright”) and s/he has given The University of Manchester certain rights to use such Copyright, including for administrative purposes.
- ii.** Copies of this thesis, either in full or in extracts and whether in hard or electronic copy, may be made **only** in accordance with the Copyright, Designs and Patents Act 1988 (as amended) and regulations issued under it or, where appropriate, in accordance with licensing agreements which the University has from time to time. This page must form part of any such copies made.
- iii.** The ownership of certain Copyright, patents, designs, trade marks and other intellectual property (the “Intellectual Property”) and any reproductions of copyright works in the thesis, for example graphs and tables (“Reproductions”), which may be described in this thesis, may not be owned by the author and may be owned by third parties. Such Intellectual Property and Reproductions cannot and must not be made available for use without the prior written permission of the owner(s) of the relevant Intellectual Property and/or Reproductions.
- iv.** Further information on the conditions under which disclosure, publication and commercialisation of this thesis, the Copyright and any Intellectual Property and/or Reproductions described in it may take place is available in the University IP Policy (see <http://documents.manchester.ac.uk/DocuInfo.aspx?DocID=487>), in any relevant Thesis restriction declarations deposited in the University Library, The University Library’s regulations (see <http://www.manchester.ac.uk/library/aboutus/regulations>) and in The University’s Policy on Presentation of Theses.

Acknowledgements

The people that contributed to this journey to be completed are definitely several. First of all, I would like to sincerely thank my supervisors, Prof. Nico Gray and Dr Chris Johnson, for all the help and support. During the last four years, I had the great pleasure and privilege of working with Nico and Chris, in a gratifying, constructive, and open-minded process of learning, where since the first moment the goal was to make all ideas come true. For this, I will always be heart-fully thankful to them.

A special thank goes to my parents, Heitor and Cecília, and to my sister Beatriz, for always supporting my decisions and understanding the lack of communication at various times during the last years. I'll always be thankful to my partner in crime, Debi, for all the joyful moments, and for tolerating the absence of patience some (several) times.

I would also like to thank all the past and present colleagues from the granular group, especially James Baker and Sylvain Viroulet for all the help through the years. I could not forget to mention how profoundly thankful I am to Aaron Russell for his support since the very first moment I arrived in Manchester. Also, to present and past tenants of office 2.210, in particular to Jonathan Deakin, Puneet Matharu and Matt Russell, thanks for making this journey much smoother and more enjoyable. To the really good friends that I made in the maths department, in particular to Martin, Mante, Monica (the Big Boss), Ulla and Mike Crabb, I thank you for all the wisdom, especially in moments with pints in hands.

I am extraordinarily grateful to the friends I made in the UK and to the brothers and sisters from across the ocean, who came to visit me in person or telepathically in Manchester. It's invaluable all the formal knowledge gained over the most informal situations. All my love to them.

I would like to thank my friend and housemate in Manchester, João, for all the

favours, discussions and his peculiar way of saying when you are wrong, and to Pablo de Castro who is always there with his love and attention able to uplift any situation. I also thank my Masters' supervisor and friend, Prof. José Américo Miranda, who transmitted his passion for science and arts, without which I would probably not be here.

I am also thankful to Profs. Andrew Hazel, Mathias Heil and Rich Hewitt for being examiners in my annual examinations, and to Dr Raphael Assier for the lectures and support during these last four years, which importantly contributed to my development as a researcher. I would like to thank the examiners of my thesis, Prof. Matthias Heil and Dr Yoel Forterre, for carefully reading the manuscript and the extremely constructive comments and suggestions made.

Finally, I would like to thank the Brazilian National Council for Scientific and Technological Development — CNPq — for financial support.

Contributions

The main body of this PhD thesis is composed of three chapters in the form of journal papers that have been accepted or are under consideration for publication. Each chapter is a self-contained piece of work that has been developed in a very constructive collaboration with several colleagues, without which this thesis could not be presented the way it is. The contributing authors that will appear in the papers presented hereafter are listed below:

- Dr. Chris Johnson (CGJ) — Manchester Centre for Nonlinear Dynamics & Department of Mathematics, University of Manchester, UK.
- Dr. James L. Baker (JLB) — School of Civil Engineer, University of Sydney, Australia.
- Prof. Nico Gray (JMNTG) — Manchester Centre for Nonlinear Dynamics & Department of Mathematics, University of Manchester, UK.
- Dr. Parmesh Gajjar (PG) — Henry Moseley X-Ray Imaging Facility, Department of Materials, University of Manchester, UK.
- Prof. Peter Kokelaar (BPK) — School of Environmental Science, University of Liverpool, UK.
- Dr. Sylvain Viroulet (SV) — Institut de Mécanique de Fluides de Toulouse (IMFT), Université de Toulouse, CNRS, France.

In chapter 3, entitled “Self-channelisation and levee formation in monodisperse granular flows”, Francisco M. Rocha (FMR) did all the experiments, as well as the theoretical and numerical work supervised by CGJ and JMNTG. FMR, CGJ and JMNTG co-wrote the paper.

The following chapter, “Granular fingering on a cone” was initially presented as a traditional thesis chapter in the PhD thesis of PG. JMNTG gave the initial idea and PG designed the experimental setup. PG, SV and FMR performed the experiments, PG derived the equations in the conical frame of reference and started the post processing of the data, which was then carried on by FMR. FMR performed the theoretical and numerical work presented in the paper, supervised by CGJ and JMNTG. All the authors co-wrote the article.

The last chapter on the kinematics of bidisperse granular roll waves is the result of a much longer process, where SV, JLB and FMR performed the lab experiments, and SV processed the experimental data. SV, JLB and FMR worked on the ODE solution, and JLB performed the numerical simulations. BPK provided the geophysical motivation and insights into the kinematics of the waves. The paper was mainly written by SV and JLB with inputs from FMR, CGJ and JMNTG.

“You have to systematically create confusion, it sets creativity free. Everything that is contradictory creates life”

Salvador Dalí

“No one is born fully-formed: it is through self-experience in the world that we become what we are.”

Paulo Freire

1 | Introduction

1.1 Granular materials

Granular materials are generally defined as a collection of macroscopic particles of size typically larger than $100\ \mu\text{m}$ surrounded by an interstitial fluid, like air, water or a more viscous liquid (Andreotti *et al.*, 2013). One consequence of this definition is that, due to the size of the individual constituents, thermal fluctuations are negligible in the microscopic level, and particles do not experience Brownian motion. This broad definition also embodies in the same group, systems which in a quick inspection may appear completely dissimilar. The granular family includes from daily-used products, such as sugar, cereals, rice, and sand, to enormous-scale natural phenomena like dunes, landslides, pyroclastic flows, snow avalanches, debris flow and interplanetary aggregates (figure 1.1). The study of granular physics is, therefore, of great interest for different communities, from scientists seeking to understand fundamental physics, to industrially-motivated researchers trying to design smart techniques to avoid wasting. Understanding large-scale granular phenomena has a vitally important role in the prediction and mitigation of natural hazards, and also provide a way to better interpret images and data of interplanetary events. On the other hand, many sectors of industry, such as civil engineering, chemical, food, pharmaceutical and mining, use grains either as raw material and/or manufacture them as a final product, in such a large proportion that is estimated that grains appear as second most used materials in industry (Duran, 1997; Bates, 2006).

A full understanding of the physics of granular materials in its various configurations remains as a long-standing open question until these days. The complexity intrinsic to granular media relates to the fact the these materials behave differently



Figure 1.1: Examples of granular materials. Starting from the top left, the first figure shows a collection of different alimentary grains (taken from Flavor 2017), then moving to the right a collection of pharmaceutical pills. In the second row, on the left an image of Saturn’s rings (photo credit: NASA), and on the right a debris flow on the Moon (image taken from Kokelaar *et al.* 2017). At the bottom row the first is a photo of a slush avalanche in the region of central Svalbard, Norway (Eckerstorfer & Christiansen, 2012), whilst bottom right displays a discharge of a corn silo.

than any other familiar materials (solids, liquids or gases), which could classify granular materials as an independent state of matter — the granular state (Jaeger & Nagel, 1992; Jaeger *et al.*, 1996). Some of the main reasons that make granular materials so special, and why it is not trivial to apply well-known techniques used to describe traditional solids, liquids or gases in its description are pointed out by Andreotti *et al.* (2013). First of all, even a small sample of granular media, for example a handful of sand, can contain millions of particles with sizes in the order of hundreds of micron meters, which makes the job of computing Newton’s law for each single grain and track individual trajectories extremely expensive in computational cost. Interactions

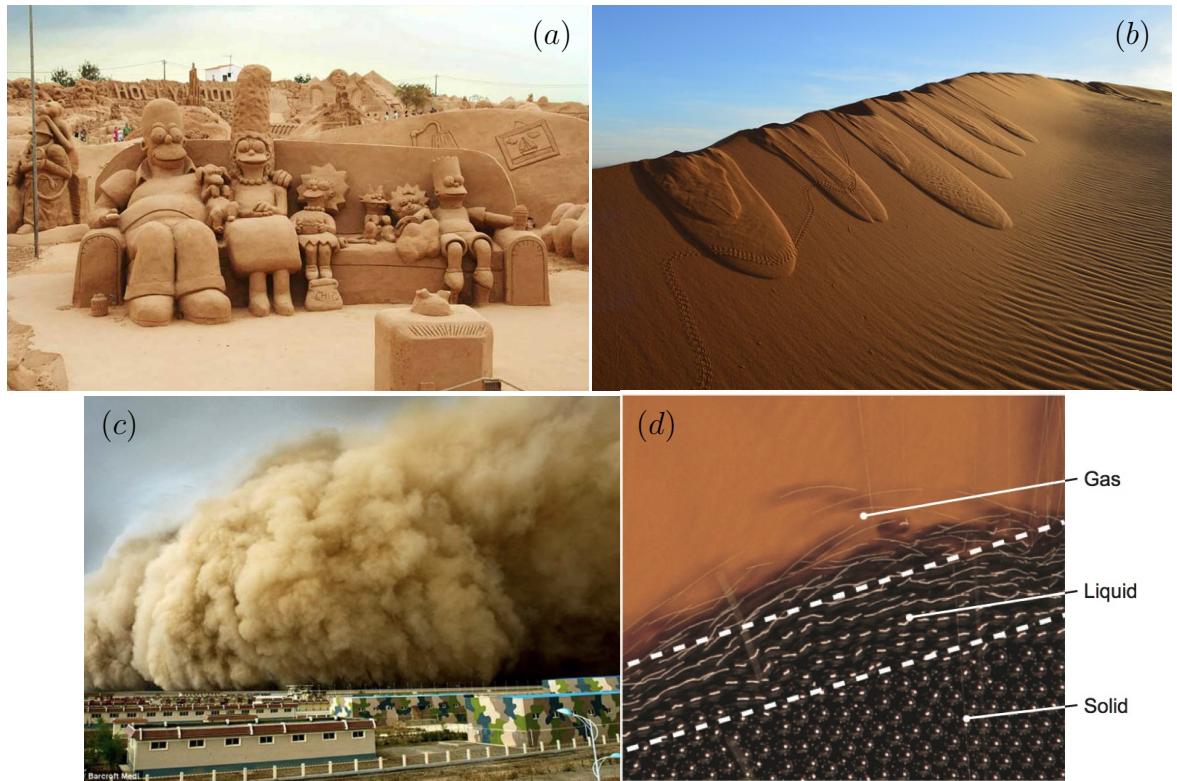


Figure 1.2: Granular materials in different states of matter. In (a) acting like a solid in the form a sand sculpture (photo credit: Monllar 2011), whilst (b) shows a dense liquid-like granular flow on a desert sand dune in Erg Chebbi, Morocco (Barale, 2015) and (c) a dust storm, example of a granular gas, in Golmud, China (photo credit: Shepherd *et al.* 2016). In panel (d) is shown a zoomed-in image of steel beads being poured in a pile showing all three regimes in the same experiment (Forterre & Pouliquen, 2008).

at the grain level are also very complicated once highly non-linear effects, such as friction between particles, are observed. On the other hand, two features make granular media non-trivial in the light of classical statistical mechanics: Granular materials are athermal and collisions between grains are mainly inelastic. The first of these carries the information that grains are too big to feel thermal fluctuations, and one cannot assume that intermediate equilibrium states are reached to guarantee that all possible configurations are visited with some probability related to its statistical weight.. The other, that at the microscopic level the material is extremely effective in dissipating energy, and, hence, models based on purely elastic collisions, like the ones for ideal gases, are not applicable (Jaeger *et al.*, 1996). Furthermore, granular materials do not have a pre-established state of matter. Depending on the way it is handled, it can act as a solid and support shear to form, for example, a sandpile (Fig. 1.2a). When the

applied shear exceeds a certain threshold, the material may flow like a fluid (Fig. 1.2b), whilst for high degrees of agitation and low particle concentration, it can behave like a gas (Fig. 1.2c). In fact, most practical flows involve all three regimes (Fig. 1.2d).

Hereafter in this thesis we will focus our attention on the dense regime of granular flows, where the grains are dry and interactions are mainly collisional and by friction, so the surrounding fluid, here air, can be neglected. In these flows, the granular medium behaves like a liquid, but, nonetheless, depending on the stress distribution inside the material, portion of the flow may solidify, creating coexistence zones of solid- and liquid-like behaviours. In practical applications to geophysical and/or industrial situations the numbers of individual particles is so high that a microscopic description is infeasible. This inspired many scientists to pursue a continuum description of granular media.

1.2 Granular rheology

The rheology of granular materials is not yet fully understood, in the sense that there is no unique constitutive law able to describe its different states of matter. From a continuum point of view, a granular medium behaves like a viscoplastic fluid, such that it resists movement for an applied shear below a certain threshold. Above that value, the material starts to move with flow characteristics depending on the shear rate. However, in contrast to known viscoplastic fluids, such as mayonnaise and toothpaste, where a yield-stress condition defines the solid-liquid transition, for granular materials the flow threshold is given in terms of friction due to particle-particle interactions (Andreotti *et al.*, 2013). The first attempt to model a dense granular flow, and the simplest of the models, was developed by Charles Coulomb in the 18th century, where a response to shear in terms of a constant friction was considered.

The resultant equations from the model were, however, proved to be mathematically ill-posed (Schaeffer, 1987). The consequence of ill-posedness is that the system of equations produce an unbounded growth rate for small-wavelength perturbations and, therefore, when the model is solved numerically, numerical random noise, introduced by limitations of the machine precision, grows faster than the physical most unstable mode and the results do not correspond to reality.

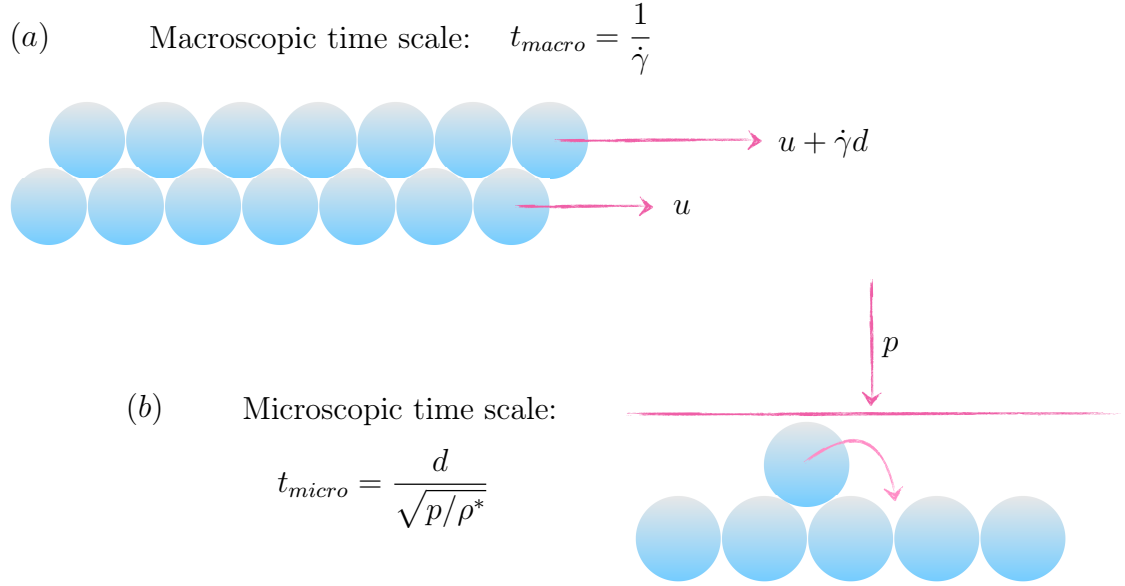


Figure 1.3: Schematic illustration of (a) the macroscopic time scale $1/\dot{\gamma}$ for a particle in the upper layer to cross a particle underneath and (b) the microscopic characteristic time $d/\sqrt{p/\rho^*}$ for the upper-layer particle to snap into a hole of size proportional to the grain diameter d .

The Groupement de Recherche Milieux Divisés (GDR-MiDi, 2004) provided an empirical law which has proved its ability to describe many observed features in dense granular flows, the $\mu(I)$ -rheology. They collapsed experimental data with discrete element simulations of steady granular flows in different configurations (plane shear, annular shear, vertical-chute flow, inclined plane, heap flow and rotating drum) to analyse the set of governing parameters of the flow. As a result of dimensional analysis and numerical simulations, they found that the effective friction coefficient was a function depending only on the non-dimensional inertial number I (da Cruz *et al.*, 2005; Jop *et al.*, 2005; Jordanoff & Khonsari, 2004), given by

$$I = \frac{\dot{\gamma}d}{\sqrt{p/\rho^*}}, \quad (1.2.1)$$

where the particle diameter d and intrinsic density ρ^* are the material parameters, whilst the confining pressure p and the steady shear rate $\dot{\gamma}$ are variable quantities. The inertial number can be interpreted as a normalised measurement of the flow rate. To understand the physical meaning of I , imagine two layers of identical particles being compressed against each other with pressure p and the upper layer being sheared against the other at a fixed shear rate $\dot{\gamma}$ (see figure 1.3). The macroscopic characteristic time scale associated with the process of the top layer travelling a distance d relative

to the bottom layer is $1/\dot{\gamma}$. On the other hand, in the micro-scale, when each particle of the top layer traverses a particle of the bottom layer, it snaps down into the gap between two particles due to the confining pressure p . From Newton's law in the vertical direction $F_z = md^2z/dt^2$, it is possible to show that the time scale for this process is given by $d/\sqrt{p/\rho^*}$, by noting that $F_z \sim pd^2$, $m \sim \rho^*d^3$, and $d^2z/dt^2 \sim d/t_{micro}^2$. Therefore, the inertial number $I = t_{micro}/t_{macro}$ is the ratio between the microscopic time scale associated with the movement of particles falling down into the gaps between two particles of the bottom layer, and the macroscopic time for the entire process of the upper-layer particle crossing a grain underneath.

The inertial number I may be used to classify the different granular regimes. When I is small, the macroscopic time scale is large compared to t_{micro} , which means that microscopic rearrangements are very long-lived contacts, the particles remain always in contact, and no bouncing is observed. This characterises the quasi-static regime and occur when $I < 10^{-3}$ (da Cruz *et al.*, 2005; Andreotti *et al.*, 2013). On the other hand, when the microscopic time scale gets to the order of the overall motion in the macro scale and I becomes large ($I > 10^{-1}$), the flow is rapid and dilute, corresponding to a granular gas. In between these two regimes lies the dense ‘‘liquid’’ phase for $10^{-3} < I < 10^{-1}$ (da Cruz *et al.*, 2005). It is worth mentioning that the two main assumptions taken in the dimensional analysis performed by da Cruz *et al.* (2005) are (i) that d is the only intrinsic length scale and (ii) that collisions are purely inelastic and, hence, fully dissipative. Although this appears to be the case for dense flows in the ‘‘liquid’’ regime, questions arise for the other two extremes. In the dilute collisional gaseous regime the restitution coefficient starts playing a role and the fully dissipative assumption breaks; on the other hand, in the quasi-static regime non-local effects introduce new correlation length scales between particles which are not in direct contact (Aranson & Tsimring, 2002; GDR-MiDi, 2004; Kamrin & Bazant, 2007).

The explicit dependence of the coefficient of friction μ with the inertial number can be extracted by comparing results from simple-shear experiments (figure 1.4a) with measurements of the basal friction in dense granular flows down inclined rough planes (Pouliquen, 1999a; Pouliquen & Forterre, 2002; GDR-MiDi, 2004; Jop *et al.*, 2005). As the shear rate goes to zero ($\dot{\gamma} \rightarrow 0$) the friction coefficient reaches a non-zero critical value μ_1 , whilst it asymptotically converges to a constant μ_2 for high inertial

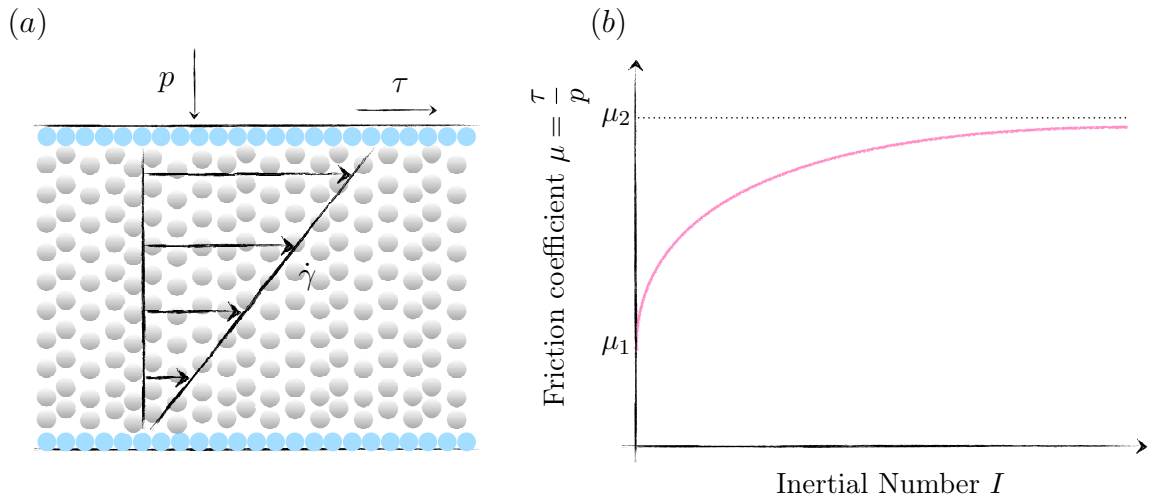


Figure 1.4: (a) Schematic representation of a simple shear experiment, where the material is confined in between two rough plates by a confining pressure p , and the top plate is sheared with a shear stress τ leading to a shear rate $\dot{\gamma}$. (b) Typical behaviour of the coefficient of friction μ with the inertial number I . The friction coefficient reaches a finite value when I goes to zero, whilst it asymptotes a constant μ_2 when $I \rightarrow \infty$.

numbers, or, equivalently, shear rate (see figure 1.4b). By fitting the experimental data the following functional form of μ was proposed (GDR-MiDi, 2004; Jop *et al.*, 2005, 2006)

$$\mu(I) = \mu_1 + \frac{\mu_2 - \mu_1}{1 + I_0/I}, \quad (1.2.2)$$

where I_0 , μ_1 and μ_2 are constants associated with properties of the flowing material and the rough base.

The rheology has been able to predict a linear steady-state velocity profile across flows in shear cells and, for chute flows, a Bagnold dependence of the velocity field u with the thickness of the flow h , i.e. $u \sim h^{3/2}$ (Bagnold, 1954; Silbert *et al.*, 2001), which are in agreement with discrete element method simulations and experiments of spherical glass beads (GDR-MiDi, 2004). Jop *et al.* (2006) extended the local rheology to a full tensorial formulation, allowing more complex configurations, in which shear occurs in more than one direction to be investigated. The central assumption in the 3D generalisation is to that the granular material is incompressible, which is motivated by the fact that, although the solids volume fraction within the material is also a function of the inertial number I , in the dense regime it only varies slightly (GDR-MiDi, 2004). The internal stress tensor in the granular medium is then described by a relation in which the shear-stress is considered to be collinear with the strain-rate.

Gradually, the $\mu(I)$ -rheology has been proving its ability to predict many characteristics of granular avalanches, such as steady-state velocity profile of flows down inclined planes (Baran *et al.*, 2006), flows on granular piles (Jop *et al.*, 2005) and collapses in silo flows (Lagrée *et al.*, 2011; Staron *et al.*, 2012). For flows down inclines, the local rheology predicts a range of angles $\zeta \in [\zeta_1, \zeta_2]$, for which steady uniform flows are possible, a fact that is also observed in experiments (Pouliquen, 1999a; Silbert *et al.*, 2001; Börzsönyi & Ecke, 2006). However, the theory predicts that the minimum slope angle required for the material to flow is a constant, whereas in the experiments, instead, it is observed that the minimum angle depends on the thickness of the granular layer, i.e. for thick layers it is possible to observe flows in shallower angles than for thin layers. Another feature that is not captured by the local rheology is the transition from the Bagnold velocity scaling, when the avalanche thickness is relatively thick (Pouliquen, 1999a; Baran *et al.*, 2006), to a linear velocity profile for thin flows (Silbert *et al.*, 2003). In addition, Barker *et al.* (2015) have shown that the theory exhibits zones of ill-posedness for both high and low inertial number, being well-posed for a wide range of intermediate I , which also supports the $\mu(I)$ -rheology as an appropriate constitutive law for dense granular flows.

In many practical applications, such as rotating flows in drums (Gray, 2001; Zuriguel *et al.*, 2006) (figure 1.5a,b), formation of heaps (Grasselli & Herrmann, 1997; Baxter *et al.*, 1998) (figure 1.5c) and self-channelised flows (Johnson *et al.*, 2012; Félix & Thomas, 2004; Deboeuf *et al.*, 2006; Takagi *et al.*, 2011; Rocha *et al.*, 2019) (figure 1.5d), the granular material display more than one state of matter, with solid- and liquid-like regions coexisting in the same flow. Although the $\mu(I)$ -rheology is able to predict the coexistence of solid and liquid granular layers (Jop *et al.*, 2006; Staron *et al.*, 2014; Hung *et al.*, 2016), the transition between flowing and static regions is described by a simple Coulomb criterion via the friction angle μ_1 . This leads to a discontinuous interface between the two phases, whereas an exponential tail is observed in experiments, which is associated with a creeping flow in the static region (Komatsu *et al.*, 2001; Crassous *et al.*, 2008; Andreotti *et al.*, 2013). Among the limitations of considering the solid-liquid transition in granular materials as a simple Coulomb description is that the $\mu(I)$ -rheology is not able to predict the hysteresis in the flow onset (Carrigy, 1970; Daerr & Douady, 1999; Pouliquen, 1999a; Pouliquen & Forterre,

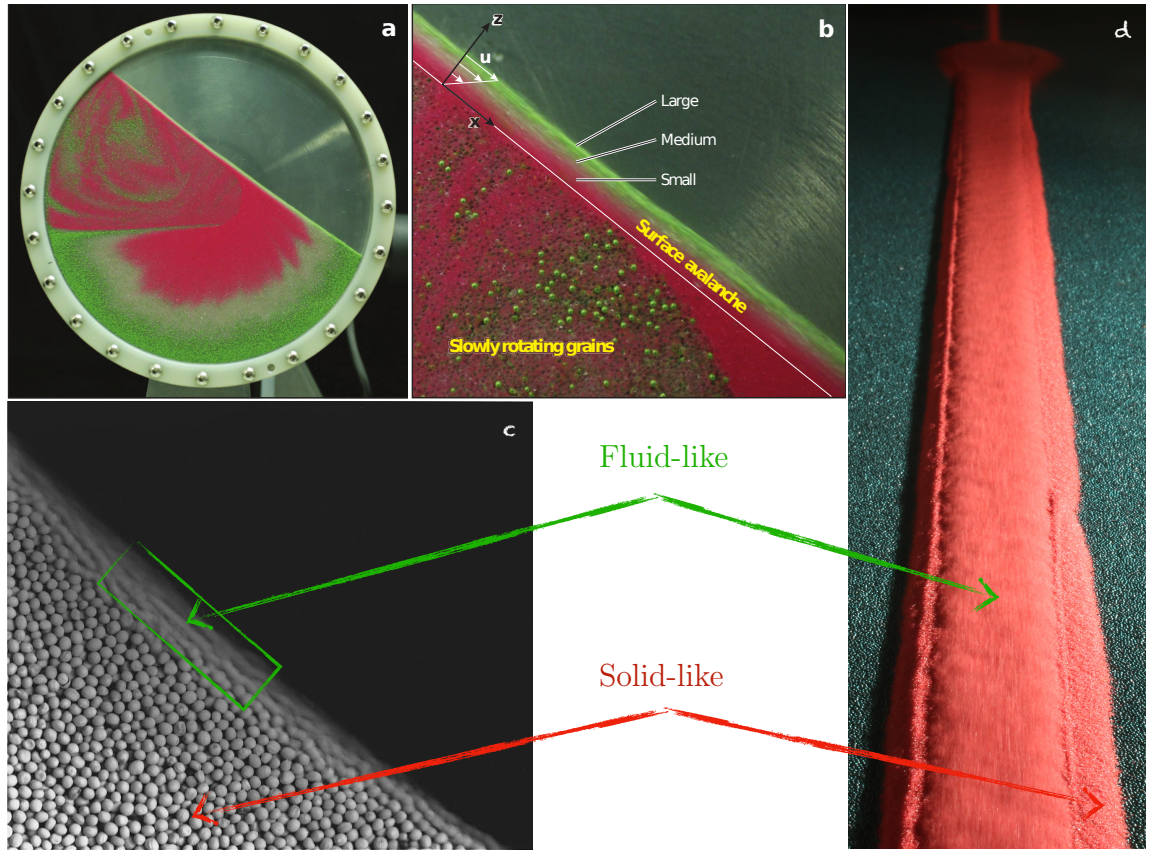


Figure 1.5: Examples of dense granular flows with solid- and liquid-like regimes co-existing. Panels (a) and (b) show a rotating drum in which near the free surface the material behaves like a liquid whereas the bulk move in solid-body rotation with the drum, behaving like a solid (image from Gray & Ancy 2011). (b) When a pile of mustard seed is tilted above the angle of repose, an avalanche is triggered at the surface, whilst deeper grains are not in motion (image from Jaeger *et al.* 1996). Panel (d) shows a lab experiment of a self-channelised flow, where the flow spontaneously solidify creating the lateral static boundaries (solid-like) at each side of the confined liquid-like flow (image from Rocha *et al.* 2019).

2002; Edwards *et al.*, 2017; DeGiuli & Wyart, 2017; Edwards *et al.*, 2019). The hysteretic nature of granular materials implies that a static layer of thickness h needs to be inclined to an angle $\zeta_{start}(h)$ to start flowing spontaneously, however, to stop a moving layer of the same thickness the slope needs to decrease to $\zeta_{stop}(h) < \zeta_{start}(h)$ (Daerr & Douady, 1999; Pouliquen & Forterre, 2002). In between these two extreme angles the granular layer is in a metastable regime (Daerr & Douady, 1999; Daerr, 2001; Aranson & Tsimring, 2001, 2002; Pouliquen & Forterre, 2002; Russell *et al.*, 2019), where the material can be static, but a small perturbation may be enough to fluidise the media and produce an avalanche. An important observation is that the stop ζ_{stop} and

start angle ζ_{start} are functions of the layer thickness, with both angles being asymptotically constant for deep layer ($h > 20d$), whilst they increase when the flow depth decreases (Pouliquen & Renaut, 1996; Daerr & Douady, 1999; Pouliquen & Forterre, 2002).

1.3 Depth-averaged avalanche models

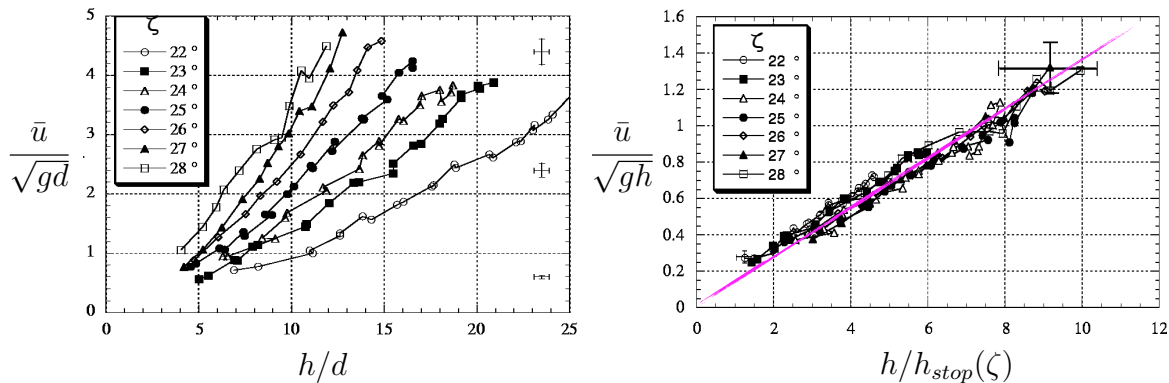
Through the years, depth-averaged models (de Saint-Venant, 1871) have proved to be a promising alternative to model dense granular flows, in particular because the dominant effect of the granular rheology in the depth-integrated formulation reduces to a basal shear stress, which is easier to characterise than the full rheology.

In many dense granular flows, in particular in the geophysical world, characteristic length scales within the plane of propagation, such as the width and run-out distance of an avalanche, are much larger than out-of-plane characteristic dimensions, like the thickness of the flow. When that is the case, a very useful mathematical tool is to average the governing equations over the smallest dimension, which normally simplifies the problem by reducing its effective dimension. This type of approach was first proposed by the French mathematician Adh emar Jean Claude Barr e de Saint-Venant while he was studying the problem of flows in open channels (de Saint-Venant, 1871). Once the averaging process is done, the final set of mass and momentum conservation laws are known as the Saint-Venant, depth-averaged, or, simply, shallow-water equations.

In the light of depth-averaged theories, the first continuum model for granular flows was presented to calculate paths of snow avalanches (Grigorian *et al.*, 1967) back in 1967, whilst a formal derivation of these equations was published by Savage & Hutter (1989) twenty years later, and its ability to model a finite mass of granular material down an incline was proved afterwards (Savage & Hutter, 1991; Greve & Hutter, 1993). The theory was formally generalised for two-dimensional flows over different basal geometries (Gray *et al.*, 1999; Wieland *et al.*, 1999; Pudasaini & Hutter, 2003; Bouchut & Westdickenberg, 2004; Luca *et al.*, 2009), and, by applying numerical shock-capturing and front-tracking methods (Tai *et al.*, 2002), rapid flows past obstacles were computed (Gray *et al.*, 2003; H akonard ottir & Hogg, 2005; Cui *et al.*, 2007; Vreman *et al.*,

2007; Gray & Cui, 2007; Cui & Gray, 2013). As an important application, those advances have been applied to model geophysical mass flows such as debris flows (Iverson, 1997; Iverson & Denlinger, 2001; Denlinger & Iverson, 2001), landslides (Kuo *et al.*, 2009), pyroclastic flows (Pitman *et al.*, 2003; Doyle *et al.*, 2011), and also in the development of safety strategies in mountainous regions (Barbolini *et al.*, 2009). The works mentioned here consider a constant coefficient of friction between flow and underlying surface. Although this might be a good approximation for granular flows over a smooth base, where experiments show that fully developed uniform flows exist only for a unique critical slope angle (Hungr & Morgenstern, 1984; Patton *et al.*, 1987; Ahn *et al.*, 1991), when the bed is rough the situation is more complex and the friction coefficient is observed to be thickness and shear-rate dependent.

In the depth-averaged framework, the $\mu(I)$ -rheology (Jop *et al.*, 2006) reduces to an effective basal friction law that is much easier to characterise experimentally. A realistic friction coefficient must take into account (i) that there are steady uniform flows for a range of slope angles, so the friction coefficient is rate dependent, and (ii) that, for a fixed slope angle, thicker avalanches move faster than thinner ones and, hence, friction is a function of the avalanche thickness as well. Pouliquen (1999a) performed experiments with steady uniform flows of spherical glass beads down a rough inclined plane and found that the depth-averaged Froude number Fr , which is defined as the ratio of depth-averaged velocity to the speed of gravity waves (figure 1.6), is a linear function of the avalanche depth. However, Pouliquen (1999a) showed that to observe a collapse of the data for different slope angles and obtain a flow rule, which relates the depth-averaged velocity and the thickness of steady uniform flows, length scales should be normalised by the thickness of the deposit left by the flow h_{stop} , instead of the particle diameter d (figure 1.6). The proportionality coefficient β and the function $h_{stop}(\zeta)$ are properties of the flowing material and the rough bed found by fitting the experimental data. The friction coefficient for these steady uniform flows, called thereafter dynamic friction, was then constructed by assuming an equilibrium between the component of gravity pulling the material downslope and friction. Using the dynamic friction law, Pouliquen (1999b) was able to compute the frontal shape of a steady uniform flow, and several other studies have been done that confirm the



$$Fr = \frac{\bar{u}}{\sqrt{gh}} = \beta \frac{h}{h_{stop}(\zeta)}$$

Figure 1.6: Figure adapted from Pouliquen (1999a), showing the flow rule for steady uniform flows of spherical glass beads. The Froude number Fr , which is the ratio between depth-averaged speed \bar{u} to the speed of surface gravity waves, is a linear function of the flow thickness h . Pouliquen (1999a) has shown that the deposit thickness $h_{stop}(\zeta)$ is the appropriate scaling to obtain a collapse of the data.

robustness of the dynamic friction law (e.g. Forterre & Pouliquen, 2003; Mangeney-Castelnau *et al.*, 2003; Forterre, 2006; Gray & Edwards, 2014). However, the dynamic law is valid only for fast and thick flows, where a steady uniform configuration is reached and the whole flow behaves in a similar fashion. In order to account for different phases of the granular material coexisting in the same flow one needs to understand what happens in the low-velocity regime, when the granular material gets closer to the liquid-solid phase transition.

A more complex basal friction law has been proposed by Pouliquen & Forterre (2002) in order to account for frictional hysteresis. To characterise the resistive basal force they used a similar experimental setup to the one of Pouliquen (1999a), in which steady uniform flows of spherical glass beads were triggered on an inclined plane, which was made rough by glueing a monolayer of the same beads to the base. Different particles were used both in the flow and in the bed to investigate the effect of relative roughness to basal law parameters. The experimental procedure and outputs of Pouliquen & Forterre's (2002) experiments are schematically illustrated in figure 1.7. A steady uniform flow is generated down an inclined plane and then it drains out, leaving behind a static layer of thickness $h^{(1)}$ inclined at an angle $\zeta^{(1)}$ (point 1). The

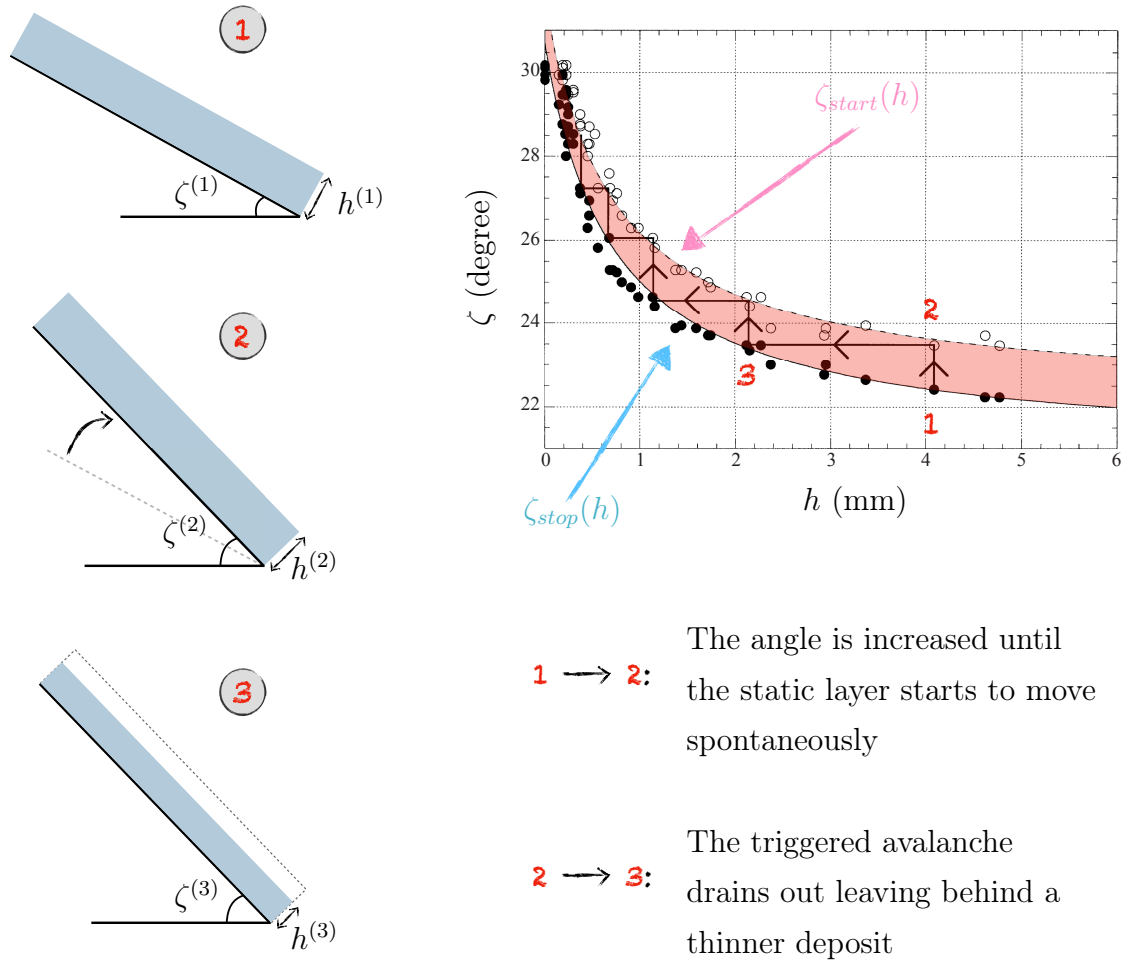


Figure 1.7: Figure adapted from Pouliquen & Forterre (2002), illustrating the experiment performed to obtain $\zeta_{stop}(h)$ and $\zeta_{start}(h)$. These functions can be used to characterise a non-monotonic basal friction law that incorporates frictional hysteresis.

inclination is increased very gently until the static layer starts to move spontaneously when the slope reaches $\zeta^{(2)} > \zeta^{(1)}$ and the thickness $h^{(2)} = h^{(1)}$ (point 2). The angle is then fixed and the flow drains out, depositing uniformly a new static layer of thickness $h^{(3)} < h^{(2)}$ over the inclined bed, which remains at the same inclination, i.e. $\zeta^{(3)} = \zeta^{(2)}$ (point 3). The same loop is repeated several times following the “staircase procedure”, until the final deposit gets too thin to be measured, and the stairs are bounded by two curves in (ζ, h) -space. The lower fitted curve, which records the thickness of the deposits, such as points **1** and **3**, is called $\zeta_{stop}(h)$ ¹, whilst the upper fit that reports the angle at which the static layers have failed spontaneously,

¹Equivalently, since $\zeta_{stop}(h)$ is a strictly decreasing function of h , it can be inverted to give $h_{stop}(\zeta)$.

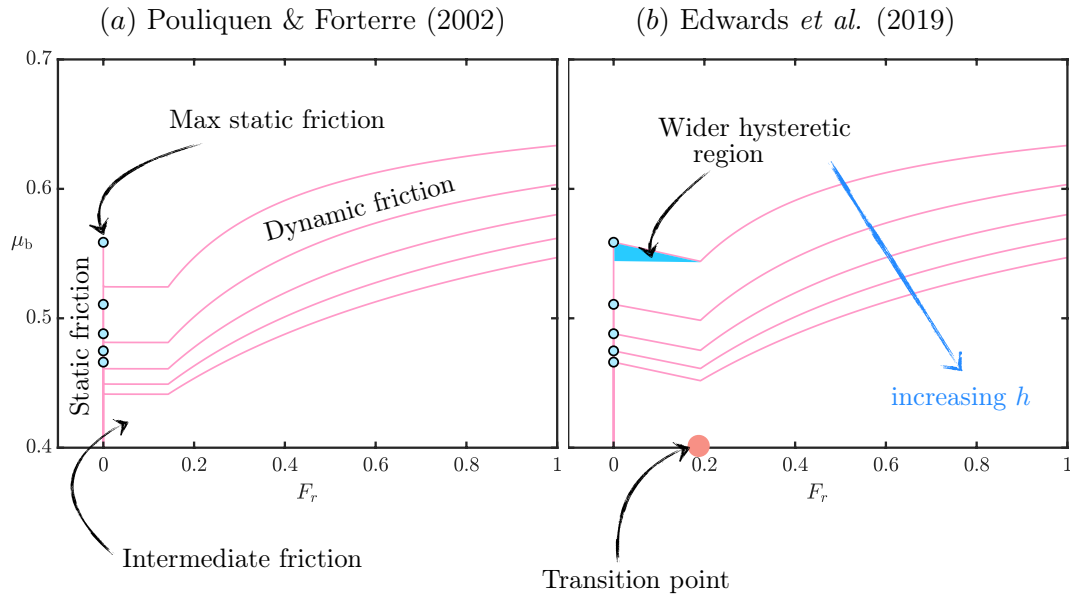


Figure 1.8: Coefficient of basal friction μ_b as a function of the Froude number Fr for different flow thickness h as proposed by (a) Pouliquen & Forterre (2002) and (b) Edwards *et al.* (2019). Blue dots represent the maximum static friction and the blue region in (b) indicates the hysteretic region between the minimum obeying the dynamic law and the maximum static.

like point ②, is denominated $\zeta_{start}(h)^2$. In between the two extreme curves (light red region in figure 1.7), the system is in a metastable regime where static and flowing layers can coexist, i.e. the *hysteretic* region (Pouliquen & Forterre, 2002; Edwards *et al.*, 2019). Since the *start* curve is defined when the material is on the brink of motion, it is used to determine the maximum static friction required to hold the layer stationary, whereas the *stop* curve and the flow rule for steady uniform flows (figure 1.6) are used to compute the dynamic friction coefficient (Pouliquen, 1999a; Pouliquen & Forterre, 2002).

A typical friction coefficient μ_b as a function of the Froude number Fr for different flow thickness h is displayed in figure 1.8. The static friction balances the resultant driving force (due to gravity and pressure for example) until it reaches its maximum value, above which any increment in the applied force, such as a tiny increase in slope angle, would cause the failure of the layer. In the dynamic regime, friction is shear-rate dependent, with the material feeling a higher resistive force for higher velocities. Both the maximum static and the dynamic friction decrease as the thickness of the flow

²By using the same argument as for the *stop* curve, $h_{start}(\zeta)$ is obtained by inverting $\zeta_{start}(h)$.

increases (figure 1.8). In these two regimes, since the system reaches a stable equilibrium (either static or dynamic) it is possible to characterise the friction coefficient directly via experiments on an inclined plane. In the low-velocity, intermediate friction, regime (light blue area in figure 1.8), however, no stable equilibrium is observed and a simple balance between friction and gravitational force does not correspond to what is seen in the experiments. In this regime, instabilities start to develop and the dynamics become much more complex. The lack of stable equilibria suggests that friction is a decreasing function of the velocity (Heslot *et al.*, 1994; Baumberger *et al.*, 1994; Pouliquen & Forterre, 2002), which led Pouliquen & Forterre (2002) to assume a power-law interpolation connecting the minimum point obeying the dynamic rule to the maximum static friction, as shown in figure 1.8. One feature to notice here is the extremely sharp decrease of μ_b close to zero velocities, which depends on the chosen power-law exponent. The reason for such a rapid change is that it guaranteed that the theoretical results were independent of this, in principle ad-hoc, exponent, and also ensured that their steady uniform flow of glass beads deposited a layer of thickness h_{stop} (Pouliquen & Forterre, 2002). The non-monotonicity of the $\mu_b(Fr)$ curve is the key characteristic to incorporate hysteresis into the friction law, which allows portions of the flow moving with different velocities to feel the same resistive force, and, hence, being able to balance gravity in different states.

Recently, Russell *et al.* (2019) have used an experiment to measure indirectly the power-law exponent of the friction law. The experiment is similar to stages ① and ② illustrated in figure 1.7. First, a static layer of thickness $h_{stop}(\zeta_{initial})$ is created, exactly like point 1 in figure 1.7. The slope angle is increased to ζ_{final} , but not enough to mobilise the static layer, leaving the system in the metastable state. If the variation in inclination $\Delta\zeta = \zeta_{final} - \zeta_{initial}$ is high enough, a backwards propagating wave is triggered when the layer is perturbed, which fluidises the whole material. Russell *et al.* (2019) have shown that the speed of the erosion wave, which is a function of $\Delta\zeta$, is strongly related to the structure of the intermediate branch of the friction law, and to correctly predict the experimentally measured wave speed the power-law exponent should be order unity. Moreover, the extended friction law of Pouliquen & Forterre (2002) is valid for spherical glass beads, but it does not hold for more complex materials, such as sand, for which the flow rule assumes a slightly more complicated

form (Forterre & Pouliquen, 2003; Edwards *et al.*, 2017). This led Edwards *et al.* (2017, 2019) to propose a friction law that incorporates the order unity exponent and has a different transition point between dynamic and intermediate friction in order to make the extended law also valid for angular particles (figure 1.8b). The technical details of the difference between Pouliquen & Forterre’s (2002) and Edwards *et al.*’s (2019) friction laws will be discussed further in chapters 2 and 3.

In the vast majority of the depth-averaged models mentioned so far (e.g. Savage & Hutter, 1989, 1991; Pouliquen, 1999a; Pouliquen & Forterre, 2002), the momentum balance consists in a balance between the acceleration terms, pressure gradients, gravity and the basal friction. This is a result of many terms being neglected in the depth integration process under the shallowness assumption. In some situations, however, in order to capture more subtle effects some of the previously neglected terms become more important to recover the right physics. The first to propose an extension in this sense was Forterre (2006), where contributions from the in-plane deviatoric stress are incorporated to introduce longitudinal dissipation into the model in order to capture the cut-off frequency of granular roll waves. Nevertheless, this approach introduces a new dimensionless unknown parameter, and also the new viscous-like term in the momentum balance had a singularity when the thickness goes to zero, e.g. at the flow front. Taking a different approach, Gray & Edwards (2014) have derived a viscous depth-averaged $\mu(I)$ -rheology also able to predict the cut-off frequencies of roll waves, but the coefficient associated with the depth-averaged viscosity is given by parameters of the friction law and can be accessed via experiments. The viscous theory has been applied to predict erosion-deposition waves (Edwards & Gray, 2015; Edwards *et al.*, 2017) and extended to two dimensions (Baker *et al.*, 2016a) so it can be applied to more complex systems. This viscous term will be crucial in providing the width selection mechanism for self-channelised flows, as it will be shown in chapter 3.

1.4 Particle size segregation

So far, we have been discussing dense granular flows of identical spherical particles, where it is possible to recognise a unique characteristic length scale for the whole material, the grain diameter. In reality, however, dense granular avalanches are often

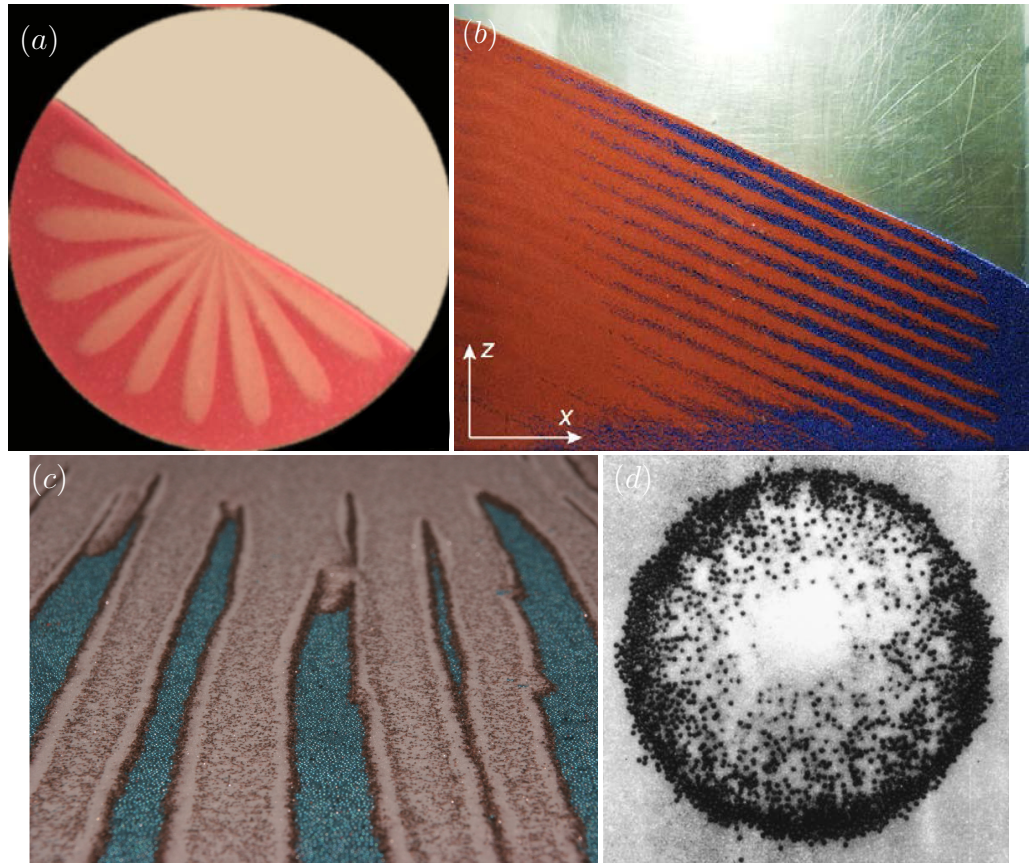


Figure 1.9: Examples of segregation patterns. (a) Petal-like fingers formed in a rotating drum (taken from Zuriguel *et al.* (2006)), (b) stratified pattern generated by modulated granular flows (taken from Lueptow *et al.* (2017)), (c) segregation-induced fingering (taken from Gray *et al.* (2015)) and (d) segregation pattern formed by a flow down a granular heap (taken from Thomas (2000)).

composed of particles with one or more different physical properties, such as size, density and/or shape. In particular, granular materials are extremely effective in segregate particles by size when they are sheared (Savage & Lun, 1988; Gray & Hutter, 1997; Vallance, 2000; Golick & Daniels, 2009). Particle size segregation can occur, for example, in rotating drums (Zuriguel *et al.*, 2006), modulated granular flows (Lueptow *et al.*, 2017), flow over inclined rough planes (Pouliquen *et al.*, 1997; Pouliquen & Vallance, 1999; Baker *et al.*, 2016b) and vibrated granular materials (Thomas, 2000), leading to stunning patterns that can be visualised by distinguishing the different-sized constituents by colour (figure 1.9).

Although there are several different physical mechanisms that can lead to segregation (Scott & Bridgwater, 1975; Ehrichs *et al.*, 1995; Schröter *et al.*, 2006; Jenkins & Yoon, 2001; Schulze, 2008; Mullin, 2000), perhaps the most frequently observed is

gravity-driven segregation (Gray, 2018). The key driving mechanism for gravity-driven particle size segregation is a combination of kinetic sieving and squeeze expulsion (Middleton, 1970; Savage & Lun, 1988; van der Vaart *et al.*, 2015; Gajjar *et al.*, 2016). The idea is that during the flow small particles tend to fill gaps left by the bigger ones, and, as a result, large particles feel an upward squeeze expulsion force, leading to an effective motion of large grains to the top and small particles to the bottom of the flow. When large particles are segregated to the top of an avalanche, where the velocity is greater, they are preferentially transported to the front. Once at the front, the particles are over-run and can recirculate, uprising again, or can be advected to the sides, creating an accumulation zone of large particles at the front and at the lateral edges of the flow (Gray & Kokelaar, 2010a,b; Gray, 2018). The dynamics near the accumulation zones are very complex, with a remixing circulation area, where small and large grains coexist, called breaking-size segregation wave (Shearer *et al.*, 2008).

The enhancement in the concentration of large particles leads to regions of much greater local friction, which has a strong feedback in the bulk flow. In geophysical flows, such as mud flows (Sharp & Nobles, 1953), snow avalanches (Bartelt *et al.*, 2012) and pyroclastic flows (Calder *et al.*, 2000), this plays a crucial role in producing lateral stationary zones of predominantly large particles, commonly called levees, on both sides of the flows, confining a flowing mixture of large and finer grains in the middle that can reach much longer run-out distances (Johnson *et al.*, 2012; Kokelaar *et al.*, 2014). Particle segregation can also generate granular fronts unstable to transverse perturbations, which can trigger fingering-like instabilities (Pouliquen *et al.*, 1997; Pouliquen & Vallance, 1999; Woodhouse *et al.*, 2012; Baker *et al.*, 2016b). Moreover, the inversely-graded distribution with large-enriched regions at the top of the flow and a layer of small grains at the bottom generates a lubrication-like effect, which increases the mobility of the flow, when the smaller beads are less frictional than larger ones (Goujon *et al.*, 2007; Linares-Guerrero *et al.*, 2007). Beyond the geophysical world, size segregation is also a mechanism that is extremely efficient in preventing good mixing in mixture of grains, and, therefore, can strongly affect the quality of final products in industry (Johanson, 1978; Bates, 1997).

Several models have been proposed to capture the feedback of size segregation on the bulk flow (e.g. Savage & Lun, 1988; Bridgwater *et al.*, 1985; Dolgunin & Ukolov,

1995; Gray & Thornton, 2005; Gray *et al.*, 2006; Gray & Ancey, 2011; Tunuguntla *et al.*, 2014; Gray & Ancey, 2015). Multicomponent mixture theory and pressure arguments can be used to compute the percolation velocity at which each species move through the flow, and construct a multicomponent segregation theory (Gray & Thornton, 2005; Gray & Ancey, 2011; Gray, 2018). Another way to attack the problem is by just assuming that the concentration of each species ϕ^v will be governed by a convection-diffusion equation, where each species is advected both by the bulk flow and also as a result of segregation. Different approaches have been proposed to compute the segregation flux for bidisperse mixture, some of which suppose that segregation is symmetric between small and large particles, (Dolgunin & Ukolov, 1995), whilst others, motivated by experimental observations (van der Vaart *et al.*, 2015), account for asymmetric segregation (Gajjar & Gray, 2014). Recent numerical simulations show that small particles percolate downwards through the voids without enduring contacts, whilst large particles roll against neighbour particles in their motion to the top of the flow (Jing *et al.*, 2017; Gray, 2018).

In order to obtain a full description of a polydisperse granular flow, the segregation equation is coupled with conservation of mass and the balance of linear momentum, where the granular rheology is incorporated. In terms of the $\mu(I)$ -rheology (GDR-MiDi, 2004; Jop *et al.*, 2006), this coupling is not trivial, since the inertial number I is a function of the grain diameter. For bidisperse flow, the diameter could be a generalised concentration-weighted grain size $\bar{d} = \phi^l d_l + \phi^s d_s$, where ϕ^v and d_v are, respectively, the concentration and the grain diameter of each species (small and large), but, nonetheless, this implies that the inertial number changes locally with the concentration (Rognon *et al.*, 2007).

A possible approach that has been used to model segregation-induced granular fingering (Baker *et al.*, 2016b; Woodhouse *et al.*, 2012), levee formation (Johnson *et al.*, 2012) and bulbous head formation in bidisperse flows down inclines (Denissen *et al.*, 2019), is to use a depth-averaged segregation equation, which describes the evolution of the depth-averaged concentration $\bar{\phi}$ (Gray & Kokelaar, 2010b,a; Baker *et al.*, 2016b). In this framework, the depth-integrated segregation equation governs the dynamics of the concentration of each species of particle, and is coupled to the momentum balance equation, since the amount of each type of particle affects the effective rheology.

There are different methods to account for the effect of the different-sized particles in the basal friction law. It may be assumed that the effective basal friction is a function of the global concentration, which, at least in the lab, is a known quantity determined by the proportion of large and small grains in the experiment. This approach leads to a significantly simpler mathematical description, since it allows the momentum equation to be computed separately from the segregation equation. The *uncoupled* approach is able to access, at least qualitatively, some physical properties of the system, but it does not correspond accurately to reality, where friction depends locally on the concentration, which is evolving in space and time. Another option is to go for a fully coupled description, and incorporate an explicit dependence on the depth-averaged concentration field in the momentum balance, and then the system of conservation laws needs to be solved together. It is worth mentioning that, although depth-integrated models are a useful tool able to predict many segregation patterns, the depth-averaging process misses some features associated with the vertical dynamics, such as the breaking size-segregation wave, which is replaced by discontinuous shocks in the concentration field (Baker *et al.*, 2016*b*). In order to recover such three-dimensional structures one could reconstruct the full velocity field from depth-averaged solutions (e.g Baker *et al.*, 2016*a*), using the incompressibility assumption to obtain the out-of-plane velocity component, in order to solve the full three-dimensional segregation equation.

1.5 What's next? – Thesis structure

This thesis is divided into two main parts; one that investigates the phenomenon of self-channelisation in monodisperse flows, which is very strongly related to the hysteretic nature of granular flows, and the second is the formation of roll waves in dry granular avalanches, and more specifically the effect that particle size segregation has on the waves kinematics. The thesis is composed of three body chapters in the format of journal papers, of which two have already been published in the *Journal of Fluid Mechanics*, and one is in preparation to be submitted to a peer-reviewed journal. Each article is a self-contained piece of work, with independent page, equation, figure and table numbering and its own bibliography. Some concepts are essential for

more than one paper, so there is some content overlap between chapters in order to keep each of them self-explanatory. Before starting the core of the thesis, the next chapter is dedicated to the derivation of the equations of motion, such as mass conservation, momentum balance and the segregation equation, and also discusses how to incorporate the granular rheology into the depth-averaged formulation.

In chapter 3, the first in journal format and entitled “Self-channelisation and levee formation in monodisperse granular flows”, we develop a depth-integrated avalanche model for self-channelised flows of monodisperse particles. We show that frictional hysteresis and depth-averaged viscous-like stresses are the essential physical mechanisms to uniquely select the self-channelised equilibrium state, and the inviscid limit is discussed. To test our model, the steady-state theoretical predictions are compared with experimental data collected for both spherical (Félix & Thomas, 2004) and irregular (Takagi *et al.*, 2011) grains. Fully time- and space-dependent solutions are computed to investigate the process of how the levees are initially formed, and how the systems responds to changes in the supply mass flux, dynamically transitioning between steady states. For low flow rates, the system switches to an unsteady avalanching regime, where erosion-deposition pulses are triggered periodically. The viscous model is also able to capture this behavioural transition in fairly good qualitative agreement with the laboratory experiments of Takagi *et al.* (2011).

In chapter 4, we present a study of a monodisperse granular flow over a rough conical surface. The chapter starts with the description of the experimental setup and a discussion about how the combination of frictional hysteresis and effects of the conical geometry leads to the development of fully developed granular fingers. Importantly, the experiments show that fingering instability can be triggered in monodisperse flows, contrary to what is commonly observed for flows down inclined flat planes, where particle segregation is required to destabilise the flow. We proceed by formulating the problem in an appropriate conical frame of reference, in order to predict the critical radial position at which the fingers start to develop. The theory consists of a depth-averaged viscous model, with a non-monotonic friction law that can incorporate the hysteretic nature of granular materials. In addition, we propose that downstream, at the position where the fingers are fully formed, the cone may be considered, for shallow flows, as a flat inclined plane and the self-channelised solution presented in chapter 3

is applied to estimate the number of fully developed fingers.

The last in a journal-type format, chapter 5 is dedicated to the investigation of the effect of particle size segregation in the formation of granular roll waves. We start by performing small-scale experiments with spherical glass spheres of two different sizes down an inclined rough chute. The particles have different colours to help visualisation and experiments are performed for different concentrations of large and small particles. It is observed that there is a more significant concentration of large particles at the wave crests, a fact which is further investigated by adding coloured tracers at the surface of the flow and analysing their space-time evolution. A “splitter plate” technique is used, which allows the internal structure of the flow to be accessed for different particle concentrations. We use a depth-averaged model for the bulk flow, as well as to model particle size segregation, which is able to capture the formation of the waves and the higher concentration of large particles at the crest of the waves. Travelling waves solutions for the bulk thickness and depth-averaged velocity are constructed, showing that waves can develop with different wavespeeds, wavelengths and amplitudes, with the larger-amplitude waves moving faster, and merging with slower waves, as observed in experiments. Moreover, we find that there are three distinct flow regimes depending on the speed of surface particles relative to the wave and on the particle concentration, which is in agreement with fully time-dependent solutions to the set of conservation laws.

2 | Deriving the governing equations of motion

This chapter is dedicated to the derivation of the equations which will be used in the following chapters of the thesis. We first derive the depth-averaged viscous model in one and two dimensions, and subsequently we discuss how the granular rheology is incorporated in the depth-integrated framework (Pouliquen, 1999a; Pouliquen & Forterre, 2002; Gray & Edwards, 2014; Baker *et al.*, 2016a; Edwards *et al.*, 2019). In the following part, we discuss how particle-size segregation can be modelled and coupled with the depth-averaged mass and momentum equations (Gray & Ancey, 2009; Baker *et al.*, 2016b). This chapter serves as a second introduction, and the story presented here is a compilation of different results existent in the literature.

2.1 Depth-averaged viscous theory in one dimension

2.1.1 Equating the problem

Consider a mass of granular material flowing down an inclined plane at an angle ζ to the horizontal, and that Oxz is the rectangular coordinate system with x pointing downslope and z being upward perpendicular to the plane. The plane has a basal topography described by $b(x, t)$ whilst the upper free surface of the flow is denoted by $s(x, t)$, such that the thickness of the avalanche is given by $h(x, t) = s(x, t) - b(x, t)$, as shown in figure 2.1. The velocity field inside the granular medium is \mathbf{u} , which has components (u, w) in the (x, z) directions respectively. Here, the intrinsic density of the grains ρ^* , the solid volume fraction Φ , and, hence, the bulk density $\rho = \Phi\rho^*$ are assumed to be constant and uniform throughout the material. Since the bulk density is then constant in time and uniform in space, the conservation of mass leads to the

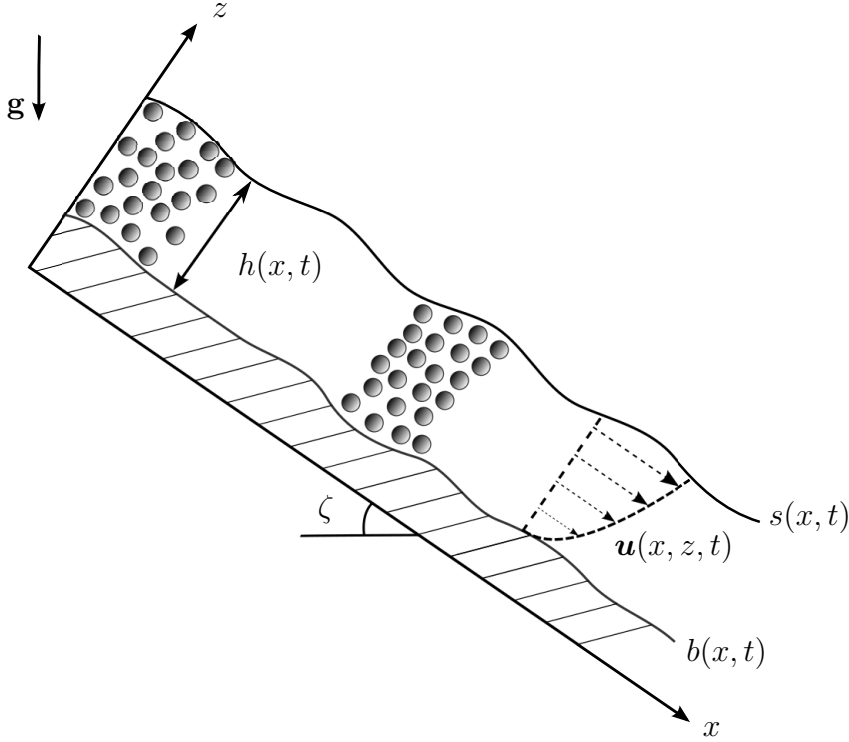


Figure 2.1: Schematic representation of the avalanche. The chute is inclined at an angle ζ to the horizontal and the material flows above the basal topography which is defined by the function $b(x, t)$ with velocity field $\mathbf{u}(x, z, t)$. The free surface of the flow is described by $s(x, t)$ which leads to the definition of the thickness of the avalanche $h(x, t) = s(x, t) - b(x, t)$.

incompressibility condition (e.g. Batchelor, 1967)

$$\nabla \cdot \mathbf{u} = 0, \quad (2.1.1)$$

and the momentum balance can be written as a Cauchy equation (e.g. Batchelor, 1967)

$$\rho \left(\frac{\partial \mathbf{u}}{\partial t} + \nabla \cdot (\mathbf{u} \otimes \mathbf{u}) \right) = \nabla \cdot \boldsymbol{\sigma} + \rho \mathbf{g}, \quad (2.1.2)$$

where t is time, \mathbf{g} is the constant of gravitational acceleration, $\boldsymbol{\sigma}$ is the Cauchy stress tensor, ‘ \cdot ’ is the dot product, \otimes is the dyadic product, and ∇ is the gradient operator.

The stress tensor

$$\sigma_{ij} = -p\delta_{ij} + \tau_{ij}, \quad (2.1.3)$$

is divided into an isotropic part related to the pressure $p(\mathbf{x}, t)$ plus a traceless deviatoric stress $\boldsymbol{\tau}$, which is entirely due to the motion of the “fluid”, and δ_{ij} is the Kronecker delta function (e.g. Batchelor, 1967).

The deviatoric stress contains the particular information about the constitutive relation for the granular material, i.e. how stresses relate to strain, velocities and density, and here we will be using the rheological law defined by the $\mu(I)$ -rheology (GDR-MiDi, 2004; Jop *et al.*, 2006). According to the full tensorial approach of the rheology, the deviatoric stress tensor has pressure-dependant components aligned with the strain rate tensor, i.e.,

$$\boldsymbol{\tau} = \mu(I)p \frac{\mathbf{D}}{\|\mathbf{D}\|}, \quad (2.1.4)$$

where \mathbf{D} is the standard strain rate

$$\mathbf{D} = \frac{1}{2} (\nabla \mathbf{u} + \nabla \mathbf{u}^T), \quad (2.1.5)$$

and $\|\mathbf{D}\|$, the second invariant of \mathbf{D} , is given by

$$\|\mathbf{D}\| = \sqrt{\frac{1}{2} \text{tr}(\mathbf{D}^2)} \quad (2.1.6)$$

where tr represents the trace. Since we are using the standard definition of the strain rate tensor, equation (2.1.5), which is twice the one used in Jop *et al.* (2006), an extra factor of two appears in the definition of the inertial number

$$I = \frac{2\|\mathbf{D}\|d}{\sqrt{p/\rho^*}}, \quad (2.1.7)$$

where d and ρ^* are the diameter and the intrinsic density of the grains respectively. In this formulation, the deviatoric stress can also be written as

$$\boldsymbol{\tau} = \eta(p, \|\mathbf{D}\|) \mathbf{D}, \quad (2.1.8)$$

where $\eta(p, \|\mathbf{D}\|) = \mu(I)p/\|\mathbf{D}\|$ can be interpreted as an effective non-Newtonian granular viscosity, which depends on the coefficient of friction $\mu(I)$ and on the pressure p . Interestingly, the granular viscosity diverges when the shear rate $\|\mathbf{D}\|$ goes to zero, indicating the existence of a threshold below which the material behaves like a rigid solid. As mentioned in the previous chapter, the expression for μ has been empirically proposed to take the form (Jop *et al.*, 2005, 2006)

$$\mu(I) = \mu_1 + \frac{\mu_2 - \mu_1}{1 + I_0/I}, \quad (2.1.9)$$

with I_0 , μ_1 and μ_2 being constants values. In the $\mu(I)$ -rheology, the yield criterion assumes a Drucker-Prager-type law (Drucker & Prager, 1952), which states that the

granular material only flows if the anisotropic part of the stress exceeds a threshold given by

$$\|\boldsymbol{\tau}\| > \mu_1 p, \quad (2.1.10)$$

where $\|\boldsymbol{\tau}\|$ is the second invariant of $\boldsymbol{\tau}$, whose definition is analogous to equation (2.1.6). At this stage, two points are worth mentioning. First, if the friction coefficient μ is set to a constant in (2.1.4) the model reduces to a rate-independent purely plastic law, which has been shown to be always ill-posed and, hence, it cannot be used to obtain transient solutions, as we discussed in chapter 1 (Schaeffer, 1987). Also, the effective granular viscosity being a function of both the shear rate and also the local pressure is a characteristic associated with the frictional nature that, for instance, distinguishes granular materials from classical Bingham and Herschel-Bulkley fluids (Jop *et al.*, 2006).

2.1.2 Free-surface boundary conditions

In order to close the system of equations we need to specify the boundary conditions at the base and at the free surface of the flow, which are subjected to kinematic conditions. Suppose that the free surface and the base are described by functions $F^{(s)}$ and $F^{(b)}$, respectively, where

$$F^{(s)} = z - s(x, t) = 0, \quad (2.1.11)$$

$$F^{(b)} = b(x, t) - z = 0. \quad (2.1.12)$$

Since both functions are identically zero, each material derivative will also vanish, meaning that

$$\frac{\partial F^{(s)}}{\partial t} + \mathbf{u}^{(s)} \cdot \nabla F^{(s)} = 0, \quad \text{at } z = s(x, t), \quad (2.1.13)$$

$$\frac{\partial F^{(b)}}{\partial t} + \mathbf{u}^{(b)} \cdot \nabla F^{(b)} = 0, \quad \text{at } z = b(x, t). \quad (2.1.14)$$

Based on experiments where grains glued at the base are the same as the flowing beads (Pouliquen, 1999a,b; Pouliquen & Forterre, 2002; GDR-MiDi, 2004) it is reasonable to assume that the base of the flow is subjected to no-slip boundary conditions,

whilst the free surface is assumed to be traction free (Gray & Edwards, 2014), i.e.,

$$\mathbf{u}^{(b)} = \mathbf{0}. \quad (2.1.15)$$

$$\sigma^{(s)} \mathbf{n}^{(s)} = \mathbf{0}, \quad (2.1.16)$$

$$(2.1.17)$$

The outward pointing normal vector $\mathbf{n}^{(k)}$ to the free surface ($k = s$) or to the base ($k = b$) is defined in terms of the gradient of $F^{(k)}$ as

$$\mathbf{n}^{(k)} = \frac{\nabla F^{(k)}}{|\nabla F^{(k)}|}. \quad (2.1.18)$$

Note that the no-slip condition is consistent with granular flows over rough bases, in which the similar size and shape allow for a geometrical interlock between the particles at the base and their first neighbours. The condition breaks for flows over smooth beds, where a tangential slip may be assumed (e.g. Savage & Hutter, 1989; Gray, 1999).

2.1.3 Non-dimensionalisation

In order to gain some insight regarding the dominant effects for the dynamics we now proceed to rewrite the equations of motion in terms of non-dimensional quantities, taking advantage of some characteristics of the system. As we discussed before, for shallow dense granular flows the depth of the avalanche is much smaller than its lateral extent, which means that, if H is a typical thickness and L a characteristic length of the flow, the aspect ratio $\epsilon = H/L \ll 1$. Thus, velocities may be non-dimensionalised by a typical value $U = \sqrt{gH}$ and pressure by ρgH . Note that here we are choosing the same non-dimensional parameters as in Gray & Edwards (2014), where the typical velocity is chosen to be the order of the gravity wave speed instead of using the more pronounced length scale, i.e., L , as done by Savage & Hutter (1989). This way, the set of non-dimensional and dimensional quantities are related in the following form:

$$\left. \begin{aligned} (x, z, s, b, h, d, \mathcal{L}) &= L(\hat{x}, \epsilon \hat{z}, \epsilon \hat{s}, \epsilon \hat{b}, \epsilon \hat{h}, \epsilon \hat{d}, \epsilon \hat{\mathcal{L}}), \\ (u, w, \mathbf{u}, |\mathbf{u}|) &= U(\hat{u}, \epsilon \hat{w}, \hat{\mathbf{u}}, |\hat{\mathbf{u}}|), \\ (D_{xx}, D_{xz}, D_{zz}, \|\mathbf{D}\|) &= \sqrt{g/H} (\epsilon \hat{D}_{xx}, \hat{D}_{xz}, \epsilon \hat{D}_{zz}, \|\hat{\mathbf{D}}\|), \\ (p, \tau_{xx}, \tau_{xz}, \tau_{zz}, \sigma) &= \rho g H (\hat{p}, \epsilon \hat{\tau}_{xx}, \hat{\tau}_{xz}, \epsilon \hat{\tau}_{zz}, \hat{\sigma}), \\ t &= (L/\sqrt{gH}) \hat{t}, \end{aligned} \right\} \quad (2.1.19)$$

where the hat indicates non-dimensional quantities. Substituting (2.1.19) into the incompressibility condition (2.1.1) and into the momentum balance (2.1.2), it is possible to write the non-dimensional equations of motion in the form

$$\frac{\partial \hat{u}}{\partial \hat{x}} + \frac{\partial \hat{w}}{\partial \hat{z}} = 0 \quad (2.1.20)$$

$$\epsilon \left(\frac{\partial \hat{u}}{\partial \hat{t}} + \frac{\partial(\hat{u}^2)}{\partial \hat{x}} + \frac{\partial(\hat{u}\hat{w})}{\partial \hat{z}} \right) = \sin \zeta + \frac{\partial \hat{\tau}_{xz}}{\partial \hat{z}} - \epsilon \frac{\partial \hat{p}}{\partial \hat{x}} + \epsilon^2 \frac{\partial \hat{\tau}_{xx}}{\partial \hat{x}}, \quad (2.1.21)$$

$$\epsilon^2 \left(\frac{\partial \hat{w}}{\partial \hat{t}} + \frac{\partial(\hat{u}\hat{w})}{\partial \hat{x}} + \frac{\partial(\hat{w}^2)}{\partial \hat{z}} \right) = -\frac{\partial \hat{p}}{\partial \hat{z}} - \cos \zeta + \epsilon \left(\frac{\partial \hat{\tau}_{xz}}{\partial \hat{x}} \right), \quad (2.1.22)$$

followed by the non-dimensional version of the kinematic conditions (2.1.13) and (2.1.14)

$$\frac{\partial \hat{s}}{\partial \hat{t}} + \hat{u} \frac{\partial \hat{s}}{\partial \hat{x}} - \hat{w} = 0, \quad \text{at } \hat{z} = \hat{s}(\hat{x}, \hat{t}) \quad (2.1.23)$$

$$\frac{\partial \hat{b}}{\partial \hat{t}} + \hat{u} \frac{\partial \hat{b}}{\partial \hat{x}} - \hat{w} = 0, \quad \text{at } \hat{z} = \hat{b}(\hat{x}, \hat{t}), \quad (2.1.24)$$

and finally the components of the traction-free conditions can be written as

$$\epsilon \hat{p} \frac{\partial \hat{s}}{\partial \hat{x}} - \epsilon^2 \hat{\tau}_{xx} \frac{\partial \hat{s}}{\partial \hat{x}} + \hat{\tau}_{xz} = 0, \quad \text{at } \hat{z} = \hat{s}(\hat{x}, \hat{t}), \quad (2.1.25)$$

$$-\hat{p} - \epsilon \hat{\tau}_{xz} \frac{\partial \hat{s}}{\partial \hat{x}} + \epsilon \hat{\tau}_{zz} = 0, \quad \text{at } \hat{z} = \hat{s}(\hat{x}, \hat{t}). \quad (2.1.26)$$

2.1.4 Vertical pressure, stress and velocity profiles

The non-dimensionalised mass conservation (2.1.20) and momentum balances (2.1.21)-(2.1.22) reveal which terms have a dominant effect under the shallowness assumption, i.e. since the aspect ratio is small, each term will contribute less the higher is the power of ϵ multiplying it. At leading order, ϵ^0 , the downslope momentum equation (2.1.21) is dominated by a balance between the gravitational force and variations of the deviatoric stress with the avalanche depth, whilst in the normal direction gravity and pressure gradients dominate the dynamics. Thus, equations (2.1.22) and (2.1.26) give

$$\frac{\partial \hat{p}}{\partial \hat{z}} = -\cos \zeta, \quad \text{and} \quad \hat{p}(\hat{s}) = 0, \quad (2.1.27)$$

which can be integrated with respect to \hat{z} to give

$$\hat{p} = (\hat{s} - \hat{z}) \cos \zeta, \quad (2.1.28)$$

meaning that pressure is linear with flow depth, and, hence, the pressure field is said to be *lithostatic*, in analogy with hydrostatics.

On the other hand, comparing leading-order terms in the tangential momentum equation and traction-free condition, (2.1.21) and (2.1.25), and integrating it with respect to \hat{z} gives

$$\hat{\tau}_{xz} = (\hat{s} - \hat{z}) \sin \zeta, \quad (2.1.29)$$

showing that the dominant component of the stress is also linear through the avalanche depth. The relation above is important in the sense that now we can combine it with the exact functional form for the deviatoric stress, given here by the $\mu(I)$ -rheology relation (2.1.4), to obtain an expression for the velocity profile through the avalanche depth. First, the non-dimensional version of equation (2.1.4) reveals that at leading order the xz component of the deviatoric stress can be written as

$$\hat{\tau}_{xz} = \mu(I)\hat{p} \operatorname{sgn} \left(\frac{\partial \hat{u}}{\partial \hat{z}} \right), \quad (2.1.30)$$

where sgn is the sign function. Note that the equation above is written only in terms $\partial \hat{u} / \partial \hat{z}$ since, at leading order in ϵ , the second invariant of the strain-rate is given by

$$\|\hat{\mathbf{D}}\| = \frac{1}{2} \left| \frac{\partial \hat{u}}{\partial \hat{z}} \right| + O(\epsilon). \quad (2.1.31)$$

Substituting the expressions for the lithostatic pressure and for $\hat{\tau}_{xz}$, equations (2.1.28) and (2.1.29), respectively, into (2.1.30), follows that, at leading order, the equilibrium between gravity and friction leads to

$$\mu(I) = \tan \zeta, \quad (2.1.32)$$

provided that the downstream velocity \hat{u} is an increasing function of the normal coordinate \hat{z} . Since the slope angle is kept constant and the friction is a function of I only, (2.1.32) implies that the inertial number is a constant I_ζ , which, by substituting the expression for $\mu(I)$ (2.1.9) into (2.1.32), is found to be

$$I_\zeta = I_0 \left(\frac{\tan \zeta - \mu_1}{\mu_2 - \tan \zeta} \right). \quad (2.1.33)$$

The definition of the inertial number can be rewritten in terms of non-dimensional variables as

$$I = \frac{2\|\hat{\mathbf{D}}\|\hat{d}}{\sqrt{\Phi}\hat{p}}, \quad (2.1.34)$$

which can be inverted to yield the ordinary differential equation for the velocity profile at leading order in the form

$$\frac{\partial \hat{u}}{\partial \hat{z}} = \frac{I_\zeta \sqrt{\Phi \cos \zeta}}{\hat{d}} (\hat{s} - \hat{z})^{1/2}, \quad (2.1.35)$$

where the expressions for the leading-order second invariant of the strain-rate tensor $\|\hat{\mathbf{D}}\|$ and pressure \hat{p} were plugged in. Integrating equation (2.1.35) and imposing no-slip boundary conditions at the base, reveals the velocity profile through the avalanche depth

$$\hat{u} = \frac{2I_\zeta}{3\hat{d}} \sqrt{\Phi \cos \zeta} \left(\hat{h}^{3/2} - (\hat{s} - \hat{z})^{3/2} \right), \quad (2.1.36)$$

where $(\hat{s} - \hat{b})$ has been replaced by \hat{h} . This Bagnold-like velocity profile, i.e. the scaling of the velocity with \hat{h} to the power $3/2$, is a well-known characteristic of the $\mu(I)$ -rheology which is corroborated by experimental observations and discrete-element method (DEM) simulations of steady uniform granular flows (GDR-MiDi, 2004; Silbert *et al.*, 2003). It is important to note, however, that the convex Bagnold scaling law is a good approximation for thick flows, i.e., $h \gg h_{stop}(\zeta)$, but, as observed in experiments and direct numerical simulations, the vertical velocity profile may transition to a concave profile when the thickness approaches h_{stop} , possibly as a response of cooperative effects becoming more prominent (Kamrin & Henann, 2015; Silbert *et al.*, 2003; Komatsu *et al.*, 2001). The downstream velocity profile depends on the inertial number I_ζ , which has an interesting dependence on the slope angle ζ . It goes to infinity when $\zeta \rightarrow \zeta_2$, and vanishes when $\zeta \rightarrow \zeta_1$. This fact is consistent with the classification of granular states via inertial number that we have discussed in chapter 1, where low inertial number corresponds to a quasi-static regime, whilst for greater values of I the flow assumes higher velocities, characterising a rapid and dilute gaseous state.

2.1.5 Depth-averaged mass and momentum equations

In order to find an effective one-dimensional system of equations we will average the conservation laws, equations (2.1.20)-(2.1.22), through the avalanche depth, and, therefore, obtain a \hat{z} -independent set of equations. This procedure consists in first defining the depth-averaged quantity of a generic field f as

$$\bar{f} = \frac{1}{\hat{h}} \int_{\hat{b}(x,t)}^{\hat{s}(x,t)} f d\hat{z}, \quad (2.1.37)$$

which means that, for example, the depth-averaged velocity is given by

$$\hat{u} = \frac{1}{\hat{h}} \int_{\hat{b}}^{\hat{s}} \hat{u} d\hat{z} = \frac{2I_\zeta}{5\hat{d}} \sqrt{\Phi \cos \zeta} \hat{h}^{3/2}. \quad (2.1.38)$$

Then, mass (2.1.20) and momentum equations (2.1.21)-(2.1.22) can be integrated through the avalanche depth, i.e.,

$$\int_{\hat{b}(\hat{x}, \hat{t})}^{\hat{s}(\hat{x}, \hat{t})} \left[\frac{\partial \hat{u}}{\partial \hat{x}} + \frac{\partial \hat{w}}{\partial \hat{z}} \right] d\hat{z} = 0, \quad (2.1.39)$$

$$\int_{\hat{b}(\hat{x}, \hat{t})}^{\hat{s}(\hat{x}, \hat{t})} \left[\epsilon \left(\frac{\partial \hat{u}}{\partial \hat{t}} + \frac{\partial(\hat{u})^2}{\partial \hat{x}} + \frac{\partial(\hat{u}\hat{w})}{\partial \hat{z}} \right) \right] d\hat{z} = \int_{\hat{b}(\hat{x}, \hat{t})}^{\hat{s}(\hat{x}, \hat{t})} \left[\sin \zeta + \frac{\partial \hat{\tau}_{xz}}{\partial \hat{z}} - \epsilon \frac{\partial \hat{p}}{\partial \hat{x}} + \epsilon^2 \frac{\partial \hat{\tau}_{xx}}{\partial \hat{x}} \right] d\hat{z}, \quad (2.1.40)$$

$$\int_{\hat{b}(\hat{x}, \hat{t})}^{\hat{s}(\hat{x}, \hat{t})} \left[\epsilon^2 \left(\frac{\partial \hat{w}}{\partial \hat{t}} + \frac{\partial(\hat{u}\hat{w})}{\partial \hat{x}} + \frac{\partial(\hat{w})^2}{\partial \hat{z}} \right) \right] d\hat{z} = \int_{\hat{b}(\hat{x}, \hat{t})}^{\hat{s}(\hat{x}, \hat{t})} \left[-\frac{\partial \hat{p}}{\partial \hat{z}} - \cos \zeta + \epsilon \left(\frac{\partial \hat{\tau}_{xz}}{\partial \hat{x}} \right) \right] d\hat{z}, \quad (2.1.41)$$

where one can observe that the limits of integration depend both on \hat{x} and \hat{t} . So, seeking to exchange the order between integration and differentiation to use our definition for depth-averaged quantities (2.1.37), we will use Leibniz' rule, which states that (Abramowitz & Stegun, 1970)

$$\frac{d}{d\alpha} \int_{b(\alpha)}^{s(\alpha)} f dz = \int_{b(\alpha)}^{s(\alpha)} \frac{\partial f}{\partial \alpha} dz + \left[f \frac{\partial z}{\partial \alpha} \right]_{b(\alpha)}^{s(\alpha)}, \quad (2.1.42)$$

identifying that in our case $\alpha = \hat{x}$, \hat{z} or \hat{t} . Hence, mass conservation becomes

$$\frac{\partial}{\partial \hat{x}} \int_{\hat{b}(\hat{x}, \hat{t})}^{\hat{s}(\hat{x}, \hat{t})} \hat{u} d\hat{z} - \left[\hat{u} \frac{\partial \hat{z}}{\partial \hat{x}} \right]_{\hat{b}(\hat{x}, \hat{t})}^{\hat{s}(\hat{x}, \hat{t})} + [\hat{w}]_{\hat{b}(\hat{x}, \hat{t})}^{\hat{s}(\hat{x}, \hat{t})} = 0, \quad (2.1.43)$$

which, using the kinematic conditions (2.1.13)-(2.1.14) and the depth-averaged velocity (2.1.38), gives

$$\begin{aligned} \frac{\partial(\hat{h}\hat{u})}{\partial \hat{x}} + \frac{\partial \hat{s}}{\partial \hat{t}} - \hat{w}^{(\hat{s})} - \frac{\partial \hat{b}}{\partial \hat{t}} + \hat{w}^{(\hat{b})} + [\hat{w}]_{\hat{b}(\hat{x}, \hat{t})}^{\hat{s}(\hat{x}, \hat{t})} = \\ \frac{\partial \hat{h}}{\partial \hat{t}} + \frac{\partial(\hat{h}\hat{u})}{\partial \hat{x}} = 0. \end{aligned} \quad (2.1.44)$$

The averaging process of the LHS of (2.1.21) is extremely similar to the one for the mass balance, so we will focus on the depth-integration of the RHS of (2.1.21). Starting by integrating both sides with respect to \hat{z} and reorganizing terms using the Leibniz

rule gives

$$\begin{aligned}
& \epsilon \left[\frac{\partial(\hat{h}\hat{u})}{\partial t} + \frac{\partial(\hat{h}\hat{u}^2)}{\partial \hat{x}} \right] = \\
& \hat{h} \sin \zeta - \epsilon \frac{\partial(\hat{h}\hat{p})}{\partial \hat{x}} + \epsilon^2 \frac{\partial(\hat{h}\overline{\hat{\tau}_{xx}})}{\partial \hat{x}} - \underbrace{\hat{\tau}_{xz}^{(\hat{b})} + \hat{\tau}_{xz}^{(\hat{s})} + \epsilon \hat{p} \frac{\partial \hat{z}}{\partial \hat{x}} \Big|_{\hat{z}=\hat{s}} - \epsilon^2 \left[\hat{\tau}_{xx} \frac{\partial \hat{z}}{\partial \hat{x}} \right]_{\hat{z}=\hat{s}}}_{= 0 \text{ from (2.1.25)}} \\
& - \left[\hat{p} \frac{\partial \hat{z}}{\partial \hat{x}} \right]^{\hat{z}=\hat{b}} + \epsilon^2 \left[\hat{\tau}_{xx} \frac{\partial \hat{z}}{\partial \hat{x}} \right]^{\hat{z}=\hat{b}} = \\
& \hat{h} \sin \zeta - \hat{\tau}_{xz}^{(\hat{b})} - \epsilon \frac{\partial(\hat{h}\hat{p})}{\partial \hat{x}} - \epsilon \left[\hat{p} \frac{\partial \hat{z}}{\partial \hat{x}} \right]^{\hat{z}=\hat{b}} + \epsilon^2 \frac{\partial(\hat{h}\overline{\hat{\tau}_{xx}})}{\partial \hat{x}} + \epsilon^2 \left[\hat{\tau}_{xx} \frac{\partial \hat{z}}{\partial \hat{x}} \right]^{\hat{z}=\hat{b}}. \quad (2.1.45)
\end{aligned}$$

The last term of (2.1.45) vanishes because no-slip is assumed at the base, and hence $\hat{D}_{xx}^b = 0$. As a result, the incompressibility condition (2.1.1) implies that $\partial \hat{w} / \partial \hat{z} = -\partial \hat{u} / \partial \hat{x} = 0$, and therefore

$$\frac{\hat{D}_{xz}^b}{|\hat{\mathbf{D}}^b|} = \frac{\hat{D}_{xz}^b}{|\hat{D}_{xz}^b|} = \text{sgn}(\hat{D}_{xz}^b) = \text{sgn}\left(\frac{\partial \hat{u}}{\partial \hat{z}}\right) = \text{sgn}(\hat{u}), \quad (2.1.46)$$

where (2.1.35) and (2.1.38) have been used to exchange from the sign of $\partial \hat{u} / \partial \hat{z}$ to the sign of just \hat{u} . Instead of formally expanding the basal friction to first order in ϵ , Gray & Edwards (2014) assumed that gravity balances friction to leading order, but their difference is small, in order to keep these effects at $O(\epsilon)$. Dividing the resultant equation by ϵ , the system of depth-averaged conservation laws can be written as

$$\frac{\partial \hat{h}}{\partial t} + \frac{\partial(\hat{h}\hat{u})}{\partial \hat{x}} = 0, \quad (2.1.47)$$

$$\frac{\partial(\hat{h}\hat{u})}{\partial t} + \frac{\partial}{\partial \hat{x}} \left(\chi \hat{h}\hat{u}^2 \right) + \frac{\partial}{\partial \hat{x}} \left(\frac{1}{2} \hat{h}^2 \cos \zeta \right) = \hat{h}\hat{S}, \quad (2.1.48)$$

where the source term \hat{S} is represented by

$$\hat{S} = \cos \zeta \left(\tan \zeta - \mu(I_\zeta) \text{sgn}(\hat{u}) - \frac{\partial \hat{b}}{\partial \hat{x}} \right), \quad (2.1.49)$$

which is a balance between gravity, the driving force that pushes the avalanche downstream, and resistive effects which split into the basal friction that always opposes the downslope velocity and gradients of the basal topography. The shape factor χ is the ratio between $\overline{\hat{u}^2}$ and \hat{u}^2 , and, hence, depends on the specific functional form of the velocity profile through the depth.

At this stage is worth mentioning that equation (2.1.48) is the traditional shallow-water-type avalanche equation which has been used for several years (e.g. Grigorian *et al.*, 1967; Savage & Hutter, 1989; Gray, 1999; Pouliquen, 1999b; Pouliquen & Forterre, 2002; Gray *et al.*, 2003). Although the theory has been able to model many fundamental physical properties of dense granular flows, some subtle effects, such as cut-off frequencies of granular roll waves (Forterre, 2006; Gray & Edwards, 2014), steady-state selection mechanism in leveed channels (Rocha *et al.*, 2019) and regularisation of segregation-induced fingering (Woodhouse *et al.*, 2012; Baker *et al.*, 2016b), can only be captured by introducing higher-order terms in ϵ .

2.1.6 Adding a depth-averaged viscous-like dissipation

A formal mathematical derivation that takes into account all the contributions up to second order in ϵ should be done by expanding the shallow-water equations consistently up to $O(\epsilon^2)$. In this section we will follow the steps of Gray & Edwards (2014), who instead decided to develop a pragmatic approach, where they retained the contribution from the in-plane deviatoric stress, which includes a higher-order derivative term, introducing a singular perturbation to the system of conservation laws. In order to do that they considered a modified downslope momentum balance in the form

$$\frac{\partial(\hat{h}\hat{u})}{\partial\hat{t}} + \frac{\partial}{\partial\hat{x}}\left(\chi\hat{h}\hat{u}^2\right) + \frac{\partial}{\partial\hat{x}}\left(\frac{1}{2}\hat{h}^2\cos\zeta\right) = \hat{h}\hat{S} + \epsilon\frac{\partial(\hat{h}\hat{\tau}_{xx})}{\partial\hat{x}}, \quad (2.1.50)$$

where we use the $\mu(I)$ -rheology to express the in-plane deviatoric stress as

$$\hat{\tau}_{xx} = \mu(I)\hat{p}\frac{\hat{D}_{xx}}{\|\hat{\mathbf{D}}\|}. \quad (2.1.51)$$

Using the fact that friction balances gravity at leading order, which leads to $\mu(I) = \tan\zeta$, as well as the leading-order velocity profile (2.1.36), we conclude that

$$\hat{D}_{xx} = \frac{\partial\hat{u}}{\partial\hat{x}} = \frac{I_\zeta\sqrt{\Phi}\cos\zeta}{\hat{d}}\left(\hat{h}^{1/2}\frac{\partial\hat{h}}{\partial\hat{x}} - (\hat{s} - \hat{z})^{1/2}\frac{\partial\hat{s}}{\partial\hat{x}}\right), \quad (2.1.52)$$

whilst the second invariant, at leading order, is given by

$$\|\hat{\mathbf{D}}\| = \frac{1}{2}\frac{\partial\hat{u}}{\partial\hat{z}} = \frac{I_\zeta\sqrt{\Phi}\cos\zeta}{2\hat{d}}(\hat{s} - \hat{z})^{1/2}. \quad (2.1.53)$$

Substituting (2.1.52), (2.1.53) and the approximation for the lithostatic pressure (2.1.28) into (2.1.51) allows the in-plane deviatoric stress to be written as

$$\hat{\tau}_{xx} = 2\sin\zeta\left[\hat{h}^{1/2}(\hat{s} - \hat{z})^{1/2}\frac{\partial\hat{h}}{\partial\hat{x}} - (\hat{s} - \hat{z})\frac{\partial\hat{s}}{\partial\hat{x}}\right]. \quad (2.1.54)$$

Taking the average of $\hat{\tau}_{xx}$ through the depth using the definition (2.1.37) gives

$$\begin{aligned}\hat{h}\overline{\hat{\tau}_{xx}} &= 2 \sin \zeta \int_{\hat{b}}^{\hat{s}} \left[\hat{h}^{1/2}(\hat{s} - \hat{z})^{1/2} \frac{\partial \hat{h}}{\partial \hat{x}} - (\hat{s} - \hat{z}) \frac{\partial \hat{s}}{\partial \hat{x}} \right] d\hat{z} \\ &= \frac{1}{3} \hat{h}^2 \sin \zeta \frac{\partial \hat{h}}{\partial \hat{x}} - \hat{h}^2 \sin \zeta \frac{\partial \hat{b}}{\partial \hat{x}},\end{aligned}\quad (2.1.55)$$

where the free surface was eliminated using $\hat{s} = \hat{h} + \hat{b}$. The depth-averaged Bagnold velocity profile (2.1.36) relates the downslope velocity with the thickness of the flow, and, hence, can be used to rewrite the depth-integrated in-plane stress in terms of velocity gradients

$$\hat{h}\overline{\hat{\tau}_{xx}} = \hat{\nu} \hat{h}^{3/2} \frac{\partial \hat{u}}{\partial \hat{x}} - \hat{h}^2 \sin \zeta \frac{\partial \hat{b}}{\partial \hat{x}},\quad (2.1.56)$$

which implies that the coefficient $\hat{\nu}$ is

$$\hat{\nu} = \frac{5\hat{d} \sin \zeta}{9I_\zeta \sqrt{\Phi \cos \zeta}} = \frac{2\mathcal{L} \sin \zeta}{9\beta \sqrt{\cos \zeta}} \left(\frac{\tan \zeta_2 - \tan \zeta}{\tan \zeta - \tan \zeta_1} \right).\quad (2.1.57)$$

In Gray & Edwards's (2014) derivation, the contribution from the basal topography to the in-plane stress, the second term in (2.1.56), is neglected, based on the fact that this term scales with the square of the thickness \hat{h} , which is the smallest characteristic dimension of the flow, and also is of order ϵ . The resultant modified system of conservation laws can be written in terms of dimensional variables as

$$\frac{\partial h}{\partial t} + \frac{\partial(h\bar{u})}{\partial x} = 0\quad (2.1.58)$$

$$\frac{\partial(h\bar{u})}{\partial t} + \frac{\partial}{\partial x} (\chi h \bar{u}^2) + \frac{\partial}{\partial x} \left(\frac{1}{2} g h^2 \cos \zeta \right) = h g S + \frac{\partial}{\partial x} \left(\nu h^{3/2} \frac{\partial \bar{u}}{\partial x} \right),\quad (2.1.59)$$

where

$$S = \cos \zeta \left(\tan \zeta - \mu(I_\zeta) \operatorname{sgn}(\bar{u}) - \frac{\partial b}{\partial x} \right)\quad (2.1.60)$$

is the dimensional source term and the coefficient

$$\nu = \frac{2\mathcal{L} \sqrt{g} \sin \zeta}{9\beta \sqrt{\cos \zeta}} \left(\frac{\tan \zeta_2 - \tan \zeta}{\tan \zeta - \tan \zeta_1} \right),\quad (2.1.61)$$

which has units of $\text{m}^{3/2} \text{s}^{-1}$ and is associated with the depth-averaged granular viscosity $\nu h^{1/2}/2$. It is worth noting that, outside the range of angles $[\zeta_1, \zeta_2]$, ν changes sign and becomes negative. Above the upper limit, when $\zeta > \zeta_2$, gravity exceeds the maximum dynamic friction and any flow accelerates. On the other hand, below the minimum angle, i.e., $\zeta < \zeta_1$, the downslope component of the gravitational force is not enough

to break the yield stress and the material eventually comes to rest. So, it is reasonable that the viscous term derived by Gray & Edwards (2014) is no longer valid outside this range of angles, since no steady uniform flow is possible and, hence, the approximations for the Bagnold velocity profile and inertial number are not valid any more. The in-plane deviatoric stress incorporates a viscous-like term to the resultant momentum equation (2.1.50). For this reason, in order to distinguish the new set of equations from the classical avalanche model (2.1.47)-(2.1.48), hereafter in the thesis we refer to the modified system of conservation laws as the *viscous* depth-averaged model. However, it is important to stress here that this does not mean that the leading-order set of conservation laws (2.1.47)-(2.1.48) considers the granular material as an inviscid fluid. In fact, the main contribution of the granular viscosity, as defined in (2.1.8), to the depth-averaged momentum balance is represented by the basal stress, which is incorporated into the source terms. Despite this fact, throughout the thesis, we will refer to the classic shallow-water-type avalanche model as the *inviscid* depth-averaged theory, as a matter of differentiating the two set of equations.

In the depth-averaged framework, the basal friction law can be characterised empirically in terms of the Froude number and the thickness of the flow by measuring steady uniform flows down inclined planes (Pouliquen, 1999a; Pouliquen & Forterre, 2002; Edwards *et al.*, 2017), following the procedure we discussed in chapter 1. So, before moving forward to the derivation of the two-dimensional version of the depth-averaged viscous model presented in this section, we will discuss how the friction law is constructed.

2.1.7 The basal friction law

In the sense of calibrating a basal friction law that varies with the flow thickness and averaged velocity, Pouliquen (1999a) was the first to propose an empirical friction coefficient by investigating fast steady uniform flows down inclined rough planes. The law was extended to include the low-velocity regime by Pouliquen & Forterre (2002), in order to account for frictional hysteresis, and Edwards *et al.* (2017, 2019) have proposed a modified extended law that also encompasses flows of non-spherical particles.

The experimental procedure applied to calibrate the friction law is the one described in §1.3. After collecting the data for $h_{stop}(\zeta)$, the critical thickness that a

flowing granular layer would arrest at an angle ζ (Pouliquen, 1999a; Pouliquen & Forterre, 2002; Kamrin & Henann, 2015), and for $h_{start}(\zeta)$, which is the critical thickness at which a static granular layer would fail spontaneously at an inclination ζ , the functional form that best fits the data assumes the form (Pouliquen & Forterre, 2002; Edwards *et al.*, 2017)

$$\tan \zeta = \mu_1 + \frac{\mu_2 - \mu_1}{1 + \frac{h_{stop}(\zeta)}{\mathcal{L}}}, \quad (2.1.62)$$

$$\tan \zeta = \mu_3 + \frac{\mu_2 - \mu_1}{1 + \frac{h_{start}(\zeta)}{\mathcal{L}}}, \quad (2.1.63)$$

where $\mu_1 = \tan \zeta_1$, $\mu_2 = \tan \zeta_2$, $\mu_3 = \tan \zeta_3$ and \mathcal{L} are properties of the flowing material and the rough base. For steady uniform flows, where the basal friction balances the downslope component of gravity, i.e.

$$\tan \zeta = \mu, \quad (2.1.64)$$

it is observed empirically that the thickness and the depth-averaged downslope velocity obey a dynamic flow rule (Pouliquen, 1999a; Forterre & Pouliquen, 2003; Edwards *et al.*, 2017)

$$Fr = \frac{|\bar{\mathbf{u}}|}{\sqrt{gh \cos \zeta}} = \beta \frac{h}{h_{stop}(\zeta)} - \Gamma, \quad (2.1.65)$$

where the material parameters β and Γ come from the interaction between the granular material and the rough bed. Inverting the flow rule (2.1.65) to isolate h_{stop} , and substituting the resultant expression into (2.1.62) gives the empirical dynamic friction coefficient (Pouliquen, 1999a; Pouliquen & Forterre, 2002; Forterre & Pouliquen, 2003; Edwards *et al.*, 2017, 2019)

$$\mu_D(h, Fr) = \mu_1 + \frac{\mu_2 - \mu_1}{1 + \frac{h\beta}{\mathcal{L}(Fr + \Gamma)}}. \quad (2.1.66)$$

In the original formulation of Pouliquen (1999a) and Pouliquen & Forterre (2002) $\Gamma = 0$, which is true for flows of spherical glass beads. The modified flow rule, which accounts for other types of granular materials, was first measured by Forterre & Pouliquen (2003), and the non-zero Γ was firstly incorporated to the dynamic friction coefficient by Edwards *et al.* (2017). The dynamic friction law is compatible with the full $\mu(I)$ -rheology, in the sense that it asymptotes a constant μ_2 in the high-velocity

regime, i.e. $Fr \rightarrow \infty$, and reaches a non-zero minimum threshold μ_1 when $Fr \rightarrow 0$. However, as pointed out by Pouliquen (1999a), the empirical law does not impose any constraint on the thickness h , which means, in principle that steady uniform flows would be possible for any value of h . This contradicts the experimental observations that, for a given slope angle, no flow is observed for thickness below h_{stop} . Therefore it was proposed that the dynamic law is only valid for $h > h_{stop}$, or, equivalently, for $Fr > \beta - \Gamma$ (Pouliquen & Forterre, 2002; Forterre & Pouliquen, 2003; Edwards *et al.*, 2019).

The measurements of $h_{start}(\zeta)$ comprise granular layers, which are on the brink of yielding, and, therefore, correspond to the point where gravity has just overpassed the maximum friction able to keep the material static. Therefore, equating (2.1.63) to $\tan \zeta$ reveals the maximum coefficient of static friction (Pouliquen & Forterre, 2002)

$$\mu_{start}(h) = \mu_3 + \frac{\mu_2 - \mu_1}{1 + h/\mathcal{L}}. \quad (2.1.67)$$

Thus, the static friction, increases with the applied stress and balances the resultant force of gravity and pressure, until it reaches the maximum coefficient of static friction given above. Therefore, a complete description of the friction in the static state is that (Pouliquen & Forterre, 2002)

$$\mu_S = \min(\mu_{start}, |\tan \zeta \mathbf{i} - \nabla h|), \quad (2.1.68)$$

where \mathbf{i} is the unit vector in the downslope direction and ∇h relates to the force due to pressure differences that arise from gradients of the free surface.

These two frictional regimes, static and dynamic, are well captured in simple steady uniform flow experiments since they represent stable equilibria of the system, i.e., the equilibrium state can be sustained for long times experimentally, allowing the relevant quantities to be measured in order to characterise the friction law. In the low-velocity regime, however, experiments show a variety of complex patterns, where creeping and instabilities start to develop and the characterisation of the friction law is somewhat fuzzy. For dry frictional systems, it has been observed that the transition from an inertial regime, where the flow is steady and uniform, to a creep-dominated low-velocity regime characterises a changing in frictional behaviour, from velocity strengthening to velocity weakening (Heslot *et al.*, 1994). Pouliquen & Forterre (2002) then proposed

an extended friction law that interpolates from the dynamic friction at $Fr = \beta$ to the maximum static friction coefficient at zero Froude number, following the power law

$$\mu_I(h, Fr) = \left(\frac{Fr}{\beta}\right)^\kappa (\mu_D(h, \beta) - \mu_{start}(h)) + \mu_{start}(h), \quad (2.1.69)$$

where β is the parameter coming from the steady uniform flow rule and κ determines the exact shape of the interpolation. Pouliquen & Forterre (2002) have investigated the effect of κ to the modelling of a finite-mass release down an inclined rough plane, and found that for $\kappa < 10^{-2}$ the results of the model were insensitive to changes in κ , so the authors used $\kappa = 10^{-3}$ in their numerical simulations.

The discussion of how friction exactly behaves in the velocity-weakening regime and how it precisely transitions from the inertial regime is still under debate. Investigating a flow of irregular beads of carborundum over erodible beds, Edwards *et al.* (2017) realised that for flows where $\beta < \Gamma$ the law proposed by Pouliquen & Forterre (2002) would predict that the transition between dynamic and intermediate friction would occur for a negative Froude number. Since the Froude number is, by definition, a positive quantity this means that friction obeys the dynamic law for all possible values of Fr , and, hence, hysteresis is eliminated. Instead, to account for these type of materials Edwards *et al.* (2019) proposed that the transition between dynamic and intermediate friction occurs at $Fr = \beta_* > 0$, or, equivalently at $h = h_* > h_{stop}(\zeta)$, enforcing the existence of an hysteretic region for all types of flows. The way β_* and h_* are defined and how they are incorporated in the friction law will be discussed in chapter 3.

In summary, the extended friction law that incorporates frictional hysteresis can be written as

$$\mu(h, Fr) = \begin{cases} \mu_D, & Fr \geq Fr_t \\ \left(\frac{Fr}{Fr_t}\right)^\kappa (\mu_D(h, Fr_t) - \mu_{start}(h)) + \mu_{start}(h), & 0 < Fr \leq Fr_t, \\ \mu_S, & Fr = 0, \end{cases} \quad (2.1.70)$$

where μ_D and μ_S are given by (2.1.66) and (2.1.68), respectively. The structure of the dynamic and static friction law is similar in the formulations of Pouliquen & Forterre (2002) and Edwards *et al.* (2019), with the main difference being the transition Froude number Fr_t and the value of the power-law exponent κ , which changes significantly

the functional form of intermediate friction. In the vast majority of this thesis we will use the friction law of Edwards *et al.* (2019), i.e. equation (2.1.70) with $Fr_t = \beta_*$ and $\kappa = 1$. However, in chapter 5, where we will investigate the kinematics of bidisperse granular roll waves, which are triggered for high Froude numbers (Forterre & Pouliquen, 2003; Gray & Edwards, 2014; Viroulet *et al.*, 2018), only the dynamic law will be applied.

Now that we have a complete one-dimensional viscous depth-averaged model, and also know how to calibrate the extended friction law to incorporate hysteresis into the model, we can move forward and extend the results discussed so far to two dimensions.

2.2 Two-dimensional depth-averaged $\mu(I)$ -rheology

In order to construct a two-dimensional version of the viscous depth-averaged model derived in the previous section, consider a three-dimensional Cartesian coordinate system $Oxyz$, where the xz -plane is the same as illustrated in figure 2.1, whilst y is the cross slope direction inward to the plane of the paper. If the depth-averaged velocity field $\bar{\mathbf{u}}$ has components (\bar{u}, \bar{v}) in the (x, y) directions, respectively, and the basal topography is assumed to be rigid and flat, i.e. $\partial b/\partial x = \partial b/\partial y = 0$, the two-dimensional depth-averaged mass and momentum equations are

$$\frac{\partial h}{\partial t} + \nabla \cdot (h\bar{\mathbf{u}}) = 0 \quad (2.2.1)$$

$$\frac{\partial(h\bar{\mathbf{u}})}{\partial t} + \nabla \cdot (\chi h\bar{\mathbf{u}} \otimes \bar{\mathbf{u}}) + \nabla \cdot \left(\frac{1}{2} gh^2 \cos \zeta \right) = gh\mathbf{S} + \frac{1}{\rho} \nabla \cdot (h\bar{\boldsymbol{\tau}}), \quad (2.2.2)$$

where

$$S_x = \cos \zeta \left(\tan \zeta - \mu_b \frac{\bar{u}}{|\bar{\mathbf{u}}|} \right) \quad \text{and} \quad S_y = -\cos \zeta \left(\mu_b \frac{\bar{v}}{|\bar{\mathbf{u}}|} \right). \quad (2.2.3)$$

Motivated by Gray & Edwards's (2014) derivation for the viscous term and its success to model the cutoff frequency of granular roll waves, Baker *et al.* (2016a) proposed a generalised tensorial version to the depth-averaged in-plane deviatoric stress in the form

$$h\bar{\boldsymbol{\tau}} = \rho\nu h^{3/2} \bar{\mathbf{D}}, \quad (2.2.4)$$

where $\bar{\boldsymbol{\tau}}$ and $\bar{\mathbf{D}}$ are the depth-averaged deviatoric stress and strain-rate, respectively, ρ is the bulk density and ν the coefficient associated to the depth-averaged viscosity,

which is given by (2.1.61). First of all, it is straightforward to verify that (2.2.4) is in complete agreement with Gray & Edwards's (2014) formulation, and the momentum balance (2.2.2) reduces to (2.1.59) in the one dimensional limit. Moreover, the deviatoric stress is part of the constitutive relation of granular materials and, therefore, must be invariant under changes of observers which preserves structures of space and time, i.e. it satisfies the principle of objectivity in a depth-averaged sense. So, assuming that $\bar{\boldsymbol{\tau}}$ is a symmetric-valued tensorial function \mathbf{F} of $\bar{\mathbf{L}} = \nabla \bar{\mathbf{u}}$ in the form

$$h\bar{\boldsymbol{\tau}} = \mathbf{F}(\bar{\mathbf{L}}) = \frac{\nu h^{3/2}}{2} (\bar{\mathbf{L}} + \bar{\mathbf{L}}^T), \quad (2.2.5)$$

which satisfy objectivity since (Chadwick, 1976)

$$\mathbf{F}(\mathbf{Q}\bar{\mathbf{L}}\mathbf{Q}^T + \boldsymbol{\Omega}) = [\mathbf{Q}\bar{\mathbf{L}}\mathbf{Q}^T + \boldsymbol{\Omega} + (\mathbf{Q}\bar{\mathbf{L}}\mathbf{Q}^T + \boldsymbol{\Omega})^T] = \mathbf{Q}\mathbf{F}(\bar{\mathbf{L}})\mathbf{Q}^T, \quad (2.2.6)$$

for any skew-symmetric and orthogonal tensors $\boldsymbol{\Omega}$ ($\boldsymbol{\Omega}^T = -\boldsymbol{\Omega}$) and \mathbf{Q} ($\mathbf{Q}^T = \mathbf{Q}$), respectively. It is worth noting that Baker *et al.* (2016a) assumed that the coefficient ν is the same for the viscous-like dissipation in different directions. In principle these coefficients could be different in the downslope and cross-slope momentum balances, or be a function of the depth-averaged velocity and change when friction changes from dynamic to intermediate regime. However, as in Baker *et al.* (2016a), in the course of this thesis we will consider that the coefficient associated with the depth-averaged granular viscosity is homogeneous through the flow, and defined as in equation (2.1.61).

Substituting (2.2.4) into (2.2.1) and (2.2.2) yields the resultant depth-averaged mass conservation equation

$$\frac{\partial h}{\partial t} + \frac{\partial}{\partial x}(h\bar{u}) + \frac{\partial}{\partial y}(h\bar{v}) = 0, \quad (2.2.7)$$

whilst the x and y component of the momentum balance are given by

$$\begin{aligned} \frac{\partial}{\partial t}(h\bar{u}) + \frac{\partial}{\partial x}(\chi h\bar{u}^2) + \frac{\partial}{\partial y}(\chi h\bar{u}\bar{v}) + \frac{\partial}{\partial x} \left(\frac{1}{2}gh^2 \cos \zeta \right) = \\ ghS_x + \frac{\partial}{\partial x} \left(\nu h^{3/2} \frac{\partial \bar{u}}{\partial x} \right) + \frac{\partial}{\partial y} \left(\frac{1}{2}\nu h^{3/2} \left(\frac{\partial \bar{u}}{\partial y} + \frac{\partial \bar{v}}{\partial x} \right) \right) \end{aligned} \quad (2.2.8)$$

$$\begin{aligned} \frac{\partial}{\partial t}(h\bar{v}) + \frac{\partial}{\partial x}(\chi h\bar{u}\bar{v}) + \frac{\partial}{\partial y}(\chi h\bar{v}^2) + \frac{\partial}{\partial y} \left(\frac{1}{2}gh^2 \cos \zeta \right) = \\ ghS_y + \frac{\partial}{\partial x} \left(\frac{1}{2}\nu h^{3/2} \left(\frac{\partial \bar{u}}{\partial y} + \frac{\partial \bar{v}}{\partial x} \right) \right) + \frac{\partial}{\partial y} \left(\nu h^{3/2} \frac{\partial \bar{v}}{\partial y} \right), \end{aligned} \quad (2.2.9)$$

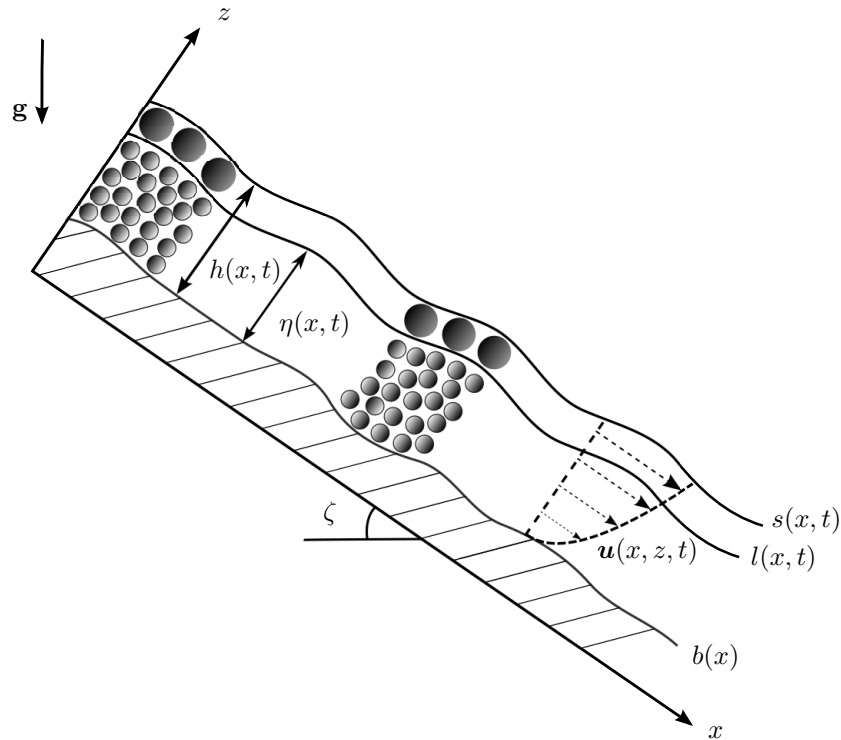


Figure 2.2: Schematic representation of the avalanche. An inverse graded configuration is assumed for the whole flow with an upper layer of large particles between $l(x, t)$ and the free surface $s(x, t)$. The finer grains flows in the middle between the basal topography $b(x)$ and $l(x, t)$. The thickness of flow is defined as $h(x, t) = s(x, t) - b(x)$ whilst the layer of small particles is $\eta(x, t) = l(x, t) - b(x)$ thick. The chute is inclined at an angle ζ to the horizontal, \mathbf{g} is the gravitational acceleration and $\mathbf{u}(x, z, t)$ the velocity field of the material.

with S_x and S_y being the down- and cross-slope components of the source term, which are determined by (2.2.3). The conservation laws (2.2.7)-(2.2.9) govern the dynamics of a monodisperse granular material flowing down an inclined rough plane, which will be used to model granular self-channelisation in chapter 3.

2.3 Depth-averaged model for particle-size segregation in bidisperse flows

In chapter 5, we will investigate the effect of particle-size segregation in the formation of granular roll waves. So, in addition to the conservation of mass and balance of momentum that we have discussed earlier in this chapter, the theoretical approach adds an extra conservation law for the depth-averaged concentration, which accounts

for segregation. The idea of this section is then to revisit the derivation of Gray & Kokelaar (2010b,a) and Baker *et al.* (2016b) of a depth-averaged model for gravity-driven segregation in one and two dimensions, and discuss how it can be coupled with the conservation laws discussed previously.

We start by considering a rectangular coordinate system with x pointing in the downslope direction and z being the upward direction perpendicular to the chute, as shown in Fig. 2.2. Again, the velocity field \mathbf{u} has components (u, w) in the (x, z) and the avalanche has thickness $h(x, t) = s(x, t) - b(x)$, where $s(x, t)$ is the free surface and $b(x)$ represents the basal topography. Note that here we are assuming that the base changes along the chute but not with time. In a bidisperse system, since $\phi^s + \phi^l = 1$, the dynamics of how the concentration of each species, large and small, evolve in space and time can be described by the concentration of small particles $\phi \in [0, 1]$, which obeys an advection-segregation-diffusion equation (Bridgwater, 1976; Savage & Lun, 1988; Dolgunin & Ukolov, 1995; Gray & Chugunov, 2006; Gray & Ancy, 2011) given by

$$\frac{\partial \phi}{\partial t} + \frac{\partial(\phi u)}{\partial x} + \frac{\partial(\phi w)}{\partial z} = \frac{\partial Q(\phi)}{\partial z} + \frac{\partial}{\partial z} \left(D \frac{\partial \phi}{\partial z} \right). \quad (2.3.1)$$

The terms on the left-hand-side take into account the transport of the concentration ϕ due to the bulk flow, whilst, on the right-hand-side, the first term addresses segregation effects, and, hence, must vanish in the monodisperse limit ($Q(\phi) \geq 0$ is zero for $\phi = 0$ or $\phi = 1$), whereas the second term accounts for diffusion with D being the diffusivity.

Using the same idea as in § 2.1.2, where the basal topography and the free surface are described by functions identically zero, whose material derivatives are also zero. However, since the base now does not depend on time, kinematic boundary conditions are expressed as

$$u \frac{\partial b}{\partial x} - w = 0, \quad \text{at } z = b(x), \quad (2.3.2)$$

$$\frac{\partial s}{\partial t} + u_s \frac{\partial s}{\partial x} - w_s = 0, \quad \text{at } z = s(x, t), \quad (2.3.3)$$

plus there is no flux of large or small particles at the boundaries, which means that

$$Q(\phi) + D \frac{\partial \phi}{\partial z} = 0, \quad \text{at } z = b(x) \quad \text{and} \quad z = s(x, t). \quad (2.3.4)$$

As proposed by Gray & Kokelaar (2010b,a), equation (2.3.1) can be depth-averaged, using Leibniz' rule (2.1.42) to swap the order integration and differentiation, which

gives

$$\frac{\partial(h\bar{\phi})}{\partial t} + \frac{\partial(h\bar{\phi}u)}{\partial x} - \underbrace{\left[\phi \left(\frac{\partial z}{\partial t} + u \frac{\partial z}{\partial x} - w \right) \right]_{b(x)}^{s(x,t)}}_{=0 \text{ from (2.3.2)-(2.3.3)}} = \underbrace{\left[Q(\phi) + D \frac{\partial \phi}{\partial z} \right]_{b(x)}^{s(x,t)}}_{=0 \text{ from (2.3.4)}}, \quad (2.3.5)$$

where the definition of depth-averaged quantities is the same as in § 2.1.5 and, hence, the depth-averaged segregation equation is given by

$$\frac{\partial}{\partial t} (h\bar{\phi}) + \frac{\partial}{\partial x} (h\bar{\phi}u) = 0. \quad (2.3.6)$$

In order to close the conservation law (2.3.6), one needs to know how the depth-averaged concentration $\bar{\phi}$ relates to the flux $\bar{\phi}u$. Following Baker *et al.* (2016b), we assume that

$$u(x, z, t) = \bar{u}(x, t)f(\hat{z}) \quad (2.3.7)$$

where $\hat{z} = (z - b)/h$ is a re-scaled vertical position in the flow, and $f(\hat{z})$ is the vertical shear profile. Besides of being a monotonically increasing function of \hat{z} , $f(\hat{z})$ should also satisfy

$$\int_0^1 f(\hat{z})d\hat{z} = 1, \quad (2.3.8)$$

to be coherent with the definition for the depth-averaged velocity. In addition, motivated by experimental observations (Gray & Hutter, 1997; Gray & Ancy, 2009), we assume here, as in Gray & Kokelaar (2010a,b), that the upper layer is composed purely of large particles, whilst the smaller ones are confined underneath, in a layer of depth $\eta(x, t) = l(x, t) - b(x)$ all along the chute (figure 2.2). Therefore, the concentration has a vertical profile, which can be written as

$$\phi = \begin{cases} 0, & \text{if } l(x, t) < z < s(x, t), \\ 1, & \text{if } b(x) < z < l(x, t), \end{cases} \quad (2.3.9)$$

for all values of x . Note that integrating the vertical small-particle concentration profile (2.3.9) through the avalanche depth and using the definition (2.1.37) reveals that, under the assumption of an inversely-graded concentration profile uniform in x , the thickness of the layer of small particles is $\eta(x, t) = l(x, t) - b(x) = h\bar{\phi}$.

Using (2.3.9) and (2.3.7) the depth-averaged flux becomes

$$\bar{\phi}u = \frac{1}{h} \int_{b(x)}^{s(x,t)} \phi u(x, z, t) dz = \quad (2.3.10)$$

$$= \bar{u}(x, t) \int_0^{\eta/h} f(\hat{z}) d\hat{z} = \bar{u}(x, t) \int_0^{\bar{\phi}} f(\hat{z}) d\hat{z} \quad (2.3.11)$$

and the depth-averaged segregation equation finally is given by

$$\frac{\partial(h\bar{\phi})}{\partial t} + \frac{\partial(h\bar{\phi}\bar{u})}{\partial x} - \frac{\partial}{\partial x} (h\bar{u}G(\bar{\phi})) = 0, \quad (2.3.12)$$

where

$$G(\bar{\phi}) = \bar{\phi} - \int_0^{\bar{\phi}} f(\hat{z}) d\hat{z}. \quad (2.3.13)$$

Equation (2.3.12) governs the evolution of the concentration of small particles $\bar{\phi}$, with its first two terms stemming from the advection of grains with the bulk flow and the third addresses the preference of large grains to reach the front whilst finer ones are sheared to the rear. This derivation as followed here was firstly presented by Baker *et al.* (2016*b*) and represents a general transport equation for a homogeneously inverse-graded concentration profile, in which the transport function $G(\bar{\phi})$ strongly depends on the specific vertical shear profile $f(\hat{z})$. The depth-averaged segregation equation can be extended to two spatial dimensions, using the same coordinate system as in § 2.2, which results in a generalised segregation equation in the form (Baker *et al.*, 2016*a*)

$$\frac{\partial}{\partial t} (h\bar{\phi}) + \nabla \cdot (h\bar{\mathbf{u}}\bar{\phi}) - \nabla \cdot (h\bar{\mathbf{u}}G(\bar{\phi})) = 0. \quad (2.3.14)$$

In order to solve the evolution equation for depth-averaged concentration of small particles $\bar{\phi}$, (2.3.14), one needs to know the depth-averaged velocity $\bar{\mathbf{u}}$ and thickness h profiles of the flow. In some cases, information may be extracted from experiments and these fields, h and $\bar{\mathbf{u}}$, are then prescribed based on experimental data (e.g. Johnson *et al.*, 2012). In most situations, however, the velocity field and thickness profile are unknowns that can be computed by solving mass conservation and momentum balance, equations (2.2.7) and (2.2.8)-(2.2.9), respectively. Nevertheless, as the grains segregate and the depth-averaged concentration evolves in space and time, it has a strong feedback in the bulk flow, which may lead to segregation-induced fingering (Pouliquen *et al.*, 1997; Pouliquen & Vallance, 1999; Woodhouse *et al.*, 2012; Baker *et al.*, 2016*b*), bulbous head formation (Denissen *et al.*, 2019) and large-rich levees (Kokelaar *et al.*, 2014). This segregation-mobility feedback can be taken into account by introducing a $\bar{\phi}$ dependence in the coefficient of basal friction, such that (Pouliquen & Vallance, 1999; Woodhouse *et al.*, 2012; Baker *et al.*, 2016*b*)

$$\mu_b(h, Fr, \bar{\phi}) = \bar{\phi}\mu_b^S(h, Fr) + (1 - \bar{\phi})\mu_b^L(h, Fr), \quad (2.3.15)$$

where μ_b^S and μ_b^L are the basal friction law for the small and large constituent, respectively, which can be characterised by (2.1.70) for each type of particle. In the same way, the changing in local concentration also affects the depth-averaged viscous term, by having an influence on the coefficient ν associated with the depth-integrated viscosity. Following the same idea as for the basal friction, Baker *et al.* (2016b) assumed as a sensible choice to consider a concentration-weighted law in the form

$$\nu(\bar{\phi}) = \bar{\phi}\nu^S + (1 - \bar{\phi})\nu^L, \quad (2.3.16)$$

in which $\nu^{\mathcal{N}}$ ($\mathcal{N} = S, L$) is given by the expression derived by Gray & Edwards (2014), expression (2.1.61), for the respective parameters, \mathcal{L} , β , μ_1 and μ_2 , for each type of particles. This approach fully couples the segregation equation with the momentum balance, and, although it seems to be the most realistic thing to do, it considerably enhances the mathematical complexity of the equations, and the only way to extract physical information of the flow is by using sophisticated numerical methods able solve the coupled system of conservation laws.

A possible way to take into account that the flow is composed of different-sized particles, but to keep the mathematical simplicity is to average the parameters in the friction law (2.1.70) and the steady uniform flow rule (2.1.65) using the total concentration of each type particles in the mixture $\bar{\phi}_0$, which is constant. By doing so, mass and momentum equations for the bulk are decoupled from the depth-averaged segregation equation and the velocity and thickness profiles can be computed independently of the local concentration $\bar{\phi}(x, t)$. This method will be used in this thesis to investigate the kinematics of bidisperse granular roll waves in chapter 5. Obviously, this simpler approach will not have the same quantitative precision as the fully coupled, but they can be very useful to gain some insight on the effect of size segregation, keeping the mathematical simplicity.

Now, we have discussed the governing equations, mass conservation, momentum balance and the depth-averaged segregation equation, and how these equations couple to take into account the mobility feedback introduced when the flow is composed of particles with different sizes. These conservation laws in one and two dimensions will be the backbone of the theoretical model, which will be used to investigate the systems presented hereafter in this thesis. So, having said that, we are ready to start!

3 | Self-channelisation and levee formation in monodisperse granular flows

This chapter is a reprint of the article titled “Self-channelisation and levee formation in monodisperse granular flows” by F. M. Rocha, C. G. Johnson and J. M. N. T. Gray, which was published in the volume **867** of the Journal of Fluid Mechanics (2019), pages 591–641. The article is an Open Access article, distributed under the terms of the Creative Commons Attribution licence (<http://creativecommons.org/licenses/by/4.0/>), which permits unrestricted re-use, distribution, and reproduction in any medium, provided the original work is properly cited. The digital object identifier (DOI) for this article is doi:10.1017/jfm.2019.518.

Self-channelisation and levee formation in monodisperse granular flows

F. M. Rocha¹, C. G. Johnson¹ and J. M. N. T. Gray^{1†}

¹School of Mathematics and Manchester Centre for Nonlinear Dynamics,
University of Manchester, Oxford Road, Manchester M13 9PL, UK

(Received 16 July 2018; revised 19 June 2019; accepted 21 June 2019;
first published online 05 August 2019)

Dense granular flows can spontaneously self-channelise by forming a pair of parallel-sided static levees on either side of a central flowing channel. This process prevents lateral spreading and maintains the flow thickness, and hence mobility, enabling the grains to run-out considerably further than a spreading flow on shallow slopes. Since levees commonly form in hazardous geophysical mass flows, such as snow avalanches, debris-flows, lahars and pyroclastic flows, this has important implications for risk management in mountainous and volcanic regions. In this paper an avalanche model that incorporates frictional hysteresis, as well as depth-averaged viscous terms derived from the $\mu(I)$ -rheology, is used to quantitatively model self-channelisation and levee formation. The viscous terms are crucial for determining a smoothly varying steady-state velocity profile across the flowing channel, which has the important property that it does not exert any shear-stresses at the levee-channel interfaces. For a fixed mass flux, the resulting boundary value problem for the velocity profile also uniquely determines the width and height of the channel, and the predictions are in very good agreement with existing experimental data for both spherical and angular particles. It is also shown that in the absence of viscous (second-order gradient) terms, the problem degenerates, to produce plug-flow in the channel with two frictionless contact discontinuities at the levee-channel margins. Such solutions are not observed in experiments. Moreover, the steady-state inviscid problem lacks a thickness or width selection mechanism and consequently there is no unique solution. The viscous theory is therefore a significant step forward. Fully time-dependent numerical simulations to the viscous model are able to quantitatively capture the process in which the flow self-channelizes and show how the levees are initially emplaced behind the flow head. Both experiments and numerical simulations show that the height and width of the channel

† Email address for correspondence: nico.gray@manchester.ac.uk

are not necessarily fixed by these initial values, but respond to changes in the supplied mass flux, allowing narrowing and widening of the channel long after the initial front has passed by. In addition, below a critical mass flux the steady-state solutions become unstable and time-dependent numerical simulations are able to capture the transition to periodic erosion-deposition waves observed in experiments.

Key words: granular media, rheology, shallow water flows

1. Introduction

Self-channelisation and levee formation can occur in a wide range of geophysical mass flows that take place in volcanic and mountainous regions throughout the world. These include highly mobile and destructive pyroclastic flows (Wilson & Head 1981; Rowley, Kuntz & MacLeod 1981; Branney & Kokelaar 1992; Calder, Sparks & Gardeweg 2000; Jessop *et al.* 2012), water-saturated lahars (Vallance 2000; Vallance & Iverson 2015) and debris flows (Sharp & Nobles 1953; Costa & Williams 1984; Pierson 1986; Iverson 1997; Major 1997) as well as wet snow avalanches (Jomelli & Bertran 2001; Ancey 2012; Bartelt *et al.* 2012; Schweizer *et al.* 2014). Although these flows vary greatly in composition, a unifying feature is that, on shallow slopes, they spontaneously form static parallel-sided levees that bound a central flowing channel. The static levees prevent lateral spreading, allowing deeper flows to be sustained for longer than a spreading flow, and thereby increase the flow's mobility and its eventual run-out distance.

Although the mobility of grains is important for both industrial and geophysical applications, modelling the self-channelisation process still presents a significant theoretical challenge. This is firstly because it is a particularly subtle test of the granular rheology, since the flow spontaneously selects its own width, rather than being laterally unconfined or having the width imposed by sidewalls. Secondly, it also raises fundamental questions about how static and flowing regions can coexist, which is a longstanding issue in modelling granular materials. Although this paper is motivated by complex geophysical granular flows, it is focussed on determining the simplest possible formulation that will capture the levee formation process in

quasi-monodisperse dry granular flows (Félix & Thomas 2004; Deboeuf *et al.* 2006; Takagi, McElwaine & Huppert 2011).

In order to narrow down the physical mechanisms required for levee formation, Félix & Thomas (2004) performed small-scale experiments with 300–400 μm spherical dry glass beads that were steadily released from a point source onto an inclined plane roughened with a glued layer of 425–600 μm glass beads, to ensure that there was no slip at the base. For illustration, a similar experiment using 160–200 μm red sand on a bed of turquoise ballotini (750–1000 μm) is shown in figures 1 and 2 as well as supplementary movie 1 (online). Both of these sets of experiments are dry and have a very narrow range of particle sizes, but, as Félix & Thomas (2004) showed, static levees still form. This suggests that neither interstitial fluid nor particle-size segregation are essential to the self-channelisation process, although they may strongly enhance its effects (Pouliquen, Delour & Savage 1997; Pouliquen & Vallance 1999; Félix & Thomas 2004; Goujon, Dalloz-Dubrujeaud & Thomas 2007; Iverson *et al.* 2010; Woodhouse *et al.* 2012; Kokelaar, Graham, Gray & Vallance 2014; Baker, Johnson & Gray 2016*b*).

A self-channelised leveed flow has three distinct phases of motion (Félix & Thomas 2004) as illustrated in figure 2(a–c) respectively and supplementary movie 1. As grains flow down the incline they form a fully mobilised head at the front of the flow, which propagates at a constant speed and lies downslope of the levees. The downslope velocity is greatest in the surface layers in the centre of the channel (Jop, Forterre & Pouliquen 2005; Kokelaar *et al.* 2014; Baker, Barker & Gray 2016*a*). This region therefore transports grains towards the flow head, but when the grains reach the front they lose their confinement and spread out. Some of the grains are over-run by the flow itself, while others are advected to the sides and come to rest, extending the static levees (Johnson *et al.* 2012), which advance downslope at the back of the head (figures 1 and 2a).

The flow within the head is slightly deeper than that in the channel (Félix & Thomas 2004), so as the head passes by there is a small decrease in flow thickness and the levees stabilize, selecting a width for the channel (figure 2b). For sufficiently wide flows the central channel is of almost constant thickness (Félix & Thomas 2004), but in narrower channels the flow may have a pronounced cross-slope

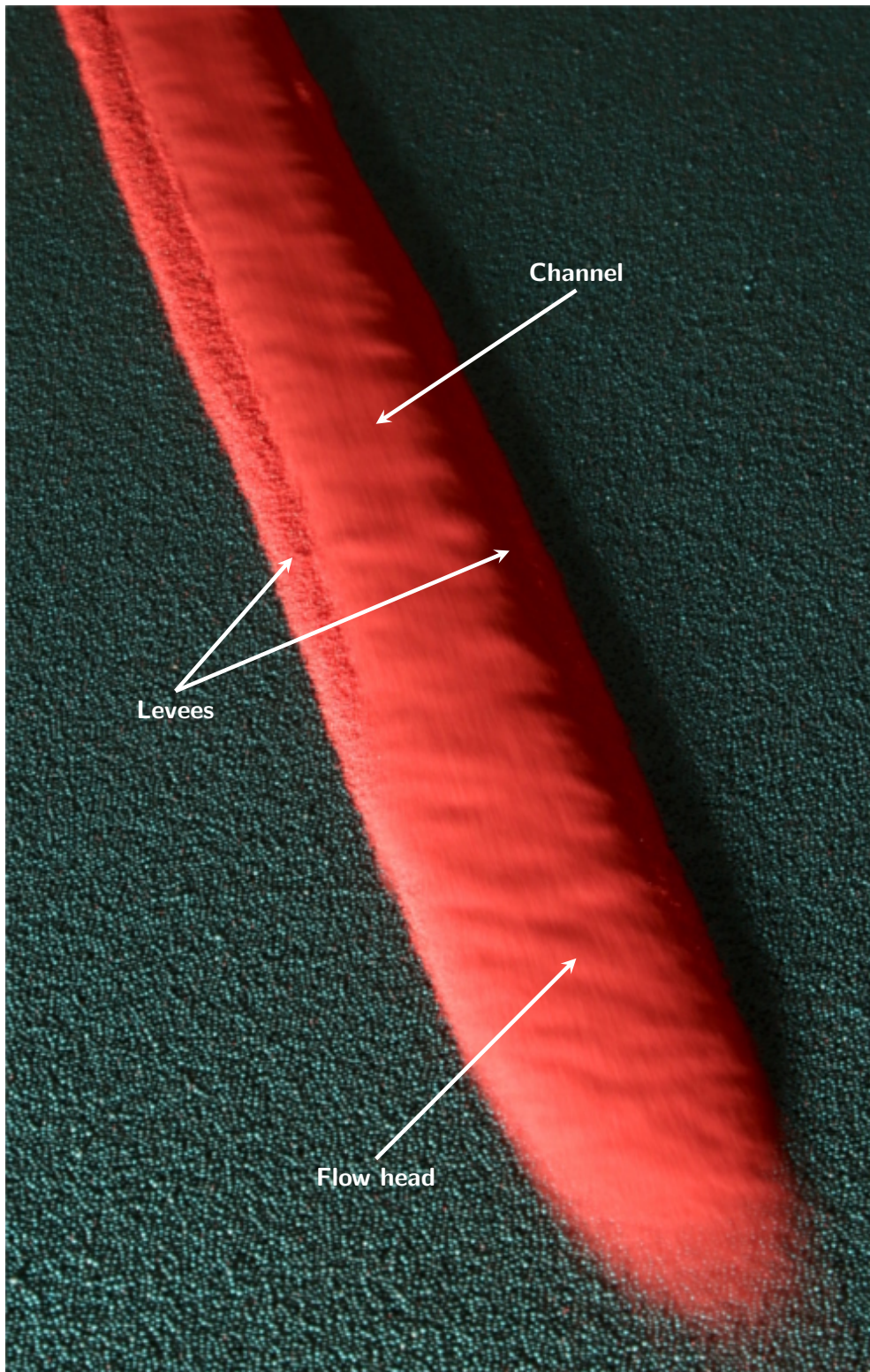


FIGURE 1. An oblique view of a self-channelled leaved flow of 160–200 μm red sand on a plane roughened with a layer of 750–1000 μm turquoise spherical ballotini and inclined at $\zeta = 34^\circ \pm 0.1^\circ$. The granular material is released from a funnel at the top of the chute, and a self-channelled flow rapidly develops, which moves down the plane at constant speed. The grains spontaneously select a flowing channel width $W = 3.60 \pm 0.05$ cm and the total width of the levees and the channel is $W_{total} = 5.00 \pm 0.05$ cm. A long shutter time is used to blur the moving grains and thus highlight the parallel-sided static levees where the grains are in sharp focus. The steady-state mass flux $Q_M = 8.6 \pm 0.1$ g/s is measured as the grains flow off the end of the chute. A movie showing the time-dependent evolution is available in the online supplementary material (movie 1).

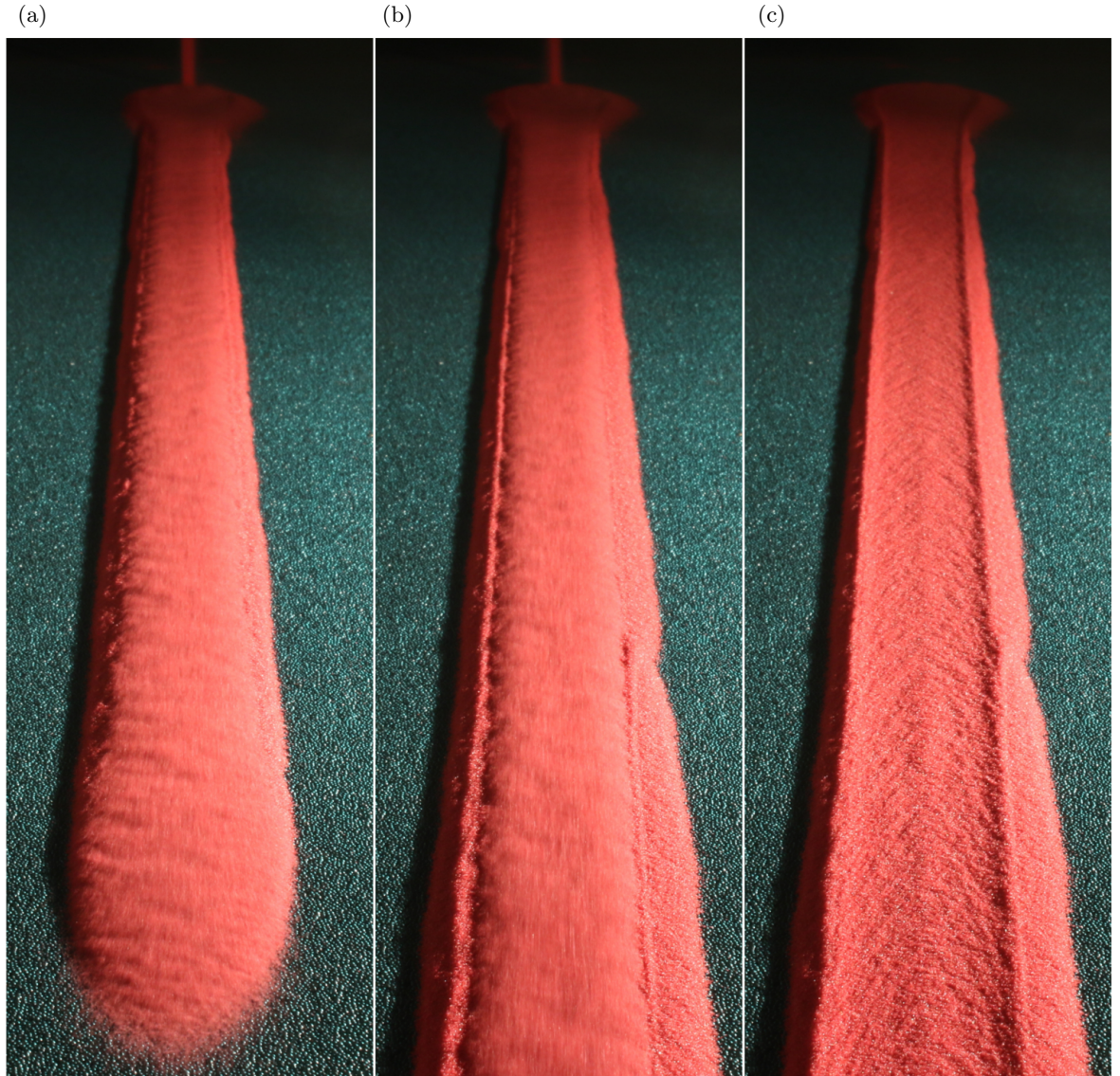


FIGURE 2. Photographs of a self-channelised leveed flow of 160–200 μm red sand on a rough plane inclined at $\zeta = 34^\circ \pm 0.1^\circ$. They show (a) the flow front propagating down the plane and forming static parallel-sided levees just behind the head, (b) the steady-state fully developed levee-channel morphology and (c) the static partially drained channel, which forms when the inflow ceases. Grains are supplied from a funnel near the top of the plane (a,b) with a mass flux $Q_M = 8.6 \pm 0.1$ g/s. The central flowing channel very rapidly selects its own width $W = 3.60 \pm 0.05$ cm and the total width of the channel and the static levees is $W_{total} = 5.00 \pm 0.05$ cm. A movie showing the time-dependent evolution is available in the online supplementary material (movie 1).

gradient in the free surface (Félix & Thomas 2004; Takagi *et al.* 2011), with the deepest flow in the centre of the channel. This gradient may be an indication that normal stress differences are an important component of the underlying granular rheology (McElwaine, Takagi & Huppert 2012). Once the parallel-sided levee-channel morphology has been established, it persists until the inflow ceases and the channel then partially drains to leave pronounced levee walls on either side of a thinner deposit

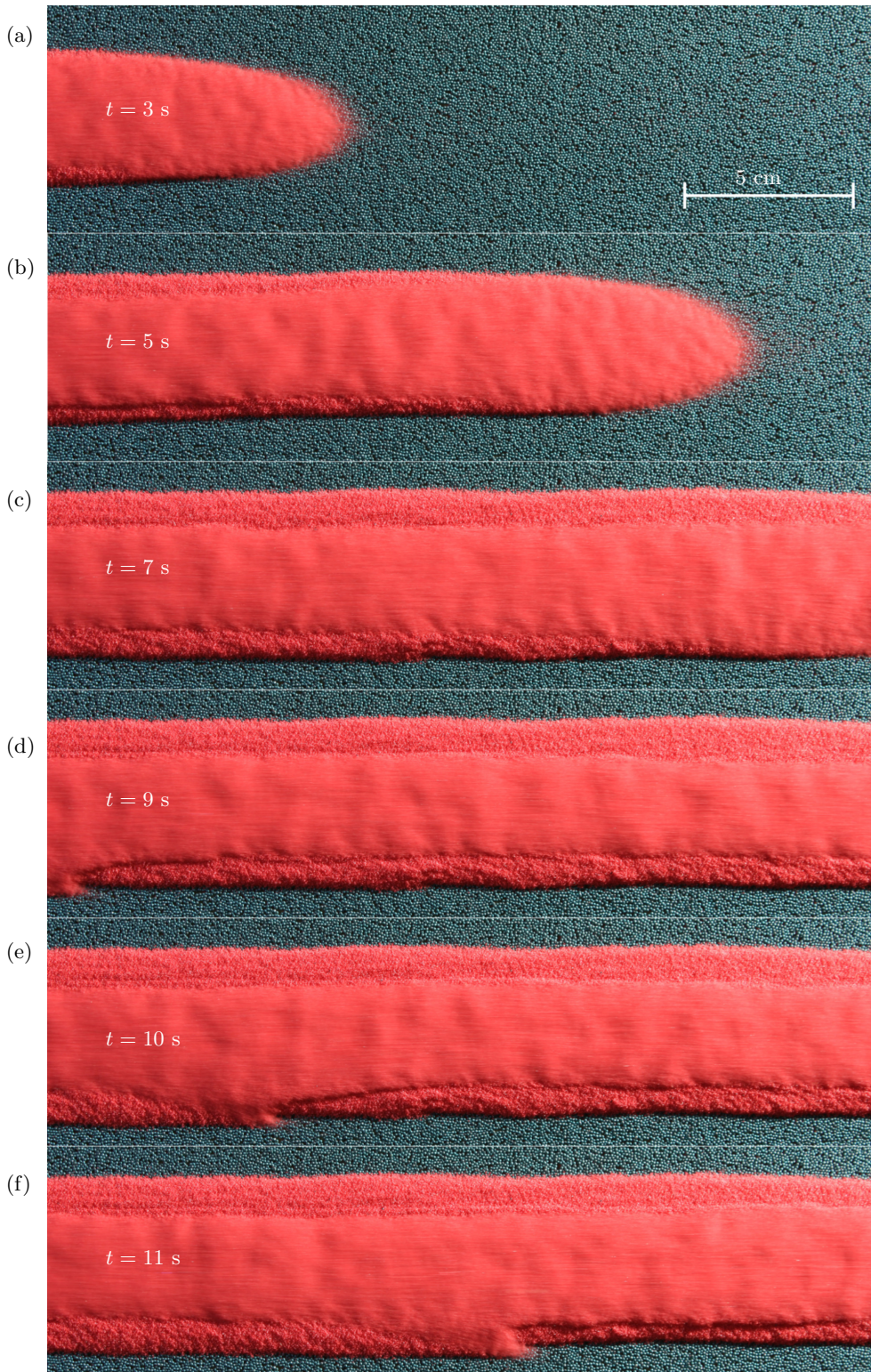


FIGURE 3. (a–f) A series of overhead images at $t = 3, 5, 7, 9, 10,$ and 11 s showing (a–c) the initial formation of the static levees and (d–f) their subsequent reworking by levee-bank overtopping. The mass flux $Q_M = 8.6 \pm 0.1$ g/s, $\zeta = 34^\circ \pm 0.1^\circ$ and the final width of the flow (moving channel plus levees) is $W_{total} = 5.00 \pm 0.05$ cm. Note that at 9 s a wave begins to propagate down the channel and continuously overtops the levee-bank on one side, forming a new levee that is slightly further out. This allows the flowing channel width to readjust to its steady-state value $W = 3.60 \pm 0.05$ cm. The downslope flow direction is from left to right. A movie showing the time-dependent evolution is available in the online supplementary material (movie 1).

within the channel (figure 2c). The thickness of these levees is similar to the thickness of the flow that generated them, especially for wide channels.

The width of the flowing channel is not necessarily set at the point where the levees are emplaced immediately behind the head. Figure 3(a–c) shows an overhead view of the flow front advancing from left to right down the slope and depositing levees behind the flow head. A subsequent internal surge in the flow (figure 3d–f) then pushes material over the top of one of the levee walls and re-mobilises it. This allows the central channel to become slightly wider and a new levee is formed, further out, which maintains the self-channelisation of the flow. This process of levee-bank overtopping allows the channel to adjust to its final steady-state width after the initial passage of the flow head. For the angular red sand particles used in this paper, the final steady-state levee width is achieved within a few tens of seconds. Smaller fluctuations around the steady state constantly erode and deposit small amounts of material on the inside of the levee walls (see movie 2) without remobilizing the entire levee. The levees are therefore in active equilibrium with the flow, constantly undergoing minor readjustments that ensure that the width of the channel reflects its current inflow mass flux.

Particle shape strongly influences the formation of self-channelised leveed flows. In flows of spherical glass ballotini, the levees are considerably less stable (resistant to erosion) than they are for sand, and the levees creep outwards over a timescale that is much longer than that of their initial emplacement. Deboeuf *et al.* (2006) found that for flows of 300–400 μm spherical glass beads on a rough plane made of 200 μm sandpaper, the channel widened and the flow thickness decreased very slowly until an asymptotic state was approached after very long times (> 1 hour). Similar experiments for even longer times (Takagi *et al.* 2011) indicated that the flow widened and eventually became intermittent, with waves further widening the levees, implying that a steady-state width was never attained.

In contrast, Takagi *et al.* (2011) showed that flows of 300–600 μm angular sand particles, on a bed made of the same sand, rapidly established a steady-state leveed channel for sufficiently high mass fluxes. The flow had a fixed channel width and thickness, as well as a well-defined downslope surface velocity profile across the channel. As the mass flux was increased, Takagi *et al.* (2011) found that the flow thickness

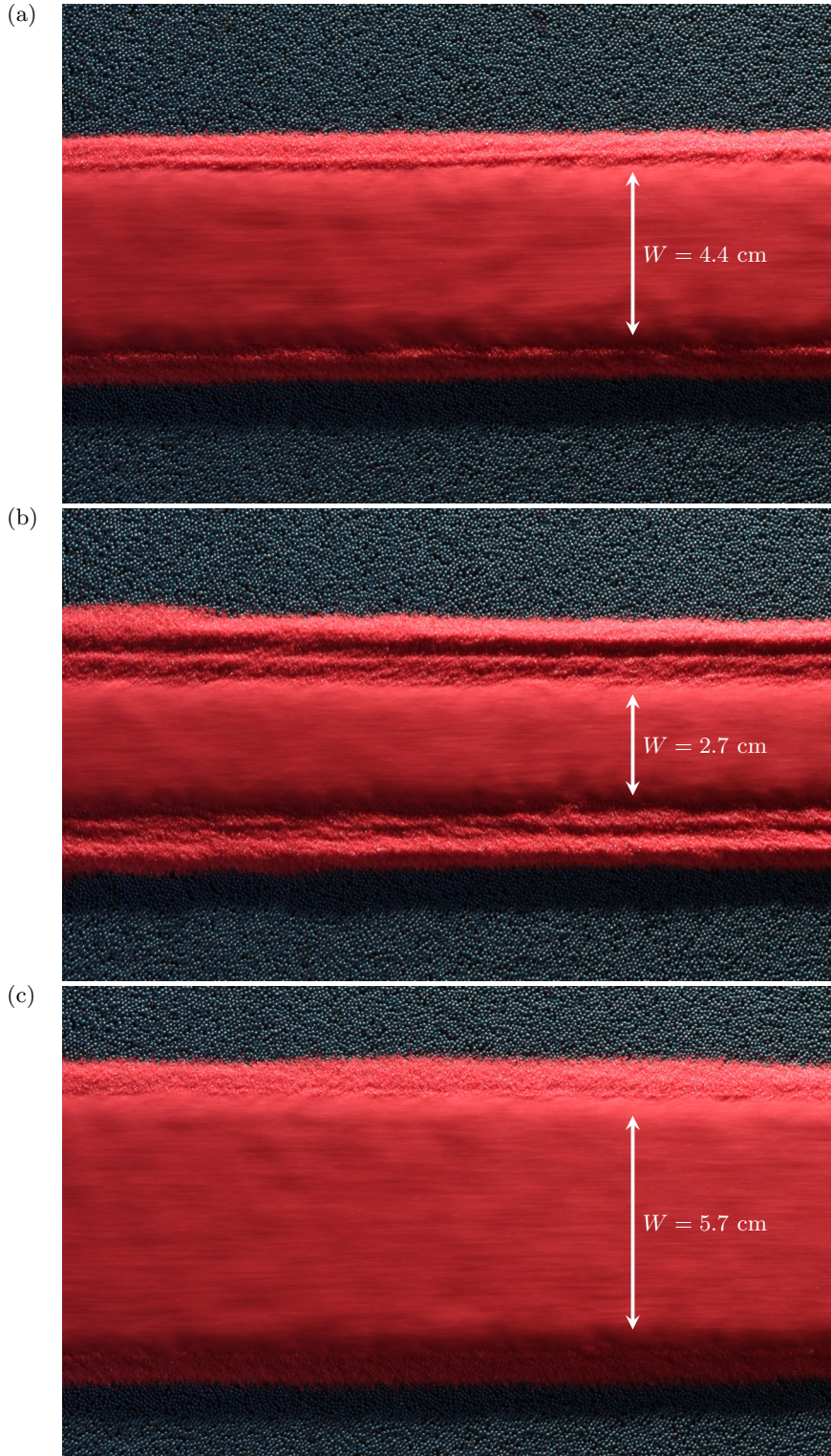


FIGURE 4. Sequence of overhead images of a self-channelised flow of 160–200 μm red sand on a rough plane inclined at $\zeta = 34^\circ \pm 0.1^\circ$. The aperture of the funnel supplying the grains to the top of the chute is changed in order to reduce the mass flux from (a) its initial value of $Q_M = 17.0 \pm 0.1$ g/s to (b) 7.7 ± 0.1 g/s and then (c) back up to 27.0 ± 0.1 g/s. As the mass flux is reduced, the flowing channel width narrows from (a) $W = 4.40 \pm 0.05$ cm to (b) $W = 2.70 \pm 0.05$ cm by mass accretion to the inside of the levee walls. The old levees are left in situ and record the fact that a higher flux once propagated down the channel. When (c) the mass flux is subsequently increased again the levee walls are pushed out by levee-bank overtopping and the old levees are fully remobilized to form a new channel of width $W = 5.70 \pm 0.05$ cm. The downslope flow direction is from left to right. A movie showing the narrowing and widening of the channel is available in the online supplementary material (movie 3).

stayed approximately constant, but the width of the channel increased. If the mass flux was decreased below a critical threshold, however, an unsteady regime developed in which regular pulses of material flowed down the static channel as a series of erosion-deposition waves (Daerr 2001; Börzsönyi, Halsey & Ecke 2005; Clément *et al.* 2007; Börzsönyi, Halsey & Ecke 2008; Takagi *et al.* 2011; Edwards & Gray 2015; Edwards *et al.* 2017).

A less well studied aspect of self-channelised leveed flow is the changing shape of the static levees as the inflow mass flux is altered (figure 4). For an inflow mass flux of $Q_M = 17.0 \pm 0.1$ g/s a stable central channel forms with a width $W = 4.40 \pm 0.05$ cm (figure 4a). When the flux is reduced to $Q_M = 7.7 \pm 0.1$ g/s the channel narrows to a new steady-state width $W = 2.70 \pm 0.05$ cm (figure 4b). The old levee is left in situ and, as the flowing region retreats into the centre of the channel, very small leveed structures are left on the inside of the old levee walls. For these small-scale experiments these features are barely one grain-diameter thick, but they can be still be seen in figure 4(b) due to the oblique lighting. An immediate consequence of this observation is that the shape of the material outside of the central flowing channel is not unique and at least partially records the history of the flow. If, on the other hand, the inflow mass flux is increased to $Q_M = 27.0 \pm 0.1$ g/s a new stable width $W = 5.70 \pm 0.05$ cm rapidly develops by levee-bank overtopping (figure 4c) and the history, preserved in the old stacked levees, is erased. The significance of this process is that it may allow information about the time-history of natural geophysical flows to be inferred from the deposit, for example from sequences of subtly stacked levees that occur in pyroclastic deposits (Wilson & Head 1981; Rowley *et al.* 1981; Branney & Kokelaar 1992; Calder *et al.* 2000).

The fact that static levees are deposited on an inclined plane alongside flowing grains led Félix & Thomas (2004) to suggest that levee formation is related to frictional hysteresis (Daerr & Douady 1999; Pouliquen 1999; Pouliquen & Forterre 2002; Edwards & Gray 2015; Edwards *et al.* 2017). A simple example of this hysteresis is when a steady uniform flow is brought to rest on a slope of angle ζ , it leaves a deposit of thickness $h = h_{stop}(\zeta)$, but a layer of this thickness will not start to flow again until the inclination angle is increased to $\zeta = \zeta_{start}(h)$. Since the inverse function $h_{start}(\zeta)$ is greater than $h_{stop}(\zeta)$, there are a range of thicknesses over which static

and flowing layers can coexist. The underlying cause of this behaviour is a non-monotonic relationship between the flow velocity and the basal friction coefficient, as expressed by the friction law of Pouliquen & Forterre (2002). This phenomenological law is applicable to spherical grains and combines a flow rule for steady uniform flows (Pouliquen 1999) with measurements of $\zeta_{start}(h)$ to describe the friction of both static and flowing layers.

Mangeney *et al.* (2007) used Pouliquen & Forterre's (2002) non-monotonic empirical friction law to model the self-channelisation process within the framework of classical depth-averaged avalanche equations (e.g. Grigorian, Eglit & Iakimov 1967; Savage & Hutter 1989; Naaim, Vial & Couture 1997; Gray, Wieland & Hutter 1999; Heinrich, Piatanesi & Hebert 2001; Gray, Tai & Noelle 2003; Mangeney-Castelnau *et al.* 2003; Pitman *et al.* 2003). Mangeney *et al.*'s (2007) numerical simulations exhibited both a central flowing channel and parallel-sided static/very-slowly-creeping margins that were similar to those seen in experiments. The computations explicitly demonstrated how the material flowing down the central channel spread out laterally at the flow front, slowed down and then deposited to form static lateral margins behind the head. These simulations therefore implied that a heterogenous rheology, due to interstitial fluid and/or size segregation, was not essential for modelling levee formation. Despite the ground-breaking nature of this work, the computed flow thickness in the fully-developed flowing channel was only very slightly greater than h_{stop} , the minimum thickness for steady uniform flow in the friction law of Pouliquen & Forterre (2002). The channel was therefore significantly thinner and wider than those observed experimentally (Félix & Thomas 2004) as Mangeney *et al.* (2007) acknowledged themselves. Moreover, the downslope velocity in Mangeney *et al.*'s (2007) simulations was plug-like across the channel, which contradicted the experimental observation that the downslope velocity decreases smoothly to zero at the levee-channel interfaces across a shear band (Félix & Thomas 2004; Deboeuf *et al.* 2006; Takagi *et al.* 2011).

In this paper a depth-integrated model for self-channelised flows is developed, taking into account contributions of the in-plane deviatoric stress, which lead to depth-averaged viscous-like terms (Gray & Edwards 2014; Baker *et al.* 2016a). This model is referred to as the *viscous* depth-averaged model in this paper to distinguish

it from classical *inviscid* shallow-water-like depth-averaged avalanche models, which do not have viscous second order gradient terms in their depth-averaged momentum balances. A steady-state equation of motion is derived, which describes the balance of stresses that cause shear bands (e.g. Schall & van Hecke 2010; Pouliquen & Gutfraind 1996) to form, and shows that these stresses provides the vital missing physics that sets the steady-state thickness and width of the whole channel. This stress balance results from the interaction of two physical mechanisms, namely frictional hysteresis (Daerr & Douady 1999; Pouliquen & Forterre 2002; Mangeney *et al.* 2007; Edwards *et al.* 2017, 2019) and lateral viscous stresses (Baker *et al.* 2016a). Steady-state theoretical predictions of the width, thickness and velocity profile across the channel (as functions of mass flux and slope angle) are in good quantitative agreement with laboratory experiments performed with spherical glass beads (Félix & Thomas 2004), and also sand (Takagi *et al.* 2011). Importantly, this paper clearly demonstrates that the inviscid theory is a singular limit of the viscous case, with degenerate non-unique steady longitudinally-uniform states that have a range of channel thicknesses and widths for the same mass flux. In addition, two-dimensional time-dependent numerical solutions of this viscous avalanche model are able to explicitly compute how channels with the correct steady-state thickness and width are established dynamically, as well as allowing more complex unsteady flows to be investigated.

2. Governing equations

The depth-averaged theory of Edwards *et al.* (2017) for erosion-deposition waves is used here to model the formation of self-channelised leveed flows on non-erodible slopes.

2.1. Depth-averaged model

Granular material is supplied with constant mass flux from a funnel onto a rough plane inclined at an angle ζ to the horizontal. A rectangular Cartesian coordinate system $Oxyz$ is defined with the x -axis pointing downslope, the y -axis in the cross-slope direction, and z the upward perpendicular to the plane (figure 5). The granular material is assumed to be incompressible with constant bulk density ρ and velocity components $\mathbf{u} = (u, v, w)$ in the downslope, cross-slope and normal directions, respectively. The depth-averaged velocity field $\bar{\mathbf{u}} = (\bar{u}, \bar{v})$ in the downslope and cross-slope directions is

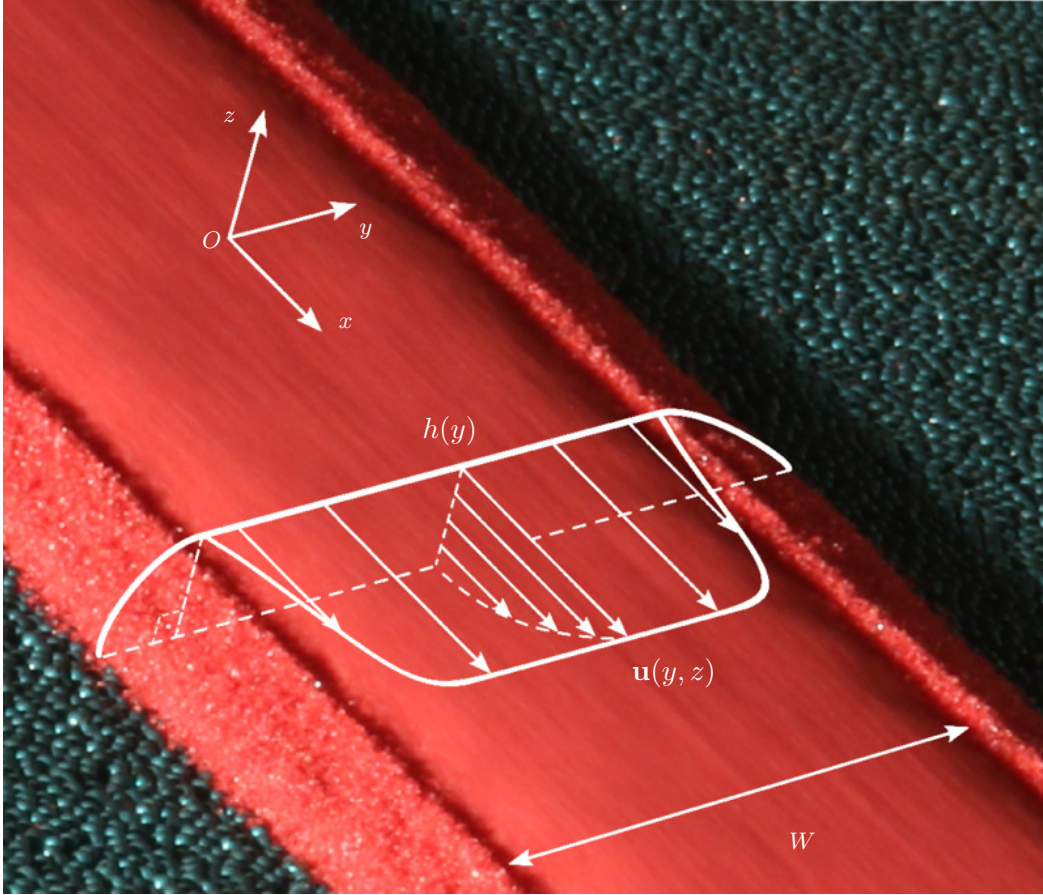


FIGURE 5. A schematic diagram of the coordinate system $Oxyz$ inclined at an angle ζ to the horizontal, where the x -axis points downslope, the y -axis is the cross-slope direction and the z -axis is the upward normal to the chute. For a steady uniform self-channelised flow, the cross slope thickness profile is $h(y)$, whilst the velocity field is given by $\mathbf{u}(y, z)$. The moving central channel has width W and is bounded on either side by parallel static levees.

then defined as

$$\bar{u} = \frac{1}{h} \int_0^h u \, dz, \quad \text{and} \quad \bar{v} = \frac{1}{h} \int_0^h v \, dz, \quad (2.1)$$

where h is the avalanche thickness. Depth averaging the incompressibility condition and applying kinematic boundary conditions (Savage & Hutter 1989) yields the depth-averaged mass balance

$$\frac{\partial h}{\partial t} + \frac{\partial}{\partial x}(h\bar{u}) + \frac{\partial}{\partial y}(h\bar{v}) = 0. \quad (2.2)$$

A similar procedure (Gray & Edwards 2014; Baker *et al.* 2016a) for the momentum balance equation, implies that the depth-averaged momentum balances in the downslope and cross-slope directions are

$$\begin{aligned} & \frac{\partial}{\partial t}(h\bar{u}) + \frac{\partial}{\partial x}(h\bar{u}^2) + \frac{\partial}{\partial y}(h\bar{u}\bar{v}) + \frac{\partial}{\partial x} \left(\frac{1}{2}gh^2 \cos \zeta \right) \\ & = ghS_1 \cos \zeta + \frac{\partial}{\partial x} \left(\nu h^{3/2} \frac{\partial \bar{u}}{\partial x} \right) + \frac{\partial}{\partial y} \left(\frac{1}{2} \nu h^{3/2} \left(\frac{\partial \bar{u}}{\partial y} + \frac{\partial \bar{v}}{\partial x} \right) \right), \end{aligned} \quad (2.3)$$

$$\begin{aligned} \frac{\partial}{\partial t}(h\bar{v}) + \frac{\partial}{\partial x}(h\bar{u}\bar{v}) + \frac{\partial}{\partial y}(h\bar{v}^2) + \frac{\partial}{\partial y}\left(\frac{1}{2}gh^2\cos\zeta\right) \\ = ghS_2\cos\zeta + \frac{\partial}{\partial x}\left(\frac{1}{2}\nu h^{3/2}\left(\frac{\partial\bar{u}}{\partial y} + \frac{\partial\bar{v}}{\partial x}\right)\right) + \frac{\partial}{\partial y}\left(\nu h^{3/2}\frac{\partial\bar{v}}{\partial y}\right), \end{aligned} \quad (2.4)$$

where g is the constant of gravitational acceleration and ν is a coefficient in the depth-averaged kinematic viscosity $\nu h^{1/2}/2$, discussed in §2.3. Implicit in the momentum transport terms of these equations is the assumption that the shape factor ($\overline{u^2}/\bar{u}^2$) is unity (Pouliquen 1999; Pouliquen & Forterre 2002; Hogg & Pritchard 2004; Saingier, Deboeuf & Lagrée 2016; Gray & Edwards 2014; Viroulet *et al.* 2017).

The source term has components

$$S_1 = \tan\zeta - \mu_b e_1 \quad \text{and} \quad S_2 = -\mu_b e_2, \quad (2.5)$$

which arise from the gravitational force that pulls the grains downslope and the effective basal friction. The direction of the frictional force is determined by the vector

$$\mathbf{e} = (e_1, e_2) = \begin{cases} \frac{\bar{\mathbf{u}}}{|\bar{\mathbf{u}}|}, & |\bar{\mathbf{u}}| > 0, \\ \frac{\tan\zeta\mathbf{i} - \nabla h}{|\tan\zeta\mathbf{i} - \nabla h|}, & |\bar{\mathbf{u}}| = 0, \end{cases} \quad (2.6)$$

where \mathbf{i} is the unit vector in the downslope direction and ∇ is the two-dimensional gradient operator. This ensures that the friction opposes the motion when $\bar{\mathbf{u}}$ is non-zero, and opposes the resultant force due to gravity and the depth-averaged pressure gradient when the material is stationary.

Equations (2.2)–(2.4) were originally derived by assuming that the flow was shallow and depth-averaging the mass and momentum balance equations, assuming the $\mu(I)$ -rheology (GDR-MiDi 2004; Jop, Forterre & Pouliquen 2006) and a no-slip condition at the base (Gray & Edwards 2014; Baker *et al.* 2016a). To leading and first order in the aspect ratio, this process yielded the classical inviscid depth-averaged avalanche equations (given by setting $\nu = 0$), with an effective basal friction law corresponding to that measured empirically by Pouliquen & Forterre (2002) for steady uniform flows (which is referred to as the dynamic frictional regime in §2.2). The depth-averaged viscous terms (i.e. those terms multiplied by ν) emerge at second order, by retaining the in-plane normal and shear stresses and approximating them using the leading order lithostatic pressure distribution and Bagnold velocity profile through the flow depth. This explicitly determines the coefficient ν in terms of known frictional parameters, see §2.3, rather than it being a fitting parameter. The viscous terms are usually very small,

but the fact that they are the highest gradient terms makes their inclusion a singular perturbation of the equations. As a result there are some problems where they play a crucial role. These include (i) obtaining the correct cut-off frequency of roll waves (Forterre 2006; Gray & Edwards 2014), (ii) generating cross-stream velocity profiles in channels (Baker *et al.* 2016a) and (iii) producing well-posed models of segregation induced fingering (Baker *et al.* 2016b). It shall be shown in this paper that they are also play a vital role in the selection of the height, width and velocity profile across a monodisperse leveed channel.

2.2. The effective basal friction law

The effective coefficient of basal friction μ_b encodes information about the $\mu(I)$ -rheology (Jop *et al.* 2006; GDR-MiDi 2004) as well as the hysteretic behaviour of the granular material (Daerr & Douady 1999; Pouliquen & Forterre 2002; Mangeney *et al.* 2007; Edwards *et al.* 2017, 2019). This hysteretic behaviour is described by a non-monotonic friction law (Pouliquen & Forterre 2002; Forterre & Pouliquen 2003; Edwards *et al.* 2017, 2019)

$$\mu_b(h, Fr) = \begin{cases} \mu_D, & Fr \geq \beta_*, \\ \mu_I, & 0 < Fr < \beta_*, \\ \mu_S, & Fr = 0, \end{cases} \quad (2.7)$$

which is split into dynamic, μ_D , intermediate, μ_I , and static, μ_S , regimes, depending on the local Froude number

$$Fr = \frac{|\bar{\mathbf{u}}|}{\sqrt{gh \cos \zeta}}, \quad (2.8)$$

and the threshold β_* between the dynamic and intermediate regimes.

In Pouliquen & Forterre (2002) the dynamic friction μ_D is based on the empirical flow rule for glass beads $Fr = \beta h/h_{stop}$ (Pouliquen 1999), where β is a constant obtained experimentally. By combining this with measurements of h_{stop} , Pouliquen (1999) derived a dynamic friction law that was an increasing function of Fr/h and was valid for $Fr \geq \beta$. Angular sand grains obey a more general flow rule (Forterre & Pouliquen 2003)

$$Fr = \beta \frac{h}{h_{stop}} - \Gamma, \quad (2.9)$$

where $\Gamma = 0.84$, and $\beta = 0.71$ is considerably higher than the value $\beta = 0.15$ for glass beads (Forterre & Pouliquen 2003). Note that these values have been corrected from

the previously published values to account for the factor $\sqrt{\cos \zeta}$ in the Froude number (2.8). The flow rule (2.9) implies that a steady uniform flow at $h = h_{stop}$ has a Froude number $Fr = \beta - \Gamma$ that is negative for the parameters for sand, a contradiction since $Fr \geq 0$ from (2.8). This led Edwards *et al.* (2017) to suggest that (2.9) is valid only for $Fr \geq \beta_*$, where β_* is both strictly positive and greater than $\beta - \Gamma$.

The flow rule (2.9) can be used to eliminate h_{stop} in the reciprocal form of the empirical h_{stop} curve (Pouliquen & Forterre 2002) to derive the dynamic friction law

$$\mu_D = \mu_1 + \frac{\mu_2 - \mu_1}{1 + h\beta/(\mathcal{L}(Fr + \Gamma))}, \quad (2.10)$$

where $Fr \geq \beta_*$ and the parameters $\mu_1 = \tan \zeta_1$, $\mu_2 = \tan \zeta_2$ and \mathcal{L} are fitted to measurements of the $h_{stop}(\zeta)$ curve (Pouliquen 1999; Pouliquen & Forterre 2002; Forterre & Pouliquen 2003). The angles ζ_1 and ζ_2 are the minimum and maximum angles, respectively, at which steady uniform flow is observed.

The friction force for static material ($Fr = 0$) is exactly that which is required to keep the material stationary, up to a maximum static friction coefficient. This coefficient therefore takes the form

$$\mu_S = \min \left(|\tan \zeta \mathbf{i} - \nabla h|, \mu_3 + \frac{\mu_2 - \mu_1}{1 + h/\mathcal{L}} \right), \quad (2.11)$$

where the first argument to the min function is the friction required to balance the other forces acting on the static layer and the second argument is the maximum static friction. The maximum static friction is obtained by fitting measurements of $h_{start}(\zeta)$, and introduces a further friction law parameter $\mu_3 = \tan \zeta_3$, where ζ_3 is the minimum angle at which an infinitely deep static layer will start to flow spontaneously (Daerr & Douady 1999; Pouliquen & Forterre 2002).

The friction in the intermediate regime $0 < Fr < \beta_*$ is a power-law interpolation between the maximum static friction and the minimum dynamic friction at $Fr = \beta_*$ and takes a much more complicated form for angular particles than for spherical ballotini (Pouliquen & Forterre 2002). The general form that accounts for spherical and irregular particles is given by Edwards *et al.* (2017) as

$$\mu_I = \left(\frac{Fr}{\beta_*} \right)^\kappa \left(\mu_1 + \frac{\mu_2 - \mu_1}{1 + h\beta/(\mathcal{L}(\beta_* + \Gamma))} - \mu_3 - \frac{\mu_2 - \mu_1}{1 + h/\mathcal{L}} \right) + \mu_3 + \frac{\mu_2 - \mu_1}{1 + h/\mathcal{L}}, \quad (2.12)$$

where κ is a constant interpolation power. In the absence of experimental measurements for slow flows $0 < Fr < \beta_*$, Pouliquen & Forterre (2002) suggested that

$\kappa = 10^{-3}$. However, this value produces an extremely rapid decrease in the friction as the Froude number is increased from zero, so sharp that it cannot be resolved numerically using standard double-precision floating-point numbers (Edwards *et al.* 2019). Edwards *et al.* (2017) instead suggest that κ needs to be at least 10^{-1} to create a robust metastable state, in which a static layer, just slightly thinner than h_{start} (i.e. within the hysteretic region), remains stationary unless it is perturbed. In this paper it is assumed for simplicity, as in Edwards *et al.* (2017, 2019), that $\kappa = 1$, which is consistent with the experimental results of Russell *et al.* (2019) on retrogressive failures.

The parameter β_* sets the Froude number of the transition between the dynamic and intermediate regimes. It also defines the thickness h_* of the minimum steady uniform flow, which lies between $h_{stop}(\zeta)$ and $h_{start}(\zeta)$. In Pouliquen & Forterre (2002) $\beta_* = \beta$ (and thus $h_* = h_{stop}$), while Edwards *et al.* (2017) assumed that h_* was half way between h_{stop} and h_{start} . This paper follows Edwards *et al.* (2019) who suggested that h_* was a multiple of h_{stop}

$$h_* = \Lambda h_{stop}(\zeta), \quad (2.13)$$

where Λ is a constant for all slope angles. Since steady uniform flows satisfy the empirical flow rule (2.9) it follows that the transition Froude number is constant

$$\beta_* = \Lambda\beta - \Gamma. \quad (2.14)$$

In general, Λ must be greater than unity and chosen so that $h_* < h_{start}$, to ensure that there is hysteresis in flows of thickness $h \in [h_*, h_{start}]$. The new approach (Edwards *et al.* 2019) has the advantage that it defines h_* over the complete range of steady uniform flow angles $\zeta \in [\zeta_1, \zeta_2]$, rather than just in the range $[\zeta_3, \zeta_2]$, as in Edwards *et al.* (2017). It also allows the intermediate friction to be accessed even for materials, such as sand, for which $\Gamma > \beta$.

It is important to note that the extended law proposed by Edwards *et al.* (2019) preserves exactly the same structure as that of Edwards *et al.* (2017), it just changes the functional dependence of the transition point $\beta_* = \beta_*(\zeta)$ on the inclination angle ζ . Both approaches makes a clear distinction between the thickness of a deposit left by a steady uniform flow, h_{stop} , and the thickness of the slowest possible steady uniform flow h_* . In the original formulation of Pouliquen & Forterre (2002) this distinction

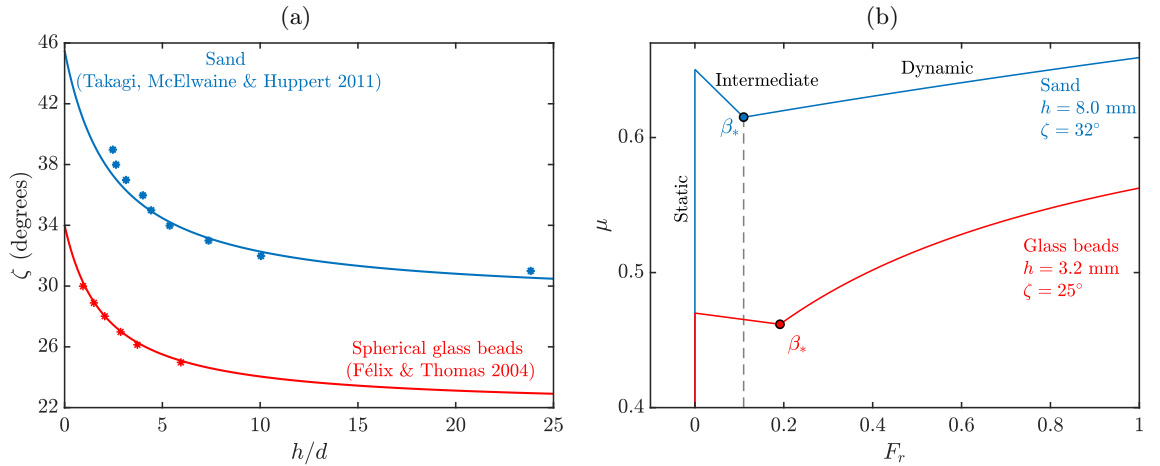


FIGURE 6. (a) Experimental measurements of $h_{stop}(\zeta)$ for sand (Takagi *et al.* 2011, blue markers) and glass beads (Félix & Thomas 2004, red markers), with best-fit h_{stop} curves using the friction law parameters calibrated from these experiments (table 1). (b) The two friction laws for sand (blue curve) and glass beads (red curve) as a function of the Froude number Fr at fixed thickness and inclination angle. Parameters $h = 8$ mm and $\zeta = 32^\circ$ for sand and $h = 3.2$ mm and $\zeta = 25^\circ$ for glass beads are chosen to match those in the respective experiments.

<i>Sand</i>	$\zeta = 32^\circ$	$\zeta_1 = 29^\circ$	$\zeta_2 = 45.5^\circ$	$\zeta_3 = 31^\circ$	$\beta = 0.71$
	$\mathcal{L} = 0.9$ mm	$d = 0.45$ mm	$\Gamma = 0.84$	$\Lambda = 1.34$	$\rho = 1500$ kg/m ³
<i>Glass beads</i>	$\zeta = 25^\circ$	$\zeta_1 = 22^\circ$	$\zeta_2 = 34^\circ$	$\zeta_3 = 23^\circ$	$\beta = 0.143$
	$\mathcal{L} = 0.65$ mm	$d = 0.35$ mm	$\Gamma = 0$	$\Lambda = 1.34$	$\rho = 1500$ kg/m ³

TABLE 1. Physical parameters used for all steady-state and time-dependent solutions obtained throughout the paper. The parameters for sand are obtained, where possible, from the h_{stop} curve of Takagi *et al.* (2011). The parameters for glass beads are those used by Mangeney *et al.* (2007) to model the experiments of Félix & Thomas (2004), but with a smaller \mathcal{L} to quantitatively fit the h_{stop} measurements of Félix & Thomas (2004). Note that the values for β and Γ differ from those in Pouliquen & Forterre (2002) and Forterre & Pouliquen (2003) to account for the factor $\sqrt{\cos \zeta}$ in the definition of the Froude number (2.8).

was not made and hence $h_* = h_{stop}$. Evidence that h_* and h_{stop} are indeed different is provided by a wide range of existing experimental measurements (see, for example, Fig. 4 Pouliquen 1999; Fig. 8 Forterre & Pouliquen 2003; Fig. 3 Deboeuf *et al.* 2006; Fig. 11 Edwards *et al.* 2017), which all show that the minimum steady uniform flow thickness is in the range $[h_{stop}, 2h_{stop}]$. As a result the value of $\Lambda = 1.34 \in [1, 2]$ is used in this paper to best match experimental results. This is very close to the value $h_*/h_{stop} = 1.33$ measured in flows of glass beads by Russell *et al.* (2019).

To enable quantitative comparison between theory and experiment, the material parameters used throughout the paper (table 1) correspond as closely as possible to the sand used by Takagi *et al.* (2011) and the glass beads used by Félix & Thomas (2004). For the experiments with sand, the angles in the friction law, ζ_1 and ζ_2 , are

obtained by fitting $h_{stop}(\zeta)$ to the experimental data of Takagi *et al.* (2011) using the functional form proposed by Pouliquen & Forterre (2002) (figure 6a), which leads to friction coefficients in the form of (2.10)–(2.12). The characteristic length scale \mathcal{L} and the parameters β and Γ are taken from measurements of Forterre & Pouliquen (2003) for a similar flow of sand on a rough bed of the same material. The angle ζ_3 is determined from measurements of $h_{start}(\zeta)$, but these measurements are not reported by Takagi *et al.* (2011). Instead, $\zeta_3 = \zeta_1 + 2^\circ$ is chosen, based on measurements of similar flows of sand over a rough bed. For the experiments with glass beads performed by Félix & Thomas (2004), the parameters are chosen to be the same as the ones used by Mangeney *et al.* (2007) to simulate these flows, although here a value of \mathcal{L} smaller than that of Mangeney *et al.* (2007) is used to quantitatively match the experimental h_{stop} curve (figure 6a). The resultant friction laws are plotted in figure 6(b) as a function of the Froude number. The frictional hysteresis of the angular sand particles ($\mu(Fr = 0) - \mu(Fr = \beta^*)$) is much greater than that of glass beads, which makes the sand levees significantly stronger.

2.3. Depth-averaged kinematic viscosity

The second order depth-averaged viscous-like terms in the momentum balances (2.3)–(2.4) contain a parameter ν in the depth-averaged kinematic viscosity $\nu h^{1/2}/2$, for which Gray & Edwards (2014) derived the formula

$$\nu = \frac{2\mathcal{L}\sqrt{g}\sin\zeta}{9\beta\sqrt{\cos\zeta}} \left(\frac{\tan\zeta_2 - \tan\zeta}{\tan\zeta - \tan\zeta_1} \right). \quad (2.15)$$

This is a function of the slope angle ζ and parameters that are already known from the effective basal friction law, so no new parameters are introduced into the theory. It is well-defined provided $\zeta \in [\zeta_1, \zeta_2]$, i.e. in the range of angles where steady uniform flows develop. Outside this range, some form of regularization is required to ensure that it does not become negative. In this paper, the two-dimensional viscous terms derived by Baker *et al.* (2016a) are used for flows in all three frictional regimes, even though their original derivation (Gray & Edwards 2014) implicitly assumed the flow was in the dynamic frictional regime.

3. Fully developed self-channelised flow

This section presents exact steady-state solutions for the height, width and down-slope velocity profile across the central flowing channel. The depth-averaged granular viscosity provides the vital mechanism for producing a smoothly varying velocity profile across the channel, allowing appropriate boundary conditions to be imposed at the levee-channel interfaces. These boundary conditions together with an integral mass flux constraint are then able to determine a unique equilibrium channel thickness and width, completely independently of the flow head dynamics. In the absence of viscosity the equations are not closed, so there is no unique solution and inviscid theories therefore lack a crucial thickness and width selection mechanism.

Outside of this region, in the levees, there are multiple static states (as demonstrated experimentally in figure 4) because the static friction encoded in (2.11) can take any value between zero and its maximum value. While there is not a unique solution for the width of the levees, the minimum levee width necessary to support a central flowing channel of a given thickness, can be determined by assuming all the static grains are at the maximum static friction.

3.1. Steady-state depth-averaged equations in the flowing channel

Consider a fully-developed steady-state parallel-sided leveed flow that has a central flowing channel of width W and is supplied by a mass flux Q_M . It follows that the flow is independent of time t and the downstream coordinate x . In the central channel the depth-averaged mass balance (2.2) then reduces to

$$\frac{\partial}{\partial y} (h\bar{v}) = 0, \tag{3.1}$$

which is subject to a condition of no flow across the levee-channel interfaces,

$$\bar{v} = 0 \quad \text{at} \quad y = \pm W/2. \tag{3.2}$$

Integrating (3.1) directly, it follows that for non-trivial solutions, in which $h \neq 0$, the depth-averaged lateral velocity is zero everywhere, i.e. $\bar{v} = 0$ for all y . In flowing regions ($\bar{u} \neq 0$), the cross-slope component of the momentum balance (2.4) then implies that the depth-averaged pressure is constant across the channel

$$\frac{d}{dy} \left(\frac{1}{2}gh^2 \cos \zeta \right) = 0. \tag{3.3}$$

This can be integrated to show that the flow thickness is constant

$$h(y) = H, \quad (3.4)$$

where the constant H is, as yet, unknown. The downslope component of the depth-averaged momentum balance (2.3) then reduces to

$$\frac{d^2\bar{u}}{dy^2} = \frac{2g \cos \zeta}{\nu\sqrt{H}} (\mu_b(H, \bar{u}) - \tan \zeta), \quad (3.5)$$

where \bar{u} is assumed to be strictly positive. This is a second order autonomous Ordinary Differential Equation (ODE) for the downslope velocity profile $\bar{u}(y)$ across the central flowing channel. Motivated by experimental observations of Félix & Thomas (2004)(see their inset image in figure 4), Deboeuf *et al.* (2006)(see their figure 2) and Takagi *et al.* (2011)(see their figure 5), it is assumed that there is no slip

$$\bar{u} = 0 \quad \text{at} \quad y = \pm \frac{W}{2}, \quad (3.6)$$

and no lateral shear-stress

$$\frac{d\bar{u}}{dy} = 0 \quad \text{at} \quad y = \pm \frac{W}{2} \quad (3.7)$$

at both channel-levee interfaces. In the fully developed steady state, the mass flux of grains entering the chute is equal to the mass flux flowing down the central channel at any downstream location. Hence, $\bar{u}(y)$ is subject to the integral constraint

$$Q_M = \rho H \int_{-W/2}^{W/2} \bar{u} dy. \quad (3.8)$$

The thickness H , width W and the depth-averaged downslope velocity $\bar{u}(y)$ across the flowing channel, are direct predictions of the model (3.5)–(3.8). To visualise the solution for the entire flow including the levees, two additional assumptions can be made, which are described in appendices A and B. The first assumption is of a constant velocity profile through the depth of the flow, which allows the downslope velocity $u(y, z)$ to be reconstructed from the depth averaged downslope velocity $\bar{u}(y)$. The second assumption is that the static levees are everywhere on the brink of yield (Hulme 1974; Balmforth, Burbidge & Craster 2001), which allows the thickness profile of the static levee to be computed. These assumptions are not intrinsic to the model, but extend its predictions to allow comparison with experimental measurements of the surface velocity and the combined width of the flow and levees, respectively.

3.2. Inviscid solutions

In the inviscid case, the coefficient $\nu = 0$ and the steady-state equation of motion (3.5) reduces from a second-order ODE to an algebraic balance between friction and gravity only, $\mu_b = \tan \zeta$. This reduction in order is indicative of a singular perturbation problem in which, as is the case here, the inviscid $\nu = 0$ model differs qualitatively from the model with any nonzero viscosity $\nu > 0$. Since the thickness H is constant across the channel, solving $\mu_b(H, \bar{u}) = \tan \zeta$ with μ_b in the dynamic regime (3.4) gives a constant velocity

$$\bar{u}_{steady} = \sqrt{gH \cos \zeta} \left(\frac{H\beta}{\gamma \mathcal{L}} - \Gamma \right), \quad (3.9)$$

across the channel, where

$$\gamma = \frac{\mu_2 - \tan \zeta}{\tan \zeta - \mu_1}, \quad (3.10)$$

and the thickness H is still a free parameter. The reduction of order in the inviscid system means that both tangential velocity boundary conditions (3.6) and (3.7) must be relaxed. Instead, since the material in the central channel moves at constant speed \bar{u}_{steady} and the grains in the levee are static, there will be contact discontinuities at the levee-channel boundaries $y = \pm W/2$ (i.e. jumps in the downslope velocity parallel to the margins, see e.g. Chadwick 1976) as shown in figure 7. This is not what is observed in experiment (Félix & Thomas 2004; Deboeuf *et al.* 2006; Takagi *et al.* 2011), where there are smoothly varying velocity profiles across the channel, rather than frictionless surfaces sliding past one another.

Assuming that there is a single channel, the integral constraint (3.8) together with the velocity field (3.9) provide one equation expressing the flowing channel width W as a function of the thickness H ,

$$W = \frac{Q_M}{\rho H \bar{u}_{steady}(H)}. \quad (3.11)$$

With no further boundary conditions imposed in the inviscid model, there is no equation to determine the thickness H . The only additional constraint on the inviscid solution is that the depth-averaged pressure across the contact discontinuities must be equal (Chadwick 1976), i.e. the depth-averaged pressure in the levee is just sufficient to balance the depth-averaged pressure in the central channel at $y = \pm W/2$. This is equivalent to the condition that the thickness must be continuous across the contact discontinuities. Since static and moving grains must coexist for the same thickness, it

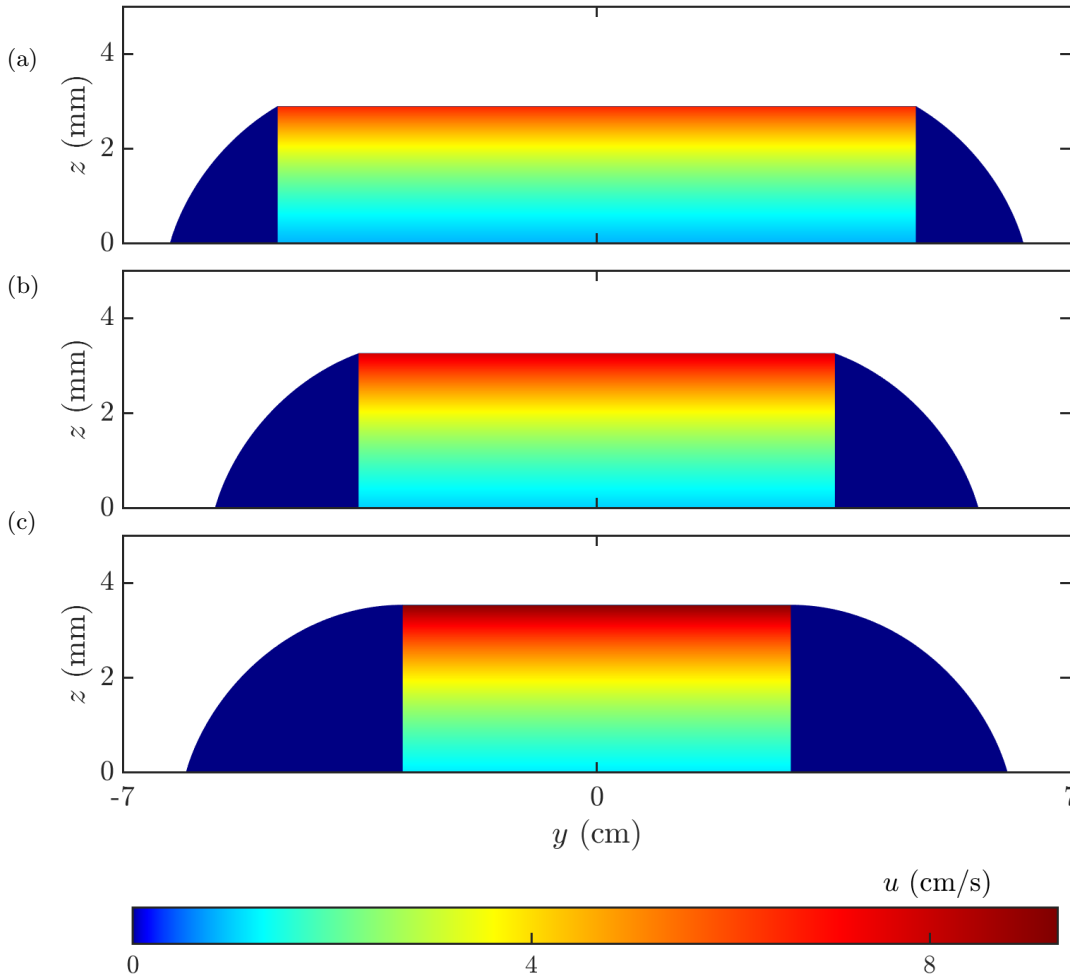


FIGURE 7. Steady-state downstream inviscid velocity profile $u(y, z)$ for a self-channelised flow of glass beads at an angle $\zeta = 25^\circ$, mass flux $Q_M = 12$ g/s and the parameters for glass beads in table 1. The velocity is reconstructed using an exponential velocity profile defined in equation (A 2) with $\lambda = 2.05$. This is appropriate for thin flows close to h_* , which feel the non-local effect of the base. There are an infinite number of solutions for $H \in [h_*, h_{start}]$. The thinnest and widest flowing channel is obtained when (a) $H = h_*$, whilst the deepest and narrowest is recovered for (c) $H = h_{start}$. The minimal static levees required to hold up the central channel are also shown (see appendix B). The narrowest levees occur at $H = h_*$, while the widest levees occur at $H = h_{start}$. As a result, the total width of the channel is not a monotonically increasing function of the channel height H , i.e. the total channel width in panel (b) is narrower than the end members in panels (a,c).

follows that H must lie in the metastable range $h_* \leq H \leq h_{start}$. These inequalities are not sufficient, however, to determine H uniquely, and hence equations (3.9) and (3.11) do not determine $\bar{u}(H)$ and $W(H)$ uniquely either.

For a given mass flux Q_M , the inviscid avalanche model has an infinite set of solutions that are parameterized by the $H \in [h_*, h_{start}]$. Figure 7 shows three cases for $Q_M = 12$ g/s and a slope angle $\zeta = 25^\circ$ using the parameters for glass beads from table 1. The widest and slowest moving central channel ($W = 9.42$ cm, $\bar{u}_{steady} = 2.93$ cm/s) occurs when $H = h_* = 2.9$ mm, while the narrowest and fastest moving flow ($W = 5.73$ cm, $\bar{u}_{steady} = 3.94$ cm/s) is obtained when $h = h_{start} = 3.54$ mm. It follows, that even a

relatively modest range of thicknesses ($H \in [2.9, 3.54]$ mm) can lead to a substantial range of channel widths. In this case the widest flowing channel is 1.64 times wider than the narrowest. Interestingly, the total width, including the minimal static levees on either side of the central flowing channel, is almost the same for both cases (i.e. $W_{total}(h_*) = 12.61$ cm, $W_{total}(h_{start}) = 12.14$ cm) as shown in figure 7(a,c). The relative insensitivity of the total channel width arises because the static levees need to be much wider to support the central flowing channel as its thickness approaches h_{start} . This is due to the fact that $dh/dy \rightarrow 0$ in equation (B 4) as $h \rightarrow h_{start}$, i.e. the levee becomes less stable (in the sense that it finds it harder to support thickness gradients) as the thickness approaches h_{start} . Note that the total width of the channel is a non-monotonic function of H , since $W_{total} = 11.27$ cm when $H = 0.5(h_* + h_{start})$ as shown in figure 7(b).

A prime example of a physical system that has an infinite number of steady-states are the static levees. As shown in figure 4, these can have arbitrary free-surface shapes that are dependent on the history of the flow that emplaced them. Having an infinite number of steady-states for the inviscid flowing channel is not, however, physically realistic, because there is strong experimental evidence (Félix & Thomas 2004; Deboeuf *et al.* 2006; Takagi *et al.* 2011) that the thickness H and width W are functions of the imposed mass flux Q_M . Since the model is not able to uniquely determine the central channel thickness H , and therefore equations (3.9) and (3.11) can not be used to calculate $W(H)$ and $\bar{u}(H)$ uniquely either, the inviscid theory is missing an important physical mechanism for selecting the channel thickness, width and velocity profile.

3.3. Viscous solutions for the central flowing channel

A solution to the steady-state equation of motion (3.5) will now be constructed that includes the effects of lateral viscous stresses. The system to be solved comprises of the second order ODE (3.5) with two unknown parameters H and W . Four boundary conditions are therefore required to close the system. These are provided by the boundary conditions at the levee-channel interface (3.6) and (3.7) (which, due to the symmetry of the solutions as $y \rightarrow -y$, provide three independent conditions) and by the integral mass flux condition (3.8). The boundary value problem, associated boundary conditions and the flux constraint therefore provide a closed system of equations, which determines the thickness, width, and velocity profile of a self-channelised flow.

Much of the solution can be obtained algebraically if the problem is written in terms of the flow thickness H , and the mass flux Q_M is obtained as a function of H using (3.8). This relationship $Q_M(H)$ can then be inverted to numerically solve for the thickness at a specified mass flux. The symmetry implies that it is sufficient to solve the problem in the half domain $y \in [-W/2, 0]$ and it is therefore convenient to define a new coordinate system that is centred at the levee-channel interface

$$\hat{y} = y + \frac{W}{2}. \quad (3.12)$$

Immediately adjacent to the levees there is a slowly moving region that lies in the intermediate frictional regime. Recalling that $\kappa = 1$, the transformed ODE (3.5) with the intermediate friction law (2.12) takes a particularly simple form,

$$\frac{d^2 \bar{u}}{d\hat{y}^2} = b - a\bar{u}, \quad (3.13)$$

where the coefficients are thickness dependent,

$$a = \frac{2\sqrt{g \cos \zeta}}{\nu H \beta_*} \left(\mu_3 + \frac{\mu_2 - \mu_1}{1 + H/\mathcal{L}} - \left(\mu_1 + \frac{\mu_2 - \mu_1}{1 + H\beta/(\mathcal{L}(\beta_* + \Gamma))} \right) \right), \quad (3.14)$$

$$b = \frac{2g \cos \zeta}{\nu \sqrt{H}} \left(\mu_3 + \frac{(\mu_2 - \mu_1)}{1 + H/\mathcal{L}} - \tan \zeta \right). \quad (3.15)$$

Solving (3.13) subject to the boundary conditions (3.6) and (3.7) it follows that

$$\bar{u} = \frac{b}{a} (1 - \cos(\sqrt{a}\hat{y})) \quad (3.16)$$

in the slowly moving layer adjacent to the levee. If the Froude number $Fr < \beta_*$ everywhere in the channel, the solution (3.16) is valid everywhere and the channel width is equal to one period of the cosine function, i.e. $W = 2\pi/\sqrt{a}$. These solutions are, however, not the ones that are observed physically.

Instead, the velocity increases until $Fr = \beta_*$ and then the flow transitions across to the dynamic frictional regime. From the definition of the friction law (2.7) and the Froude number (2.8), it follows that this occurs when \bar{u} is equal to a transition velocity

$$\bar{u}_{transition} = \beta_* \sqrt{gH \cos \zeta}. \quad (3.17)$$

From (3.16) this transition occurs when

$$\hat{y} = \hat{y}_{transition} = \frac{1}{\sqrt{a}} \cos^{-1} \left(1 - \frac{a}{b} \bar{u}_{transition} \right), \quad (3.18)$$

and, from (3.16)–(3.18), the velocity gradient at this point is

$$\left. \frac{d\bar{u}}{d\hat{y}} \right|_{\hat{y}_{transition}} = \frac{b}{\sqrt{a}} \sin(\sqrt{a} \hat{y}_{transition}) = \sqrt{\bar{u}_{transition} (2b - a\bar{u}_{transition})}. \quad (3.19)$$

These transition points are shown with yellow filled circles in the phase-plane and physical space in figure 8 and lie at a local minimum in the friction. Equations (3.17)–(3.19) determine the interfacial boundary conditions for the dynamic problem in the centre of the channel for $\hat{y} \geq \hat{y}_{transition}$. The green circular markers in figure 8 show where the magnitude of the shear rate is maximum and the curvature of the solutions in physical space changes sign. This lies in the intermediate friction regime, so the solution (3.16) is vital to smoothly connect the interior solution with zero velocity gradient at the levee-channel interfaces.

The ODE for the dynamic regime is determined by substituting (2.10) into (3.5) and applying the coordinate transformation (3.12) to give

$$\frac{d^2\bar{u}}{d\hat{y}^2} = \frac{\bar{u} - \bar{u}_{steady}}{c\bar{u} + d}, \quad (3.20)$$

where \bar{u}_{steady} is the steady uniform flow velocity defined in (3.9),

$$c = \frac{\nu\sqrt{H}}{2g(\mu_2 - \tan\zeta)\cos\zeta} \quad \text{and} \quad d = \frac{\nu H(\Gamma\mathcal{L} + H\beta)}{2(\mu_2 - \tan\zeta)\mathcal{L}\sqrt{g}\cos\zeta}. \quad (3.21)$$

Since H is constant, \bar{u}_{steady} , c and d are constant, and hence (3.20) is an autonomous second order ODE that can be solved by making the substitution $p = d\bar{u}/d\hat{y}$ and using the chain rule to give

$$p \frac{dp}{d\bar{u}} = \frac{\bar{u} - \bar{u}_{steady}}{c\bar{u} + d}. \quad (3.22)$$

Integrating (3.22) subject to the boundary conditions that $\bar{u} = \bar{u}_{centre}$ and $p = d\bar{u}/d\hat{y} = 0$ on the symmetry line, and taking the positive root, implies that

$$\frac{d\bar{u}}{d\hat{y}} = \frac{1}{c} \sqrt{2(c\bar{u}_{steady} + d) \ln\left(\frac{c\bar{u}_{centre} + d}{c\bar{u} + d}\right) - 2c(\bar{u}_{centre} - \bar{u})}. \quad (3.23)$$

Evaluating (3.23) at the transition $\hat{y} = \hat{y}_{transition}$ yields an implicit equation for the centreline velocity \bar{u}_{centre} ,

$$\left. \frac{d\bar{u}}{d\hat{y}} \right|_{\hat{y}_{transition}} = \frac{1}{c} \sqrt{2(c\bar{u}_{steady} + d) \ln\left(\frac{c\bar{u}_{centre} + d}{c\bar{u}_{transition} + d}\right) - 2c(\bar{u}_{centre} - \bar{u}_{transition})}, \quad (3.24)$$

where a , b , c , d , $\bar{u}_{transition}$, $d\bar{u}/d\hat{y}|_{\hat{y}_{transition}}$ and \bar{u}_{steady} are all functions of H , given by (3.14), (3.15), (3.21), (3.17), (3.19) and (3.9).

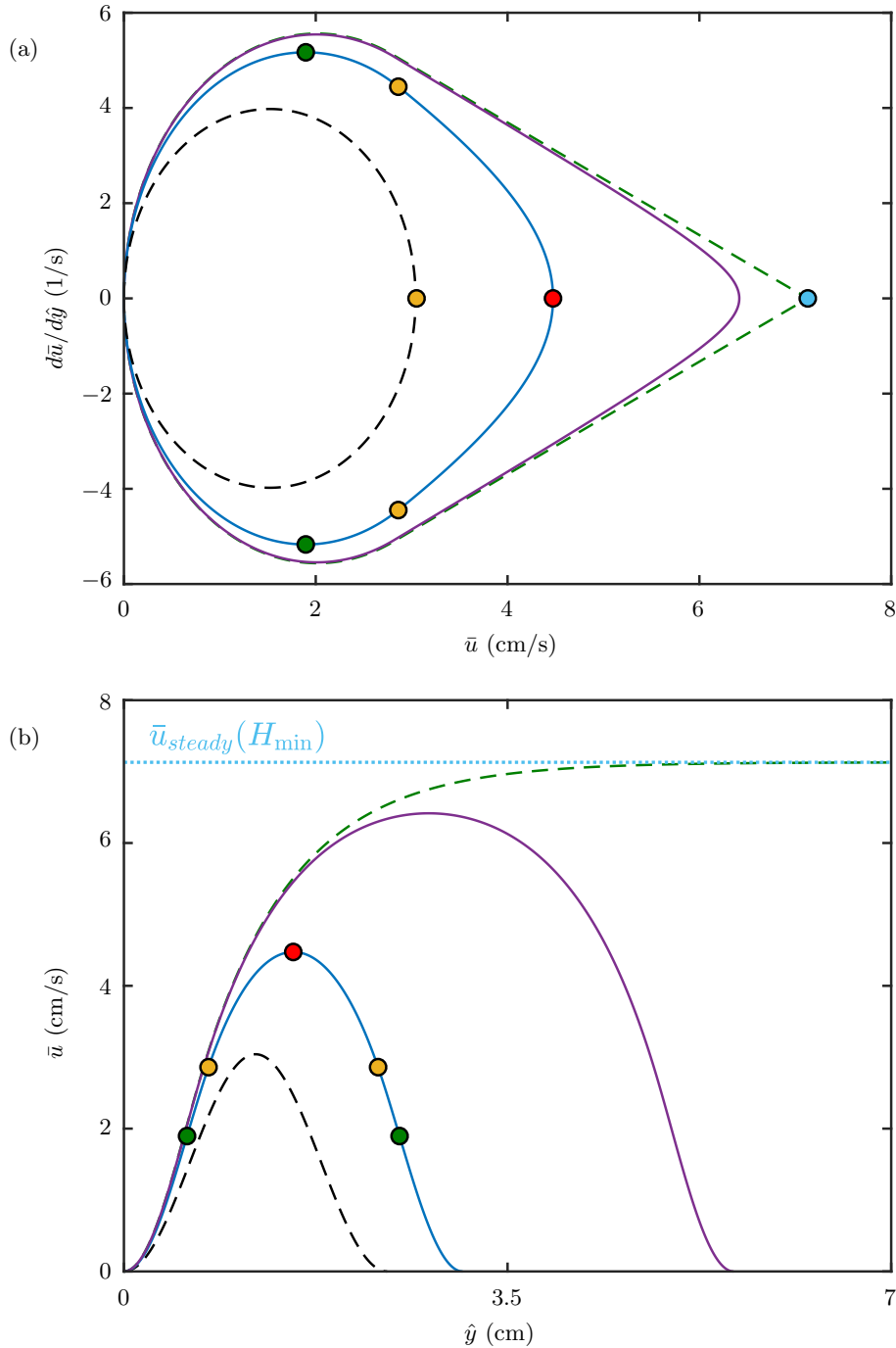


FIGURE 8. Schematic diagram of the velocity solutions in (a) the phase plane, and (b) physical space using the parameters for sand in table 1. A typical solution is shown by the blue curve for $H = 8.2$ mm ($Q_M = 9.6$ g/s) which forms a closed orbit in phase space. The yellow circular markers on this line indicate the transition between the intermediate and dynamic frictional regimes. The green markers, which lie in the intermediate frictional regime, show where the velocity gradient is a maximum/minimum and the curvature of the velocity profile changes sign. The red marker lies in the dynamic regime and is where the maximum velocity is reached in the centre of the channel. Solutions only exist for $H \in [H_{min}, H_{max}]$ and these limiting cases are shown with the green and black dashed lines, respectively. The light blue point corresponds to where the velocity in the centre of the flow is equal to the steady uniform value \bar{u}_{steady} and the channel is infinitely wide, while the yellow marker on the dashed black curve shows the case when $\bar{u}_{centre} = \bar{u}_{transition}$. The purple curve shows another solution for $H = 7.92$ mm ($Q_M = 28.4$ g/s), which produces a wider flow with higher velocities even though it is thinner than the blue solution. The blue dotted line shows the maximum attainable steady uniform velocity $\bar{u}_{steady}(H_{min})$.

Valid solutions are only found for certain values of \bar{u}_{centre} , and since the centre-line velocity is a function of the thickness, there should be a range of possible values for H . In fact, it is observed that in order to obtain a self-channelised solution the thickness is limited to a finite interval, i.e. $H \in [H_{min}, H_{max}]$. The first boundary can be found by assuming that the central steady flow is at the transition between dynamic and intermediate friction, i.e. that the centre-line velocity $\bar{u}_{centre} = \bar{u}_{transition}$. In this case, the right hand side of (3.24) is zero, so $d\bar{u}/d\hat{y}|_{\hat{y}_{transition}} = 0$. Using (3.19) it follows that $\bar{u}_{transition}(H) = 2b(H)/a(H)$, which can be solved to determine an upper bound for $H \leq H_{max}(\zeta)$. The second limit, H_{min} , is found by noticing that \bar{u}_{centre} is a decreasing function of H , and that there is a value of the thickness, for which the self-channelised orbit in the phase space becomes homoclinic. For this value of H trajectories starting at the origin of the phase plane go directly to the saddle point given by the equilibrium point between dynamic friction and gravity (dashed green line in figure 8a). Hence, the lower boundary $H_{min}(\zeta)$ is determined by setting $\bar{u}_{centre} = \bar{u}_{steady}$ in (3.24). For the friction law parameters and slope angle calibrated to the experiments of Takagi *et al.* (2011) (table 1), $H_{min} \approx 7.9$ mm and $H_{max} \approx 9.2$ mm, which are significantly deeper than both $h_{stop} \approx 5$ mm and $h_* \approx 6.7$ mm. On the other hand, for the glass beads parameters (Félix & Thomas 2004; Mangeney *et al.* 2007) (table 1) the range is much narrower, $H_{min} \approx 3.152$ mm and $H_{max} \approx 3.166$ mm, but, nonetheless, is still deeper than $h_{stop} \approx 2.16$ mm and $h_* \approx 2.9$ mm.

By choosing $H \in [H_{min}, H_{max}]$ a solution to (3.24) for the centre-line velocity \bar{u}_{centre} is guaranteed to exist and can be found by numerical root finding techniques. Once this is given, the separable ODE (3.23) can then be solved by quadrature, i.e.

$$\hat{y} = \hat{y}_{transition} + \int_{\bar{u}_{transition}}^{\bar{u}} \frac{c}{\sqrt{2(c\bar{u}_{steady} + d) \ln\left(\frac{c\bar{u}_{centre} + d}{c\bar{u}' + d}\right) - 2c(\bar{u}_{centre} - \bar{u}')}} d\bar{u}'. \quad (3.25)$$

By construction the velocity gradient in (3.23) is zero when $\bar{u} = \bar{u}_{centre}$, so it follows that the integrand in (3.25) is singular as $\bar{u} \rightarrow \bar{u}_{centre}$. However, as $\bar{u}_{centre} \rightarrow \bar{u}_{steady}$ there is a large central region of the flow where the downslope velocity profile is flat and the integral (3.25) is difficult to evaluate. It is therefore useful to linearise the right-hand side of (3.23) about $\bar{u} = \bar{u}_{steady}$ and then solve to obtain the approximate

solution

$$\bar{u} = \bar{u}_{steady} - (\bar{u}_{steady} - \bar{u}_{centre}) \cosh \left(\frac{\hat{y} - W/2}{\sqrt{c\bar{u}_{steady} + d}} \right). \quad (3.26)$$

By integrating (3.25) to $\bar{u} = \bar{u}_{centre}(1 - \varepsilon)$, where $\varepsilon \ll 1$, and then using the approximation (3.26) it is possible to accurately determine the solution close to \bar{u}_{steady} and hence the half width of the channel $\hat{y}_{centre} = W/2$. The solutions for the velocity profile and channel width W are shown in figure 8(b) for a range of flow thicknesses H . This relationship is inverted numerically to find the solution corresponding to a given mass flux Q_M . For a fixed slope angle, flows with larger mass flux are wider and faster-moving (but, somewhat counter-intuitively, are thinner) than those with a smaller mass flux.

3.4. Shear-band structure adjacent to the levees

The physical mechanism that prevents erosion of the levees is the granular viscosity, since it allows steady-state solutions to be constructed that do not exert any shear stress on the inside of the levee walls, even though material is flowing down the central channel. It is therefore of interest to understand the boundary layer structure that allows this.

For sufficiently large mass flux the thickness H is almost equal to H_{min} and hence the constants $a(H)$, $b(H)$, $c(H)$, $d(H)$ and $\bar{u}_{steady}(H)$ barely change in the ODEs (3.13) and (3.20). As a result, the position of the centre at $\bar{u} = b/a$ and the saddle point at $\bar{u} = \bar{u}_{steady}$ (see e.g. Strogatz 1994) are almost independent of mass flux and the orbits in the phase plane lie almost on top of each other (figure 9a), with a slight difference visible only close to the saddle point (figure 9a inset). These small variations in phase space are more significant in physical space (figure 9b). At $Q_M = 50$ g/s the solution has a rounded profile with the fastest velocity occurring in the centre of the channel. As the mass flux is increased, the centreline velocity approaches the steady uniform flow solution \bar{u}_{steady} and the velocity profile flattens, forming a central region of material of uniform thickness and approximately uniform depth-averaged velocity. As $H \rightarrow H_{min}$ the orbit becomes homoclinic, directly connecting the origin and the saddle point, and the period of the orbit, channel width W and mass flux Q_M all diverge. The centreline velocity \bar{u}_{centre} tends to the steady uniform flow velocity \bar{u}_{steady} , given by (3.9). Equation (3.9) therefore defines an upper bound for the velocity in a self-

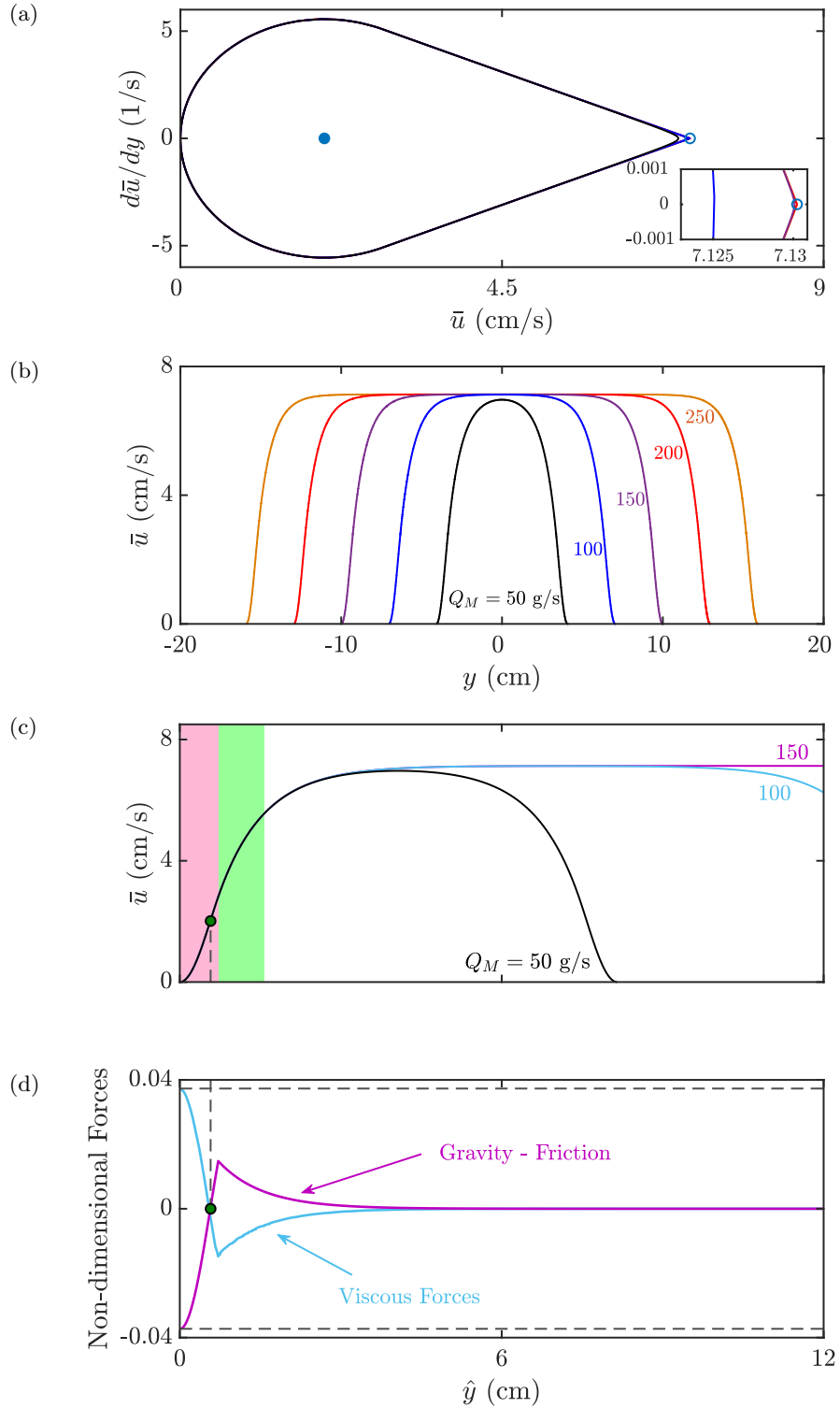


FIGURE 9. (a) Phase space (b) downslope velocity profiles across the central flowing channel, and (c) downslope velocity profiles centred on the levee-channel interface for mass fluxes $Q_M = 50, 100, 150, 200$ and 250 g/s. In (a) the filled blue circle is the position of the centre and the open blue circle is the saddle point for the case of $Q_M = 250$ g/s, although these points are almost the same for all the fluxes. The inset graph shows a close up of the solutions close to the saddle. The pink shaded region in panel (c) is the width of the inner boundary layer W_{inner} and the green shaded region is the width of the outer boundary layer W_{outer} . (d) Non-dimensional forces are plotted as a function of the levee-centred cross-slope direction for $Q_M = 150$ g/s. All the forces are rescaled by the downslope component of the gravitational force $\rho g H \sin \zeta$. The magenta solid line represents the net force due to gravity and friction, whilst the blue line is the non-dimensional viscous force. Dot-dashed lines represent the maximum static friction.

channelised flow, as observed experimentally (Takagi *et al.* 2011). Close to this limit, an increase in mass flux primarily increases the channel width, with little effect on the flow thickness or speed. At constant mass flux, an increase in slope angle decreases the flow thickness (since $H_{min}(\zeta)$ is decreasing in ζ), which, counter-intuitively, decreases the flow velocity.

Away from the saddle point the orbits are almost identical, so the boundary layers at the sides of the flow collapse on top of one another when plotted in the levee-centred coordinate \hat{y} (figure 9c). These boundary layers have a shear-band structure (Pouliquen & Gutfraind 1996; Fenistein & van Hecke 2003; Schall & van Hecke 2010) that seamlessly connects the static material in the levee with the central region. The boundary layer has two length scales associated with it: an inner boundary layer where the intermediate friction is active, and an outer layer that is in the dynamic friction regime. The exact intermediate solution (3.16) implies that the inner boundary layer is of width

$$W_{inner} = \hat{y}_{transition}, \quad (3.27)$$

while the approximate solution (3.26) suggests that the outer boundary layer has a typical width

$$W_{outer} = \sqrt{c\bar{u}_{steady} + d}. \quad (3.28)$$

For the parameters given in table 1 for sand, the inner boundary layer width $W_{inner} \approx y_{transition}(H_{min}) = 7.16$ mm, whilst the outer dynamic boundary layer is approximately 8.52 mm wide. These are shown by the pink and light green shaded regions in figure 9(c) and provide a good order of magnitude estimate for the boundary layer width.

The governing ODE (3.5) describes a balance between its three terms, the forces due to the slope-tangential component of gravity, basal friction and lateral viscous stress. Hysteresis in the basal friction results in two distinct force balances, depending on the local flow velocity. In figure 9(d) forces are plotted as a function of the levee-centred cross slope direction \hat{y} . The magenta solid line represents the resultant force of gravity and friction, whilst the blue curve shows how viscous forces vary across the channel for $Q_M = 150$ g/s. All the forces are non-dimensionalised. Right next to the levees, where the flow is slow, the basal friction is greater than the downslope component of gravity, leading to an upslope resistive force. In this region, viscous stresses act in

the downslope direction, balancing the friction and sustaining motion. As the velocity increases towards the centre, friction decreases and eventually is balanced by gravity at the intermediate equilibrium (the green circle in figure 9c,d). Since this is an inflection point $d^2\bar{u}/dy^2 = 0$ and viscous forces also vanish. In the faster flow away from the levee wall, $d^2\bar{u}/dy^2 < 0$ and the viscous stress instead acts in the upslope direction, slowing the flow. In the absence of viscous stresses the flow in this region would accelerate to the steady uniform flow velocity \bar{u}_{steady} (3.9). In the central region, where the profile flattens ($\hat{y} > 5$ cm), viscous contributions are extremely small and the flow is basically governed by the balance between gravity and friction explaining why the velocity approaches \bar{u}_{steady} . Therefore, lateral viscous stresses provide the mechanism that connects the flow in these two regions and allow the interface between static and flowing granular layers to be modelled.

3.5. Comparison with experiments

The steady-state viscous theory is now compared with the experimental results of Takagi *et al.* (2011), for sand, and Félix & Thomas (2004) for glass beads. The width W and thickness H of the central flowing channel are direct results from the depth-averaged theory and provide the strongest comparisons with the experiments. The theory also solves for the depth-averaged velocity profile across the channel $\bar{u}(y)$, but this is not directly comparable with the surface velocities $u_s(y)$ measured in Takagi *et al.*'s (2011) experiments, because there is shear through the depth of the avalanche. The additional assumptions necessary to make a comparison are summarized in appendix A. Similarly Félix & Thomas (2004) report the total width of the flow W_{total} , rather than the width of the flowing channel W , so a comparison requires additional assumptions about the minimal width of the levees as detailed in appendix B.

3.5.1. Takagi et al.'s (2011) experiments with sand

The predicted flow thickness H is plotted in figure 10(a) as a function of the mass flux Q_M for the slope angle 32° used by Takagi *et al.* (2011). The solution consists of two regimes. At low mass fluxes, only the intermediate friction is active and the solution is given by (3.16), while above a critical threshold ($Q_{min} = 5.045$ g/s) the solutions also have a region of dynamic friction. These will be referred to as the intermediate

and dynamic regimes. In the intermediate regime, the thickness $H \in [H_{max}, h_{start}]$ is a rapidly decreasing function of the mass flux Q_M and is not physically realized. In the dynamic regime, the thickness $H \in [H_{min}, H_{max}] \approx [7.9, 9.2]$ mm is almost constant and asymptotes to H_{min} as $Q_M \rightarrow \infty$. This is significantly above $h_{stop} = 5$ mm and $h_* = 6.7$ mm. These observations are consistent with the experiments of Takagi *et al.* (2011) with 300–600 μm angular sand particles on a 32° slope who found that maximum flow thickness stayed approximately constant at a value of $H = 8.3 \pm 0.4$ mm as the mass flux was increased as shown in figure 10(a). Notably, if $\kappa = 10^{-3}$ is chosen, as in Pouliquen & Forterre (2002), instead of $\kappa = 1$, both H_{min} and H_{max} are only slightly ($\sim 0.1\%$) greater than $h_* = 6.7\text{mm}$, in contradiction with the experimental measurements.

For $\kappa = 1$, the intermediate and dynamic regimes for the flowing channel width W , as a function of Q_M , are compared to the experimental data of Takagi *et al.* (2011) in figure 10(b). The width in the dynamic regime rises approximately linearly as a function of the mass flux. This is in very good agreement with the Takagi *et al.*'s (2011) experimental data. An approximate solution for the width can be found by substituting $\bar{u} = 0$ at $\hat{y} = 0$ in equation (3.26) to show that

$$W \approx 2\sqrt{c\bar{u}_{steady} + d} \cosh^{-1} \left(\frac{\bar{u}_{steady}}{\bar{u}_{steady} - \bar{u}_{centre}} \right), \quad (3.29)$$

where the velocities \bar{u}_{steady} and \bar{u}_{centre} are given by (3.9) and by solving (3.24), respectively. The approximate solution is shown by the magenta line in figure 10(b) and lies very close to the experimental data, as well as the physical solution. The approximation (3.29) therefore provides a useful formula for the channel width.

The maximum depth-averaged velocity increases initially with the mass flux and then saturates above $Q_M = 50$ g/s. This trend is broadly in line with what Takagi *et al.* (2011) observed for the maximal surface velocity (figure 11a). The near-constant ratio of the surface velocity to the depth-averaged velocity provides information about shear through the depth of the avalanche. The best fit for the data implies $u_s/\bar{u} = 2.35$, which lies significantly above the ratio $u_s/\bar{u} = 1.67$ for Bagnold flow. This is consistent with the Discrete Element Method (DEM) simulations of Silbert, Landry & Grest (2003) and non-local theory of Kamrin & Henann (2015), which predict a transition from Bagnold flow to exponential-like velocity profiles with depth, as the flow gets close to h_* , even in the complete absence of sidewalls. The ratio of the surface velocity to

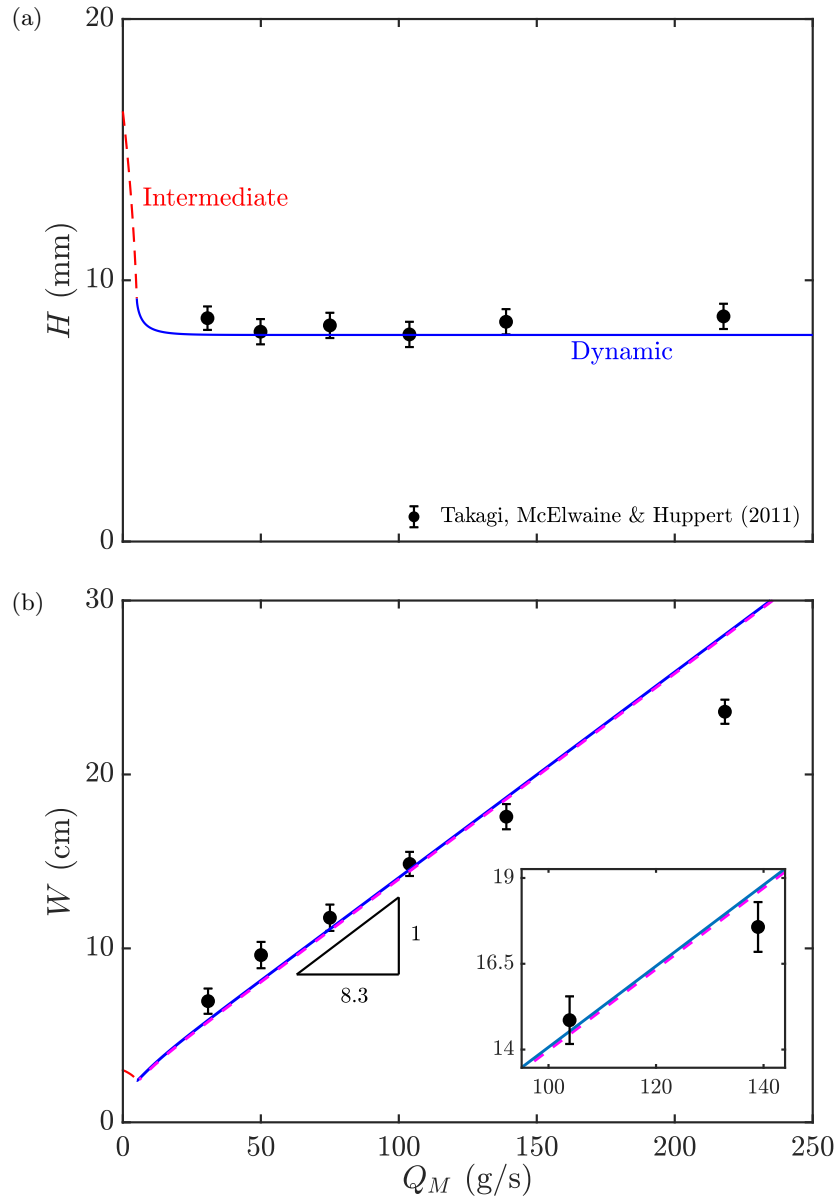


FIGURE 10. The solutions for (a) the thickness H and (b) the channel width W as a function of the mass flux Q_M . The markers and error bars correspond to the data of Takagi *et al.* (2011). Blue solid lines correspond to solutions that have active zones of dynamic and intermediate friction, while the red dashed lines are purely in the intermediate regime. The magenta dashed line in (b) shows an approximate solution for the width.

depth-averaged velocity in figure 11 strongly motivates the use of a concave exponential velocity profile with $u_s/\bar{u} = 2.35$ to reconstruct the non-depth-averaged velocity in this paper, which is discussed in more detail in appendix A.

Figure 11(b) shows a comparison between the predicted surface velocity across the channel, assuming $u_s = 2.35\bar{u}$, and that derived from Particle Image Velocimetry (PIV) measurements of Takagi *et al.* (2011) for a flow of sand on a 32° slope 2 m down from the source. The steady-state theory predicts a slightly narrower channel with a slightly faster maximum surface velocity than that observed in the experiments. This

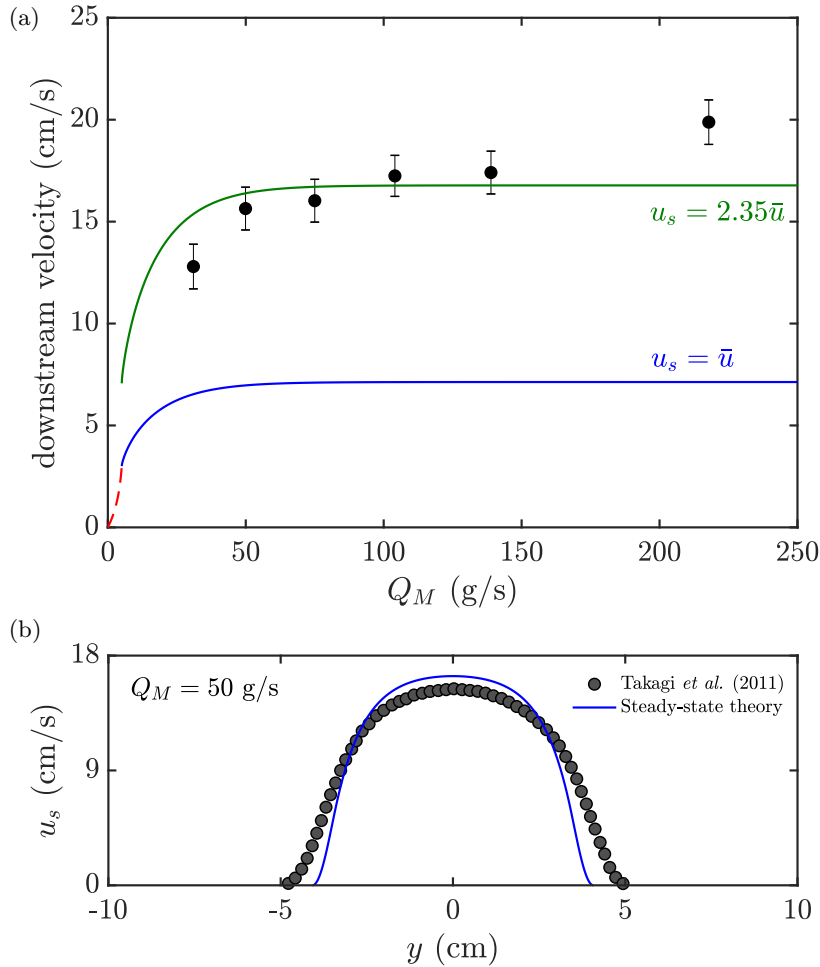


FIGURE 11. (a) Solutions for the maximum surface velocity as a function of the mass flux Q_M . The solid blue line is the maximum depth-averaged downslope velocity, whilst the green line is the best fit to the data, which suggests that the surface velocity $u_s = 2.35\bar{u}$. (b) A comparison between surface velocity profile across the channel (assuming that $u_s = 2.35\bar{u}$) with Takagi *et al.*'s (2011) data for $Q_M = 50$ g/s on a 32° slope.

may be an indication that the depth-averaged viscosity $\nu h^{1/2}$ is slightly larger than that assumed in the theory, which is derived for thicker flows that have well-developed Bagnold profiles.

Takagi *et al.* (2011) observed that there was a minimum mass flux below which the steadily flowing leveed channel was replaced by an unsteady sequence of avalanches triggered at equal time intervals as the grains piled up near the source and failed periodically. An illustrative movie showing the equivalent experiment with the red sand used in this paper is available online (movie 4). This will be investigated further in §4.4.

3.5.2. Félix & Thomas's (2004) experiments with glass beads

The solution for glass beads has the same structure as that for sand, consisting of an unphysical intermediate regime for low fluxes and a physically realised dynamic regime

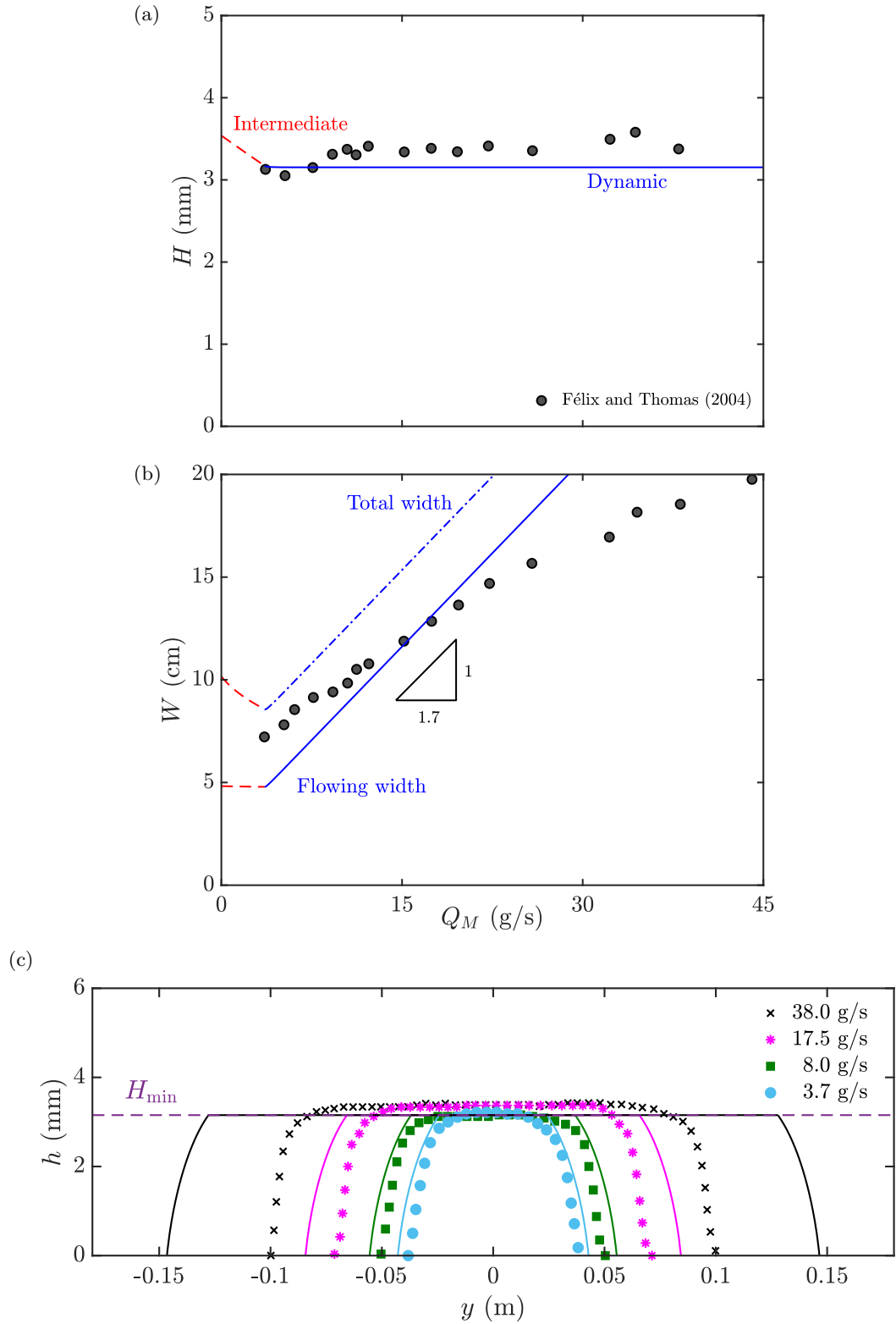


FIGURE 12. The solutions for (a) the channel thickness H and (b) the width W for galss beads as a function of the mass flux Q_M . The blue solid lines correspond to solutions that have active zones of dynamic friction, while the red dashed lines are purely in the intermediate regime. In addition the dot-dash line in (b) shows an approximation for the total width of the channel (see appendix B). The solutions are compared to Félix & Thomas's (2004) experimental data for (a) the thickness and (b) the total width (markers). Solid lines in (c) represent exact steady-state solutions for the thickness profile of the whole flow, including the minimal levees, when $Q_M = 3.7, 8.0, 17.5, 38$ g/s, whereas the dots are experimental laser profiles from Félix & Thomas (2004). The theoretical levee profiles assume a perfect balance between gravity, pressure gradient and maximum static friction as described in appendix B.

above $Q_{min} = 3.6$ g/s. The small range of $H \in [H_{min}, H_{max}] \approx [3.152, 3.166]$ mm implies that the predicted channel thickness is almost independent of the mass flux Q_M and is also significantly larger than both $h_{stop} \approx 2.16$ mm and $h_* \approx 2.9$ mm. The agreement between H and the experimental thickness data of Félix & Thomas (2004) is very good, as shown in figure 12(a). As with sand, the channel thickness H is in agreement with experiments when $\kappa = 1$, but if $\kappa = 10^{-3}$ is chosen the thickness is under-predicted, with both H_{min} and H_{max} extremely close to $h_* \approx 2.9$ mm.

Félix & Thomas (2004) also reported the total width of the flow as a function of the mass flux. This makes direct comparison with experiments more difficult, not least because frictional hysteresis implies that the levee widths are not unique. However, by assuming that all points in the levee are on the brink of yield (Hulme 1974; Balmforth *et al.* 2001) a unique solution for the minimal levee width can be obtained, as described in detail in appendix B. Adding two minimal levees widths to the flowing channel width W then gives a good approximation for the minimum total width W_{total} of the channel.

Figure 12(b) shows a comparison of both W_{total} and W to the total width measured by Félix & Thomas (2004) as a function of the mass flux Q_M . For relatively low mass fluxes most of the experimental data lies close to the minimum total width W_{total} predicted by the solutions in which the dynamic friction is active. However, for larger values of Q_M the width appears to be over predicted by the steady-state theory. Félix & Thomas (2004) do not report the time or position at which their steady-state data was collected, but their chute was relatively short (2 m) and they only collected data for 80 s. The most likely explanation for the apparent discrepancy at high mass fluxes is therefore not that the steady-state predictions are wrong, but that the experimental data was not collected far enough downstream or after long enough times. For instance, Deboeuf *et al.* (2006) performed experiments at $Q_M = 25$ g/s on a 3 m chute and found that although the thickness was close to steady-state within 100 s the width of the channel adjusted on a much longer time scale and was still slowly widening at 3500 s (see their figure 2). Even longer experiments by Takagi *et al.* (2011) found that the levee margins for glass beads eventually became unstable after 70-90 minutes.

Deboeuf *et al.*'s (2006) and Takagi *et al.*'s (2011) observations suggests that for

weakly hysteretic materials, such as glass beads, it can take a long time and/or distance for the width of the flow to reach steady state and that steady state may itself be unstable. This is borne out by a comparison between the experiments of Félix & Thomas (2004) and the full steady-state thickness profiles (including the levees and the central channel) in figure 12(c). All of the experimental flows have thicknesses that are close to their steady-state value and the widths also agree for low mass fluxes $Q_M = 3.7$ and 8.0 g/s. However, as the mass flux is increased to $Q_M = 17.5$ and 38 g/s the width of the channel is seen to be far from steady-state. As stated above, this apparent lack of agreement at high mass fluxes is most likely due to the experiments having not been run for long enough and/or the measurement position not being far enough downstream.

3.6. Reconstruction of the smoothly varying velocity field

Figure 13 shows a reconstruction of the steady-state downslope velocity for glass beads in a cross section through the channel for $Q_M = 3.7, 8.0, 17.5, 38$ g/s. These solutions assume an exponential velocity profile through the avalanche depth, which is appropriate for thin flows close to h_* (see appendix A). It is striking that the velocity varies smoothly across the whole channel, with a maximum at the surface and centre of the flow, as well as boundary layers adjacent to the levee-channel interfaces providing a seamless connection to the static levees. This is in stark contrast to the inviscid model, which has a uniform velocity profile across the channel with contact discontinuities (velocity jumps) at the levee-channel margins as shown in figure 7. These plots also highlight that for a given mass flux Q_M and inclination angle ζ , the viscous model has a unique solution for the height, width and velocity, rather than an infinite number of steady states, parameterized by $H \in [h_*, h_{start}]$, in the inviscid case. Moreover the height of the flows is approximately the same and the minimal levees are therefore closely similar. It should be noted that in the bottom left and right corners of the central channel the flow is moving very slowly. This is consistent with Deboeuf *et al.*'s (2006) and Kokelaar *et al.*'s (2014) colour change observations, which demonstrated that the material in these regions was either static or very slowly moving. Such linings of the channel do not occur in the inviscid model as shown in figure 7.

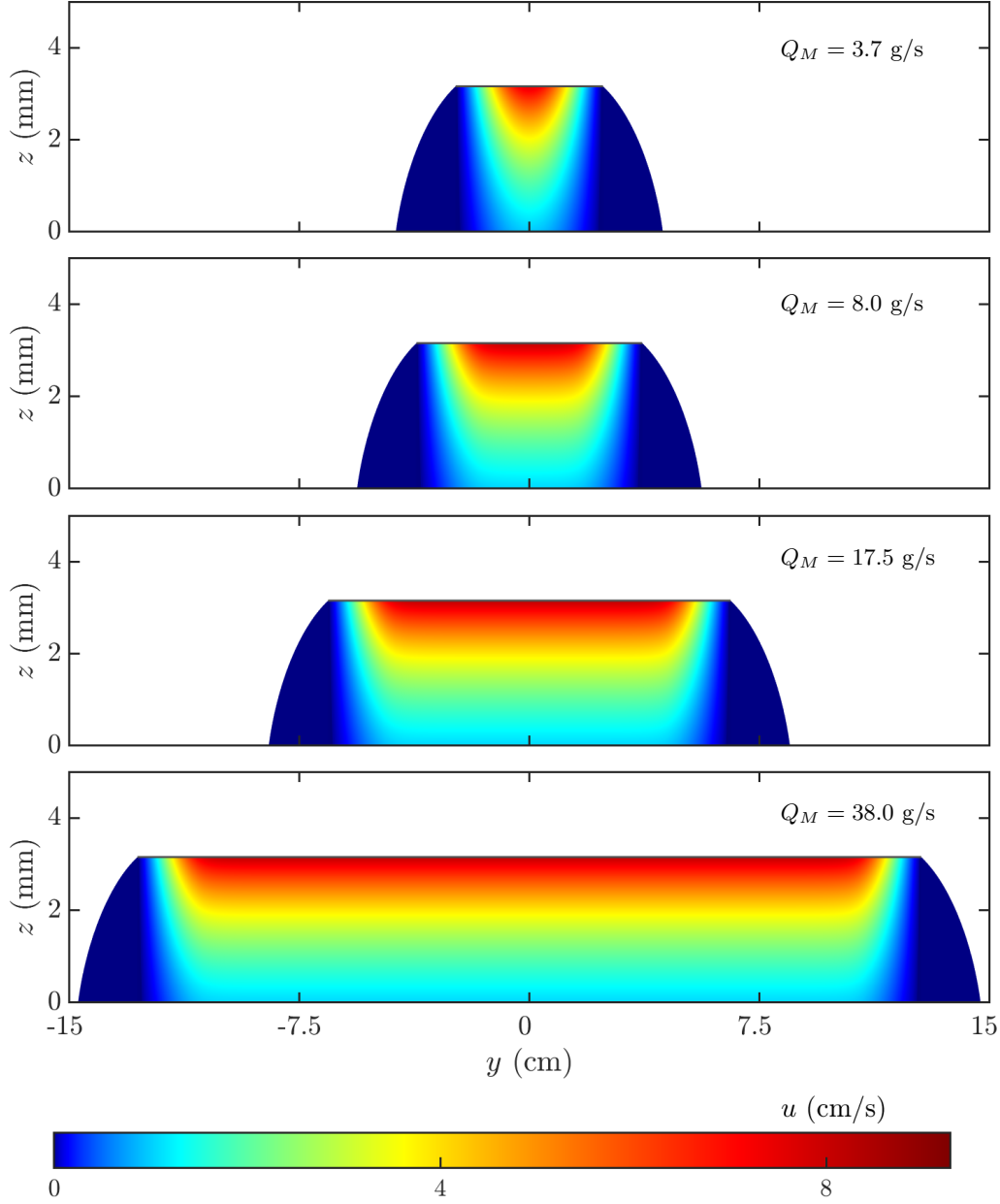


FIGURE 13. Steady-state downstream velocity profile $u(y, z)$ for a self-channelled flow of glass beads at an angle $\zeta = 25^\circ$, and mass fluxes $Q_M = 3.7, 8.0, 17.5, 38$ g/s. The velocity is reconstructed using an exponential profile with $\lambda = 2.05$ as discussed in appendix A. The viscous formulation predicts a unique solution for each mass flux and slope angle. This contrasts with the inviscid case, where there is an infinite set of solutions parameterized by $H \in [h_*, h_{start}]$ as shown in figure 7. In the viscous case, the thickness of the central channel is almost independent of the mass flux and hence the shape of the minimum levees required to support the flowing central channel are almost the same for all fluxes.

4. Time-dependent numerical simulations

To investigate the evolution towards the steady-state, fully time and spatially dependent numerical solutions to the system of conservation laws (2.2)–(2.4) are now computed.

4.1. Numerical method

Numerical solutions are calculated using a high-resolution semi-discrete Non-Oscillatory Central (NOC) scheme for convection-diffusion equations (Kurganov & Tadmor 2000). This method has proved its ability to solve similar systems of conservation laws for erosion-deposition waves (Edwards & Gray 2015; Edwards *et al.* 2017), segregation-induced finger formation (Baker *et al.* 2016*b*) and bi-disperse roll waves (Viroulet *et al.* 2018). The equations are solved in conservative form,

$$\frac{\partial \mathbf{U}}{\partial t} + \frac{\partial \mathbf{c}_1(\mathbf{U})}{\partial x} + \frac{\partial \mathbf{c}_2(\mathbf{U})}{\partial y} = \mathbf{S}(\mathbf{U}) + \frac{\partial \mathbf{D}_1(\mathbf{U}, \mathbf{U}_x, \mathbf{U}_y)}{\partial x} + \frac{\partial \mathbf{D}_2(\mathbf{U}, \mathbf{U}_x, \mathbf{U}_y)}{\partial y}, \quad (4.1)$$

where $\mathbf{U} = (h, h\bar{u}, h\bar{v})^T$ is the vector of conserved fields, with \mathbf{U}_x and \mathbf{U}_y being the derivatives of \mathbf{U} with respect to x and y , respectively. Comparing the governing equations (2.2)–(2.4) with (4.1) yields convective fluxes

$$\mathbf{c}_1 = \begin{pmatrix} m \\ \frac{m^2}{h} + \frac{h^2}{2}g \cos \zeta \\ \frac{mn}{h} \end{pmatrix}, \quad \mathbf{c}_2 = \begin{pmatrix} n \\ \frac{mn}{h} \\ \frac{n^2}{h} + \frac{h^2}{2}g \cos \zeta \end{pmatrix}, \quad (4.2)$$

and diffusive fluxes

$$\mathbf{D}_1 = \nu h^{1/2} \begin{pmatrix} 0 \\ \frac{\partial m}{\partial x} - \frac{m}{h} \frac{\partial h}{\partial x} \\ \frac{1}{2} \left(\frac{\partial m}{\partial y} - \frac{m}{h} \frac{\partial h}{\partial y} + \frac{\partial n}{\partial x} - \frac{n}{h} \frac{\partial h}{\partial x} \right) \end{pmatrix}, \quad (4.3)$$

$$\mathbf{D}_2 = \nu h^{1/2} \begin{pmatrix} 0 \\ \frac{1}{2} \left(\frac{\partial n}{\partial x} - \frac{n}{h} \frac{\partial h}{\partial x} + \frac{\partial m}{\partial y} - \frac{m}{h} \frac{\partial h}{\partial y} \right) \\ \frac{\partial n}{\partial y} - \frac{n}{h} \frac{\partial h}{\partial y} \end{pmatrix}, \quad (4.4)$$

where $\mathbf{m} = (m, n)^T = (h\bar{u}, h\bar{v})^T$. The source term vector is

$$\mathbf{S} = \begin{pmatrix} S_{inflow}(x, y) \\ hg \sin \zeta - \mu_b e_1 hg \cos \zeta \\ -\mu_b e_2 hg \cos \zeta \end{pmatrix}, \quad (4.5)$$

where an additional volume source term $S_{inflow}(x, y)$ has been added to the right-hand side of the depth-averaged mass balance equation (2.2). This provides a simple way of modelling the experimental supply of grains onto the chute from a funnel (see §1). Grains are added to the domain in a small circular region, described by

$$S_{inflow} = \begin{cases} \tilde{S}(R^2 - ((x - x_0)^2 + y^2))^2, & \text{if } (x - x_0)^2 + y^2 \leq R^2, \\ 0, & \text{otherwise} \end{cases}, \quad (4.6)$$

where \tilde{S} is a normalisation constant, $R = 2.5$ cm is the radius of the circular inflow and $x_0 = 15$ cm is the downstream position of its centre. Defining polar coordinates with an origin at the centre of the circle by $x = x_0 + r \cos \theta$ and $y = r \sin \theta$, the total volume flux of material entering the chute is

$$Q = \int_{\theta=0}^{2\pi} \int_{r=0}^R S_{inflow} r dr d\theta. \quad (4.7)$$

Since the total mass flux is

$$Q_M = \rho Q, \quad (4.8)$$

the normalisation factor in (4.6) is

$$\tilde{S} = \frac{3Q_M}{\pi \rho R^6}. \quad (4.9)$$

The numerical solutions start with initial conditions of an empty chute, $h = 0$, $\mathbf{m} = \mathbf{0}$ at $t = 0$. An outflow boundary condition is implemented at the bottom of the chute by extrapolating the solution to a row of ghost cells beyond the computational domain (LeVeque 2002). The flow does not reach the top ($x = 0$) or sides ($y = \pm L_y/2$) of the domain and so a boundary condition $h = 0$ is trivially satisfied here.

The two-dimensional numerical domain $(L_x, L_y) = (2.5, 0.3)$ m is discretised into a rectangular grid with $(n_x, n_y) = (1000, 300)$ grid points, respectively. Numerical fluxes are computed by a generalised minmod limiter with $\theta = 2$ (Kurganov & Tadmor 2000) and the spatially-discretised equations are integrated in time using a second-order Runge-Kutta method, with time-steps determined by a CFL (Courant-Friedrichs-Lewy) number of 0.225, and a maximum step-size $\Delta t = 10^{-4}$ s (LeVeque 2002), which

is required to minimise creep of the levees. Numerical errors caused by the degeneracy in the conservative form of the equations when $h = 0$ are mitigated by introducing a minimum thickness threshold (set to 10^{-5} m or approximately one tenth of a grain diameter), below which the thickness and momentum are set to zero.

4.2. Formation and partial drainage of a self-channelised flow

The downslope velocity \bar{u} and thickness h of a typical numerical solution are shown in figures 14(a) and 15(a) respectively (supplementary movies 5 and 6). For the parameters of sand at a slope angle $\zeta = 32^\circ$, the mass flux $Q_M = 85$ g/s is large enough for a self-channelised avalanche to form. After an initial adjustment from the source condition in the uppermost ~ 1 m, the simulated flow spontaneously selects its own steady-state channel thickness, width and cross-slope velocity profile. A flow head is rapidly established and propagates down the plane at constant speed (figure 14a), laying down a steady-state levee-channel morphology behind it once some initial transients have dissipated. Figure 14(d) shows the downslope velocity at $x = 1.75$ m. At $t = 32$ s the whole width of the flow is mobile at $x = 1.75$ m, but, as the front passes by, the sides of the flow rapidly solidify and by $t \geq 60$ s the velocity profile across the channel is rapidly tending to the steady-state solution computed directly from equation (3.5). The velocity therefore is almost constant in the centre of the channel and smoothly connects to the levee-channel-interfaces on either side across two boundary-layers. The thickness in this flowing section is constant, as shown in figure 15(b) and by the thickness profile lines across the channel at $x = 0.5, 1, 1.5$ and 2 m in figures 14 and 15.

By $t = 60$ s (figures 14b and 15b) the velocity profile and constant channel thickness $H = 7.9$ mm are in good agreement with the steady state predictions in §3.3 (figures 14d and 15d). Once established the width of the flowing channel remains constant in the numerical simulations. The outer edges of the levees have some residual creep, which is less than 1% of the flow velocity in the channel, for the timestep of 10^{-4} s used here. Importantly this creep velocity scales with the timestep and so the levees converge to a static state under time-step refinement.

The timescale for establishment of the steady state is comparable to that in the experiments with 160–200 μm red sand (see supplementary movie 1), but is much quicker than Takagi *et al.*'s (2011) experiments which took up to 20 minutes. This

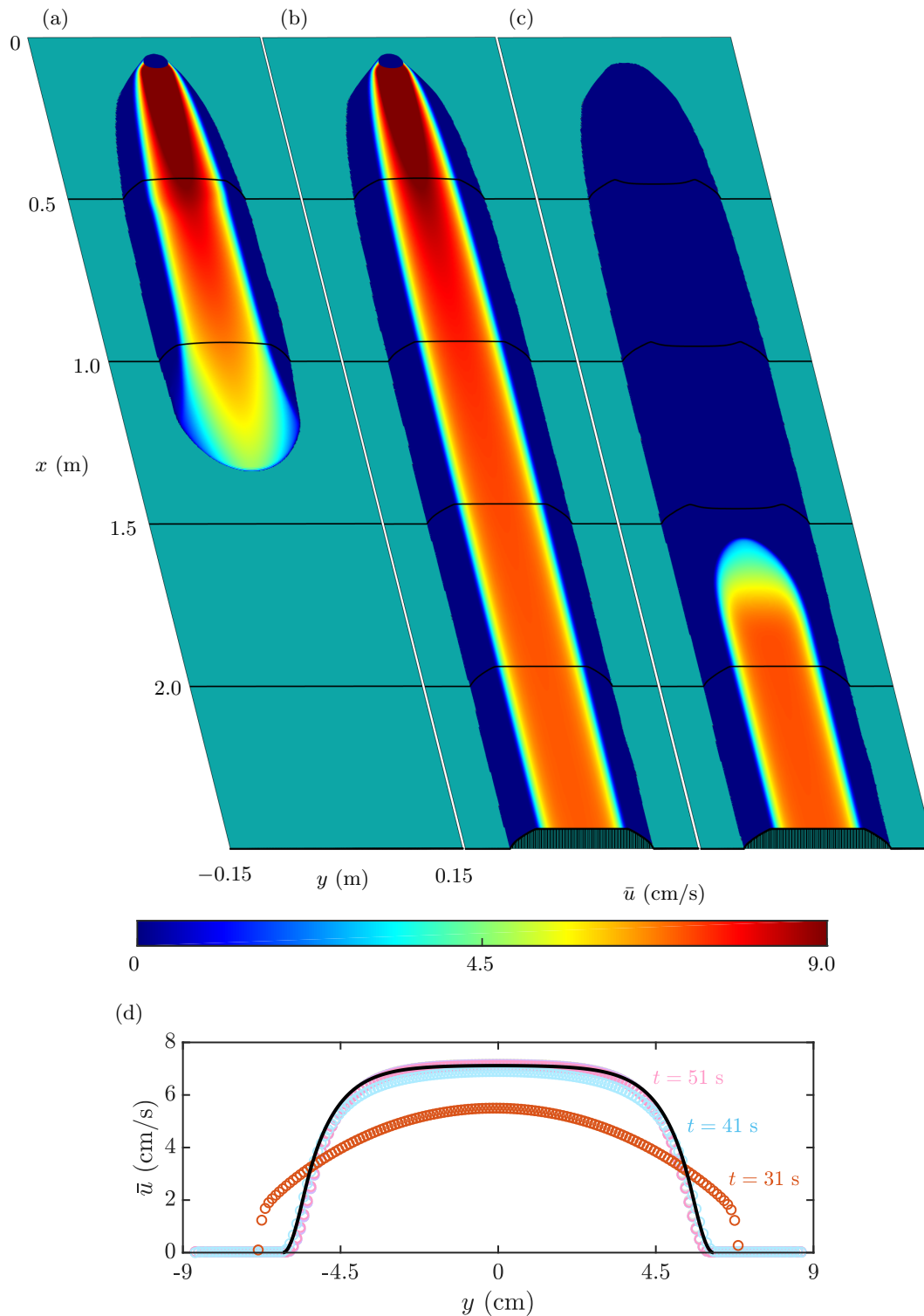


FIGURE 14. Fully time and spatially dependent numerical solutions for the downslope velocity of sand at (a) $t = 20$ s, (b) $t = 80$ s and (c) $t = 105$ s for an inflow mass flux $Q_M = 85$ g/s and inclination $\zeta = 32^\circ$. (a) Shows the flow front propagating steadily down the plane and forming the levee-channel morphology behind it, (b) shows the steady-state fully-developed self-channelled flow and (c) the channel in the process of draining out to leave behind a static deposit with parallel-sided levees and a partially drained central channel. The final panel (d) shows the downslope velocity profile across the channel $\bar{u}(y)$ at $x = 1.75$ m at $t = 31$ to 91 s in intervals of 10 seconds. Markers indicate fully time dependent simulations, whereas the solid black line represents the exact steady-state solution. A movie showing the time and spatially evolving flow is available in the online supplementary material (movie 5).

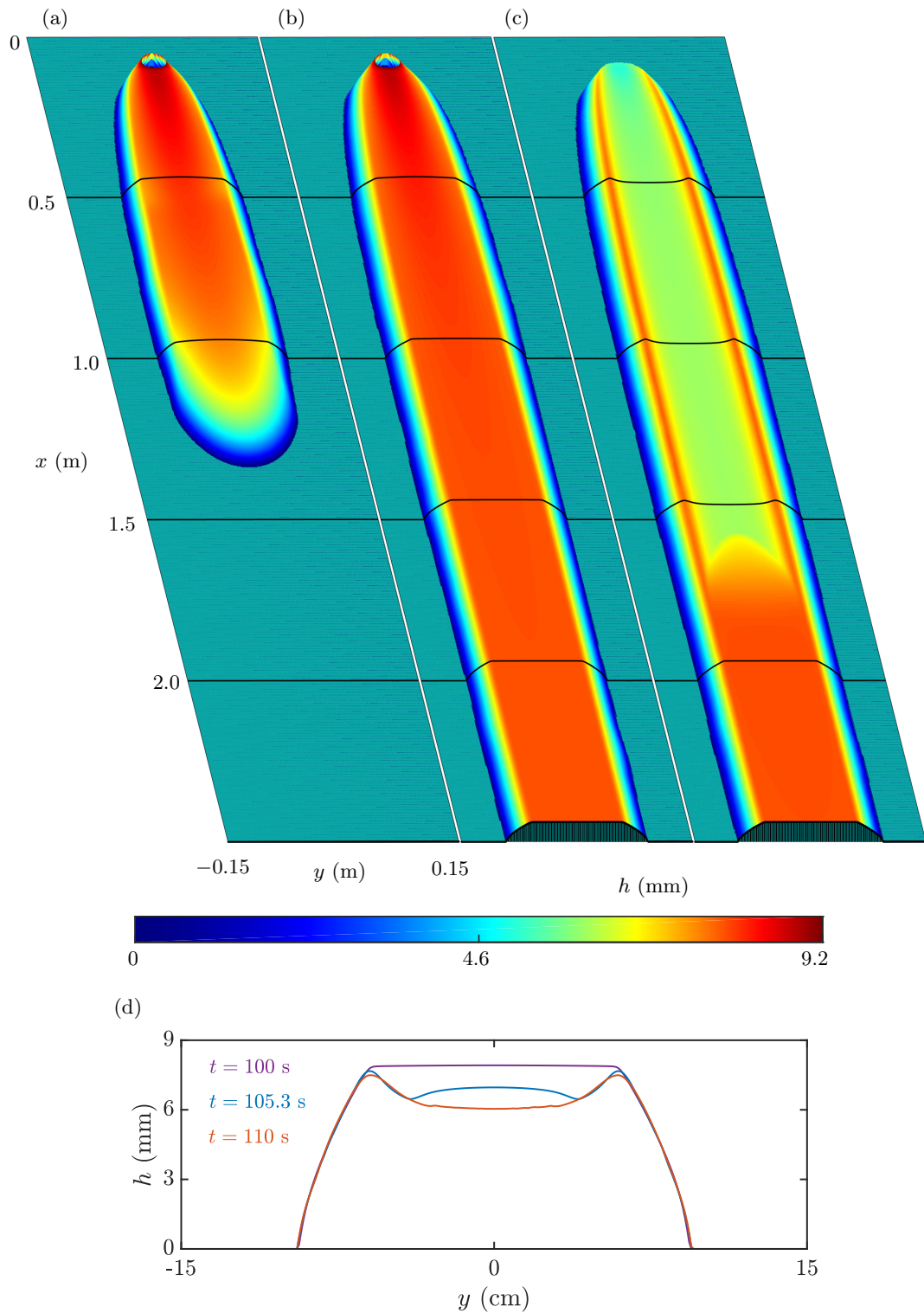


FIGURE 15. Fully time and spatially dependent numerical solutions for the thickness of sand at (a) $t = 20$ s, (b) $t = 80$ s and (c) $t = 105$ s for an inflow mass flux $Q_M = 85$ g/s and inclination $\zeta = 32^\circ$ as in figure 14. (a) Shows the flow front propagating steadily down the plane and forming the levee-channel morphology behind it, (b) shows the steady-state fully-developed self-channelised flow and (c) the channel in the process of draining out to leave behind a static deposit with parallel-sided levees and a partially drained central channel. The final panel (d) shows numerical solutions for the thickness profile at $x = 1.75$ m at three different times. A movie showing the time and spatially evolving flow is available in the online supplementary material (movie 6).

discrepancy may be due to a difference in bed roughness: whereas Takagi *et al.* (2011) used a base roughened by grains of the same size as the grains in the flow, the experiments in this paper use larger particles in the bed than in the flow, which reduces slip between the levee and base.

The steady fully-developed state is maintained until $t = 100$ s when the inflow is shut off (supplementary movies 5 and 6). The flow then thins near the top of the chute and a deposition wave moves rapidly downslope, thinning and then depositing material that was previously flowing in the central channel (figures 14c and 15c). This process is illustrated by cross-slope thickness profiles at $x = 1.75$ for $t = 100, 105.3, 110$ s in figure 15(d). At $t = 100$ s the channel thickness is still equal to the theoretically predicted steady-state value $H = 7.9$ mm and the surface gradient of the levee-walls is below the maximum static friction, so they are stable and support the central channel. At $t = 105.3$ s, in the middle of the deposition wave, the flow wanes and only a region near the centre of the channel remains flowing. This deposition wave leaves behind a static deposit with super-elevated levee walls that have a maximum thickness close to the original flow thickness H and a deposit in the central channel that lies just above h_{stop} (figure 15d, $t = 110$ s). As noted by Félix & Thomas (2004) and Mangeney *et al.* (2007), the flow thickness H and channel width W are preserved in the deposit, allowing field observations to be used to estimate the inflow mass flux required to sustain the channel during flow. This provides an important constraint on the time-evolution of the geophysical processes that created the levees, even when the flow event was not observed directly.

4.3. Narrowing and widening of the central flowing channel

The response of the steady fully-developed solution to changes in the inflow mass flux is now investigated. The initial state is chosen to be the same as in figures 14(b) and 15(b) for an inflow mass flux $Q_M = 85$ g/s and slope angle $\zeta = 32^\circ$. The mass flux is then reduced to $Q_M = 70$ g/s at $t = 100$ s as shown in movies 7 and 8. The channel does not narrow uniformly as shown in figure 16(a,b). An expanding wave travels rapidly downslope, which separates a downstream region, where the channel is still at the steady-state for $Q_M = 85$ g/s, and an upstream region where the flow attains the new steady-state for $Q_M = 70$ g/s. The front section of this wave travels slightly faster than the rear, so the flowing regions pinch off and separate from one another.

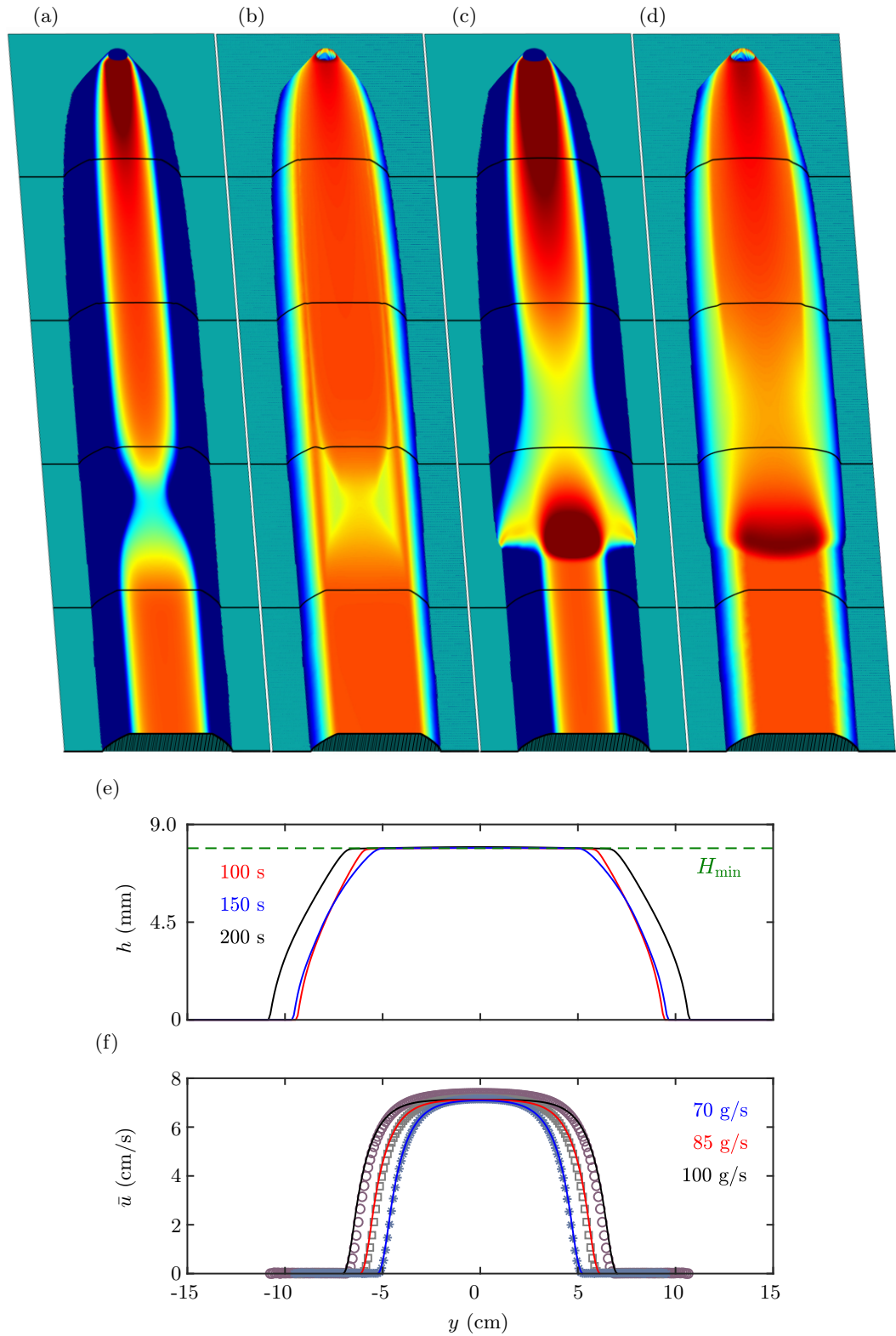


FIGURE 16. Spatial contours of (a,c) the depth-averaged downslope velocity and (b,d) the thickness at (a,b) time $t = 105.5$ s and (c,d) 155 s using the same contour scales as in figures 14 and 15. Panels (a,b) show the mass flux being reduced from $Q_M = 85$ g/s to $Q_M = 70$ g/s, while (c,d) show the flux being increased from $Q_M = 70$ g/s and $Q_M = 100$ g/s on a slope inclined at $\zeta = 32^\circ$. (e) Shows the computed thickness at $x = 1.75$ m at $t = 100, 150$ and 200 s and (f) shows the computed downslope velocity across the channel at the same location and times and a comparison with the steady-state solution in §3.1. In (f) the steady-state theory is shown with red, blue and black solid lines and the computed solutions are shown with markers. Two movies showing the evolving velocity and thickness are available online (movies 7 and 8).

As a result there is a brief period where the grains come to rest in the channel, before they are remobilised by the second half of the wave as shown in figure 16(a,b). This behaviour is also observed in the experiments with red sand as shown in movie 3. The wave eventually propagates out of the domain to leave a parallel-sided leveed channel with a width $W = 10.3$ cm that is narrower than the original width $W = 12.1$ cm for $Q_M = 85$ g/s. The thickness of the channel before and after the change in flux are $H_{before} = 7.9145$ mm and $H_{after} = 7.904$ mm, respectively, which are virtually the same as shown in figure 16(e). Once the channel has established itself the computed downslope velocities at $x = 1.75$ m are almost identical to the steady-state theory in §3.3 as shown in figure 16(f). During the process of channel narrowing, grains are deposited on the inside of the pre-existing levee walls, but there is no change to the existing levees, so the total width of the channel does not change, as shown in figure 16(b).

Once the new fully-developed steady-state for $Q_M = 70$ g/s has been established the inflow flux is increased to $Q_M = 100$ g/s at $t = 150$ s as shown in movies 7 and 8. A wave again propagates down the channel, which adjusts its width. This time the wave remobilises the levees on both sides, broadening the central channel and then re-solidifying to form levees that are slightly further out as shown in figure 16(c,d). This process is inherently unsteady and so the outer margins of the new levees are no longer perfectly parallel. The initial wavefront, associated with the change in mass flux, grows in size as it erodes the static material in the pre-existing wide levees and deposits a narrower levee behind it. As a result it moves faster than the steady uniform flow behind it and therefore detaches from it, producing a brief period where the grains come to rest before the new steady-state flow establishes itself. The computed steady-state thickness and velocity profiles across the channel are shown in figure 16(e) and (f), respectively. These show that, as the mass flux is increased, the width increases to $W = 13.7$ cm, the thickness barely changes and the velocity profile lies very close to the steady-state value in §3. All traces of the previous history of the flow that was recorded in the earlier levees are therefore destroyed, which is consistent with the experiments in figure 4.

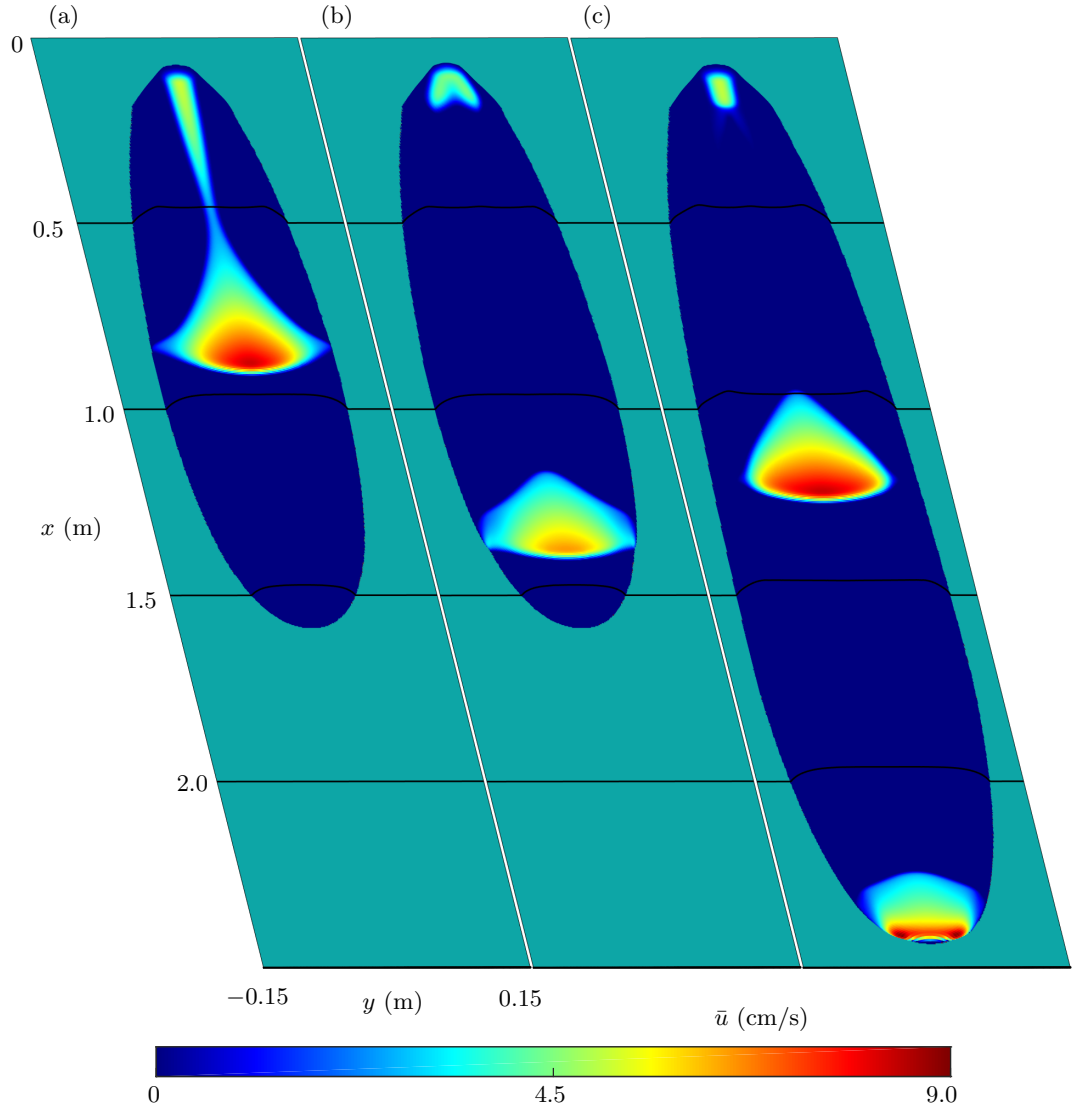


FIGURE 17. Fully time and spatially dependent numerical solutions for the downslope velocity of sand at (a) $t = 125.5$ s, (b) $t = 127.3$ s and (c) $t = 250$ s for an inflow mass flux $Q_M = 16$ g/s and inclination $\zeta = 32^\circ$. In the unsteady flow regime a series of erosion-deposition waves flow over the previously deposited grains until they overrun the front and rapidly stop. The flow front therefore advances intermittently downslope. A thicker layer of material forms at the centre line, as well as at the sides of the source. A movie showing the time and spatially evolving velocity is available in the online supplementary material (movie 9).

4.4. Unsteady periodic avalanching regime

When the mass flux is reduced to $Q_M = 16$ g/s grains pile up near the source, fail periodically and then come to rest again by upslope propagating stopping waves. The initial phases of this solution are very complicated with a sequence of pile collapses that produce two avalanches that propagate down either side of a central ridge, as shown in the online supplementary movies 9 and 10. However, after approximately 95 s the collapses become more structured, producing a single erosion-deposition wave that propagates downslope over a thin deposit that has been laid down by previous

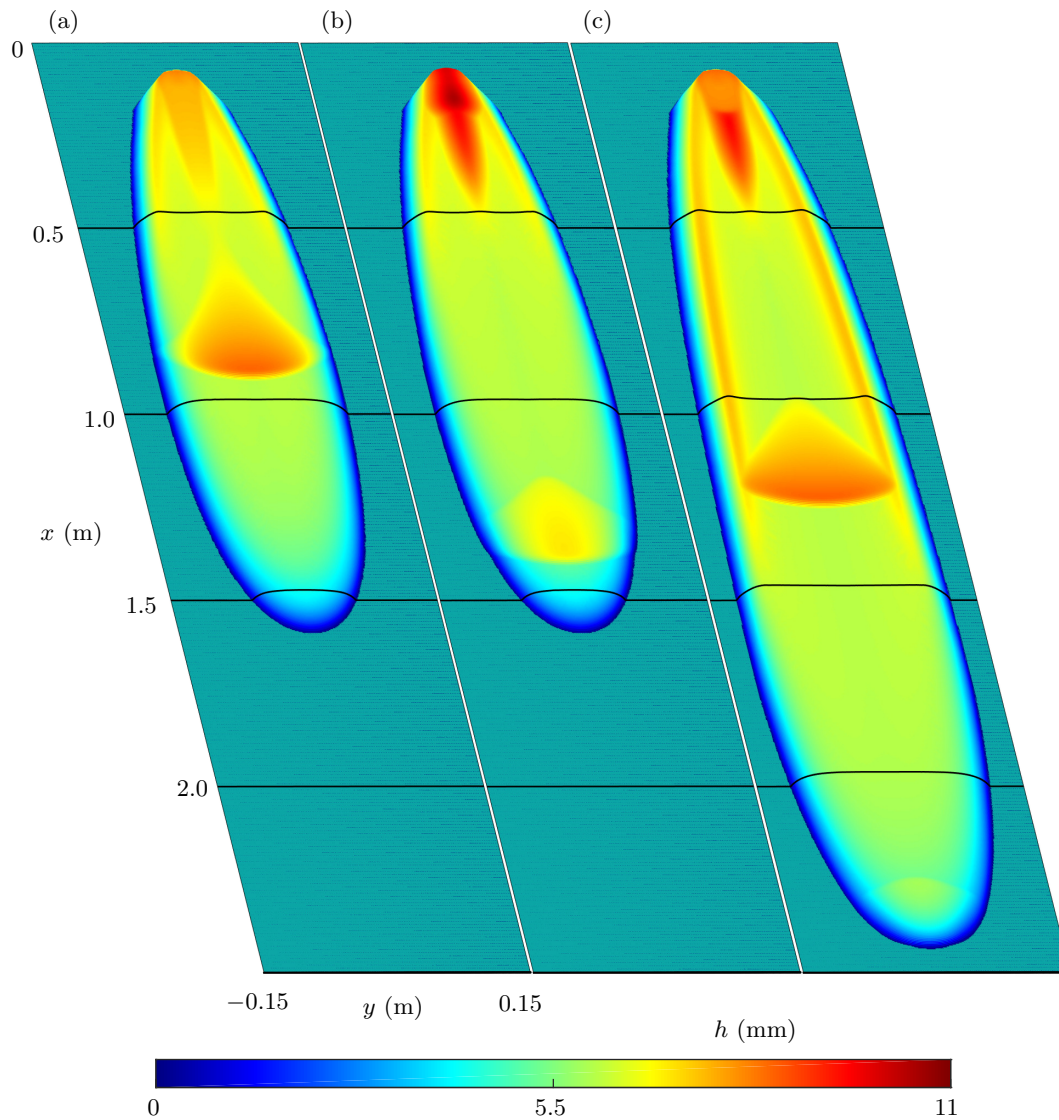


FIGURE 18. Fully time and spatially dependent numerical solutions for the thickness of sand at (a) $t = 125.5$ s, (b) $t = 127.3$ s and (c) $t = 250$ s for an inflow mass flux $Q_M = 16$ g/s and inclination $\zeta = 32^\circ$ as in figure 17. In the unsteady flow regime a series of erosion-deposition waves flow over the previously deposited grains until they overrun the front and rapidly stop. The flow front therefore advances intermittently downslope. A thicker layer of material forms at the centre line, as well as at the sides of the source. A movie showing the time and spatially evolving thickness is available in the online supplementary material (movie 10).

flows, as shown in figures 17 and 18. Erosion-deposition waves continuously erode material at their leading edge and deposit material at the rear as they propagate downslope (Edwards & Gray 2015; Edwards *et al.* 2017). The waves therefore do not represent a single body of material that is released from the collapse, but a constantly changing body of grains. From $t = 95$ – 300 s the static deposit has an approximately elliptical shape that becomes progressively elongated with increasing time, with the source centred at the upstream focus point. The erosion-deposition waves are able to propagate easily on top of this deposit and grow in size in the first half of the ellipse

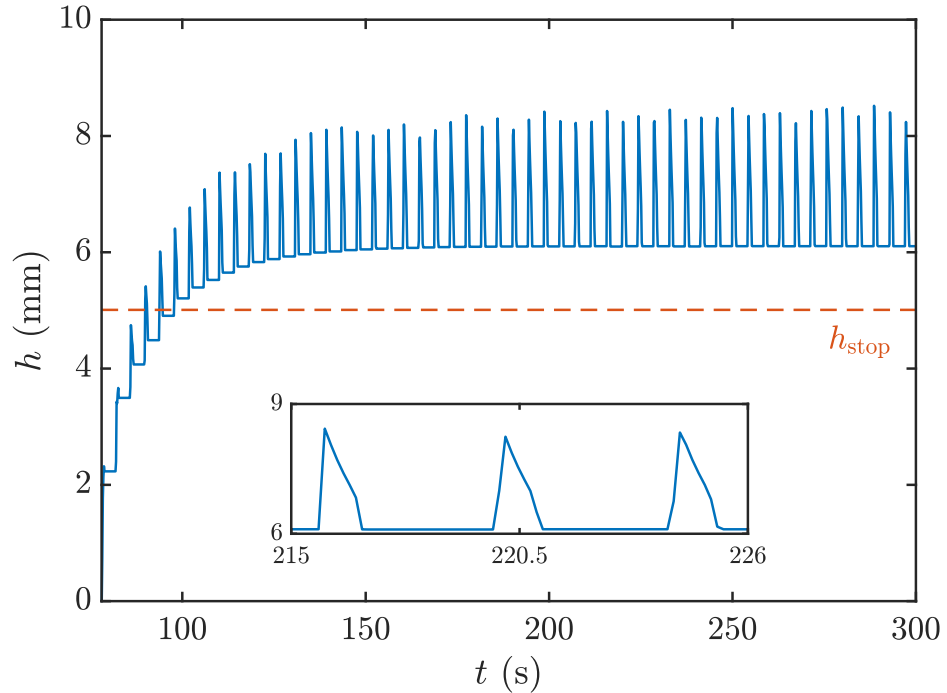


FIGURE 19. Computed thickness h for sand as a function of time at $x = 1.25$ m and $y = 0$ m for a mass flux $Q_M = 16$ g/s and inclination $\zeta = 32^\circ$. The flow front first reaches this point at $t = 78$ s, the flow thickness then builds up above h_{stop} , and the waves rapidly develop a constant period $T_\infty \approx 4$ s as shown in the inset space-time plot.

expanding laterally to span its width. However, as the width of the elliptical deposit narrows, the avalanche overtops the sides and the material on the static bed travels a short distance before it stops. As a result, as the avalanche continues to propagate downslope, it is progressively deposited at the sides and decreases in size, before it eventually overtops the deposit front and then rapidly comes to rest. The front and sides of the deposit are therefore progressively advanced in a sequence of steps as each avalanche passes by.

The movies also show that as the erosion-deposition wave propagates downslope it detaches from the flowing material at the source and a retrogressive (upslope propagating) stopping wave forms that travels up to the source and brings the grains to rest. As material then builds up at the source it eventually overcomes the static friction and collapses to form the next erosion-deposition wave. In this way a quasi-periodic sequence of avalanches is formed that transport the grains downslope in a series of steps. This process is visualised in figure 19, which shows the thickness at a fixed position $x = 1.25$ m as a function of time. The front first reaches this position at approximately 90 s. During the passage of the first five or six waves the deposit thickness builds up to just over 6 mm, which lies between $h_{stop} = 5$ mm

and $h_* = 6.7$ mm. The presence of this erodible layer allows the avalanches to propagate easily downslope with a total thickness of approximately 8 mm. The erodible layer reduces the apparent friction experienced by the grains, in the sense that an avalanche of the same volume released on the same slope, but without the erodible layer, would rapidly come to rest. Each of the individual waves have the same shape as the one-dimensional erosion-deposition waves modelled by Edwards & Gray (2015) and develop into a periodic wave-train with a period of about 4 s. Qualitatively, the simulated thickness as a function of time (figure 19) is very similar to that observed experimentally (figure 17 of Takagi *et al.* 2011); indeed, the trough thickness and the final amplitude of the waves are in close quantitative agreement. However, Takagi *et al.* (2011) observed experimental waves of period about 11.5 s, which is significantly longer than the 4 s period that emerges from the simulations. This is probably because the depth-averaged theory is not able to accurately model the complicated failure processes that occur during the build-up and collapse of the pile near the source. The model can nevertheless predict the onset of unstable flow at low mass fluxes, which was observed experimentally by Takagi *et al.* (2011) as well as for the red sand in movie 4. Periodic waves propagating over previously deposited material have been observed in debris flows at Illgraben, Switzerland (McArdell 2016) and the Jiangjia Valley, China (Yong, Jingjing, Kaiheng & Pengcheng 2012).

4.5. Comparison with Mangeney *et al.*'s (2007) inviscid numerical simulations

Mangeney *et al.* (2007) developed a depth-averaged inviscid model for levee formation using the conservation laws (2.2)–(2.4) with $\nu = 0$ (no viscous terms) and the non-monotonic friction law of Pouliquen & Forterre (2002) for glass beads (obtained by setting $\Gamma = 0$, $\beta_* = \beta$, $\kappa = 10^{-3}$, and introducing δ_4 , the maximum slope angle at which a static layer exists). Using a shock-capturing numerical method to solve the time-dependent equations, Mangeney *et al.* (2007) qualitatively captured the process of self-channelisation, with grains spreading laterally at the flow front, slowing, and then depositing to form parallel-sided very-slowly-moving levees behind the head, that supported the flow in the central channel. The thickness and downslope velocity were approximately constant in the central moving channel with a rapid decrease in downstream velocity at the levee-channel boundary as shown in their figures 12 and 15, for a mass flux $Q_M = 12$ g/s of glass beads on a slope of 25° . At $t = 145$ s (just prior

to their inflow being stopped) the width of the shear layer that connected the central flow to the static levees was $W_{\text{boundary}} \approx 0.0022$ m. Since their numerical experiments were performed on a rectangular domain $(L_x, L_y) = (2.2, 0.2)$ m that was divided into $(n_x, n_y) = (400, 300)$ grid points, this implies that the downslope velocity dropped from the steady uniform value to zero over $(n_y/L_y)W_{\text{boundary}} \approx 3.3$ grid cells.

Mangeney *et al.* (2007) used friction parameters corresponding to those in the experiments of Félix & Thomas’s (2004), but with a thickness lengthscale $\mathcal{L} = 0.8$ mm that was larger than the experimental best fit of $\mathcal{L} = 0.65$ mm, leading to a numerical h_{stop} about 25% larger than that in experiments. Despite this, their simulated flow thickness of $H \approx 1.03h_{\text{stop}} = 2.754$ mm was still considerably thinner than the 3.12 mm and 3.37 mm measured experimentally by Félix & Thomas (2004) for $Q_M = 8$ g/s and $Q_M = 17.5$ g/s, respectively. Mangeney *et al.* (2007) acknowledged this discrepancy, and concluded that “In particular, the absence of lateral dissipation between the flowing mass and the quasi-static shoulders likely leads to underestimation of the flowing thickness and the thickness of the deposit in the central channel”.

As shown in this paper, lateral dissipation (viscosity) is required to produce a unique steady channel thickness, but a hysteretic friction law with $\kappa = 1$ (a gradual transition from static to dynamic friction coefficient) is also required, in order for this unique thickness to be significantly greater than both h_{stop} and h_* , as observed in experiments.

As has been seen in §3, the depth-averaged viscous terms in equations (2.3)–(2.4) are a singular perturbation of the model that produces qualitatively different solutions. Rather than the unique solution found when the viscous terms are present, in the inviscid case ($\nu = 0$) there are an infinite family of steady-state solutions with constant channel thicknesses in the metastable range $[h_{\text{stop}}, h_{\text{start}}]$, plug-like downslope velocity profiles across the slope and contact discontinuities at the channel edge (§3.2). Mangeney *et al.*’s (2007) numerical simulations are consistent with a flow that is approaching one of these steady-state inviscid solutions. Indeed, Mangeney *et al.* (2007) derived equations for the velocity and width of the flow (their equations 24 and 25), which are directly equivalent to the steady-state equations (3.9) and (3.11) for glass beads ($\Gamma = 0$). However, they did not draw out the fact that the steady-state inviscid system of equations is not uniquely determined, nor why the observed thickness $H \approx 1.03h_{\text{stop}}$ is so close to the thinnest possible steady-state solution.

In the absence of any numerical viscosity, the initial conditions and time-dependent evolution of the inviscid equations could, in principle, select the observed channel width from the many possible steady-state solutions. In reality, this time-dependence does not appear to be the mechanism setting the channel width, since Deboeuf *et al.* (2006) found that the width was independent of past changes in flux and Takagi *et al.* (2011) showed that an initial layer of erodible particles covering the chute did not influence the equilibrium flowing channel width.

Based on solutions of Mangeney *et al.*'s (2007) inviscid equations and quantitative reproduction of their observations made using the numerical scheme of this paper, there appear to be two reasons why the numerical solutions of Mangeney *et al.* (2007) select a flow thickness very close to h_{stop} . These relate to the Mangeney *et al.*'s (2007) use of an extremely rapid transition from static to flowing friction ($\kappa = 10^{-3}$) and the interaction of this with small but unavoidable errors in numerical schemes.

Firstly, as pointed out by Edwards *et al.* (2019), the initial sharp decrease in the friction as Fr increases from zero, when $\kappa = 10^{-3}$, is extremely difficult to represent in standard floating-point numerical computations. For instance, at the smallest non-zero value the Froude number ($\sim 10^{-16}$, based on IEEE-754 double precision round-off error of $O(1)$ numerical quantities in the finite-volume scheme) the friction coefficient drops to a value that is well below the maximum static friction and is insufficient to bring to rest any flowing material thicker than $1.02h_{stop} = 2.727$ mm. This suggests that when Mangeney *et al.* (2007) stopped their numerical simulations (when $H \sim 1.03h_{stop}$) the flow was still slowly spreading, but that it was very close to the range of thicknesses where inviscid steady-state solutions could exist.

Secondly, the singular nature of the viscous terms in the governing equations means that even a small amount of numerical viscosity results in the solution of the viscous equations, with the viscosity coefficient in this case determined artificially by the grid resolution and details of the numerical scheme. As noted previously, when $\kappa = 10^{-3}$ the unique steady viscous solution for a given flux lies in a very narrow range of thicknesses $[H_{min}, H_{max}]$ that is slightly ($\sim 0.1\%$) greater than the thinnest steady uniform flow (i.e. h_{stop} , for the friction law used by Mangeney *et al.* 2007). It is therefore possible that Mangeney *et al.*'s (2007) *inviscid* solutions are approaching a steady state of the

viscous equations, but this relies entirely on the mesh-size dependent and numerical scheme dependent viscosity.

In contrast, the combination in this paper of physically-derived viscous terms and the friction law of Edwards *et al.* (2019) (with $\kappa = 1$) provides (a) a unique steady channel thickness and width in good agreement with experiments, and (b) a time-dependent model that unambiguously approaches this unique steady state at late times.

5. Discussion and conclusions

5.1. Summary of results

This paper shows that two physical processes are needed to quantitatively predict self-channelisation and levee formation in monodisperse granular flows using depth-averaged avalanche models. These are (i) a non-monotonic effective basal friction law (Pouliquen & Forterre 2002; Félix & Thomas 2004; Deboeuf *et al.* 2006; Mangeney *et al.* 2007; Edwards & Gray 2015; Edwards *et al.* 2017, 2019) and (ii) depth-averaged lateral viscous stresses (Gray & Edwards 2014; Baker *et al.* 2016a). The non-monotonic friction models the hysteretic behaviour that allows static and flowing regions to coexist, while the viscous terms are vital to close the system of equations and produce smooth transitions between the static and flowing regions that do not exert shear stresses on the levee walls.

The two-dimensional time-dependent simulations in figures 14 and 15 show that the resultant equations (2.2)–(2.15) model the formation of a central flowing channel bounded by parallel-sided static levees. When material flowing down the channel reaches the front, it loses its lateral confinement, spreads out and slows down. The grains that are still in the centre of the flow are then over-run, while the particles that migrate to the sides come to rest and build a new section of the levee wall, advancing it downslope (Félix & Thomas 2004; Johnson *et al.* 2012). In this way the flow front is able to propagate downslope as a steadily travelling wave, continuously laying down a pair of levees at the back of the flow head. The final width of the channel is not always set immediately behind the head; an equilibrium width of the central channel is established when the flow thickness and depth-averaged velocity profile are such that there is no net erosion or deposition at the levee-channel boundaries. Once the channel has formed, the levees prevent the flow spreading laterally and thereby maintain the

flow's thickness, and hence mobility, leading to enhanced run-out. The flow can widen by levee-bank overtopping in response to an increase in mass flux, and retreat into the centre of the channel if the flux is reduced, as shown experimentally (figure 4, movie 3) and in the numerical simulations (figure 16, movies 7 and 8).

To understand the force balance leading to the leveed channel, a steady-state problem is formulated in §3.1, which shows that across the width W of a parallel-sided flowing channel, the thickness h is equal to a constant H and the downslope velocity profile $\bar{u}(y)$ satisfies the second order ODE (3.5). For a given mass flux Q_M , this can be solved as a boundary value problem for W , H and $\bar{u}(y)$, subject to zero velocity (3.6) and zero shear stress (3.7) boundary conditions at the levee-channel interfaces, as well as the integral constraint (3.8) on the mass flux. The viscous terms allow the static shear-stress-free levees to be connected to the central flow, where steady uniform flow dominates, across a viscous boundary layer or shear-band (see figure 9c). There is a unique solution to the problem for all values of the mass flux Q_M although the character of the solution changes at $Q = Q_{min}$. For $Q_M < Q_{min}$ the solutions are purely in the intermediate frictional regime (2.12), whilst for $Q_M > Q_{min}$, the solutions also have regions of dynamic friction (2.10). It is these latter solutions that are physically realised.

The solutions to the boundary value problem (see figures 8–9) are in excellent quantitative agreement with the experimental measurements of the height and width of the central flowing channel (Takagi *et al.* 2011) as shown in figure 10 for sand. These solutions show that, as the mass flux Q_M is increased, the thickness of the central flowing channel remains nearly constant and its width increases approximately linearly. The constant thickness H in the channel is significantly above both h_{stop} and h_* . Takagi *et al.* (2011) also made measurements of the surface velocity profile across the channel. These are harder to compare, because the velocity shear through the depth of the avalanche necessarily implies that the surface velocity is not equal to the depth-averaged velocity calculated by the theory. Figure 11 shows that the depth-averaged velocity \bar{u} and the surface velocity measurements u_s have the same functional behaviour with the mass flux Q_M , and that $u_s/\bar{u} \approx 2.35$. This large ratio of surface velocity to depth-averaged velocity is consistent with the Discrete Element Method (DEM) simulations of Silbert *et al.* (2003) and non-local theory of Kamrin & Henann

(2015), which predict a transition from Bagnold flow to exponential-like velocity profiles as the flow gets close to h_* .

The model is also in very good agreement with the thickness measurements of Félix & Thomas (2004) for glass beads as shown in figure 12 for a wide range of mass fluxes. However, the predictions of the steady-state minimal total width of the channel (see §3.5.2 and appendix B) do not agree with those measured by Félix & Thomas (2004) at high mass fluxes. The most likely explanation for this discrepancy is that either Félix & Thomas's (2004) experimental chute was not long enough, or the flow was not observed for a sufficiently long time, to measure a true steady-state. This is certainly consistent with the observations of Deboeuf *et al.* (2006) and Takagi *et al.* (2011) who found that for weakly hysteretic materials, such as glass beads, the width of the flow adjusted on very long timescales (~ 70 -90 minutes).

Below a critical mass flux the steady-state solutions go unstable in experiments (Félix & Thomas 2004; Takagi *et al.* 2011) as shown for red sand in movie 4. This also occurs in the numerical solutions (figures 17, 18 and 19), which produce a series of finite pulses of flowing material separated by intervals during which the grains are completely static. These are another example of erosion-deposition waves, which have previously been observed on erodible beds (Daerr & Douady 1999; Börzsönyi *et al.* 2005; Clément *et al.* 2007; Edwards & Gray 2015; Edwards *et al.* 2017) and have been simulated numerically by Edwards *et al.* (2017) using the same system of equations used in this paper. The governing equations (2.2)–(2.15) are therefore extremely versatile and have the potential to explain many flows with qualitatively very different behaviour.

The viscous terms play a critical role in setting the velocity profile and hence the thickness and width of the self-channelised flow. In the absence of viscosity, the system of equations (2.2)–(2.5) reduce to the classical avalanche equations, which are hyperbolic in character (see e.g. Grigorian *et al.* 1967; Savage & Hutter 1989; Gray *et al.* 1999, 2003; Mangeney *et al.* 2007). As shown in §3.2, in this inviscid model the constant channel thickness H implies that the velocity is equal to the steady-uniform value (3.9) across the whole channel, with contact discontinuities at the levee-channel interfaces where the downslope velocity jumps from the steady-uniform value \bar{u}_{steady} to zero. The thickness of the flow H is not determined, and may lie anywhere

in the range $[h_*, h_{start}]$, where $h_* > h_{stop}$ is the minimum observable thickness of a steady uniform flow (Edwards *et al.* 2019). As a result, even for the same mass flux Q_M , there are a corresponding range of possible widths (see figure 7), which implies that inviscid theories lack the physical mechanism to set the steady-state thickness and width of the flow.

In practical numerical computations there is usually some mesh-size dependent numerical diffusion. It follows that numerical computations with Mangeney *et al.*'s (2007) inviscid model will appear to behave somewhat like the theory presented in this paper (see §4.5). The important distinction is that it is the mesh-size dependent numerical diffusion that selects the solution, rather than the physically based depth-averaged viscosity (Gray & Edwards 2014; Baker *et al.* 2016a) derived from the $\mu(I)$ -rheology (GDR-MiDi 2004; Jop *et al.* 2006). The viscous-depth-averaged theory presented in this paper is therefore a significant advance over previous models.

Despite the theory's clear success in simulating many features of the flow, one subtle aspect that is not captured correctly is the shape of the free-surface. Experimental measurements of self-channelised flows (Félix & Thomas 2004; Deboeuf *et al.* 2006; Takagi *et al.* 2011) show that, instead of having a constant depth across the channel, the maximum thickness occurs in the centre, where the material moves faster. The curvature in the free surface appears to coincide with regions of high shear, i.e. for narrow channels, with a parabolic-like velocity profile, experiments suggest that the free surface is curved across the whole channel. For wider channels, the free surface is almost flat in the central steady uniform region, with curvature observed only at the boundary layers at the sides (Félix & Thomas 2004). This observation may be important in the development of new constitutive equations for granular flows that go beyond the $\mu(I)$ -rheology (see e.g. Kamrin & Koval 2012; Bouzid *et al.* 2013; Henann & Kamrin 2013; Kamrin & Henann 2015; Lee & Yang 2017). For example, second normal stress differences can result in variations in free surface height as a function of the downstream velocity (McElwaine *et al.* 2012). Another possible explanation is that the low velocity regions, on the inside walls at the base levees, jam and become quasi-static rather than inertial (Deboeuf *et al.* 2006; Kokelaar *et al.* 2014). This would change the height of the effective topography that the avalanche was flowing over and potentially allow cross-slope variations in thickness. Understanding

how to model this quantitatively would probably require a compressible granular theory (see e.g. Barker *et al.* 2017; Heyman *et al.* 2017; Schaeffer *et al.* 2019) that could span the quasi-static and inertial regimes (Chialvo, Sun & Sundaresan 2012). There is, however, a long way to go before either of these effects can be included in depth-averaged avalanche models, and the existing theory appears to be able to make accurate predictions without them.

5.2. Implications for the interpretation of levee-channel deposits

The results of this paper provide a theoretical framework for the interpretation of leveed deposits from geophysical mass flows such as debris flows and pyroclastic density currents. Specifically, the predictions of the thickness and width of a self-channelised leveed flow in §3.3 may be inverted to infer information about the mass flux or rheology of the original flow from measurements of the deposit. A key observation is that the thickness of a levee is similar to the thickness of the flow that created it, and is nearly independent of the mass flux of that flow (figures 10a and 12a). A difference in thickness between levees in successive flows therefore suggests a change in flow composition and rheology, not simply mass flux. The width of the static channel between the levees is roughly proportional to the mass flux of the originating flow (figures 10b and 12b). Very wide levees, with a sequence of nested parallel levees inside the main channel, are strongly indicative of a decrease in mass flux prior to deposition (figure 4b). However, an increase in flux with time may not be reflected in the deposit, due to erosion of the existing levees (figure 4c).

Interpretation of deposits with levee-channel morphology is complicated by the existence of other levee-forming flows. A disturbance to an erodible layer of grains on an inclined plane may lead to a localised erosion-deposition wave, in which the static layer is continuously eroded at the flow front and deposited a short time later at the back of the avalanche (Edwards *et al.* 2017). This flow leaves behind a pair of static parallel-sided levees that are raised above the surface of the original erodible layer, located either side of a depression or trough. The leveed deposit resulting from this erosion-deposition wave therefore looks similar to that produced by a continuous flux of grains (figure 2c), which might make the two cases difficult to distinguish in geophysical flow deposits. A key difference between these flows is the origin of the material that forms the levees. The levees described in this paper are composed of grains provided by

a continuous source upslope, whereas those generated by the erosion-deposition waves of Edwards *et al.* (2017) are composed of grains that are continuously eroded at the front of the avalanche.

Field observations (Wilson & Head 1981; Bartelt *et al.* 2012) suggest that the margins of the flow may be differentially fluidised during emplacement of levees, which implies that the rheology is inhomogeneous (Iverson & Vallance 2001; Iverson 2003). In debris flows, the evolving pore fluid pressure (Iverson 1997; Iverson & Denlinger 2001) and particle-size distribution due to segregation (Gray 2018) significantly alter the bulk flow by generating drier bouldery margins that resist the motion and form pronounced levees (Johnson *et al.* 2012). Although these effects present additional modelling challenges, the heterogeneous particle size distribution of a deposit also potentially provides considerably more information about the flow that created it than the deposit geometry alone. The incorporation of such heterogeneity into the model for levee formation presented here is, therefore, a promising avenue for future research.

This research was supported by NERC grants NE/E003206/1 and NE/K003011/1 as well as EPSRC grants EP/I019189/1, EP/K00428X/1 and EP/M022447/1. F.M.R. acknowledges financial support from CNPq, Conselho Nacional de Desenvolvimento Científico e Tecnológico – Brazil. J.M.N.T.G. is a Royal Society Wolfson Research Merit Award holder (WM150058) and an EPSRC Established Career Fellow (EP/M022447/1).

Appendix A. Velocity reconstruction

The full downslope velocity profile $u(y, z)$ can be reconstructed from the depth-averaged value $\bar{u}(y)$ by assuming a velocity profile $f(z)$ through the avalanche depth

$$u(y, z) = f(z)\bar{u}(y), \quad (\text{A } 1)$$

Steady uniform granular flows usually develop a convex Bagnold velocity profile (Silbert *et al.* 2001; GDR-MiDi 2004), but this can become concave when the flow is confined between lateral sidewalls (e.g. Komatsu, Inagaki, Nakagawa & Nasuno 2001; Jop *et al.* 2005; Wiederseiner *et al.* 2011; Baker *et al.* 2016a). Even in the absence

of sidewalls, the DEM simulations of Silbert *et al.* (2003) and the non-local theory of Kamrin & Henann (2015) predict a transition from Bagnold to concave velocity profiles as the flow thickness approaches h_* , which for steady uniform flow lies at the transition between dynamic and intermediate frictional regimes. The exponential profile of Wiederseiner *et al.* (2011)

$$f(z) = \frac{\lambda}{\exp(\lambda) - 1} \exp\left(\frac{\lambda z}{H}\right), \quad (\text{A } 2)$$

provides a good fit to the observations in this paper, where λ is an adjustable parameter. Evaluating this at the free-surface implies that the surface velocity u_s is related to the depth-averaged velocity \bar{u} by the relation

$$u_s = \frac{\lambda \exp(\lambda)}{\exp(\lambda) - 1} \bar{u}. \quad (\text{A } 3)$$

The surface velocity data for sand (Takagi *et al.* 2011) shown in figure 11 suggests that $u_s = 2.35\bar{u}$, which implies $\lambda = 2.05$. This is within 15% of the value $u_s = 2.7\bar{u}$ (corresponding to $\lambda = 2.45$) measured experimentally in a thin unconfined flow of glass beads (Russell *et al.* 2019).

Appendix B. Shape of the minimal levees

Outside the flowing channel, the shape of the static levees is constrained, but not determined uniquely, by the static friction. Assuming that these static levees are uniform in the x-direction, the cross-slope component of the depth-averaged momentum balance (2.4) reduces not to (3.3), but to a balance between surface gradients and friction

$$\frac{dh}{dy} = -\mu_b e_2, \quad (\text{B } 1)$$

where the second component of the friction direction (2.6) is

$$e_2 = \frac{dh/dy}{\sqrt{(\tan \zeta)^2 + (dh/dy)^2}}. \quad (\text{B } 2)$$

The static friction law (2.11) implies that $\mu_b = \mu_S$, which can take any value between zero and the maximum static friction. This implies that in general there are infinitely many solutions for the levee shape. It is, however, possible to calculate a unique minimal solution for the levee by assuming that the granular material is on the brink of yield (Hulme 1974; Balmforth *et al.* 2001), i.e. that the basal friction μ_b is at its

maximum static value everywhere

$$\mu_b = \mu_{start}(h) = \mu_3 + \frac{\mu_2 - \mu_1}{1 + h/\mathcal{L}}. \quad (\text{B } 3)$$

With the basal friction determined by (B 3), equations (B 1) and (B 2) can be rearranged to determine a first order ODE for the minimal levee wall shape

$$\frac{dh}{dy} = \pm \sqrt{(\mu_{start}(h))^2 - (\tan \zeta)^2}. \quad (\text{B } 4)$$

In this equation the \pm sign allows decreasing solutions to be calculated on either side of the central channel starting from where $h = H$ at $y = \pm W/2$. Integrating the ODE (B 4) backwards and forwards, respectively, from $y = -W/2$ and $y = W/2$, until the height is equal to zero at $y = \pm W_{total}/2$, determines the minimum total width W_{total} that is capable of sustaining a flow of thickness H .

REFERENCES

- ANCEY, C. 2012 Are there ‘‘dragon-kings’’ events (i.e. genuine outliers) among extreme avalanches? *Eur. Phys. J. Spec. Top.* **205**, 117–129.
- BAKER, J. L., BARKER, T. & GRAY, J. M. N. T. 2016*a* A two-dimensional depth-averaged $\mu(I)$ -rheology for dense granular avalanches. *J. Fluid. Mech.* **787**, 367–395.
- BAKER, J. L., JOHNSON, C. G. & GRAY, J. M. N. T. 2016*b* Segregation-induced finger formation in granular free-surface flows. *J. Fluid. Mech.* **809**, 168–212.
- BALMFORTH, N. J., BURBIDGE, A. S. & CRASTER, R. V. 2001 Shallow lava theory. In *Geomorphological Fluid Mechanics*, pp. 164–187. Springer.
- BARKER, T., SCHAEFFER, D. G., SHEARER, M. & GRAY, J. M. N. T. 2017 Well-posed continuum equations for granular flow with compressibility and $\mu(I)$ -rheology. *Proc. R. Soc. A* **473** (2201), 20160846.
- BARTELT, P., GLOVER, J., FEISTL, T., BÜHLER, Y. & BUSER, O. 2012 Formation of levees and en-echelon shear planes during snow avalanche run-out. *J. Glaciol.* **58**, 980–992.
- BÖRZSÖNYI, T., HALSEY, T. C. & ECKE, R. E. 2005 Two scenarios for avalanche dynamics in inclined granular layers. *Phys. Rev. Lett.* **95** (208001).
- BÖRZSÖNYI, T., HALSEY, T. C. & ECKE, R. E. 2008 Avalanche dynamics on a rough inclined plane. *Phys. Rev. E* **78** (011306).
- BOUZID, M., TRULSSON, M., CLAUDIN, P., CLÉMENT, E & ANDREOTTI, B 2013 Nonlocal rheology of granular flows across yield conditions. *Phys. Rev. Lett.* **111** (23), 238301.
- BRANNEY, M. J. & KOKELAAR, B. P. 1992 A reappraisal of ignimbrite emplacement: progressive aggradation and changes from particulate to non-particulate flow during emplacement of high-grade ignimbrite. *Bull. Volcanol.* **54**, 504–520.
- CALDER, E. S., SPARKS, R. S. J. & GARDEWEG, M. C. 2000 Erosion, transport and segregation of pumice and

- lithic clasts in pyroclastic flows inferred from ignimbrite at lascar volcano, chile. *J. Volcan. Geotherm. Res.* **104**, 201–235.
- CHADWICK, P. 1976 *Continuum Mechanics. Concise theory and problems*. George Allen & Unwin.
- CHIALVO, S, SUN, J & SUNDARESAN, S 2012 Bridging the rheology of granular flows in three regimes. *Phys. Rev. E* **85**, 021305.
- CLÉMENT, E., MALLOGGI, F., ANDREOTTI, B. & ARANSON, I. S. 2007 Erosive granular avalanches: a cross confrontation between theory and experiment. *Granular Matter* **10** (1), 3–11.
- COSTA, J. E. & WILLIAMS, G. 1984 Debris flow dynamics. *Tech. Rep.* 84–606. (videotape) U.S. Geological Survey.
- DAERR, A. 2001 Dynamical equilibrium of avalanches on a rough plane. *Phys. Fluids* **13**, 2115–2124.
- DAERR, A. & DOUADY, S. 1999 Two types of avalanche behaviour in granular media. *Nature* **399**, 241–243.
- DEBOEUF, S., LAJEUNESSE, E., DAUCHOT, O. & ANDREOTTI, B. 2006 Flow rule, self channelization, and levees in unconfined granular flows. *Phys. Rev. Lett.* **97**, 158303.
- EDWARDS, A. N. & GRAY, J. M. N. T. 2015 Erosion-deposition waves in shallow granular free-surface flows. *J. Fluid Mech.* **762**, 35–67.
- EDWARDS, A. N., RUSSELL, A. S., JOHNSON, C. G. & GRAY, J. M. N. T. 2019 Frictional hysteresis and particle deposition in granular free-surface flows. *J. Fluid Mech.* **875**, 1058–1095.
- EDWARDS, A. N., VIROULET, S., KOKELAAR, B. P. & GRAY, J. M. N. T. 2017 Formation of levees, troughs and elevated channels by avalanches on erodible slopes. *J. Fluid Mech.* **823**, 278–315.
- FÉLIX, G. & THOMAS, N. 2004 Relation between dry granular flow regimes and morphology of deposits: formation of levées in pyroclastic deposits. *Earth Planet. Sci. Lett.* **221**, 197–213.
- FENISTEIN, D & VAN HECKE, M 2003 Kinematics: Wide shear zones in granular bulk flow. *Nature* **425** (6955), 256.
- FORTERRE, Y. 2006 Kapiza waves as a test for three-dimensional granular flow rheology. *J. Fluid Mech.* **563**, 123–132.
- FORTERRE, Y. & POULIQUEN, O. 2003 Long-surface-wave instability dense granular flows. *J. Fluid Mech.* **486**, 21–50.
- GDR-MiDi 2004 On dense granular flows. *Eur. Phys. J. E* **14**, 341–365.
- GOUJON, C., DALLOZ-DUBRUJEAUD, B. & THOMAS, N. 2007 Bidisperse granular avalanches on inclined planes: A rich variety of behaviours. *Eur. Phys. J. E* **23**, 199–215.
- GRAY, J. M. N. T. 2018 Particle segregation in dense granular flows. *Ann. Rev. Fluid Mech.* **50**, 407–433.
- GRAY, J. M. N. T. & EDWARDS, A. N. 2014 A depth-averaged $\mu(I)$ -rheology for shallow granular free-surface flows. *J. Fluid Mech.* **755**, 503–544.
- GRAY, J. M. N. T., TAI, Y. C. & NOELLE, S. 2003 Shock waves, dead-zones and particle-free regions in rapid granular free-surface flows. *J. Fluid Mech.* **491**, 161–181.
- GRAY, J. M. N. T., WIELAND, M. & HUTTER, K. 1999 Free surface flow of cohesionless granular avalanches over complex basal topography. *Proc. Roy. Soc. A* **455**, 1841–1874.

- GRIGORIAN, S. S., EGLIT, M. E. & IAKIMOV, I. L. 1967 New statement and solution of the problem of the motion of snow avalanche. *Snow, Avalanches & Glaciers. Tr. Vysokogornogo Geofizich Inst* **12**, 104–113.
- HEINRICH, P., PIATANESI, A. & HEBERT, H. 2001 Numerical modelling of tsunami generation and propagation from submarine slumps: the 1998 papua new guinea event. *Geophysical Journal International* **145** (1), 97–111.
- HENANN, D. L. & KAMRIN, K. 2013 A predictive, size-dependent continuum model for dense granular flows. *Proc. Natl Acad. Sci.* **110** (17), 6730–6735.
- HEYMAN, J., DELANNAY, R., TABUTEAU, H. & VALANCE, A. 2017 Compressibility regularizes the $\mu(I)$ -rheology for dense granular flows. *J. Fluid Mech.* **830**, 553–568.
- HOGG, A. J. & PRITCHARD, D. 2004 The effects of hydraulic resistance on dam-break and other shallow inertial flows. *J. Fluid Mech.* **501**, 179–212.
- HULME, G. 1974 The interpretation of lava flow morphology. *Geophysical Journal International* **39** (2), 361–383.
- IVERSON, R. M. 1997 The physics of debris-flows. *Reviews in Geophysics* **35**, 245–296.
- IVERSON, R. M. 2003 The debris-flow rheology myth. In *Debris-flow hazards mitigation: Mechanics, prediction and assessment* (ed. D. Rickenmann & C. L. Chen), pp. 303–314. Rotterdam: Millpress.
- IVERSON, R. M. & DENLINGER, R. P. 2001 Flow of variably fluidized granular masses across three-dimensional terrain 1. Coulomb mixture theory. *J. Geophys. Res.* **106** (B1), 553–566.
- IVERSON, R. M., LOGAN, M., LAHUSEN, R. G. & BERTI, M. 2010 The perfect debris flow? aggregated results from 28 large-scale experiments. *J. Geophys. Res.* **115**, F03005.
- IVERSON, R. M. & VALLANCE, J. W. 2001 New views of granular mass flows. *Geology* **29** (2), 115–118.
- JESSOP, D.E., KELFOUN, K., LABAZUY, P., MANGENEY, A., ROCHE, O., TILLIER, J.-L., TROUILLET, M. & THIBAUT, G. 2012 Lidar derived morphology of the 1993 lascar pyroclastic flow deposits, and implication for flow dynamics and rheology. *J. Volcanol. Geothm. Res.* **245–246**, 81–97.
- JOHNSON, C. G., KOKELAAR, B. P., IVERSON, R. M., LOGAN, M., LAHUSEN, R. G. & GRAY, J. M. N. T. 2012 Grain-size segregation and levee formation in geophysical mass flows. *J. Geophys. Res.* **117**, F01032.
- JOMELLI, V. & BERTRAN, P. 2001 Wet snow avalanche deposits in the French Alps: Structure and sedimentology. *Geografiska Annaler. Series A, Physical Geography* **83**, 15–28.
- JOP, P., FORTERRE, Y. & POULIQUEN, O. 2005 Crucial role of sidewalls in granular surface flows: consequences for the rheology. *J. Fluid Mech.* **541**, 167–192.
- JOP, P., FORTERRE, Y. & POULIQUEN, O. 2006 A constitutive relation for dense granular flows. *Nature* **44**, 727–730.
- KAMRIN, K. & HENANN, D. L. 2015 Nonlocal modeling of granular flows down inclines. *Soft Matter* **11** (1), 179–185.
- KAMRIN, K. & KOVAL, G. 2012 Nonlocal constitutive relation for steady granular flow. *Phys. Rev. Lett.* **108** (17), 178301.

- KOKELAAR, B. P., GRAHAM, R. L., GRAY, J. M. N. T. & VALLANCE, J. W. 2014 Fine-grained linings of leveed channels facilitate runout of granular flows. *Earth & Planetary Sci. Lett.* **385**, 172–180.
- KOMATSU, T. S., INAGAKI, S., NAKAGAWA, N. & NASUNO, S. 2001 Creep motion in a granular pile exhibiting steady surface flow. *Phys. Rev. Lett.* **86**, 1757–1760.
- KURGANOV, A & TADMOR, E. 2000 New high-resolution central schemes for nonlinear conservation laws and convection-diffusion equations. *J. Comput. Phys.* **160**, 241–282.
- LEE, K. L. & YANG, F. L. 2017 Relaxation-type nonlocal inertial-number rheology for dry granular flows. *Phys. Rev. E* **96** (6), 062909.
- LEVEQUE, R. J. 2002 *Finite Volume Methods for Hyperbolic Problems*. Cambridge University Press.
- MAJOR, J. J. 1997 Depositional processes in large-scale debris-flow experiments. *J. Geol.* **105**, 345–366.
- MANGENEY, A., BOUCHUT, F., THOMAS, N., VILOTTE, J. P. & BRISTEAU, M. O. 2007 Numerical modeling of self-channeling granular flows and of their levee-channel deposits. *J. Geophys. Res.* **112**, F02017.
- MANGENEY-CASTELNAU, A., VILOTTE, J. P., BRISTEAU, M. O., PERTHAME, B., BOUCHUT, F., SIMEONI, C. & YERNENI, S. 2003 Numerical modeling of avalanches based on Saint-Venant equations using a kinetic scheme. *J. Geophys. Res.* **108**, 2527.
- MCARDELL, B. W. 2016 Field measurements of forces in debris flows at the illgraben: Implications for channel-bed erosion. *Int. J. Erosion Control Engineering* **9** (4), 194–198.
- MCÉLWAIN, J. N., TAKAGI, D. & HUPPERT, H. E. 2012 Surface curvature of steady granular flows. *Granular Matter* **14** (2), 229–234.
- NAAIM, M., VIAL, S & COUTURE, R 1997 Saint-venant approach for rock avalanches modelling. In *Saint Venant Symposium, Paris*, pp. 28–29.
- PIERSON, T. C. 1986 Flow behavior of channelized debris flows, Mount St. Helens, Washington. In *Hillslope Processes* (ed. A. D. Abrahams), pp. 269–296. Winchester, Mass.: Allen and Unwin.
- PITMAN, E. B., NICHITA, C. C., PATRA, A., BAUER, A., SHERIDAN, M. & BURSİK, M. 2003 Computing granular avalanches and landslides. *Phys. Fluids* **15** (12), 3638–3646.
- POULIQUEN, O. 1999 Scaling laws in granular flows down rough inclined planes. *Phys. Fluids* **11** (3), 542–548.
- POULIQUEN, O., DELOUR, J. & SAVAGE, S. B. 1997 Fingering in granular flows. *Nature* **386**, 816–817.
- POULIQUEN, O. & FORTERRE, Y. 2002 Friction law for dense granular flows: application to the motion of a mass down a rough inclined plane. *J. Fluid Mech.* **453**, 133–151.
- POULIQUEN, O & GUTFRAIND, R 1996 Stress fluctuations and shear zones in quasistatic granular chute flows. *Phys. Rev. E* **53** (1), 552.
- POULIQUEN, O. & VALLANCE, J. W. 1999 Segregation induced instabilities of granular fronts. *Chaos* **9** (3), 621–630.
- ROWLEY, P. D., KUNTZ, M. A. & MACLEOD, N. S. 1981 Pyroclastic-flow deposits. In *The 1980 Eruptions of Mount St. Helens, Washington* (ed. P. W. Lipman & D. R. Mullineaux), pp. 489–512. U.S. Geol. Surv. Prof. Pap. 1250.
- RUSSELL, A. S., JOHNSON, C. G., EDWARDS, A. N., VIROULET, S., ROCHA, F. M. & GRAY, J. M. N. T. 2019 Retrogressive failure of a static granular layer on an inclined plane. *J. Fluid Mech.* **869**, 313–340.

- SAINGIER, G., DEBOEUF, S. & LAGRÉE, P-Y 2016 On the front shape of an inertial granular flow down a rough incline. *Phys. Fluids* **28** (5), 053302.
- SAVAGE, S. B. & HUTTER, K. 1989 The motion of a finite mass of granular material down a rough incline. *J. Fluid Mech.* **199**, 177–215.
- SCHAEFFER, D. G., BARKER, T., TSUJI, D., GREMAUD, P., SHEARER, M. & GRAY, J. M. N. T. 2019 Constitutive relations for compressible granular flow in the inertial regime. *J. Fluid Mech.* **in press**.
- SCHALL, P. & VAN HECKE, M. 2010 Shear bands in matter with granularity. *Ann. Rev. Fluid Mech.* **42**, 67–88.
- SCHWEIZER, J., BARTELT, P. & VAN HERWIJNEN, A. 2014 Snow avalanches. In *Snow and Ice-Related Hazards, Risks and Disasters* (ed. W. Haeberli & C. Whiteman), pp. 395–436. Elsevier.
- SHARP, R. P. & NOBLES, L. H. 1953 Mudflow of 1941 at Wrightwood, Southern California. *Geol. Soc. America Bull.* **66**, 1489–1498.
- SILBERT, L. E., ERTAŞ, D., GREST, G. S., HALSEY, T. C., LEVINE, D. & PLIMPTON, S. J. 2001 Granular flow down an inclined plane: Bagnold scaling and rheology. *Phys. Rev. E* **64**, 051302.
- SILBERT, L. E., LANDRY, J. W. & GREST, G. S. 2003 Granular flow down a rough inclined plane: transition between thin and thick piles. *Phys. Fluids* **15**, 1–10.
- STROGATZ, S. H. 1994 *Nonlinear dynamics and chaos*. Westview Press.
- TAKAGI, D., MCELWAIN, J. N. & HUPPERT, H. E. 2011 Shallow granular flows. *Phys. Rev. E* **83** (3), 031306.
- VALLANCE, J. W. 2000 Lahars. In *Encyclopedia of Volcanoes* (ed. H. Sigurdsson), pp. 601–616. Academic.
- VALLANCE, J. W. & IVERSON, R. M. 2015 Lahars and their deposits. In *The Encyclopedia of Volcanoes (Second Edition)* (ed. Haraldur Sigurdsson), pp. 649–664. Elsevier.
- VIROULET, S., BAKER, J. L., EDWARDS, A. N., JOHNSON, C. G., GJALTEMA, C., CLAVEL, P. & GRAY, J. M. N. T. 2017 Multiple solutions for granular flow over a smooth two-dimensional bump. *J. Fluid Mech.* **815**, 77–116.
- VIROULET, S., BAKER, J. L., ROCHA, F. M., JOHNSON, C. G., KOKELAAR, B. P. & GRAY, J. M. N. T. 2018 The kinematics of bidisperse granular roll waves. *J. Fluid Mech.* **848**, 836–875.
- WIEDERSEINER, S., ANDREINI, N., EPELY-CHAUVIN, G., MOSER, G., MONNEREAU, M., GRAY, J. M. N. T. & ANCEY, C. 2011 Experimental investigation into segregating granular flows down chutes. *Phys. Fluids* **23**, 013301.
- WILSON, L. & HEAD, J. W. 1981 Morphology and rheology of pyroclastic flows and their deposits, and guidelines for future observations. In *The 1980 Eruptions of Mount St. Helens, Washington*. (ed. P. W. Lipman & D. R. Mullineaux), pp. 513–524. U.S. Geol. Surv. Prof. Pap. 1250.
- WOODHOUSE, M. J., THORNTON, A. R., JOHNSON, C. G., KOKELAAR, B. P. & GRAY, J. M. N. T. 2012 Segregation-induced fingering instabilities in granular free-surface flows. *J. Fluid Mech.* **709**, 543–580.
- YONG, L., JINGJING, L., KAIHENG, H. & PENGCHENG, S. 2012 Probability distribution of measured debris-flow velocity in jiangjia gully, yunnan province, china. *Nat. Hazards* **60**, 689–701.

4 | Granular fingering on a cone

This chapter is an article that is still under preparation for submission. The paper, which shares the title with this chapter of the thesis, aims to investigate monodisperse flows over a rough conical surface. At the time of writing this work is still in progress, and will be further developed for submission.

Granular fingering on a cone

F. M. Rocha¹, P. Gajjar², S. Viroulet³, C. G. Johnson¹, B. P. Kokelaar⁴ and J. M. N. T. Gray¹

¹Manchester Centre for Nonlinear Dynamics and Department of Mathematics, University of Manchester, Oxford Road, Manchester M13 9PL, UK

²Henry Moseley X-Ray Imaging Facility, School of Materials, University of Manchester, Oxford Road, Manchester M13 9PL, UK

³Institut de Mécanique de Fluides de Toulouse (IMFT) - Université de Toulouse, CNRS, France.

⁴Department of Earth and Ocean Sciences, University of Liverpool, Liverpool, L69 3GP, United Kingdom

(Received xx; revised xx; accepted xx;)

In this paper, we report the results of an experimental, theoretical and numerical study of a gravity-driven monodisperse granular flow over a conical rough surface. As the granular material spreads down the cone, the flow front slows down and the initially circular interface breaks up generating a stunning new fingering pattern. The experiments show that monodisperse fronts can be unstable to transverse perturbations, and granular fingering can occur even in the absence of particle-size segregation. As the flow spreads, thins and the front slows down, friction eventually transitions to the unstable velocity-weakening behaviour, causing the splitting. Therefore, frictional hysteresis is the driving physical mechanism responsible for triggering the instability. By using a depth-averaged avalanche model we show that the critical radius at which the interface splits, as well as the number of fully developed fingers scale linearly with the inflow volume flux, in good agreement with experimental data. Similar morphologies are observed in large-scale geophysical events on mountainous slopes such as snow avalanches, pyroclastic flows and water-saturated debris flows, as well as in extraterrestrial dry flows, such as debris flows on the surface of the Moon or Mars.

1. Introduction

Granular flows are observed in a wide variety of geophysical and industrial processes, with particle sizes that can span from a couple of hundred microns, such as a grain of sand in a sand pile, to several kilometres, such as the asteroid Ceres in the asteroid belt (Andreotti *et al.* 2013). Granular materials exhibit a diverse range of behaviours, being able to act as a solid, liquid or gas, depending on physical properties such as the solids volume fraction, applied pressure and the shear stress (Jaeger & Nagel 1992; Liu & Nagel 1998). For dense systems contact dynamics can lead to jamming and

solid-liquid phase transition, generating striking patterns, such as stratified layers in heaps (Gray & Hutter 1997; Makse *et al.* 1997; Gray & Ancey 2009), petal-like fingers in rotating drums (Hill *et al.* 1999; Gray & Chugunov 2006; Zuriguel *et al.* 2006) and self-organised leveed channels (Félix & Thomas 2004; Deboeuf *et al.* 2006; Johnson *et al.* 2012; Kokelaar *et al.* 2014).

For flows down inclined rough planes where the granular material consists of particles with different sizes, gravity-driven segregation can have a strong feedback on the bulk flow, causing the break-up of the granular front in a series of fingers (Pouliquen *et al.* 1997; Pouliquen & Vallance 1999; Woodhouse *et al.* 2012; Baker *et al.* 2016*b*). In these cases, as the grains are sheared downslope, the small particles percolate down through the matrix of coarser particles, yielding an effective motion of large constituents to the top of the flow, whilst smaller grains populate the bottom layers (Savage & Lun 1988; Vallance 1994; Gray 2018). Due to the shear through the avalanche depth, top layers move faster and, hence, large particles are preferentially transported to the flow front, and the vertical segregation far behind the granular head leads to a recirculation zone at the front (Thornton & Gray 2008), with an accumulation of larger and more frictional particles that strongly affects the local friction, which can cause the interface to break (Pouliquen *et al.* 1997; Baker *et al.* 2016*b*). In the absence of different-sized particles, however, when the granular material flows down the plane, a steady uniform state is attained behind the front, due to the shear-rate dependence of the dynamic coefficient of basal friction (Pouliquen 1999*a,b*; Pouliquen & Forterre 2002). The material then flows with constant speed, resulting in a stable scenario, where the cross-slope profile of the interface remains uniform (Pouliquen & Vallance 1999; Pouliquen 1999*b*; Baker *et al.* 2016*b*).

In this paper, we examine a monodisperse flow over a rough conical surface, in which the constant inflow volume flux in the conical geometry yields a decelerating granular front connected to a thinning flow. It is striking that even without any polydispersity and with a constant injection rate, the monodisperse flow becomes unstable when the friction transitions to a velocity-weakening behaviour (Pouliquen & Forterre 2002). The non-monotonic character of the friction law, i.e. the transition from velocity-strengthening to weakening, is related to frictional hysteresis (Carrigy 1970; Daerr & Douady 1999; Pouliquen & Forterre 2002; Edwards *et al.* 2019). The hysteretic nature

of granular materials implies that gravity-driven flows, such as the one studied here, initiate spontaneously when the slope angle reaches a critical value ζ_{start} , whereas the threshold to make the flow stop is $\zeta_{stop} < \zeta_{start}$. The physical origin of frictional hysteresis is still an open question, and some studies pointed inertia as the fundamental element to obtain hysteresis (Quartier *et al.* 2000; du Pont *et al.* 2003; DeGiuli & Wyart 2017). Recently, a study performed with viscous granular suspensions in which particle contacts can be tuned (Perrin *et al.* 2019) show that interparticle friction and solid contacts are required to observe hysteretical flow onset. Hysteresis also plays an important role in failure processes of large-scale landslides on Earth and other planetary bodies (Lucas *et al.* 2014), motivating studies to understand the physical origin of this phenomenon better. Hereafter in this article, we present the experimental results, as well as a simple depth-averaged model to make predictions of the critical position at which the interface breaks and the final number of fully developed fingers, showing that frictional hysteresis is the driving mechanism responsible for the observed pattern formation.

2. Experimental measurements

The experimental setup consists in an axisymmetric cone of basal radius 446.4 mm, height 244.4 mm and inclination angle $\zeta = 28.6^\circ$. A metal bar of diameter 20 mm attached to the apex of the cone provides support for the cylindrical hopper, which has outer and inner diameters of 63 mm and 57 mm, respectively. The granular material enters the cone through a spring-loaded release gate of diameter 79 mm, whose bottom is tapered in the same angle as the cone, so the material leaves the hopper moving parallel to the surface of the cone. A metal bracket located above the gate is used to control the upwards travel distance of the gate, H_t , which sets the inflow volume flux Q . The surface of the cone is made rough by glueing a monolayer of 750–1000 μm diameter turquoise glass particles to the bed. The experimental setup is shown in figure 1.

All the runs are performed by filling the hopper with 500 cm³ of 200–250 μm sieved spherical glass beads, which are released as the spring-loaded mechanism moves vertically upwards by the pre-set distance H_t , leading to an opening gap of $H_o = H_t \cos \zeta$ between the basal surface and the tapered bottom edge of the gate. For each



FIGURE 1. (a) The experimental setup and (b) a top-view image of the pattern formation. The granular material (200–250 μm glass beads, white) flows down an axisymmetric cone, which is made rough by attaching a monolayer of turquoise glass beads (750–1000 μm) to the surface of the cone. As it propagates down the cone, the initially circular granular front breaks down generating a stunning fingering pattern.

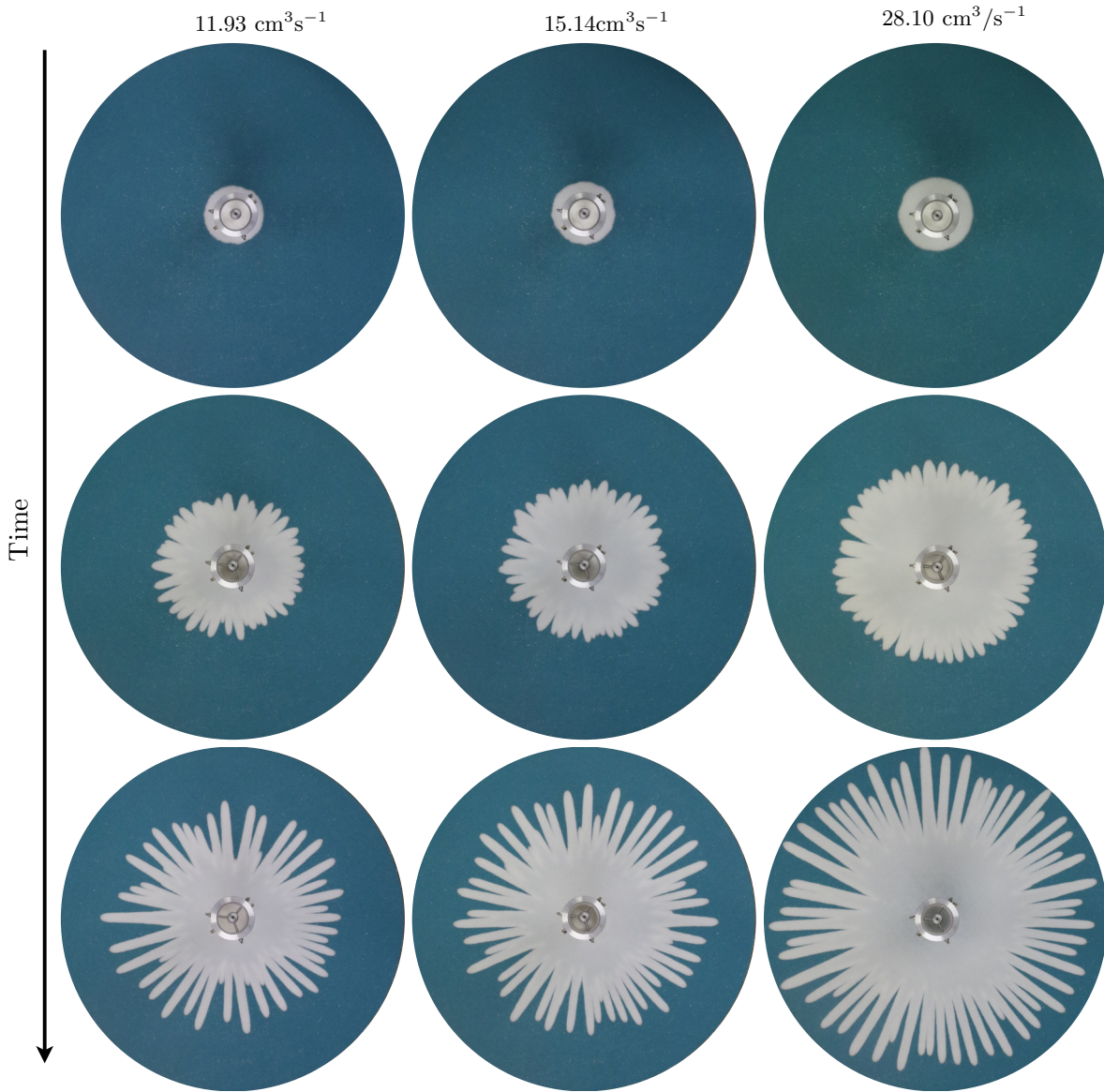


FIGURE 2. Typical pattern formation. The time evolution of the flow is shown in the top-view photographs at $t = 1, 10, 20$ s for different inflow volume fluxes.

travel distance H_t , the flux Q was measured by filming the decreasing level of the grains in the hopper over time, using a scale on the side of the hopper (inset in figure 1).

When the granular material is released from the gate, the flow initially spreads radially in a circular manner, with disturbances quickly appearing at the interface, but the whole flow is mobile, with all the grains moving downstream. At a critical radial position, portions of the flow solidify, causing the interface to split into a series of individual finger-like structures (figure 2). This beautiful fingering pattern contrasts with flow on a planar chute inclined at the same angle, where the flow is steady with a well-defined front connected to a steady uniform region, where the velocity is constant and the height uniform (Pouliquen 1999b; Baker *et al.* 2016b).

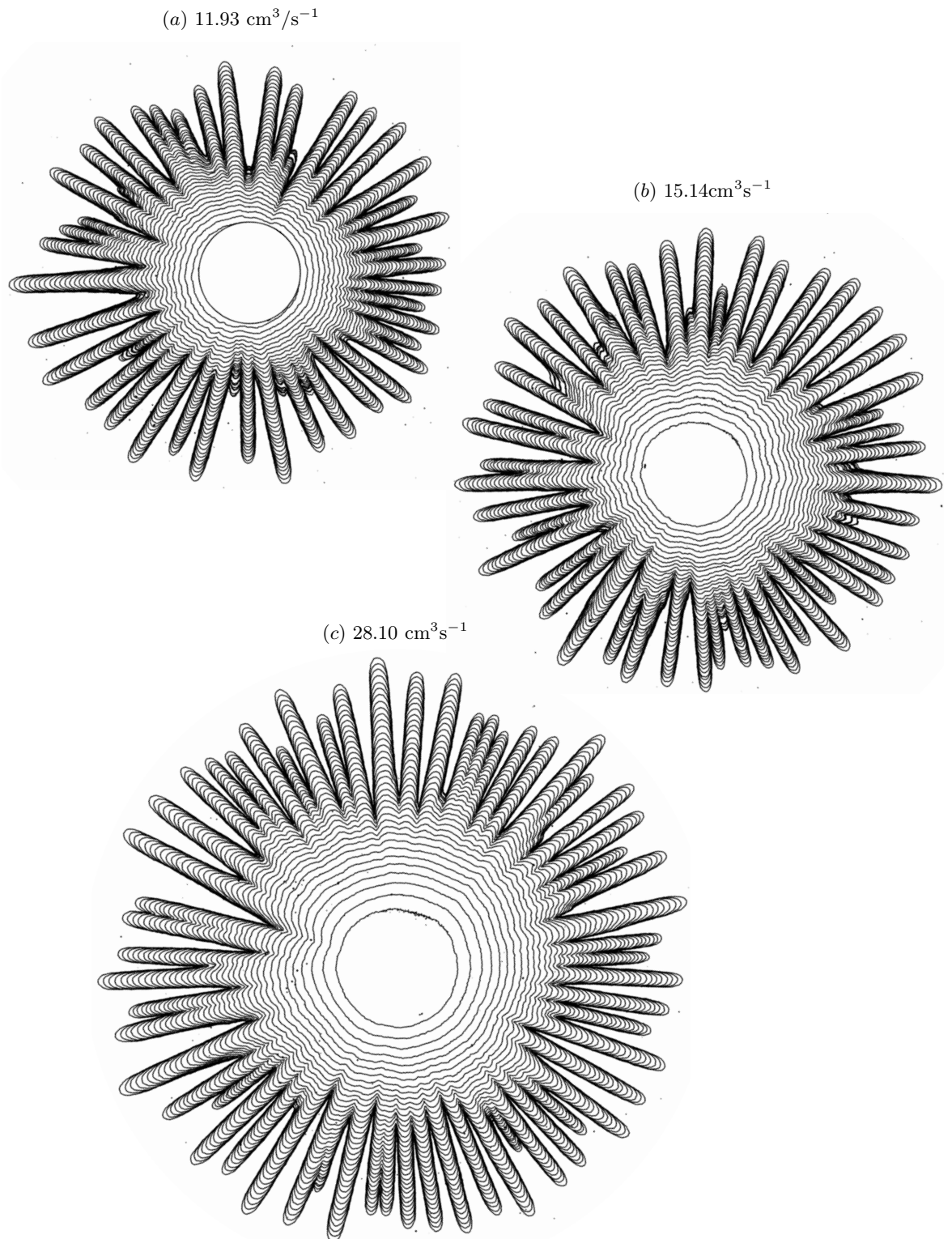


FIGURE 3. Temporal evolution of the flow is explored by plotting the contour of the interface for different times. Contours are plotted in intervals of 0.5 s, with the last contour showing the interface 20 seconds after the gate was released.

In the plane geometry, the constant-speed propagating front is stable to transverse perturbations, and, hence, the cross-slope profile of the interface remains uniform as it moves downstream (Pouliquen & Vallance 1999). On the cone, however, the granular

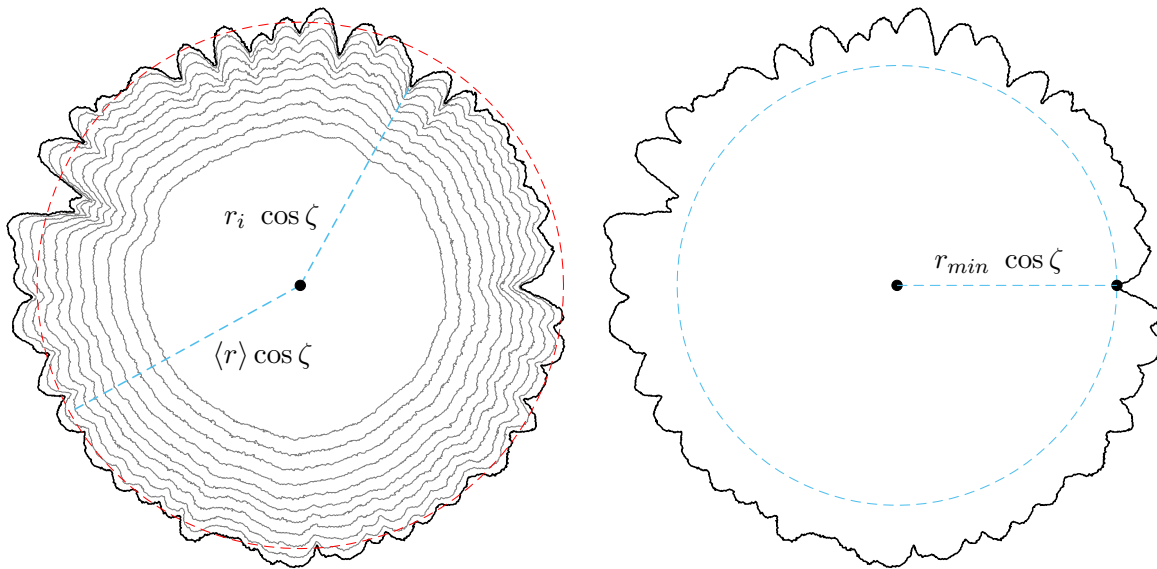


FIGURE 4. The position of the granular front associated with a inflow flux $Q = 19.68 \text{ cm}^3 \text{ s}^{-1}$ is extracted from the top-view photographs using digital image processing. Each point in the granular interface is represented by a radial position r_i , whilst the mean position of the front is given by the mean radii $\langle r \rangle$. The point with the minimum radial distance r_{min} is recorded for all the images.

front slows down as it avalanches downwards, in a similar way to what is observed for axisymmetric spreading of gravity-currents (e.g. Huppert & Simpson 1980; Huppert 1982; Takagi & Huppert 2010).

The temporal evolution can be seen in further detail in contour plots of the propagating front (figure 3). The contour plots are constructed by converting each of the top-view pictures into a binary black and white image, and then detecting the boundary between black and white regions (McAndrew 2004). The contoured interfaces are plotted in intervals of 0.5 seconds, with the last contour representing the granular front 20 seconds after the gate was released. Initially, the contours have a roughly circular shape as the granular material spreads radially, and progressively become closer together as the flow slows down. Rapidly, the initial circular-shaped contours of the radial spreading regime become subject to small axial perturbations long before the flow is seen to develop a pronounced fingering pattern. These small perturbations could be due to inhomogeneities in the bed, with small gaps between the fixed beads causing small perturbations to the flow height, or even as a consequence of the material at the gate being fluidised at slightly different times, leading to inhomogeneities since the flow

initiation. From the contour plots it is also possible to observe that (i) the contours were further apart for higher fluxes, showing that, although always decelerating, the front moves faster for higher fluxes and (ii) the fingering pattern develops at larger radii for higher fluxes. This latter observation will be analysed in further detail in the following section by examining the onset of the fingering instability.

After an initial transient regime, where the front is subjected to axial perturbations but still flowing as a whole downstream, portions of the flow solidify and eventually lock in place to form the levees for the subsequent fingers. It is interesting to note that once the levees are formed, each finger has the same morphology as a self-channelised flow, in which static edges form spontaneously to confine a fluid-like motion in a central channel (Félix & Thomas 2004; Deboeuf *et al.* 2006; Takagi *et al.* 2011; Rocha *et al.* 2019). We define the numbers of fully developed fingers as the number of channels that due to the self-channelisation process can sustain the flow and reach the bottom of the cone. The channels that form but stop midway down are not taken into account. For the fluxes tested here, the width of the fully developed fingers remained roughly the same, oscillating around a mean value of 18 mm, and once the channels detach from the others, it keeps the same width downstream. The coexistence of solid and liquid-like behaviours in the parallel-sided leveed channels suggests that frictional hysteresis is a key mechanism to generate the observed patterns.

In order to investigate and quantify the onset of the finger formation, each tracked interface is represented by a mean radial position

$$\langle r \rangle(t) = \frac{1}{N} \sum_{i=1}^N r_i(t), \quad (2.1)$$

which is simply the mean value of the individual positions r_i of each point at the interface. Since r is the radial distance downslope the cone, a factor of $\cos \zeta$ appears in the contour plots (figure 4). To capture the moment when the first material at the interface stops, we track the evolution of the point closest to the origin, which is represented by r_{min} (see figure 4b). The time t_* at which the first material point stops is defined here as the time when r_{min} stops evolving in time, and the critical radius r_{crit} is given by the mean radii, which represents the interface of the first stopped material, i.e. $\langle r \rangle(t_*)$. For illustration, the critical radius for two different volume fluxes is shown in figure 5(a,b). For a inflow flux $Q = 11.93 \text{ cm}^3\text{s}^{-1}$ the first material is arrested when

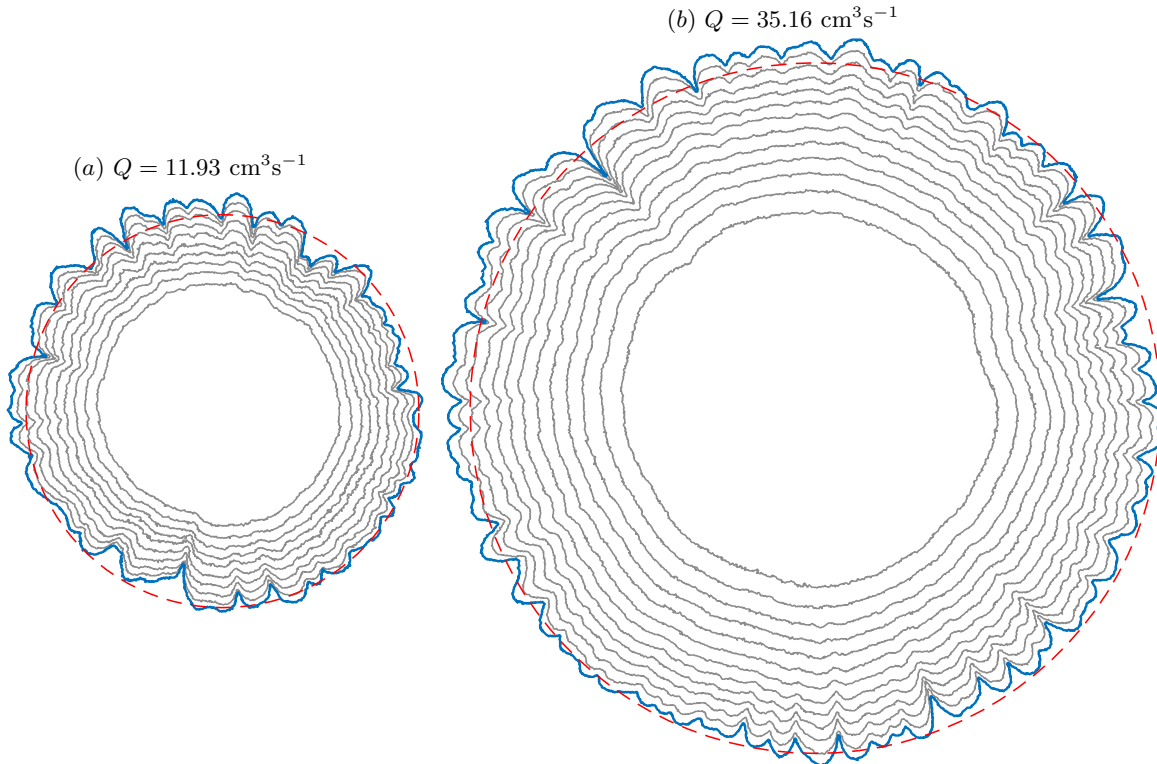


FIGURE 5. The critical radius r_{crit} is determined by the mean radius $\langle r \rangle$ of the interface of the first stopped material. For illustration, the critical radial position for two different fluxes are displayed, showing that r_{crit} increases with the flux.

$r_{crit} = 172.2$ mm, whereas for a flow rate $Q = 35.16$ cm³s⁻¹, the critical distance is $r_{crit} = 302.7$ mm. The solid blue curve shows the interface at which r_{min} stops evolving in time, whilst the dashed red circle represents the mean radius at this time, which gives r_{crit} .

3. Axisymmetric depth-averaged model

The flows investigated here share the property that their characteristic lateral extension is much larger than their thickness, leading to small flow aspect ratio. This fact motivates the use of a depth-integrated model, in which governing equations and flow fields are averaged through the avalanche depth, reducing the effective dimension of the system and simplifying the problem by using the shallowness assumption to neglect terms that depend on higher orders in the aspect ratio.

We start by defining an orthogonal frame of reference $Or\theta z'$ at the apex of the cone, with the radial axis pointing downslope the cone, θ is the polar angle, whilst the z' -axis is the upwards normal to the surface of the cone (figure 6a). The conical coordinate system relates to a standard right-handed Cartesian coordinate system $Oxyz$ centred

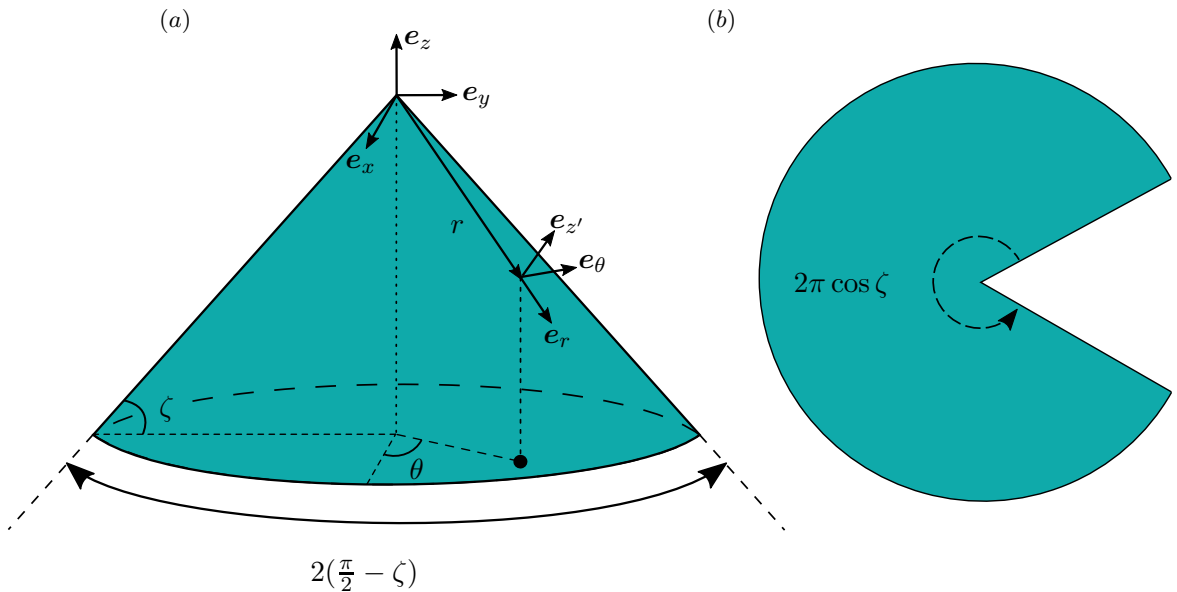


FIGURE 6. The intrinsic geometry of a cone of opening angle $2(\pi/2 - \zeta)$, where ζ is the inclination angle of the cone, can be represented by a two-dimensional flat disk with a removed wedge of angle $2\pi(1 - \cos \zeta)$.

at the apex of the cone according to the following coordinate transformation

$$x = (r \cos \zeta + z' \sin \zeta) \cos \theta, \quad (3.1a)$$

$$y = (r \cos \zeta + z' \sin \zeta) \sin \theta, \quad (3.1b)$$

$$z = -r \sin \zeta + z' \cos \zeta. \quad (3.1c)$$

In the depth-integrated framework, this yields a grad operator in the form

$$\nabla = \mathbf{e}_r \frac{\partial}{\partial r} + \frac{1}{\mathcal{M}} \mathbf{e}_\theta \frac{\partial}{\partial \theta}, \quad (3.2)$$

where, for shallow flows, $\mathcal{M} = r \cos \zeta + O(\epsilon)$. The set of depth-averaged conservation laws for mass and linear momentum are obtained by assuming the granular material to be incompressible with constant bulk density and applying the coordinate transformation (3.1a)–(3.2) to the depth-integrated avalanche model of Baker *et al.* (2016a).

In this paper, the conical frame of reference is used to estimate the critical radius r_{crit} , so we first consider the initial axisymmetric spreading, in which all the derivatives with respect to θ vanish and the velocity in the θ direction is assumed to be zero. In the axisymmetric limit, the depth-integrated conservation of mass can be expressed by (Gajjar 2016)

$$\frac{\partial h}{\partial t} + \frac{1}{r} \frac{\partial}{\partial r} (h \bar{u}_r r) = 0, \quad (3.3)$$

where h is the avalanche depth and \bar{u}_r is the depth-averaged radial velocity. Under the shallowness assumption and also assuming axisymmetric flow, the balance of linear

momentum can be written as (Baker *et al.* 2016a; Gajjar 2016)

$$\begin{aligned} \frac{\partial}{\partial t} (h\bar{u}_r) + \frac{1}{r} \frac{\partial}{\partial r} (h\bar{u}_r^2 r) + \frac{\partial}{\partial r} \left(\frac{1}{2} g h^2 \cos \zeta \right) &= g h \cos \zeta (\tan \zeta - \mu_b(h, Fr)) \quad (3.4) \\ &+ \frac{1}{r} \frac{\partial}{\partial r} \left(\nu h^{3/2} r \frac{\partial \bar{u}_r}{\partial r} \right) - \frac{\nu h^{3/2} \bar{u}_r}{r^2} \end{aligned}$$

where g is the constant of gravitational acceleration. Equation (3.4) describes the balance between the inertial terms, first two in the left-hand side, the depth-averaged pressure, which is linked to gradients of the free surface along r , the component of gravity along the radial direction, a resistive shear stress at the base governed by the coefficient of friction μ_b and a viscous-like stress, which arise in the depth-averaging process when the in-plane deviatoric stress is retained in the momentum equation (Gray & Edwards 2014; Baker *et al.* 2016a).

The coefficient of basal friction μ_b carries specific information about the nature of granular flows, and how the resistive force changes with flow properties, such as thickness and flow rate. One way to characterise the friction coefficient is to perform experiments with steady uniform flows down inclined planes. Using the equilibrium between gravity and friction, the basal friction law can be measured directly in the static and fast-moving regimes, whereas the coefficient of friction for low velocities can only be accessed indirectly (Pouliquen 1999a; Pouliquen & Forterre 2002; Forterre & Pouliquen 2003; Edwards *et al.* 2019; Russell *et al.* 2019). The pattern formation discussed in section 2 is only viable due to frictional hysteresis. This is firstly because during the initial axisymmetric spreading, the destabilisation is a signature of a transition to a velocity-weakening frictional behaviour (Pouliquen & Forterre 2002), which is essential to define the critical position r_{crit} . Moreover, once the fingers are formed and developed, the fluid-like motion is confined between two static levees in a self-channelised configuration, which requires frictional hysteresis to allow the coexistence of liquid-like layers in the channel with the parallel-sided solid levees (Félix & Thomas 2004; Mangeney *et al.* 2007; Rocha *et al.* 2019). Therefore, it is crucial to consider a basal coefficient of friction that also incorporates hysteresis. Here we use a non-monotonic friction law, in which the friction coefficient (Pouliquen & Forterre

2002; Edwards *et al.* 2019)

$$\mu_b(h, Fr) = \begin{cases} \mu_D, & Fr \geq \beta_*, \\ \mu_I, & 0 < Fr < \beta_*, \\ \mu_S, & Fr = 0, \end{cases} \quad (3.5)$$

switches between different regimes depending on the local Froude number

$$Fr = \frac{|\bar{u}_r|}{\sqrt{gh \cos \zeta}}, \quad (3.6)$$

which is the ratio of the local depth-averaged speed to the characteristic speed of surface gravity waves.

For high Froude number, friction lies in the dynamic regime, where

$$\mu_D = \mu_1 + \frac{\mu_2 - \mu_1}{1 + h\beta/\mathcal{L}Fr}, \quad (3.7)$$

and the magnitude of the basal resistance increases with the velocity of the flow. In the low-velocity regime, when $Fr < \beta_*$, friction transitions to a velocity-weakening behaviour with the coefficient given by

$$\mu_I = \left(\frac{Fr}{\beta_*}\right)^\kappa \left(\mu_1 + \frac{\mu_2 - \mu_1}{1 + h\beta/\mathcal{L}\beta_*} - \mu_3 - \frac{\mu_2 - \mu_1}{1 + h/\mathcal{L}}\right) + \mu_3 + \frac{\mu_2 - \mu_1}{1 + h/\mathcal{L}}. \quad (3.8)$$

This change in the frictional behaviour to a velocity-weakening basal friction is a rich source of instabilities (Heslot *et al.* 1994; Pouliquen & Forterre 2002), which can lead to, for example, stick-slip instability (Baumberger *et al.* 1994) and also to formation of erosion-deposition waves down inclines (Edwards & Gray 2015; Edwards *et al.* 2017; Rocha *et al.* 2019). When the material is stationary, the static friction coefficient

$$\mu_S = \min \left(\left| \tan \zeta \mathbf{e}_r - \frac{\partial h}{\partial r} \mathbf{e}_r \right|, \mu_3 + \frac{\mu_2 - \mu_1}{1 + h/\mathcal{L}} \right), \quad (3.9)$$

assures that friction exactly balances the net force due to pressure and gravity, until it gets to the maximum static friction coefficient, given by the second argument in the min function. The parameters μ_1 , μ_2 , μ_3 , \mathcal{L} and β record properties of the flowing material and the rough base and were measured directly by performing h_{stop} and h_{start} experiments (Pouliquen & Forterre 2002) and characterising a flow rule for steady uniform flow experiments in a plane geometry (Pouliquen 1999a; Pouliquen & Forterre 2002; Edwards *et al.* 2019). The power-law exponent κ and the transition Froude number β_* are assumed to be the same as the ones measured by Russell *et al.* (2019)

$$\zeta = 28.6^\circ \quad \zeta_1 = 23.57^\circ \quad \zeta_2 = 34.97^\circ \quad \zeta_3 = 26.25^\circ \quad \beta = 0.136 \quad \mathcal{L} = 0.5 \text{ mm} \quad \beta_* = 0.2$$

TABLE 1. Physical parameters measured for the spherical glass beads

for the flow of glass beads on a rough bed made of the same particles as ours. The exact values used throughout the paper are presented in table 1.

The last two terms in the right-hand-side of (3.4) are the ones linked to the in-plane deviatoric stress, which in the conical geometry results in two terms, instead of one like in the planar case, due to the unit vectors of the conical frame of reference not being constant. Using the $\mu(I)$ -rheology (GDR-MiDi 2004; da Cruz *et al.* 2005; Jop *et al.* 2005, 2006), the coefficient ν can be written as (Gray & Edwards 2014)

$$\nu = \frac{2\mathcal{L}\sqrt{g}\sin\zeta}{9\beta\sqrt{\cos\zeta}} \left(\frac{\tan\zeta_2 - \tan\zeta}{\tan\zeta - \tan\zeta_1} \right), \quad (3.10)$$

where no extra parameters were added to the model, and ν is given in terms of parameters measured in the friction law (3.5). The viscous dissipation, which is of higher order in the aspect ratio, represents a small perturbation from the traditional shallow-water model, and, for that reason can be neglected in many situations (e.g. Pouliquen 1999b; Pouliquen & Forterre 2002; Viroulet *et al.* 2017). Nevertheless, in some cases the viscous-like dissipation is crucial to regularise the set of equations, and make the system mathematically well-posed, for example when modelling segregation-induced finger formation (Woodhouse *et al.* 2012; Baker *et al.* 2016b) and to recover cut-off frequencies of granular roll waves (Forterre 2006; Gray & Edwards 2014). The viscous terms do not play an important role in the initial axisymmetric spreading, but nonetheless, since they are crucial to provide the selection mechanism for the equilibrium state of self-channelised flows (Rocha *et al.* 2019), they are required to set the steady state of each fully developed finger downstream and, hence, are also incorporated in our model for the radial spreading.

4. Predicting the critical radius and number of fingers

4.1. Critical radius

In order to provide a first estimate of the radial position at which the first portion of the flow solidifies, r_{crit} , we solve the time dependent axisymmetric system of conservation laws using a non-oscillatory central scheme for convection-diffusion

equations (Kurganov & Tadmor 2000). The one-dimensional numerical domain has the same length as the cone, i.e. $L_r = 508.4$ mm, and is discretised in $n_r = 2000$ points. Numerical fluxes are computed using a minmod limiter with $\theta = 2$ (Kurganov & Tadmor 2000), and the numerical integration is performed using a second-order Runge-Kutta method with time-steps defined by a CFL (Courant-Friedrichs-Lewy) number of 0.225 and bounded by a maximum step-size $\Delta t = 10^{-4}$ s (LeVeque 2002).

The cone is initially empty, i.e., h and \bar{u}_r are identically zero everywhere at $t = 0$. In order to set boundary conditions at the inflow boundary, which is located at a radial distance $R_{gate} = 85$ mm, we seek steady solutions to the mass conservation equation (3.3), which leads to

$$\frac{\partial}{\partial r} (h\bar{u}_r r) = 0, \quad (4.1)$$

and, since the inflow volume flux relates to the thickness and velocity at the gate as

$$Q = 2\pi R_{gate} h_{gate} \bar{u}_{gate} \cos \zeta, \quad (4.2)$$

equations (4.1) and (4.2) can be combined with the definition of the Froude number (3.6) to yield

$$\bar{u}_{gate} = \left(\frac{Q Fr^2 g}{2\pi R_{gate}} \right)^{1/3}, \quad (4.3a)$$

$$h_{gate} = \frac{Q}{2\pi R_{gate} \bar{u}_{gate} \cos \zeta}. \quad (4.3b)$$

Note that the factor $\cos \zeta$ in equation (4.2) is related to the conical geometry, which sets an unusual variation on the polar angle θ , such that $0 \leq \theta \leq 2\pi \cos \zeta$, leading to a perimeter $\mathcal{L} = 2\pi r \cos \zeta$ (see figure 6b). Simulations are performed by setting critical flow at gate, i.e. $Fr = 1$ at $r = R_{gate}$, but we observe that regardless of the values set at the gate, the thickness h , the velocity \bar{u}_r and the Froude number rapidly adjust to the steady solution of (3.3)–(3.4).

Numerical solution for the thickness, depth-averaged radial velocity and Froude number as a function of the radial distance r for different times are displayed in figures 7. In this specific case the flux is $Q = 37 \text{ cm}^3\text{s}^{-1}$, but the overall behaviour is similar for all the fluxes investigated here. Panels (a) and (b) show that as the material propagates down the cone it thins and slows down, as expected, where both $h(r, t)$ and $\bar{u}_r(r, t)$ are strictly decreasing functions of r . The solution for Fr (figure 7c) show that after the sharp drop from one at the gate, it adjusts to a decreasing function

of r until it reaches a minimum, when it switches behaviour and tends to infinity at the front, where $h = 0$ and $\bar{u}_r = u_{front}$, which is finite. As the granular material continuously propagates down the cone the minimum Froude number decreases in time until it reaches $Fr = \beta_*$, and the flow starts feeling the velocity-weakening intermediate friction. At this moment, our simulations show that the portion of the flow subjected to the intermediate friction stops, which then brings the front to a halt, triggering a deposition wave, similarly to the transition observed in self-channelised flows when the mass flux is reduced below a minimum critical value (Félix & Thomas 2004; Takagi *et al.* 2011; Rocha *et al.* 2019). We define the theoretical critical radius as the position of the granular front when the minimum Froude number touches β_* and the intermediate branch of the friction law becomes active.

Simulations were performed for volume fluxes in the same range of the ones explored in the experiments, i.e. $Q \in [10, 37] \text{ cm}^3\text{s}^{-1}$. For each of the fluxes, the position at which flow started being subjected to the velocity-weakening friction regime was recorded, in order to construct the theoretical prediction for $r_{crit}(Q)$. The comparison between theory and experiments is shown in figure 8(a), where triangles represent experimental measurements, whereas grey circles are the critical radius for the different simulations, which are carried in intervals of $1 \text{ cm}^3\text{s}^{-1}$. Both experimental and theoretical critical radii display a linear trend with the volume flux Q , and although the experiments suggests a linear increase of r_{crit} with a slightly lower gradient than the theoretically predicted, the one dimensional axisymmetric theory is able to capture well the experimental behaviour. Moreover, it is interesting to note that in the hypothesis of the critical radius being defined as the front position when the velocity-weakening friction becomes active it is implicitly assumed that the instability is triggered not at the granular front but at the position at which the Froude number is minimal. Although the good quantitative agreement between theoretical predictions and experimental data supports our assumption, experimental evidence is still required.

4.2. Number of fully developed fingers

Now, we proceed to estimate the number of fully developed fingers, which, as mentioned previously, is measured experimentally as the number of channels able to sustain the flow and reach the bottom of the cone. By inspecting each of the individual channels formed after the granular front has broken, one can observe that once the fingers

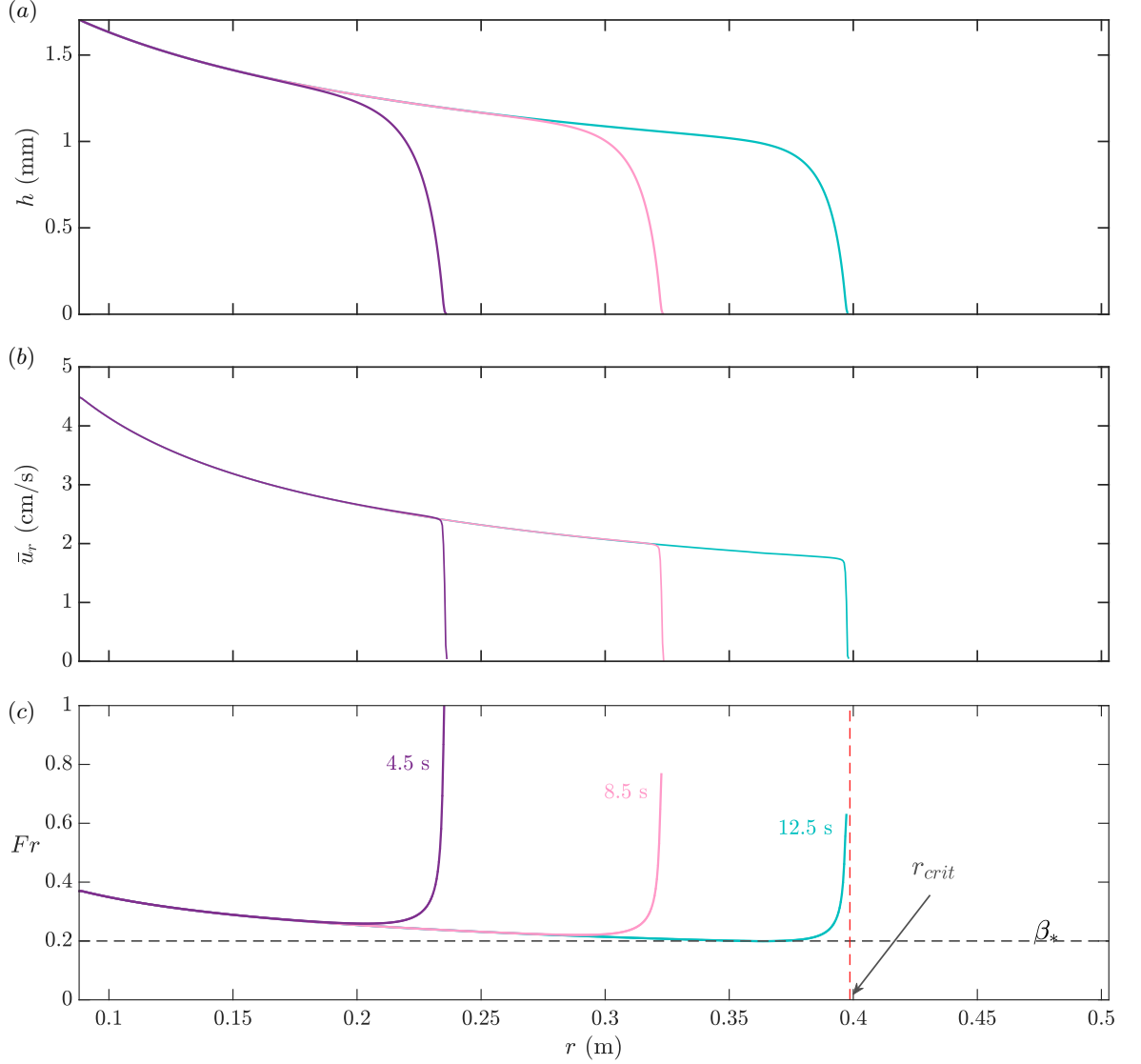


FIGURE 7. Time-dependent solutions for (a) the thickness h (b) the depth-averaged radial velocity \bar{u}_r and (c) the Froude number Fr as a function of the radial distance r for a volume flux $Q = 37 \text{ cm}^3\text{s}^{-1}$. As the minimum point of the Froude number profile reaches β_* the flow starts feeling the velocity-weakening intermediate friction, which is unstable. As a result the granular front stops, defining the theoretical r_{crit} .

completely detach from each other they keep the same width downstream of the cone, in a very similar way to what is seen for monodisperse self-channelised flows down incline planes (Félix & Thomas 2004; Deboeuf *et al.* 2006; Mangeney *et al.* 2007; Takagi *et al.* 2011; Rocha *et al.* 2019). In the plane geometry, a slow lateral creep is responsible for widening the channels and the steady-state equilibrium width is approached with a very long relaxation time (Deboeuf *et al.* 2006). The question of whether the fingers observed on the cone behave in a similar manner is still open and experiments with the inflow being sustained for longer are required to answer that.

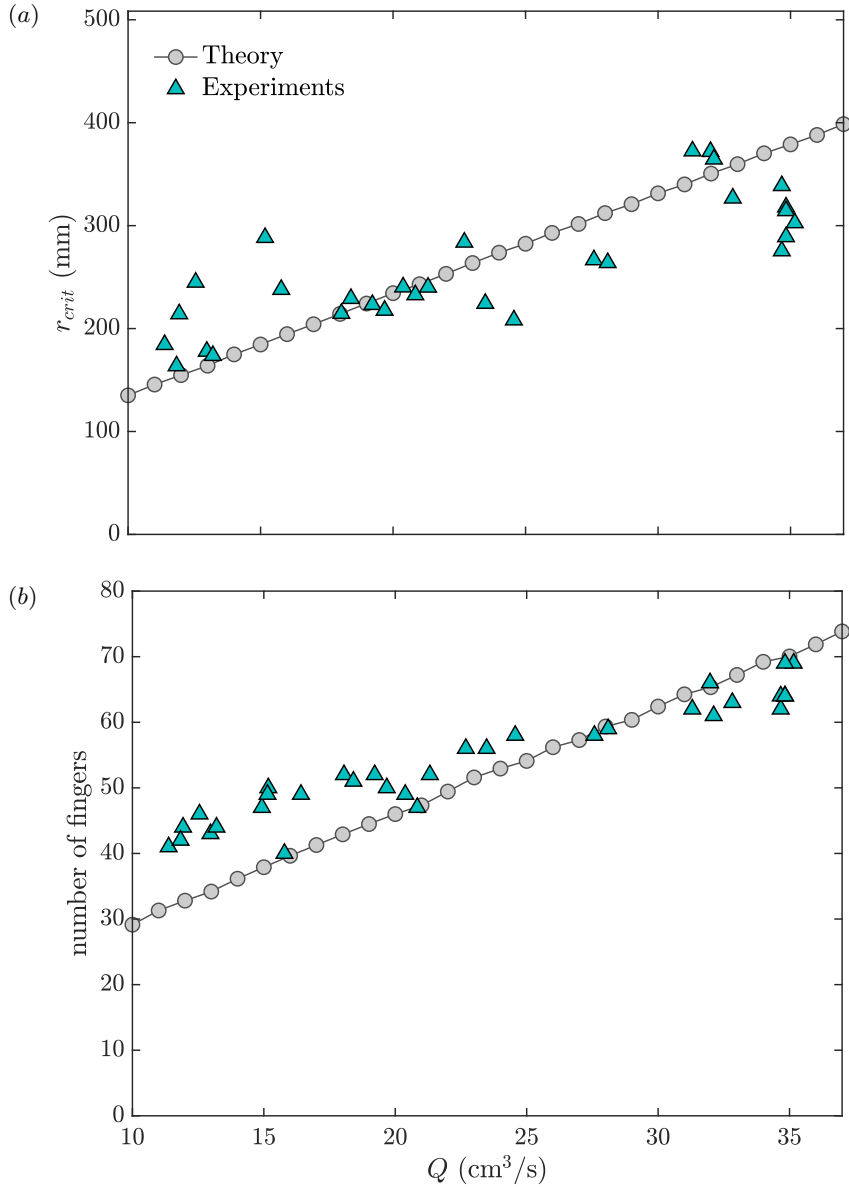


FIGURE 8. The solutions for (a) the critical radii r_{crit} and (b) the number of fully developed fingers as a function of the inflow volume flux Q . Green triangles correspond to the experimental measurements, whilst grey circles represent predictions from the depth-averaged model.

Assuming that each of the fingers is a leveed channel sustained by a flux Q_{finger} , which, in a steady-state configuration where the fingers are fully formed and the front has already left the cone, is related to the inflow flux via

$$Q = n Q_{finger}, \quad (4.4)$$

where n is the number of fully developed channels. We also assume that at the moment of splitting, at r_{crit} , the perimeter of the circular interface splits evenly between the fingers, such that

$$2\pi r_{crit} \cos \zeta = n W_{total}, \quad (4.5)$$

where W_{total} is the total width of the fingers, i.e. the width of the moving channels plus the levees. The asymptotic equilibrium state of the central moving channel of a self-channelised flow sustained by a flux Q on a slope inclined at an angle ζ is governed by a balance between gravity, friction and viscous stresses, which are responsible for cross-slope variations in the downslope velocity profile. The force balance is expressed as a second-order boundary value problem, in which the position of the boundaries and the thickness of the flow are unknowns a priori. By imposing no-slip and no velocity gradient conditions at the channel-levee interface the problem can be solved to reveal the velocity profile across the channel, the thickness and the width of the fluid-like region (Rocha *et al.* 2019).

Although the steady-state width of the central channel is a monotonic function of the flux per finger Q_{finger} , frictional hysteresis implies that there are multiple possible morphologies for the levees profile (Rocha *et al.* 2019). One possible way to compute an approximation for W_{total} is to assume that all the points within the levee are on the brink of yield (Balmforth *et al.* 2001), and use the maximum coefficient of static friction to provide a unique solution for the minimum levee profile able to hold in place.

This way, the total width of a self-channelised flow is a function only of the slope angle and the flux, i.e. $W_{total} = W_{total}(Q_{finger})$, since the slope angle is fixed. Equating (4.4) and (4.5) leads to

$$\frac{Q}{2\pi r_{crit} \cos \zeta} = \frac{Q_{finger}}{W_{total}(Q_{finger})}, \quad (4.6)$$

which can be interpreted as a condition, which states that the interface breaks in the number of fingers, such that the volume flux per unit perimeter of the circular interface at the moment of splitting is equal to the volume flux per width of each finger. Using the values for the critical radii obtained from the time-dependent solutions presented in § 4.1 and, based on the fact the curvature terms can be neglected in the depth-averaged framework, we assume that each finger is a self-channelised flow, in which the relation $W_{total}(Q_{finger})$ is given by the solution for an inclined plane of the same slope angle as the cone. As a result, the flux per finger Q_{finger} which satisfies (4.6) can be found. With the information of the flux per finger for each inflow volume flux Q , expression (4.4) can be used to find the total number of fully developed self-channelised fingers.

The comparison between theoretical prediction with experiments is displayed in figure 8(b). Again, green triangles are obtained experimentally, whilst the grey circles represent results from the model. Both experiments and theory show that the number of fingers increases linearly with the flux, but similarly to what is seen for r_{crit} the theory predicts a linear trend with a higher gradient than what the experiments suggest. The theory agrees well with experiments, being able to capture in good quantitative agreement the overall behaviour. One of the possibilities for the slightly steeper gradient could be that there is an adjustment region between the point at which the first material stops and the mean radial position where the majority of the fingers are completely developed, and therefore the expression (4.6) is an approximation. A fully two-dimensional simulations of the full set of conservation laws, which takes into account variations in the θ direction may be a potential tool to reveal the full dynamical behaviour.

5. Conclusion

Granular finger formation is typically associated with the feedback that particle-size segregation exerts on the bulk flow, which ultimately results in a local change in composition, and, hence, affect the resistive force locally, destabilising the interface and generating the fingers (Pouliquen *et al.* 1997; Pouliquen & Vallance 1999; Woodhouse *et al.* 2012; Baker *et al.* 2016*b*). On the other hand, for monodisperse mixtures down rough planes, the well-defined granular front propagates with constant speed due to the dominant balance between gravity and friction (Pouliquen 1999*b*), and the interface evolves in space and time, keeping an uniform cross-slope profile (Pouliquen & Vallance 1999; Baker *et al.* 2016*b*). By performing experiments with monodisperse particles flowing down a rough conical surface, in this paper, we show a new granular fingering instability, which is triggered in the complete absence of particle segregation. However, it is shown that in the conical geometry, the constant injection rate generates a granular front that decelerates as it spreads radially, and eventually, the interface splits revealing an astonishing fingering pattern, which is triggered by frictional hysteresis (Carrigy 1970; Daerr & Douady 1999; Pouliquen & Forterre 2002; DeGiuli & Wyart 2017; Edwards *et al.* 2019; Perrin *et al.* 2019).

In order to predict the onset of the instability and quantify critical radial position

r_{crit} a one-dimensional axisymmetric depth-averaged viscous model is applied, which can capture the overall behaviour before the splitting point, i.e. the granular material enters the surface of the cone, and after a very short relaxation time, it adjusts to a regime where the flow consistently thins and slows down. As soon as the velocity-weakening friction becomes active, the flow destabilises, which consequently causes the front to stop. The transition to a frictional regime where the coefficient of basal friction is a decreasing function of the velocity, and therefore, the non-monotonicity of the friction curve is a signature of hysteresis in frictional particulate systems (Perrin *et al.* 2019). Interestingly, our time-dependent simulations suggest that the instability is triggered not at the granular front, but just behind it, where the Froude number is minimal, which is the part of the flow where the velocity-weakening friction becomes active first. The depth-averaged axisymmetric theory is in very good quantitative agreement with experimental data, which sustain our hypothesis. However, more experiments are required to confirm the destabilisation point, which could potentially be captured via particle image velocimetry (PIV) techniques. In addition, to understand the initial regime in which time-dependent solutions for the thickness and depth-averaged velocity exhibit a rapid adjustment to a decreasing function of r , steady axisymmetric solutions may be compared with the full time-dependent simulations aiming to reveal the origin of the offset in the $r_{crit}(Q)$ curve, which in our understanding so far is related to the length of the front relative to the minimum point in the $Fr(r)$ profile.

Far downstream, where the fingers are fully formed, we assume that for shallow flows the θ -curvature terms are higher-order in the aspect ratio and can be neglected, resulting in a geometry that can be approximated locally as an inclined flat plane to estimate the number of fully developed channels. Moreover, each individual finger is considered to have the same morphology as a self-channelised flow (Félix & Thomas 2004; Deboeuf *et al.* 2006; Mangeney *et al.* 2007; Takagi *et al.* 2011; Rocha *et al.* 2019), whose equilibrium state is governed by a balance between gravity, friction and lateral viscous stresses (Rocha *et al.* 2019). The solid levees at the edges of the fingers are supposed to have the minimum levee profile, where all the points within the solid boundaries are assumed to be on the brink of yielding, with the coefficient of friction being in its maximum value (Rocha *et al.* 2019). By doing so, the number of fully developed fingers can be computed, and the good quantitative agreement supports the

aforementioned assumptions. A slow lateral creeping process of the levees is observed in flows of spherical glass beads (Deboeuf *et al.* 2006), which could be investigated via experiments with longer inflow, in order to examine the stability of the fully developed fingers.

To conclude, the results presented here demonstrate the importance of the hysteretic behaviour in the rheology of monodisperse flows, which leads to non-monotonic friction laws. Due to the unstable character of the velocity-weakening friction, there are few direct observations of this regime in experiments (Dijksman *et al.* 2011; Kuwano *et al.* 2013). However, several studies suggest the existence of this region in the basal friction (Pouliquen & Forterre 2002; Mangeney *et al.* 2007; Edwards & Gray 2015; Edwards *et al.* 2017, 2019; Rocha *et al.* 2019), and, recently, an indirect way to access this frictional regime has been proposed via retrogressive failure experiments (Russell *et al.* 2019). In this regard, contrary to the planar configuration, where the metastable regime is accessed only for finite releases (Malloggi *et al.* 2006), on the cone the flow consistently thins and slows down, and, hence, the metastable regime is always accessed. The conical geometry may be, therefore, a useful tool to shed light into the velocity-strengthening to weakening transition in the granular rheology.

REFERENCES

- ANDREOTTI, B., FORTERRE, Y. & POULIQUEN, O. 2013 *Granular media: between fluid and solid*. Cambridge University Press.
- BAKER, J. L., BARKER, T. & GRAY, J. M. N. T. 2016a A two-dimensional depth-averaged $\mu(I)$ -rheology for dense granular avalanches. *J. Fluid. Mech.* **787**, 367–395.
- BAKER, J. L., JOHNSON, C. G. & GRAY, J. M. N. T. 2016b Segregation-induced finger formation in granular free-surface flows. *J. Fluid. Mech.* **809**, 168–212.
- BALMFORTH, N. J., BURBIDGE, A. S. & CRASTER, R. V. 2001 Shallow lava theory. In *Geomorphological Fluid Mechanics*, pp. 164–187. Springer.
- BAUMBERGER, T., HESLOT, F. & PERRIN, B. 1994 Crossover from creep to inertial motion in friction dynamics. *Nature* **367** (6463), 544.
- CARRIGY, M. A. 1970 Experiments on the angles of repose of granular materials 1. *Sedimentology* **14** (3-4), 147–158.
- DA CRUZ, F., EMAM, S., PROCHNOW, M., ROUX, J. N. & CHEVOIR, F. 2005 Rheophysics of dense granular materials: Discrete simulation of plane shear flows. *Phys. Rev. E* **72** (2, 1).

- DAERR, A. & DOUADY, S. 1999 Two types of avalanche behaviour in granular media. *Nature* **399**, 241–243.
- DEBOEUF, S., LAJEUNESSE, E., DAUCHOT, O. & ANDREOTTI, B. 2006 Flow rule, self channelization, and levees in unconfined granular flows. *Phys. Rev. Lett.* **97**, 158303.
- DEGIULI, E. & WYART, M. 2017 Friction law and hysteresis in granular materials. *Proc. Nat. Acad. Scien.* **114** (35), 9284–9289.
- DIJKSMAN, J. A., WORTEL, G. H., VAN DELLEN, L. T. H., DAUCHOT, O. & VAN HECKE, M. 2011 Jamming, yielding, and rheology of weakly vibrated granular media. *Phys. Rev. Lett.* **107** (10), 108303.
- EDWARDS, A. N. & GRAY, J. M. N. T. 2015 Erosion-deposition waves in shallow granular free-surface flows. *J. Fluid Mech.* **762**, 35–67.
- EDWARDS, A. N., RUSSELL, A. S., JOHNSON, C. G. & GRAY, J. M. N. T. 2019 Frictional hysteresis and particle deposition in granular free-surface flows. *J. Fluid Mech.* **875**, 1058–1095.
- EDWARDS, A. N., VIROULET, S., KOKELAAR, B. P. & GRAY, J. M. N. T. 2017 Formation of levees, troughs and elevated channels by avalanches on erodible slopes. *J. Fluid Mech.* **823**, 278–315.
- FÉLIX, G. & THOMAS, N. 2004 Relation between dry granular flow regimes and morphology of deposits: formation of levées in pyroclastic deposits. *Earth Planet. Sci. Lett.* **221**, 197–213.
- FORTERRE, Y. 2006 Kapiza waves as a test for three-dimensional granular flow rheology. *J. Fluid Mech.* **563**, 123–132.
- FORTERRE, Y. & POULIQUEN, O. 2003 Long-surface-wave instability dense granular flows. *J. Fluid Mech.* **486**, 21–50.
- GAJJAR, P. J. S. 2016 Modelling size-segregation in dense granular flows. PhD thesis, The University of Manchester (United Kingdom).
- GDR-MIDI 2004 On dense granular flows. *Eur. Phys. J. E* **14**, 341–365.
- GRAY, J. M. N. T. 2018 Particle segregation in dense granular flows. *Ann. Rev. Fluid Mech.* **50**, 407–433.
- GRAY, J. M. N. T. & ANCEY, C. 2009 Segregation, recirculation and deposition of coarse particles near two-dimensional avalanche fronts. *J. Fluid Mech.* **629**, 387–423.
- GRAY, J. M. N. T. & CHUGUNOV, V. A. 2006 Particle-size segregation and diffusive remixing in shallow granular avalanches. *J. Fluid Mech.* **569**, 365–398.
- GRAY, J. M. N. T. & EDWARDS, A. N. 2014 A depth-averaged $\mu(I)$ -rheology for shallow granular free-surface flows. *J. Fluid Mech.* **755**, 503–544.
- GRAY, J. M. N. T. & HUTTER, K. 1997 Pattern formation in granular avalanches. *Continuum Mech. & Thermodyn.* **9**, 341–345.
- HESLOT, F., BAUMBERGER, T., PERRIN, B., CAROLI, B. & CAROLI, C. 1994 Creep, stick-slip, and dry-friction dynamics: Experiments and a heuristic model. *Phys. Rev. E* **49** (6), 4973.
- HILL, K. M., KHARKAR, D. V., GILCHRIST, J. F., MCCARTHY, J. J. & OTTINO, J. M. 1999 Segregation driven organization in chaotic granular flows. *Proc. Natl Acad. Sci.* **96**, 11701–11706.
- HUPPERT, H. E. 1982 The propagation of two-dimensional and axisymmetric viscous gravity currents over a rigid horizontal surface. *J. Fluid Mech.* **121**, 43–58.

- HUPPERT, H. E. & SIMPSON, J. E. 1980 The slumping of gravity currents. *J. Fluid Mech.* **99** (4), 785–799.
- JAEGER, H. M. & NAGEL, S. R. 1992 Physics of the granular state. *Science* **255** (5051), 1523–1531.
- JOHNSON, C. G., KOKELAAR, B. P., IVERSON, R. M., LOGAN, M., LAHUSEN, R. G. & GRAY, J. M. N. T. 2012 Grain-size segregation and levee formation in geophysical mass flows. *J. Geophys. Res.* **117**, F01032.
- JOP, P., FORTERRE, Y. & POULIQUEN, O. 2005 Crucial role of sidewalls in granular surface flows: consequences for the rheology. *J. Fluid Mech.* **541**, 167–192.
- JOP, P., FORTERRE, Y. & POULIQUEN, O. 2006 A constitutive relation for dense granular flows. *Nature* **44**, 727–730.
- KOKELAAR, B. P., GRAHAM, R. L., GRAY, J. M. N. T. & VALLANCE, J. W. 2014 Fine-grained linings of leveed channels facilitate runout of granular flows. *Earth & Planetary Sci. Lett.* **385**, 172–180.
- KURGANOV, A. & TADMOR, E. 2000 New high-resolution central schemes for nonlinear conservation laws and convection-diffusion equations. *J. Comput. Phys.* **160**, 241–282.
- KUWANO, O., ANDO, R. & HATANO, T. 2013 Crossover from negative to positive shear rate dependence in granular friction. *Geophys. Res. Lett.* **40** (7), 1295–1299.
- LEVEQUE, R. J. 2002 *Finite Volume Methods for Hyperbolic Problems*. Cambridge University Press.
- LIU, A. J. & NAGEL, S. R. 1998 Jamming is not just cool any more. *Nature* **396** (6706), 21.
- LUCAS, A., MANGENEY, A. & AMPUERO, J. P. 2014 Frictional velocity-weakening in landslides on earth and on other planetary bodies. *Nature communications* **5**, 3417.
- MAKSE, H. A., HAVLIN, S., KING, P. R. & STANLEY, H. E. 1997 Spontaneous stratification in granular mixtures. *Nature* **386**, 379–382.
- MALLOGGI, F., LANUZA, J., ANDREOTTI, B. & CLÉMENT, E. 2006 Erosion waves: Transverse instabilities and fingering. *EPL (Europhysics Letters)* **75** (5), 825.
- MANGENEY, A., BOUCHUT, F., THOMAS, N., VILOTTE, J. P. & BRISTEAU, M. O. 2007 Numerical modeling of self-channeling granular flows and of their levee-channel deposits. *J. Geophys. Res.* **112**, F02017.
- MCANDREW, A. 2004 An introduction to digital image processing with matlab notes for scm2511 image processing. *School of Computer Science and Mathematics, Victoria University of Technology* **264** (1), 1–264.
- PERRIN, H., CLAUD, C., WYART, M., METZGER, B. & FORTERRE, Y. 2019 Interparticle Friction Leads to Nonmonotonic Flow Curves and Hysteresis in Viscous Suspensions. *Phys. Rev. X* **9** (3).
- DU PONT, S. C., GONDRET, P., PERRIN, B. & RABAUD, M. 2003 Granular avalanches in fluids. *Phys. Rev. Lett.* **90** (4), 044301.
- POULIQUEN, O. 1999a Scaling laws in granular flows down rough inclined planes. *Phys. Fluids* **11** (3), 542–548.
- POULIQUEN, O. 1999b On the shape of granular fronts down rough inclined planes. *Phys. Fluids* **11** (7), 1956–1958.
- POULIQUEN, O., DELOUR, J. & SAVAGE, S. B. 1997 Fingering in granular flows. *Nature* **386**, 816–817.

- POULIQUEN, O. & FORTERRE, Y. 2002 Friction law for dense granular flows: application to the motion of a mass down a rough inclined plane. *J. Fluid Mech.* **453**, 133–151.
- POULIQUEN, O. & VALLANCE, J. W. 1999 Segregation induced instabilities of granular fronts. *Chaos* **9** (3), 621–630.
- QUARTIER, L., ANDREOTTI, B., DOUADY, S. & DAERR, A. 2000 Dynamics of a grain on a sandpile model. *Phys. Rev. E* **62** (6), 8299.
- ROCHA, F. M., JOHNSON, C. G. & GRAY, J. M. N. T. 2019 Self-channelisation and levee formation in monodisperse granular flows. *J. Fluid Mech.* **876**, 591–641.
- RUSSELL, A. S., JOHNSON, C. G., EDWARDS, A. N., VIROULET, S., ROCHA, F. M. & GRAY, J. M. N. T. 2019 Retrogressive failure of a static granular layer on an inclined plane. *J. Fluid Mech.* **869**, 313–340.
- SAVAGE, S. B. & LUN, C. K. K. 1988 Particle size segregation in inclined chute flow of dry cohesionless granular solids. *J. Fluid Mech.* **189**, 311–335.
- TAKAGI, D. & HUPPERT, H. E. 2010 Flow and instability of thin films on a cylinder and sphere. *J. Fluid Mech.* **647**, 221–238.
- TAKAGI, D., MCELWAIN, J. N. & HUPPERT, H. E. 2011 Shallow granular flows. *Phys. Rev. E* **83** (3), 031306.
- THORNTON, A. R. & GRAY, J. M. N. T. 2008 Breaking size-segregation waves and particle recirculation in granular avalanches. *J. Fluid Mech.* **596**, 261–284.
- VALLANCE, J. W. 1994 Experimental and field studies related to the behaviour of granular mass flows and the characteristics of their deposits. PhD thesis, Michigan Technological University.
- VIROULET, S., BAKER, J. L., EDWARDS, A. N., JOHNSON, C. G., GJALTEMA, C., CLAVEL, P. & GRAY, J. M. N. T. 2017 Multiple solutions for granular flow over a smooth two-dimensional bump. *J. Fluid Mech.* **815**, 77–116.
- WOODHOUSE, M. J., THORNTON, A. R., JOHNSON, C. G., KOKELAAR, B. P. & GRAY, J. M. N. T. 2012 Segregation-induced fingering instabilities in granular free-surface flows. *J. Fluid Mech.* **709**, 543–580.
- ZURIGUEL, I., GRAY, J. M. N. T., PEIXINHO, J. & MULLIN, T. 2006 Pattern selection by a granular wave in a rotating drum. *Phys. Rev. E* **73**, 061302.

5 | The kinematics of bidisperse granular roll waves

This chapter is a reprint of the article titled “The kinematics of bidisperse granular roll waves” by S. Viroulet, J. L. Baker, F. M. Rocha, C. G. Johnson, B.P. Kokeelaar and J. M. N. T. Gray, which was published in volume **848** of the *Journal of Fluid Mechanics* (2018), on pages 836—875. The article is an Open Access article, distributed under the terms of the Creative Commons Attribution licence (<http://creativecommons.org/licenses/by/4.0/>), which permits unrestricted re-use, distribution, and reproduction in any medium, provided the original work is properly cited. The digital object identifier (DOI) for this article is doi:10.1017/jfm.2018.348.

The kinematics of bidisperse granular roll waves

S. Viroulet^{1,2}, J. L. Baker^{1,3}, F. M. Rocha¹, C. G. Johnson¹,
B. P. Kokelaar⁴ and J. M. N. T. Gray^{1†}

¹School of Mathematics and Manchester Centre for Nonlinear Dynamics,
University of Manchester, Oxford Road, Manchester M13 9PL, UK

²Institut de Physique du Globe de Paris, Sorbonne Paris Cité, 75005, Paris

³School of Civil Engineering, The University of Sydney, NSW 2006, Australia

⁴School of Environmental Science, University of Liverpool, Liverpool L69 3BX, UK

(Received 22 December 2017; revised 29 March 2018; accepted 11 April 2018;
first published online 13 June 2018)

Small perturbations to a steady uniform granular chute flow can grow as the material moves downslope and develops into a series of surface waves that travel faster than the bulk flow. This roll wave instability has important implications for the mitigation of hazards due to geophysical mass flows, such as snow avalanches, debris flows and landslides, because the resulting waves tend to merge and become much deeper and more destructive than the uniform flow from which they form. Natural flows are usually highly polydisperse and their dynamics is significantly complicated by the particle size segregation that occurs within them. This study investigates the kinematics of such flows theoretically and through small-scale experiments that use a mixture of large and small glass spheres. It is shown that large particles, which segregate to the surface of the flow, are always concentrated near the crests of roll waves. There are different mechanisms for this depending on the relative speed of the waves, compared to the speed of particles at the free surface, as well as on the particle concentration. If all particles at the surface travel more slowly than the waves, the large particles become concentrated as the shock-like wavefronts pass them. This is due to a concertina-like effect in the frame of the moving wave, in which large particles move slowly backwards through the crest, but travel quickly in the troughs between the crests. If, instead, some particles on the surface travel more quickly than the wave and some move slower, then, at low concentrations, large particles can move towards the wave crest from both the forward and rearward sides. This results in isolated regions of large particles that are trapped at the crest of each wave, separated by regions where the flow is thinner and free of large particles. There is also a third regime arising when all surface

† Email address for correspondence: nico.gray@manchester.ac.uk

particles travel faster than the waves, which has large particles present everywhere but with a sharp increase in their concentration towards the wave fronts. In all cases, the significantly enhanced large particle concentration at wave crests means that such flows in nature can be especially destructive and thus particularly hazardous.

Key words: geophysical and geological flows, granular media, waves/free-surface flows

1. Introduction

Large-scale debris flows spontaneously develop wave-like disturbances that move downstream faster than the material flow (Li *et al.* 1983; McArdell *et al.* 2003; Zanuttigh & Lamberti 2007). These waves arise from flow instabilities that cause small perturbations to grow into a series of large-amplitude roll waves as they travel along a channel (Jeffreys 1925; Dressler 1949; Needham & Merkin 1984; Balmforth & Liu 2004). These roll waves can grow further through merging events until they reach a maximum size (Chang *et al.* 1996; Balmforth & Mandre 2004; Razis *et al.* 2014). As a result the destructive power of each wave can be significantly higher than a uniform flow of the same average mass flux (Razis *et al.* 2014; Köhler *et al.* 2016), and therefore understanding the flow dynamics is of crucial importance for debris-flow hazard mitigation (Hu *et al.* 2012; Jenkins *et al.* 2015).

Similar roll waves occur in experimental dry granular chute flows (Savage 1979; Forterre & Pouliquen 2003), where they likewise arise from instability of uniform flows. Steady uniform flows of monodisperse grains flowing on a rough bed are stable only if the Froude number Fr (the ratio of flow speed to surface wavespeed) is smaller than a threshold $Fr \approx 0.57$ (Forterre & Pouliquen 2003). Above this threshold, the flows are unstable to low-frequency perturbations below a cutoff frequency, but remain stable to higher-frequency perturbations (Forterre & Pouliquen 2003).

A stability analysis of the depth-averaged avalanche equations (e.g. Savage & Hutter 1989) with the basal friction law of Pouliquen (1999a) predicts that this instability occurs above a critical Froude number $Fr = 2/3$, but this model does not predict the cutoff frequency, instead predicting that the growth rate tends to a positive constant for high-frequency perturbations (Forterre & Pouliquen 2003). Both the critical Froude

number and the cutoff frequency are predicted by a stability analysis of the $\mu(I)$ -rheology (Forterre 2006), which is a full constitutive law for dense granular flows in which the friction μ is dependent on the inertial number I (GDR MiDi 2004; Jop *et al.* 2005, 2006). Depth integration of this $\mu(I)$ -rheology results in depth-averaged longitudinal viscous stresses, derived by Forterre (2006) and Gray & Edwards (2014) using two different approaches. When added into the depth-averaged avalanche equations these viscous stresses provide a prediction for the cutoff frequency for instability, although in the formulation of Forterre (2006) quantitative agreement is obtained only with an adjustable parameter. Gray & Edwards (2014) used their equations to construct the explicit thickness and velocity profiles for granular roll waves. These roll waves cannot be modelled by the full $\mu(I)$ -rheology due to its underlying ill posedness at high and low inertial numbers (Barker *et al.* 2015), but are observed in numerical solutions of a partially regularised form of the $\mu(I)$ -rheology (Barker & Gray 2017).

The monodisperse granular roll waves studied previously are an idealisation of the roll waves that occur in highly polydisperse geophysical flows. Such polydisperse granular flows have a tendency to segregate according to size. Several micro-mechanical explanations have been offered as to the cause of this segregation (Middleton 1970; Savage & Lun 1988; Gray & Thornton 2005; Hill & Tan 2014; van der Vaart *et al.* 2015; Jing *et al.* 2017) and, whilst the exact mechanism remains unclear (Staron & Phillips 2015), the common phenomenological effect is that large particles migrate towards the surface of a granular avalanche. This process is well captured by advection-segregation-diffusion equations (e.g. Bridgwater *et al.* 1985; Dolgunin & Ukolov 1995; Gray & Chugunov 2006; Gray & Ancy 2011; Fan *et al.* 2014; Gray 2018) when the underlying bulk velocity field is known.

In shearing granular avalanches the segregation of large grains to the surface causes an effective segregation in the streamwise direction. Larger particles are initially segregated to the flow surface, where the velocity is highest, and are then transported rapidly downstream towards the flow front. When this process is combined with frictional differences between the large and small grains there is a very rich variety of behaviour, for example the spontaneous self-channelisation of the flow and the formation of coarse-grained lateral levees (Félix & Thomas 2004; Johnson *et al.* 2012;

Kokelaar *et al.* 2014) and lobate finger-like channels (Pouliquen *et al.* 1997; Pouliquen & Vallance 1999; Woodhouse *et al.* 2012; Baker *et al.* 2016b), which increase the distances that geophysical mass flows travel. In shallow flows, this increased streamwise transport rate of large particles is captured by a depth-integrated segregation model (Gray & Kokelaar 2010a,b), derived by integrating the segregation equation of Gray & Chugunov (2006) through the flow depth. When combined with a depth-averaged avalanche model for the bulk mass and momentum – and a concentration-weighted basal friction law producing greater friction in coarse-rich regions (Pouliquen & Vallance 1999) – this depth-integrated segregation model predicts the formation of fingers and levees (Woodhouse *et al.* 2012). However, the system of Woodhouse *et al.* (2012) is mathematically ill posed, leading to numerical solutions that do not converge under grid refinement (Woodhouse *et al.* 2012). The equations are regularised by including a two-dimensional extension of the viscous terms of Gray & Edwards (2014) in the momentum balance (Baker *et al.* 2016a), leading to a well-posed predictive model for granular fingering (Baker *et al.* 2016b).

In this paper the flow kinematics of bidisperse roll waves are studied. In §2 the results of small-scale laboratory experiments are shown, which demonstrate an increased concentration of large particles at the crest of roll waves. A depth-averaged model for these bidisperse flows is presented in §3, which is similar to the fingering model of Baker *et al.* (2016b). In §4 this model is used to construct travelling-wave solutions for the roll waves, as well as solutions for the segregation kinematics in §5. In §6 the kinematics in more complex aperiodic roll waves are discussed.

2. Small-scale experiments

Experiments are carried out on a 3.3 m long chute, inclined at $\zeta = 29^\circ$ to the horizontal, with glass side walls 7.8 cm apart (figure 1). The base of the chute is roughened by attaching a single layer of glass beads, diameter 750 – 1000 μm , with double-sided tape. The flow consists of a bidisperse mixture of glass ballotini, consisting of small white (75–150 μm) and large green (200–250 μm) grains. These are both smaller than the beads on the bed, to produce no-slip conditions at the base, during flow, for both sets of particles (Pouliquen 1999a). An initially well-mixed sample is

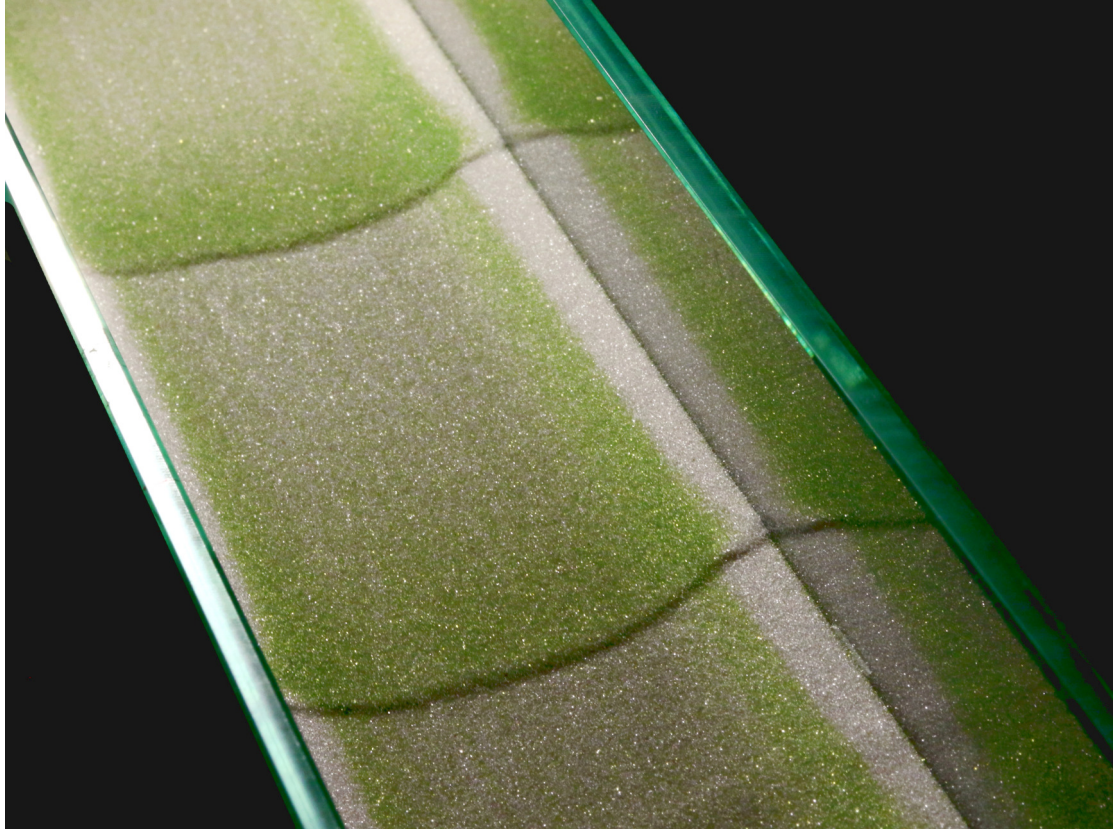


FIGURE 1: Oblique view showing a bidisperse roll wave experiment in a chute inclined at $\zeta = 29^\circ$. An initially homogeneous mixture consisting of 80% small glass ballotini (white, 75–150 μm diameter), 20% large ballotini (green, 200–250 μm) flows steadily through a hopper gate raised 3 mm from the bed. The steady flow near the inflow develops wave-like pulses further downstream, with large green particles rising to the surface of the flow and accumulating in higher concentrations at the fronts of the waves and at lower concentrations near in the troughs.

loaded into a hopper and released under two gates, one fixed at 3 mm above the bed and one movable to start and stop the flow.

As this latter gate is opened a green coarse-rich flow head rapidly forms as large particles are segregated to the surface and then preferentially transported to the front (Gray & Kokelaar 2010a,b). Behind the large rich front is an inversely graded region, with large particles concentrated at the top of the flow and small particles nearer the base. Near the gate this layer has uniform thickness, but approximately 1 m downstream (for the experiments shown here) it develops spatial and temporal instabilities. These small perturbations grow and merge into granular roll waves, which are free-surface waves that propagate faster than the bulk flow. Consequently, these waves catch up with the flow head, causing it to advance rapidly as each pulse reaches the front and more slowly between subsequent waves. Material is free to flow off the end of the chute, and, once the head has done this, the succeeding flow continues to

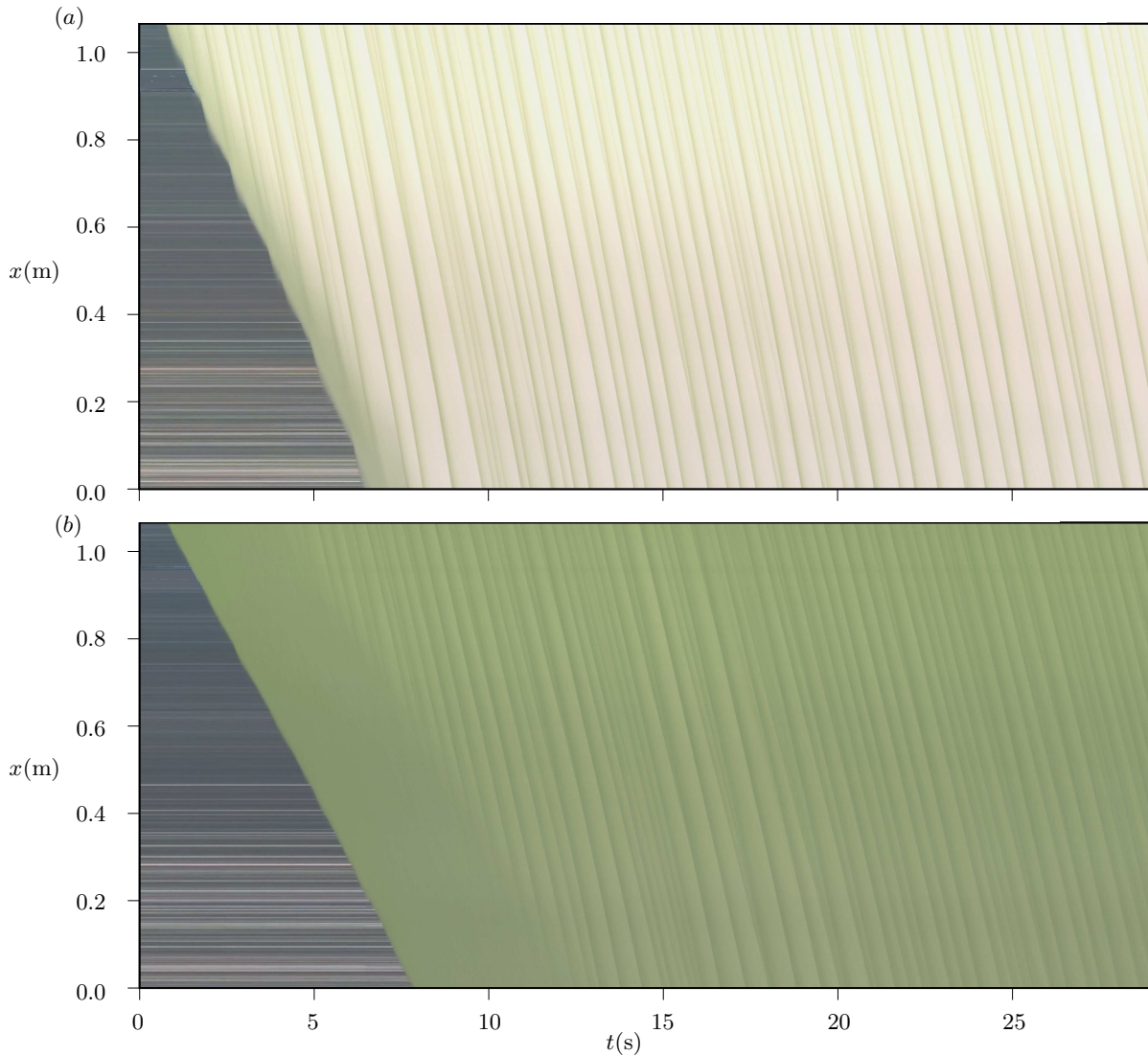


FIGURE 2: Aerial space-time plots for bidisperse mixtures consisting of (a) 80% small white ballotini (75–150 μm) 20% large green ballotini (200–250 μm) and b) 40% small 60% large particles. The plots are obtained by using a high-speed camera to capture a section of the chute from the outflow to approximately 1.05 m upstream. The central column of pixels from each image is then aligned next to each other to give the resulting figures. Straight lines represent the green coarse-rich crests of roll waves travelling at roughly constant velocities, faster than the initial flow head. Merging events correspond to where two lines intersect. Distances are given relative to the outflow.

develop roll waves (figure 1, supplementary movies 1 and 2) that are still merging and coarsening by the end of the channel (Razis *et al.* 2014). The slope angle and frictional properties of the grains are such that all material in the chute remains in motion. The resulting pulses are thus roll waves, as opposed to erosion-deposition waves (Edwards & Gray 2015), which are characterised by stationary regions between adjacent pulses, and occur at lower slope angles or with more frictional grains.

For an initial mixture consisting of 80% small particles, 20% large particles by volume, referred to as 80/20 from this point onwards (figure 1 and movie 1) the roll

waves are easily observable by the end of the chute, with each wave crest appearing green due to higher concentrations of large particles near the free surface than in the corresponding white troughs. Roll waves still develop in identical experiments using 40% fine and 60% coarse material (40/60, see supplementary movie 2), but their amplitude is much smaller. Both the initial flow head and the waves propagate slightly slower for the mixture with a higher proportion of large particles. This is consistent with the $\mu(I)$ -rheology, which suggests that for two steady uniform flows of otherwise similar material properties, the smaller particles will move faster than the larger grains. This is because to leading order the downslope and normal momentum balances (GDR MiDi 2004; Gray & Edwards 2014) imply that $\mu(I) = \tan \zeta$, where ζ is the slope angle, and hence that the inertial number I is equal to the same constant for both the large and small particles. The inertial number is defined as $I = \dot{\gamma}d/\sqrt{p/\rho_*}$, where $\dot{\gamma}$ is the shear rate, d is the particle diameter, p is the pressure and ρ_* is the density of the grains. It follows, that if the shear rate $\dot{\gamma}$ is approximated by the ratio of the depth-averaged velocity \bar{u} to the flow depth h , and the pressure p is assumed to be the same for both flows, the small particle velocity \bar{u}_{small} is related to that of the large particles \bar{u}_{large} by $\bar{u}_{small} = (d_{large}/d_{small})\bar{u}_{large}$. Since the large particles are bigger than the fines, $d_{large} > d_{small}$, it follows that $\bar{u}_{small} > \bar{u}_{large}$.

To investigate further, a high-speed colour camera (iPad Pro, Apple) is mounted perpendicular to the bed and used to capture images of the upper surface of the flow at 120 frames per second. A 1.05 m section of chute upstream from the outflow is recorded over a period of 25 s, and the central column of pixels from each image is extracted. These columns are then aligned next to each other to construct space-time plots of the flows (figure 2). The experiments are lit from directly above the chute to avoid introducing shadows, meaning the colours in figure 2 correspond directly to the colours of grains within a few grain diameters of the surface. The green lines in figure 2 represent the coarse-rich regions at the crest of waves, which are clearly visible in both of the mixtures shown. These are approximately straight lines, indicating that waves travel at a constant velocity u_w . In both flows there is slight variation in the speed of different waves, and faster waves may catch up with slower ones. This leads to merging events, which are visualised as the intersection of two lines. Averaging the speed of 20 non-coarsening waves, the

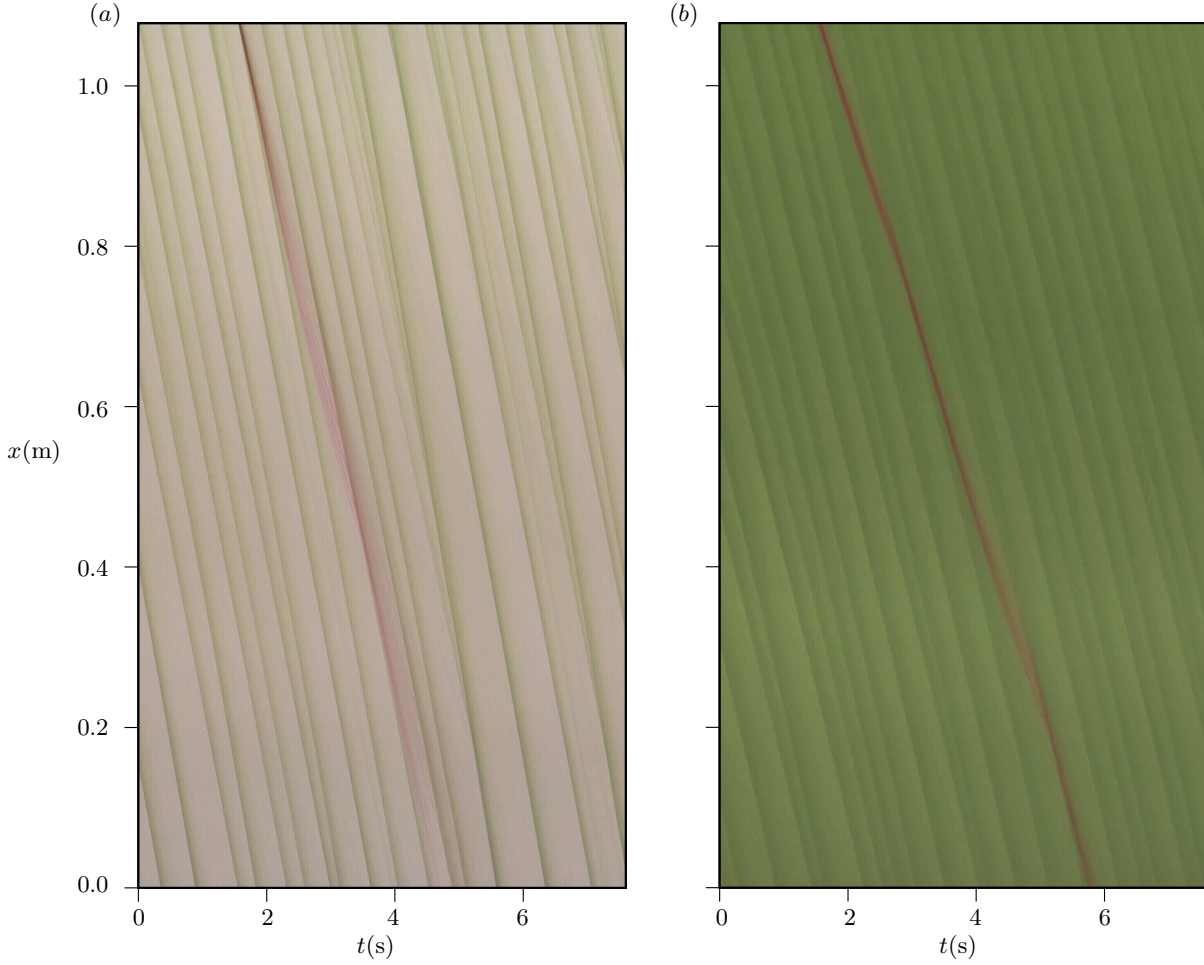


FIGURE 3: Aerial space-time plots for mixtures consisting of (a) 80% small white ballotini (75–150 μm), 20% large green ballotini (200–250 μm) and b) 40% small, 60% large, particles with red large particles (300 μm) released on the surface of the waves. The red particles travel backwards relative to the waves, and are compressed together when passing through the wave crests before being stretched out at the back of each wave.

speed $u_w = 0.42 \pm 0.035 \text{ ms}^{-1}$ is obtained for the 80/20 mixture (figure 2a) and $u_w = 0.34 \pm 0.02 \text{ ms}^{-1}$ for the 40/60 mixture (figure 2b). Thus flows with higher proportions of large particles produce waves that, on average, propagate slower. This qualitative difference has also been observed for a wide range of compositions from 100 % small to 100 % large particles. In both of the flows shown here the average wavelength is $\sim 0.2 \text{ m}$, though this varies significantly in space and time.

The flow front, visible on the left of figure 2, travels at less than half the speed of the waves behind it (approximate front speeds are 0.18 ms^{-1} and 0.15 ms^{-1} for the 80/20 and 40/60 mixes, respectively), meaning the waves catch up with the front and cause it to advance in a series of pulses. The coarse-rich nature of the flow head is particularly apparent for the 40/60 mixture, with a thick green band travelling downslope, growing in size as large particles are continuously sheared to the front.

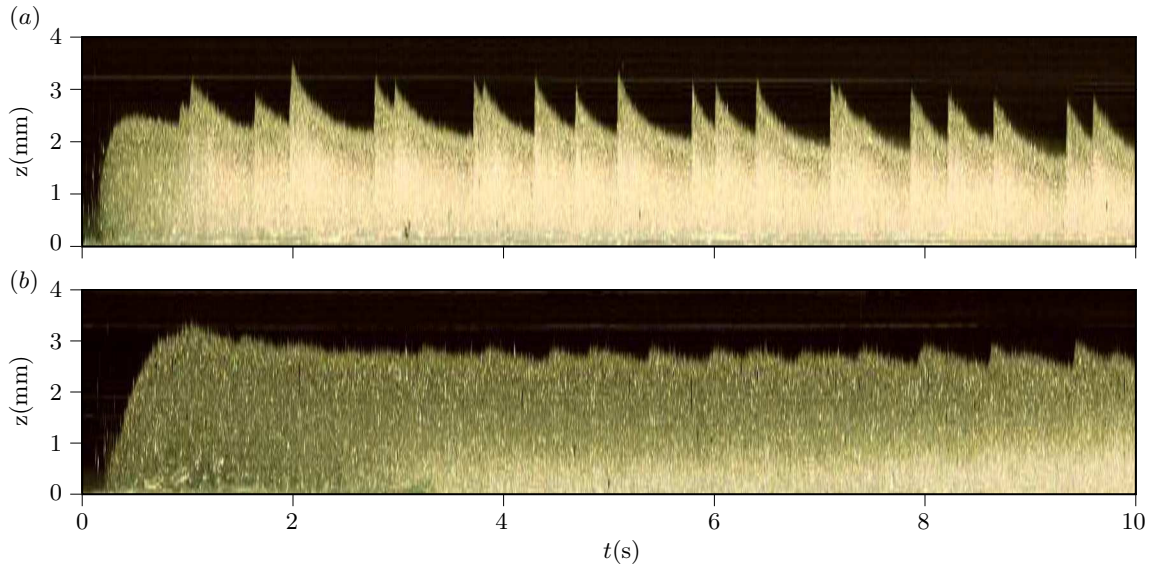


FIGURE 4: Internal space-time plots for bidisperse mixtures consisting of (a) 80% small white ballotini (75–150 μm), 20% large green ballotini (200–250 μm), and b) 40% small, 60% large particles. The plots are obtained by using a splitter plate and high-speed camera at the outflow to capture a vertical slice of the flow interior at each moment in time. Images are then aligned next to each other to give the resulting figures. In both cases a coarse-rich flow head is observed, followed by a mixing region and breaking size-segregation wave. Wave-like disturbances follow the flow front, with large green particles segregated to the surface, although these waves are much larger for higher concentrations of small particles (panel a).

To understand the kinematics responsible for the formation of the coarse rich wave fronts present in both mixtures, another experiment is performed by releasing a small quantity of large red beads (300 μm) on top of existing waves that have developed in an otherwise identical experiment. These red grains are similar in diameter to the green ones, and so act as a tracer for large particles in the flow. These red tracers move more slowly than the roll waves for both 80/20 and 60/40 mixtures, as evidenced by space-time plots (figure 3). This is consistent with Dressler’s description of roll waves as waves travelling faster than all fluid particles in the flow (Dressler 1949). In the experiments presented in this paper, the high concentration of large particles at the wave fronts is not caused by the individual particles accumulating there, because these particles move backwards relative to the waves (figure 3). Instead, large particles travel slowly backwards (relative to the wave) through the crest and are then rapidly transported down the leeward side of the wave. This results in a flux of large grains relative to the roll waves that is converging at a wave crest, increasing the concentration of large grains there, but diverging between waves, which creates a concertina effect in the concentration. The tracer grains dissipate as they move downslope due to diffusion and dispersion, particularly for the 80/20 mixture (figure 3a).

The flow interior is examined by splitting the flow along its centreline with a 0.1 mm thick microscope cover slip at the end of the chute, allowing half of the flow to fall away and the other half to continue on an extended chute (see Barker & Gray 2017). Space-time plots filmed through this cover slip at 300 frames per second, using a Teledyne DALSA Genie HM1400 camera, allow the interior grain size distribution to be observed with minimal wall effects (figure 4). A coarse-rich front can clearly be observed for both the 80/20 and 40/60 mixtures, and is much larger for the flow with more large particles (figure 4b). Immediately behind the front is a region of mixed grains, a breaking size-segregation wave (Thornton & Gray 2008; Gray & Ancey 2009; Johnson *et al.* 2012; Gajjar *et al.* 2016). Roll wave instabilities follow behind the flow front, of amplitude ~ 1 mm for the 80/20 mixture and ~ 0.5 mm for the 40/60 mixture. For both mixtures large green particles are clearly concentrated at the flow surface (inverse grading). Although the higher concentration of large particles at the wave crests is robustly observed in the oblique views (figure 1) and aerial space-time plots (figures 2 and 3), it is less clear from the internal space-time plots.

3. A depth-averaged particle size-segregation and bulk flow model

The experimental flows of §2 have a vertical length scale of ~ 1 mm, much smaller than the downslope length scale of ~ 1 m. This shallowness is now exploited by applying a depth-averaged modelling approach to the flows.

3.1. A depth-averaged model for particle size segregation

A Cartesian coordinate system Oxz is defined at an angle ζ to the horizontal, with the x -axis pointing in the downslope direction and the z -axis aligned with the upward-facing normal (figure 5). A mass of granular material of thickness $h(x, t)$ is assumed to lie between a flat, rigid base at $z = 0$ and free surface $z = h(x, t)$. The concentration of small particles per unit granular volume is denoted ϕ , and the corresponding concentration of large particles is $(1 - \phi)$. The concentration ϕ is governed by an advection-segregation-diffusion equation (e.g. Bridgwater *et al.* 1985; Dolgunin & Ukolov 1995; Gray & Chugunov 2006; Gray 2018)

$$\frac{\partial \phi}{\partial t} + \frac{\partial}{\partial x}(\phi u) + \frac{\partial}{\partial z}(\phi w) - \frac{\partial}{\partial z}(q\phi(1 - \phi)) = \frac{\partial}{\partial z} \left(D \frac{\partial \phi}{\partial z} \right), \quad (3.1)$$

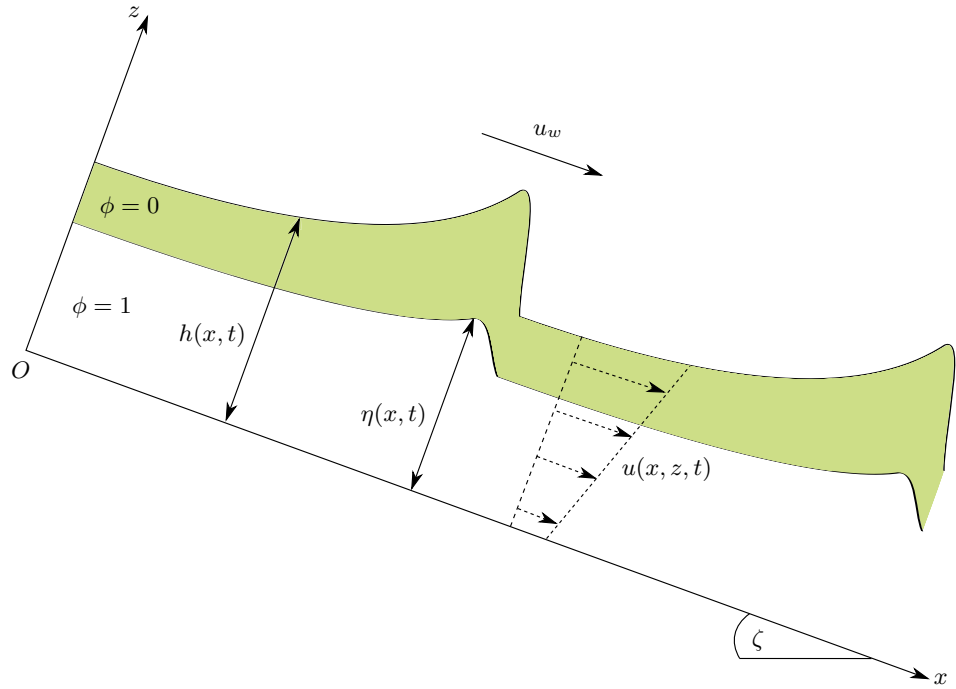


FIGURE 5: Schematic diagram of the coordinate axes Oxz aligned at an angle ζ to the horizontal, so that the x -axis points downslope and the z -axis is aligned with the upward-facing normal. The granular material is assumed to have thickness $h(x, t)$, downslope velocity $u(x, z, t)$ and consists of large green particles lying above small white particles. The interface between the two regions is located at height $\eta = h\bar{\phi}$, where $\bar{\phi}$ denotes the depth-averaged concentration of small particles. Roll wave disturbances move at a speed u_w and are faster than the bulk flow.

where $\mathbf{u} = (u, w)$ are the bulk velocity components in the downslope and normal directions. The first term on the left-hand side is the time rate of change of the small particle concentration, the second and third terms describe advection by the bulk flow and the fourth term accounts for slope normal segregation. The quadratic flux in the segregation term ensures that the segregation stops when either the large or the small particles reach a pure phase and the factor q determines the strength of the segregation. More complicated flux functions are possible, for example, the asymmetry between large and small particle segregation velocities can be included by using a cubic flux (Gajjar & Gray 2014; van der Vaart *et al.* 2015) and the segregation rate q may depend explicitly on the grain size ratio and the shear rate (Dolgunin & Ukolov 1995; Marks *et al.* 2012; Schlick *et al.* 2015) or inertial number (Gray 2018). The right-hand side of equation (3.1) describes the process of diffusive remixing of the grains through the depth of the flow. The diffusivity D may in general depend on the flow variables but is assumed constant here.

The segregation equation (3.1) can be integrated through the avalanche thickness using Leibniz' rule to interchange the order of integration and differentiation, and the

condition that there is no flux of either large or small particles across the surface and base of the flow (see e.g. Gray & Kokelaar 2010a,b). This implies that

$$\frac{\partial}{\partial t}(h\bar{\phi}) + \frac{\partial}{\partial x}(h\bar{\phi u}) = 0, \quad (3.2)$$

where by definition the depth-averaged concentration and the depth-averaged flux of small particles are

$$\bar{\phi}(x, t) = \frac{1}{h} \int_0^h \phi(x, z, t) dz, \quad \text{and} \quad \bar{\phi u}(x, t) = \frac{1}{h} \int_0^h \phi(x, z, t) u(x, z, t) dz, \quad (3.3)$$

respectively. In the depth-integration process the segregation and diffusion terms disappear in equation (3.2), however, their physical effect is still incorporated via the integrals (3.3), because ϕ still evolves according to the full segregation equation (3.1).

At this stage (3.2) is still exact and no approximations have been made. To turn the integro-differential equation (3.2) into a partial differential equation, Gray & Kokelaar (2010a,b) approximated the integrals (3.3) by assuming that (i) the segregation process dominated over the diffusion and (ii) that the segregation was sufficiently rapid that it could be considered to be instantaneous. As a result, the concentration ϕ could be approximated by a perfectly inversely graded profile, i.e all the large particles over all the small grains. These assumptions are consistent with the internal space-time plots (figure 4), which show a relatively sharp interface between large and small particles, as well as sharp changes in the concentration as the roll waves pass by. Following, Gray & Kokelaar (2010a,b) the concentration profile is therefore assumed to be

$$\phi(x, z, t) = \begin{cases} 0, & z > \eta, \\ 1, & z < \eta, \end{cases} \quad (3.4)$$

where η is the height of the sharp interface between the large and small particles as shown in figure 5. For simplicity Gray & Kokelaar (2010a,b) assumed that the velocity profile was linear with depth

$$u(x, z, t) = \bar{u} [(1 - A) + 2Az/h], \quad (3.5)$$

where \bar{u} is the depth-averaged velocity and the parameter $A \in [0, 1]$ controls the degree of shear and basal slip. The advantage of assumptions (3.4) and (3.5) is that the integrals (3.3) are particularly simple and can be explicitly evaluated to give

$$\bar{\phi}(x, t) = \frac{\eta}{h}, \quad \text{and} \quad \bar{\phi u}(x, t) = \bar{\phi} \bar{u} - \bar{u} A \bar{\phi} (1 - \bar{\phi}). \quad (3.6)$$

Substituting (3.6) into the depth-averaged segregation equation (3.2) yields what Gray & Kokelaar (2010a,b) termed the large particle transport equation

$$\frac{\partial}{\partial t}(h\bar{\phi}) + \frac{\partial}{\partial x}(h\bar{\phi}\bar{u}) - \frac{\partial}{\partial x}(h\bar{u}G(\bar{\phi})) = 0, \quad (3.7)$$

where the flux function

$$G(\bar{\phi}) = A\bar{\phi}(1 - \bar{\phi}), \quad (3.8)$$

is quadratic in the depth-averaged concentration. Assuming the thickness h is constant, the first term in (3.7) is the time rate of change of the depth-averaged concentration of small particles $\bar{\phi}$, the second term is the lateral transport of small particles due to the bulk flow and the final term is a reduction in the transport rate of fines due to velocity shear. Physically, equation (3.7) describes the process in which small particles are rapidly segregated to the bottom of the flow, where the velocity is lowest, and are therefore transported downslope slower than average.

Since the depth-averaged concentration of large particles is $1 - \bar{\phi}$, equation (3.7) may also be viewed as an equation that describes the preferential transport of large particles downslope. The physical mechanism is simple, large grains are rapidly segregated to the surface of the flow, where the velocity is greatest, and therefore move downslope faster than average. The final term in (3.7) has a quadratic flux $\bar{\phi}(1 - \bar{\phi})$ that is similar to the $\phi(1 - \phi)$ structure in the full segregation equation (3.1). Here, however, the segregation is in the lateral x -direction, rather than through the depth of the flow. It is surprising that particle segregation through the depth of the flow, combined with velocity shear, effectively generates a secondary lateral segregation mechanism. This lateral segregation is, however, a very strong effect that gives rise to commonly observed features such as the formation of bouldery fronts in geophysical mass flows, segregation-induced fingering instabilities and large particle rich levees (Pouliquen *et al.* 1997; Pouliquen & Vallance 1999; Félix & Thomas 2004; Woodhouse *et al.* 2012; Johnson *et al.* 2012; Kokelaar *et al.* 2014; Baker *et al.* 2016b).

Gray & Kokelaar's (2010a,b) derivation of the large particle transport equation (3.7) is very simple and captures the key physical effect. It is, however, possible to explore different approximations for the integrals. In their study of segregation induced fingering, Baker *et al.* (2016b) derived the equivalent large particle transport equation assuming Bagnold flow (GDR MiDi 2004). Instead of the flux function G

being symmetric about $\bar{\phi} = 1/2$ and having a maximum there, as in the quadratic case, for Bagnold $G = \frac{2}{3}(1-\bar{\phi})(1-(1-\bar{\phi})^{3/2})$, which is asymmetric with a maximum skewed towards lower concentrations of fines. This reflects the fact that the velocity gradient is stronger at the bottom of the avalanche where the small particles accumulate. In figure 7 of Baker *et al.* (2016b) a comparison is shown between the linear velocity (3.5) and the Bagnold profile. For $A = 6/7$ the linear velocity profile is close to that of Bagnold, and there is surprisingly little difference between the resulting flux curves. For simplicity, Baker *et al.* (2016b) therefore used the linear profile in their simulations, which made the code more stable at high concentrations, since it was no longer necessary to take the square root close to zero. The linear velocity profile (3.5) may therefore be thought of as an approximation to a more complex velocity profile with no slip at the base. Even more complex representations are possible. For instance, if one set of particles is considerably more frictional than the others, this may have an important feedback on the Bagnold-like velocity profile that develops in the two segregated media (Rognon *et al.* 2007). This can, in principle, also be built into the model, but it will become increasingly complex and harder to solve. In the interest of simplicity, in this paper the linear velocity profile is retained and A is treated as a control parameter with higher values corresponding to more highly sheared and segregated flows, with consequently greater preferential downslope transport of large particles.

3.2. A depth-averaged model for the bulk flow

To solve for the depth-averaged concentration $\bar{\phi}$, the large particle transport equation (3.7) is combined with a shallow-water model for the bulk thickness h and depth-averaged velocity \bar{u} . Following Gray & Edwards (2014), conservation of mass and momentum are given by the equations

$$\frac{\partial h}{\partial t} + \frac{\partial}{\partial x}(h\bar{u}) = 0, \quad (3.9)$$

$$\frac{\partial}{\partial t}(h\bar{u}) + \frac{\partial}{\partial x}(\chi h\bar{u}^2) + \frac{\partial}{\partial x}\left(\frac{1}{2}gh^2 \cos \zeta\right) = ghS + \frac{\partial}{\partial x}\left(\nu h^{3/2}\frac{\partial \bar{u}}{\partial x}\right), \quad (3.10)$$

where g is the constant of gravitational acceleration, ν is a coefficient in the depth-averaged granular viscosity $\nu h^{1/2}/2$, discussed later, and the shape factor $\chi = \overline{u^2}/\bar{u}^2$ depends on the velocity shear profile. For simple shear ($A = 1$) this implies $\chi = 4/3$, while for plug flow ($A = 0$) the shape factor $\chi = 1$. For simplicity, χ is assumed to be

equal to unity in this paper, as, in general, non-unity values change the characteristic structure of the inviscid equations and cause problems near zero-thickness regions (Hogg & Pritchard 2004; Saingier *et al.* 2016).

The source term

$$S = \cos \zeta (\tan \zeta - \mu_b \operatorname{sgn}(\bar{u})), \quad (3.11)$$

where sgn is the sign function, represents the downslope component of gravity driving the flow, and the effective basal friction opposing the direction of motion. For a monodisperse granular material the basal friction coefficient μ_b can be measured empirically, with the dynamic law of Pouliquen & Forterre (2002),

$$\mu_b(h, Fr) = \mu_1 + \frac{\mu_2 - \mu_1}{\beta h / (\mathcal{L} Fr) + 1}, \quad Fr > \beta, \quad (3.12)$$

where the Froude number

$$Fr = \frac{|\bar{u}|}{\sqrt{gh \cos \zeta}}, \quad (3.13)$$

is the ratio of the speed of the bulk flow to the speed of surface gravity waves. The parameters $\mu_1 = \tan \zeta_1$ and $\mu_2 = \tan \zeta_2$ are constants, where angles ζ_1 and ζ_2 correspond to the minimum and maximum slope angles for which steady uniform flows are observed. The length scale \mathcal{L} and dimensionless constant β depend on the granular material properties as well as the bed composition (Pouliquen 1999a; Goujon *et al.* 2003). Interestingly, Gray & Edwards (2014) showed by depth averaging the $\mu(I)$ -rheology (GDR MiDi 2004; Jop *et al.* 2005, 2006), subject to a no-slip condition at the base, the classical inviscid shallow-water-like avalanche equations (3.9)–(3.10) (with $\nu = 0$) emerge at leading order with an effective basal friction given by (3.12). For rough beds, with no slip at the base, the friction law (3.12) may therefore be thought of as an integrated effect of the internal rheology, rather than a Coulombic basal sliding friction. The effective basal friction (3.12) is vital in determining the shape of the granular roll waves (Gray & Edwards 2014; Razis *et al.* 2014; Edwards & Gray 2015) as well as the critical Froude number $Fr_c = 2/3$ for the instability (Forterre & Pouliquen 2003; Forterre 2006). Although the viscous terms in (3.9)–(3.10) are much smaller in magnitude, they are also needed in order to predict the correct cutoff frequency/wavenumber (Gray & Edwards 2014; Barker & Gray 2017) and obtain the right coarsening dynamics.

There is currently no widely accepted law for the effective basal friction of bidisperse

flows on a rough bed. Clearly the frictional properties of the mixture should strongly depend on those of its individual constituents (large and small particles), as well as the relative amount of each of these constituents in the flow. The dependence on concentration is evident from the experimental results of §2, where the bulk wave properties (amplitude and wavespeeds) depend on the composition of the mixture. In order to simplify the dynamics of the problem, this paper uses the monodisperse friction law of Pouliquen & Forterre (2002), given in equation (3.12). The changing composition in different experiments is reflected in the coefficients by using a weighted average of the large and small particle friction coefficients based on the initial concentration of the particles in the hopper $\bar{\phi}_0$, i.e.

$$\mu_1(\bar{\phi}_0) = \tan(\bar{\phi}_0\zeta_1^S + (1 - \bar{\phi}_0)\zeta_1^L), \quad (3.14)$$

$$\mu_2(\bar{\phi}_0) = \tan(\bar{\phi}_0\zeta_2^S + (1 - \bar{\phi}_0)\zeta_2^L), \quad (3.15)$$

$$\beta(\bar{\phi}_0) = \bar{\phi}_0\beta^S + (1 - \bar{\phi}_0)\beta^L, \quad (3.16)$$

$$\mathcal{L}(\bar{\phi}_0) = \bar{\phi}_0\mathcal{L}^S + (1 - \bar{\phi}_0)\mathcal{L}^L, \quad (3.17)$$

where the superscripts S, L denote the parameter values for pure small and large particles, respectively. These have been estimated for the laboratory set-up of figures 1–4, and are given in table 1, along with the other parameters that are kept constant in this paper. This basal friction law reduces to the monodisperse law when $\bar{\phi}_0$ equals zero and unity. The chute and friction angles satisfy

$$\zeta_1^S < \zeta_1^L < \zeta < \zeta_2^S < \zeta_2^L, \quad (3.18)$$

which allows for steady uniform flows of either species in a pure phase and also captures the higher effective friction of the larger grains. The linear weightings in (3.14)–(3.17) are a highly simplified description; in reality the effective friction is expected to depend on the local solid volume fraction $\bar{\phi}(x, t)$, not just the mean solid volume fraction $\bar{\phi}_0$. A dependency of friction on the local solid volume fraction was required by Woodhouse *et al.* (2012) and Baker *et al.* (2016*b*) to model segregation-induced granular fingering, but, unlike in the case of fingering, this local dependency is not central to the formation of roll waves. The friction law (3.14)–(3.17) used here is therefore sufficient to capture at least the kinematics of bidisperse roll waves.

The final expression on the right-hand side of the momentum balance (3.10) is a viscous term, after Gray & Edwards (2014). The coefficient ν is given for a monodisperse

$\zeta = 29.0^\circ$	$\zeta_1^S = 20.0^\circ$	$\zeta_2^S = 31.0^\circ$	$\beta^S = 0.150$	$\mathcal{L}^S = 3.0 \times 10^{-4}$ m
$\chi = 1$	$\zeta_1^L = 23.0^\circ$	$\zeta_2^L = 34.0^\circ$	$\beta^L = 0.150$	$\mathcal{L}^L = 5.0 \times 10^{-4}$ m

TABLE 1: Material parameters that will remain constant throughout this paper

flow by Gray & Edwards (2014) as

$$\nu = \frac{2\mathcal{L}\gamma\sqrt{g}\sin\zeta}{9\beta\sqrt{\cos\zeta}}, \quad (3.19)$$

where the constant

$$\gamma = \frac{\mu_2 - \tan\zeta}{\tan\zeta - \mu_1}, \quad (3.20)$$

is positive for slope angles $\zeta_1 < \zeta < \zeta_2$ where monodisperse steady uniform flows are possible. As in the basal friction coefficient, the definition (3.19) is extended to depend on the mean concentration by substituting (3.14)–(3.17) into (3.19) and (3.20), which ensures $\nu > 0$ and the equations are well posed for all $\bar{\phi}_0$ and angles in the range (3.18).

With these definitions of the effective friction (3.12) and the coefficient in the viscosity (3.19), the mass and momentum balance equations (3.9) and (3.10) form a closed system for h and \bar{u} . This system is very similar to the depth-averaged $\mu(I)$ -rheology of Gray & Edwards (2014), but with a dependence on the constant $\bar{\phi}_0$. With h and \bar{u} determined, the large particle transport equation (3.7) can be used to solve for the evolution of the depth-averaged concentration of small particles $\bar{\phi}$. The model is uncoupled in the sense that there is no dependence of the bulk flow equations (3.9) and (3.10) on the local concentration $\bar{\phi}$.

4. Inviscid travelling-wave solutions for the bulk

Motivated by the experimental observations of constant wavespeeds, steady travelling-wave solutions are now constructed to the bulk mass and momentum equations, (3.9) and (3.10). As noted previously, the transport equation (3.7) decouples and is solved *a posteriori*. In-plane deviatoric stresses, characterised by the viscous term in the momentum equation, are critical for predicting the correct growth rate and cutoff frequency of granular roll waves (Gray & Edwards 2014), but they are relatively small terms that do not change the essential shape of the fully developed waves. To gain greater insight the viscous terms are therefore neglected by setting

$\nu = 0$ in (3.10). This leads to a hyperbolic system of equations closely resembling the classical shallow-water theory investigated by Dressler (1949), who used a Chezy drag term and constructed periodic roll waves by piecing together discontinuous segments through suitable shock conditions. A similar approach is adopted here, but it is also shown how to construct the equivalent viscous solutions ($\nu > 0$) in appendix A.

4.1. *Solution procedure*

Introducing a travelling coordinate $\xi = x - u_w t$ moving at constant speed u_w and seeking steady travelling-wave solutions, the bulk governing equations reduce to

$$\frac{d}{d\xi}(h(\bar{u} - u_w)) = 0, \quad (4.1)$$

$$\frac{d}{d\xi}(h\bar{u}(\bar{u} - u_w)) + \frac{d}{d\xi}\left(\frac{1}{2}gh^2 \cos \zeta\right) = gh \cos \zeta(\tan \zeta - \mu_b), \quad (4.2)$$

where the depth-averaged velocity \bar{u} is assumed to be positive. The mass balance (3.9) integrates directly to give

$$h(u_w - \bar{u}) = Q_1, \quad (4.3)$$

where the constant Q_1 , corresponding to the upstream flux of particles in the frame moving with the wave, is assumed positive to ensure that waves travel faster than the bulk flow. Substituting (4.3) into the momentum balance equation (4.2) and rearranging gives the first-order Ordinary Differential Equation (ODE)

$$\frac{dh}{d\xi} = \frac{gh^3 \cos \zeta(\tan \zeta - \mu_b)}{gh^3 \cos \zeta - Q_1^2}, \quad (4.4)$$

where the Froude number dependence in the coefficient μ_b (3.12) can be written in terms of h , u_w and Q_1 using (3.13) and (4.3). Equation (4.4) therefore defines an autonomous ODE for the flow thickness h , although both constants u_w and Q_1 are unknown at this stage. A single roll wave profile can be constructed by integrating (4.4) from the wave trough to its peak, and periodic wavetrains are then formed by applying jump conditions (see e.g. Chadwick 1976) for h and \bar{u} to join the peak of one wave to the trough of the next. For a shock moving at velocity u_w , the depth-averaged mass and momentum jump conditions imply

$$h^+(\bar{u}^+ - u_w) = h^-(\bar{u}^- - u_w), \quad (4.5)$$

$$h^+\bar{u}^+(\bar{u}^+ - u_w) + \frac{1}{2}g(h^+)^2 \cos \zeta = h^-\bar{u}^-(\bar{u}^- - u_w) + \frac{1}{2}g(h^-)^2 \cos \zeta, \quad (4.6)$$

where ‘+’ denotes quantities at the forward side of the shock and ‘−’ at the backward side, which are assumed to represent the wave trough and peak respectively. For the travelling waves considered here, (4.5) implies that the constant Q_1 in (4.3) is the same on either side of the shock. All the velocities can therefore be eliminated in the momentum jump condition (4.6) by using (4.3) and (4.5). Neglecting the trivial root $h^+ = h^-$, it follows that the thicknesses satisfy the quadratic equation

$$gh^+h^- \cos \zeta (h^+ + h^-) - 2Q_1^2 = 0. \quad (4.7)$$

Taking the positive roots to ensure that thicknesses remain positive everywhere, the wave heights on either side of the shock are related by

$$h^+ = \frac{-h^- + \sqrt{(h^-)^2 + \frac{8Q_1^2}{gh^- \cos \zeta}}}{2}, \quad (4.8)$$

$$h^- = \frac{-h^+ + \sqrt{(h^+)^2 + \frac{8Q_1^2}{gh^+ \cos \zeta}}}{2}. \quad (4.9)$$

The smooth part of the solution to (4.4) for the roll wave profile is the one in which the forward thickness is less than the backward thickness, i.e. $h^+ < h^-$. Using this inequality in (4.8) and (4.9) it follows that the thickness must pass through the critical point

$$h^* = \left(\frac{Q_1^2}{g \cos \zeta} \right)^{1/3}, \quad (4.10)$$

where the denominator of the ODE (4.4) is zero, since $h^* \in [h^+, h^-]$. In order to obtain smooth solutions in the neighbourhood of h^* , the numerator must also be zero at this critical point. This implies a balance between the downslope component of gravity and basal friction at the critical point,

$$\mu_b(h^*, Fr^*) = \tan \zeta, \quad (4.11)$$

where $Fr^* = \bar{u}^* / \sqrt{gh^* \cos \zeta}$ is the corresponding Froude number and \bar{u}^* the velocity at this critical point. From the friction law (3.12), it follows that

$$Fr^* = \frac{\beta h^*}{\mathcal{L}\gamma}, \quad (4.12)$$

where the constant γ is defined in (3.20), and hence that

$$\bar{u}^* = \frac{\beta h^{*3/2} \sqrt{g \cos \zeta}}{\mathcal{L}\gamma}. \quad (4.13)$$

Evaluating (4.3) at the critical point and using the definition (4.10) allows u_w and Q_1 to be written in terms of h^* as

$$u_w = \bar{u}^* + \sqrt{gh^* \cos \zeta} = \bar{u}^* \left(1 + \frac{1}{Fr^*} \right), \quad (4.14)$$

$$Q_1 = h^{*3/2} \sqrt{g \cos \zeta} = \frac{h^* \bar{u}^*}{Fr^*}. \quad (4.15)$$

Equation (4.3) may then be rearranged to write the depth-averaged velocity as

$$\bar{u} = \bar{u}^* \left(1 + \frac{1}{Fr^*} - \frac{h^*}{Fr^* h} \right). \quad (4.16)$$

Substituting the friction law (3.12) into the ODE (4.4) and using the definition of the Froude number and equations (4.13) and (4.16) to eliminate \bar{u}^* and \bar{u} implies that the ODE becomes

$$\frac{dh}{d\xi} = \frac{(\mu_2 - \tan \zeta) h^3 f_1(h)}{(h^3 - (h^*)^3) f_2(h)}, \quad (4.17)$$

where

$$f_1(h) \equiv \left(\frac{h}{h^*} \right)^{5/2} - \left(1 + \frac{1}{Fr^*} \right) \left(\frac{h}{h^*} \right) + \frac{1}{Fr^*}, \quad (4.18)$$

$$f_2(h) \equiv \gamma \left(\frac{h}{h^*} \right)^{5/2} + \left(1 + \frac{1}{Fr^*} \right) \left(\frac{h}{h^*} \right) - \frac{1}{Fr^*}. \quad (4.19)$$

Since both the numerator and denominator of (4.17) are zero at the critical point $h = h^*$, the gradient is evaluated here using L'Hôpital's rule,

$$\left. \frac{dh}{d\xi} \right|_{h=h^*} = \frac{\mu_2 - \tan \zeta}{2Fr^*(\gamma + 1)} \left(Fr^* - \frac{2}{3} \right), \quad (4.20)$$

which is positive when $Fr^* > 2/3$, as required for roll waves. This is the same condition for instability of a steady uniform flow of thickness h^* (Forterre & Pouliquen 2003; Gray & Edwards 2014) and, using (4.12), defines a minimum critical thickness for roll wave solutions to be possible,

$$h^* > h_{min}^* \equiv \frac{2\mathcal{L}\gamma}{3\beta}. \quad (4.21)$$

In fact, the gradient $dh/d\xi$ must remain positive for all values of $h^+ < h < h^-$, not just at the critical point, in order to construct appropriate solutions. Examining the functional form of (4.17), it can be seen that this depends on the two expressions (4.18) and (4.19) making up parts of the numerator and denominator, respectively. Clearly $f_1(h^*) = 0$, and straightforward algebra shows that there is also second root of f_1 that is strictly less than h^* when $Fr^* > 2/3$. Let this root be denoted h_{min} , which can be reliably found with standard root-finding algorithms. Again, simple algebra reveals

that $f_2(h) > 0$ for $h \geq h_{min}$, and combining these results implies that $dh/d\xi > 0$ for all $h > h_{min}$. Rearranging equation (4.16) shows that the depth-averaged velocity is only positive for

$$h > h_{zero} \equiv \frac{h^*}{1 + Fr^*}. \quad (4.22)$$

Since $f_1(h_{zero}) > 0$ it follows that $h_{zero} < h_{min}$, meaning that both \bar{u} and $dh/d\xi$ are positive for $h > h_{min}$. The value h_{min} therefore provides a lower thickness bound for roll wave profiles with a given h^* , and the construction procedure can be summarised as follows: For a given critical thickness h^* satisfying (4.21), pick a minimum (trough) height h^+ in the range $h_{min} < h^+ < h^*$ and use the jump condition (4.9) with (4.15) to calculate the corresponding maximum (peak) height h^- . Then integrate (4.17) in ξ , starting from initial condition $h(0) = h^+$ and stopping when $h = h^-$, using (4.20) to integrate through the critical point. Finally, the depth-averaged velocity $\bar{u}(\xi)$ is obtained by using (4.16).

Figure 6 shows an example family of roll wave solutions, all computed using a critical thickness $h^* = 0.002$ m and mean concentration $\bar{\phi}_0 = 0.5$. All of these waves travel at the same velocity u_w , determined by (4.14), but have differing amplitudes and wavelengths depending on the forward flow thickness h^+ chosen. For h^+ close to h^* the waves have very small amplitudes and short wavelengths, but these both increase as h^+ decreases. As the trough reaches its minimum value $h^+ \rightarrow h_{min}$, the amplitude tends to the constant $h_{max} - h_{min}$, where h_{max} is the thickness calculated by substituting h_{min} into the jump condition (4.7).

4.2. Relation to inflow conditions

The method described above provides a systematic way to construct families of roll wave solutions that all travel at the same speed. This is not, however, what is observed experimentally, where constant inflow conditions lead to different velocity waves that consequently merge and coarsen as they move downstream. To directly relate the travelling-wave solutions of §4.1 to the disturbances that form in chute-flow experiments solutions are now considered that have the same flux in a stationary (laboratory) frame. Assuming that there is a steady uniform upstream flow of thickness h_0 and velocity \bar{u}_0 , which are related by replacing \bar{u}^* and h^* by \bar{u}_0 and h_0 in (4.13),

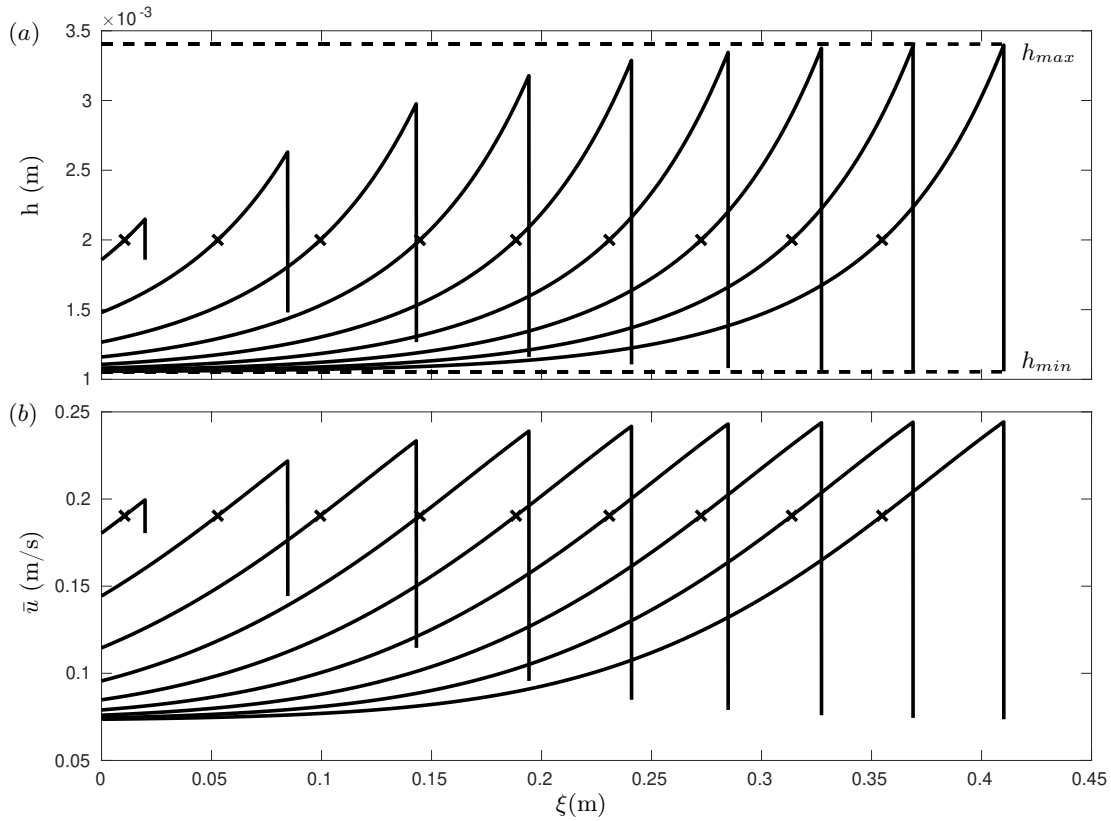


FIGURE 6: An example family of roll waves all having the same critical thickness $h^* = 0.002$ m and mean concentration $\bar{\phi}_0 = 0.5$ but varying minimum thicknesses h^+ . All of the waves shown travel at the same velocity u_w . (a) shows the thickness profile, with dotted lines denoting the absolute minimum and maximum thicknesses, h_{min} and h_{max} respectively, for this value of h^* . (b) shows the corresponding depth-averaged velocity \bar{u} . Crosses represent the critical point on both graphs. For clarity only one period is shown for each wave, but periodic trains are formed by connecting many such profiles.

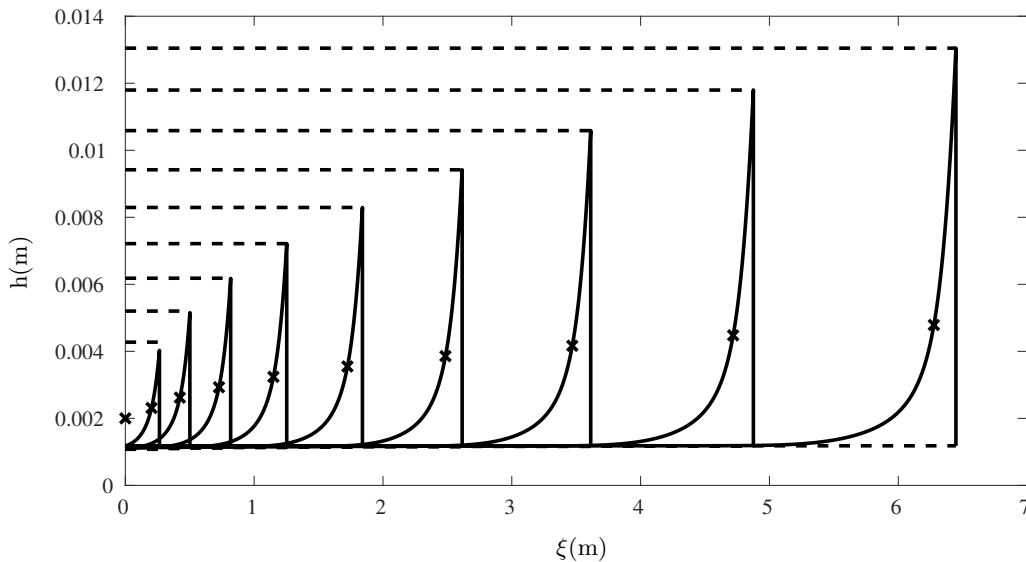


FIGURE 7: Family of roll wave solutions resulting from a steady uniform inflow of thickness $h_0 = 2$ mm for a mean concentration $\bar{\phi}_0 = 0.5$. Crosses denote the critical thickness h^* , and dashed lines the theoretical absolute minimum and maximum thicknesses, h_{min} and h_{max} respectively, for each h^* .

the upstream flux is constant in space and time and given by

$$q_0 = h_0 \bar{u}_0 = \frac{\beta \sqrt{g \cos \zeta}}{\mathcal{L} \gamma} h_0^{5/2}. \quad (4.23)$$

This flux depends on the mean concentration $\bar{\phi}_0$ through the coefficients β , \mathcal{L} and γ . A periodic train of roll waves forming downstream of this flow must have the same average flux, which for the travelling waves is given by the average flux across one wavelength Λ ,

$$q = \frac{1}{\Lambda} \int_0^\Lambda h(\xi) \bar{u}(\xi) \, d\xi. \quad (4.24)$$

Considering this average flux as a function of the critical and minimum wave thicknesses, the problem reduces to finding the pairs h^* and h^+ such that $q(h^*, h^+) = q_0$. For a fixed h^* , q is a monotonically increasing function of the trough thickness h^+ , so smaller-amplitude waves, despite having lower peak fluxes than larger waves, actually have greater average fluxes. The wave amplitude decreases to zero as $h^+ \rightarrow h^*$, and the mean flux tends to its maximum value for a given h^* , say $q_{max}(h^*)$, which corresponds to a steady uniform flow of thickness h^* , i.e.

$$q_{max}(h^*) \equiv \lim_{h^+ \rightarrow h^*} q(h^*, h^+) = h^* \bar{u}^*. \quad (4.25)$$

In the opposite limit $h^+ \rightarrow h_{min}$ the mean flux approaches a finite lower limit

$$q_{min}(h^*) \equiv \lim_{h^+ \rightarrow h_{min}} q(h^*, h^+). \quad (4.26)$$

Since q is also found to increase with increasing critical thickness (for all h^+), equations (4.25) and (4.26) imply that the critical thickness must lie in the range

$$h_{min}^* < h_0 < h^* < h_{max}^*, \quad (4.27)$$

where h_{max}^* satisfies $q_{min}(h_{max}^*) = q_0$ and the lower bound is required for the initial steady uniform flow to become unstable. For each h^* in the range (4.27) the corresponding forward shock thickness h^+ can then be found iteratively by ensuring that the mean flux q of the resulting wave is equal to q_0 . This defines a new family of roll waves, each having different amplitudes but all with the same flux as a given steady uniform inflow. Figure 7 shows one such family of waves, calculated using $h_0 = 2$ mm and $\bar{\phi}_0 = 0.5$. The individual wavespeeds are determined by h^* through (4.14), meaning that each wave now travels at a different speed and larger-amplitude, longer wavelength waves travel faster. Figure 8 explores the relationship between wavespeed, wavelength and amplitude in more detail by considering different inflow concentrations $\bar{\phi}_0$ for the

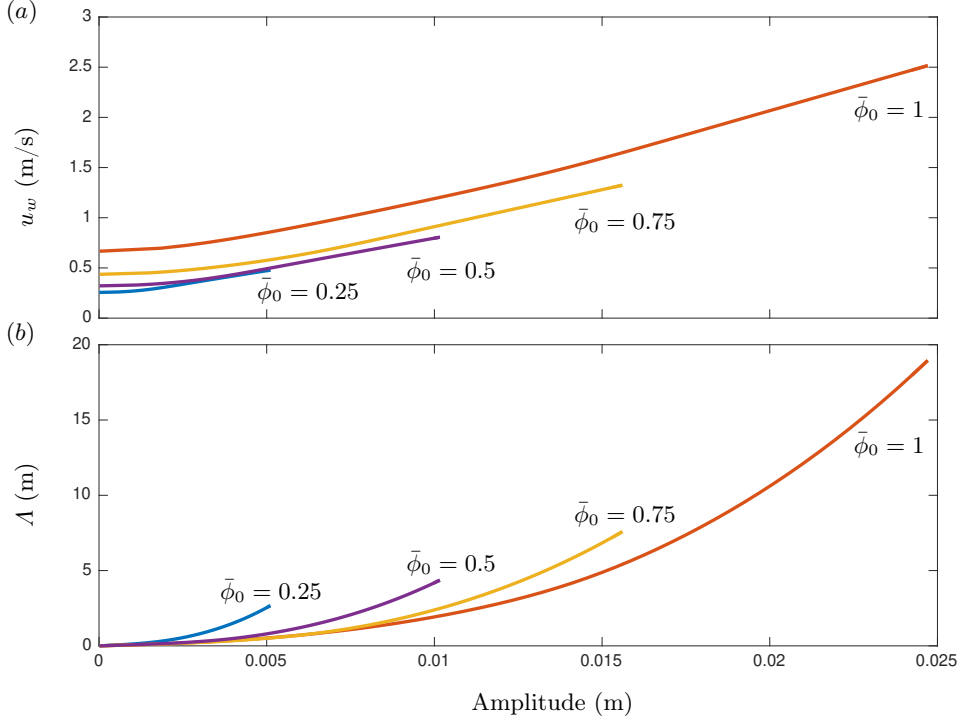


FIGURE 8: The relationship between the amplitude and (a) wavespeed u_w and (b) wavelength Λ for families of waves resulting from different steady uniform inflows, all with $h_0 = 2$ mm but different mean concentrations $\bar{\phi}_0$.

same $h_0 = 2$ mm. The maximum possible wavelength and amplitude of waves with more small particles is larger, and for a given amplitude these small-rich waves have shorter wavelengths. In general, more small particles results in faster moving waves (for a given amplitude), which is consistent with the experimental observations. Note that the pure large particles case $\bar{\phi}_0 = 0$ is not shown on figure 8 because $h_0 < h_{min}^*$ in this more frictional regime, and so the steady uniform flow cannot develop roll waves.

5. Travelling-wave solutions for the concentration profile

Having found the family of wave thickness and bulk velocity profiles that can form from a given steady uniform inflow, the large particle transport equation (3.7) can now be solved to find the resulting distribution of large and small particles within the wave. Switching to the moving-frame coordinate ξ and seeking steady travelling-wave solutions, (3.7) reduces to

$$\frac{d}{d\xi}(h\bar{\phi}(\bar{u} - u_w)) - \frac{d}{d\xi}(h\bar{u}G(\bar{\phi})) = 0, \quad (5.1)$$

which can be integrated directly using (4.3) to give

$$Q_1\bar{\phi} + h\bar{u}G(\bar{\phi}) = Q_2, \quad (5.2)$$

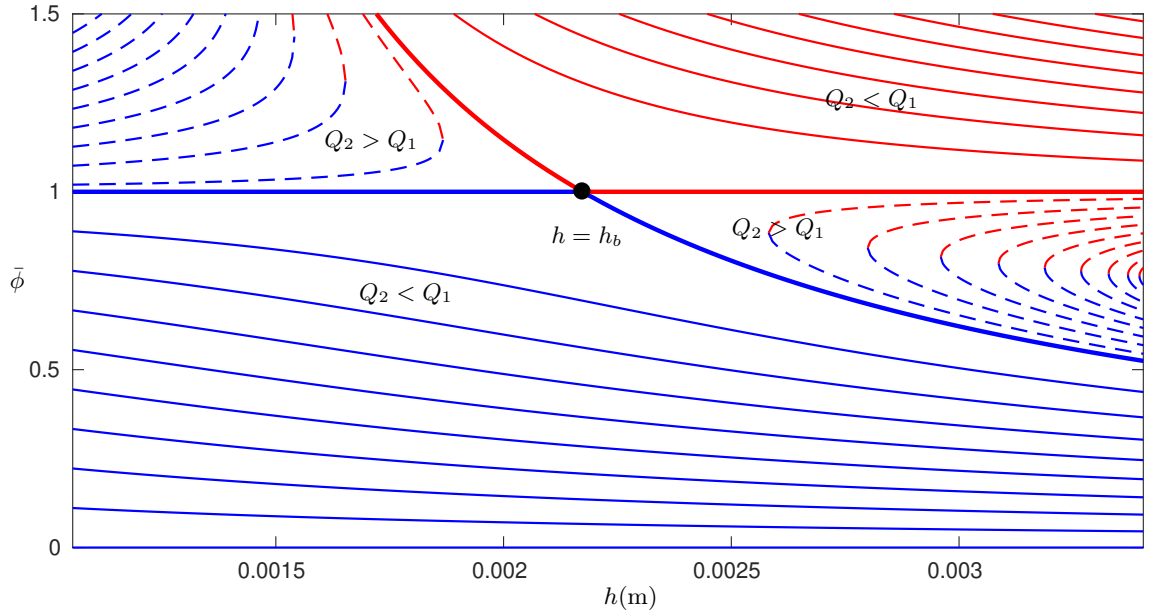


FIGURE 9: Plots of the depth-averaged concentration profiles (5.3) (blue) and (5.4) (red) as functions of flow thickness h for different values of the constant Q_2 . Solid lines denote cases where $Q_2 < Q_1$ and dashed lines where $Q_2 > Q_1$. Bold solid lines represent the boundary $Q_2 = Q_1$, and the black marker shows the bifurcation point $h = h_b$, determined by (5.14). All profiles are calculated using $h^* = 2$ mm, $\bar{\phi}_0 = 0.5$ and $A = 0.25$. Note permissible concentrations lie in the range $\bar{\phi} \in [0, 1]$.

where Q_2 is the upstream flux of small particles in the frame moving with the wave. This is a non-negative constant, equalling zero only when $\bar{\phi} = 0$. Equation (5.2) is quadratic in $\bar{\phi}$ (from the definition of $G(\bar{\phi})$ in (3.8)), and has two roots

$$\bar{\phi}^{(1)} = \frac{(Ah\bar{u} + Q_1) - \sqrt{(Ah\bar{u} + Q_1)^2 - 4Ah\bar{u}Q_2}}{2Ah\bar{u}}, \quad (5.3)$$

$$\bar{\phi}^{(2)} = \frac{(Ah\bar{u} + Q_1) + \sqrt{(Ah\bar{u} + Q_1)^2 - 4Ah\bar{u}Q_2}}{2Ah\bar{u}}. \quad (5.4)$$

For a given bulk wave, \bar{u} is a monotonically increasing function of h , determined using (4.16), and the constant Q_1 is also known explicitly via (4.15). Consequently, (5.3) and (5.4) are functions of h , with Q_2 acting as a control parameter (figure 9). To understand the different regions it is useful to consider the discriminant

$$D(h) = (Ah\bar{u} + Q_1)^2 - 4Ah\bar{u}Q_2. \quad (5.5)$$

For $Q_2 < Q_1$, the upstream flux of large particles relative to the wave $Q_1 - Q_2$ is positive, and it follows that

$$D(h) > (Ah\bar{u} - Q_1)^2 \geq 0, \quad (5.6)$$

and therefore the two roots (5.3), (5.4) are real and distinct for all values of h (figure 9, solid lines). It is also straightforward to show that, when $Q_2 < Q_1$, only the root $\bar{\phi}^{(1)}$

is admissible since,

$$0 \leq \bar{\phi}^{(1)} < \frac{Q_1}{Ah\bar{u}} < 1, \quad \text{and} \quad \bar{\phi}^{(2)} > 1, \quad \text{when} \quad Ah\bar{u} > Q_1, \quad (5.7)$$

$$0 \leq \bar{\phi}^{(1)} < 1, \quad \text{and} \quad \bar{\phi}^{(2)} > \frac{Q_1}{Ah\bar{u}} > 1, \quad \text{when} \quad Ah\bar{u} < Q_1. \quad (5.8)$$

Conversely, when $Q_2 > Q_1$ there is a net downstream flux of large particles relative to the wave and the discriminant (5.5) is no longer positive for all values of h , becoming zero when

$$Ah\bar{u} = D^\pm, \quad \text{where} \quad D^\pm = (2Q_2 - Q_1) \pm 2\sqrt{Q_2(Q_2 - Q_1)}. \quad (5.9)$$

The discriminant is therefore positive for $Ah\bar{u} > D^+$ and $Ah\bar{u} < D^-$, meaning the two concentration roots (5.3) and (5.4) are real and distinct in these cases, for $Q_2 > Q_1$ (figure 9, dashed lines). Since

$$0 < \bar{\phi}^{(1)}, \bar{\phi}^{(2)} < 1 \quad \text{when} \quad Ah\bar{u} > D^+, \quad (5.10)$$

$$\bar{\phi}^{(1)}, \bar{\phi}^{(2)} > 1 \quad \text{when} \quad Ah\bar{u} < D^-, \quad (5.11)$$

these roots are physically admissible only for $Ah\bar{u} > D^+$. Finally, when $Q_1 = Q_2$ and there is no net flux of large particles relative to the wave, equations (5.3) and (5.4) reduce to

$$\bar{\phi}^{(1)} = \begin{cases} \frac{Q_1}{Ah\bar{u}} \leq 1 & \text{if} \quad Ah\bar{u} \geq Q_1, \\ 1 & \text{if} \quad Ah\bar{u} < Q_1, \end{cases} \quad (5.12)$$

$$\bar{\phi}^{(2)} = \begin{cases} 1 & \text{if} \quad Ah\bar{u} \geq Q_1, \\ \frac{Q_1}{Ah\bar{u}} > 1 & \text{if} \quad Ah\bar{u} < Q_1, \end{cases} \quad (5.13)$$

shown by bold solid lines in figure 9.

There is a qualitative change in behaviour when $Ah\bar{u} = Q_1$, and, substituting for (4.15) and (4.16), this bifurcation point occurs at thickness

$$h = h_b \equiv \frac{h^*(1+A)}{A(1+Fr^*)}. \quad (5.14)$$

The physical significance of the bifurcation point can be seen by considering the free-surface velocity, $u_s \equiv u(z=h)$. From the definition of the shear profile (3.5) and the fact that $Q_1 = Ah\bar{u}$ at $h = h_b$, it follows that

$$u_s(h_b) = \bar{u}(h_b)(1+A) = \bar{u}(h_b) + \frac{Q_1}{h_b} = u_w, \quad (5.15)$$

and therefore surface particles at $h = h_b$ travel at precisely the velocity of the waves. It follows that $u_s < u_w$ for $h < h_b$ and $u_s > u_w$ for $h > h_b$, meaning the bifurcation point represents the divide between surface particles travelling slower or faster than the waves themselves. The relative position of h_b compared to the wave thickness range $h^+ < h < h^-$ plays an important role in determining admissible concentration profiles $\bar{\phi} \in [0, 1]$. There are three different cases to consider as shown in figure 10.

5.1. Case 1: $h < h_b$ everywhere

If $h < h_b$ at all points in the wave, meaning all particles travel more slowly than the wave, then the only permissible root is $\bar{\phi} = \bar{\phi}^{(1)}$, assuming that $Q_2 < Q_1$ as shown in figure 9. In this case there is a family of concentration profiles that are determined by the specific choice of $Q_2 \in [0, Q_1]$, which can in turn be determined by evaluating (5.2) at a given concentration $\bar{\phi} = \bar{\phi}_p \in [0, 1]$ and bulk thickness $h = h_p$. A selection of these profiles are shown in figure 10(a) and corresponding interfaces η in figure 10(b). Each profile $\bar{\phi}(\xi)$ is continuous along the wave, but must necessarily experience a jump at the peak where the thickness h and velocity \bar{u} are discontinuous. The jump condition relating the forward ($\bar{\phi}^+$) and backward ($\bar{\phi}^-$) concentrations here is

$$h^+ \bar{\phi}^+ (\bar{u}^+ - u_w) - h^+ \bar{u}^+ G(\bar{\phi}^+) = h^- \bar{\phi}^- (\bar{u}^- - u_w) - h^- \bar{u}^- G(\bar{\phi}^-), \quad (5.16)$$

which is equivalent to saying that the value of Q_2 must be the same on either side of the discontinuity. Consequently, it is not possible to jump between different permissible solutions (corresponding to different values of Q_2) at any point along the wave. This class of solution is therefore referred to as ‘continuous’, even though the profiles are still discontinuous at the end points. Figure 10(a) shows that $\bar{\phi}$ decreases as h increases, implying higher concentrations of large particles at wave crests, as observed experimentally.

5.2. Case 2: $h = h_b$ at an internal point

Next, if $h = h_b$ at an internal point in the wave, say $\xi = \xi_b$, then surface particles move slower than the waves for $\xi < \xi_b$ and faster for $\xi > \xi_b$. There are two different classes of possible solutions for the concentration profile in this regime. Similarly to case 1, continuous profiles can be constructed by specifying the concentration $\bar{\phi} = \bar{\phi}_p \in [0, 1]$ at thickness $h = h_p \leq h_b$ and selecting the first root (5.3). This again corresponds to $Q_2 < Q_1$, and example profiles are shown in figure 10(c) and (d). For $h > h_b$,

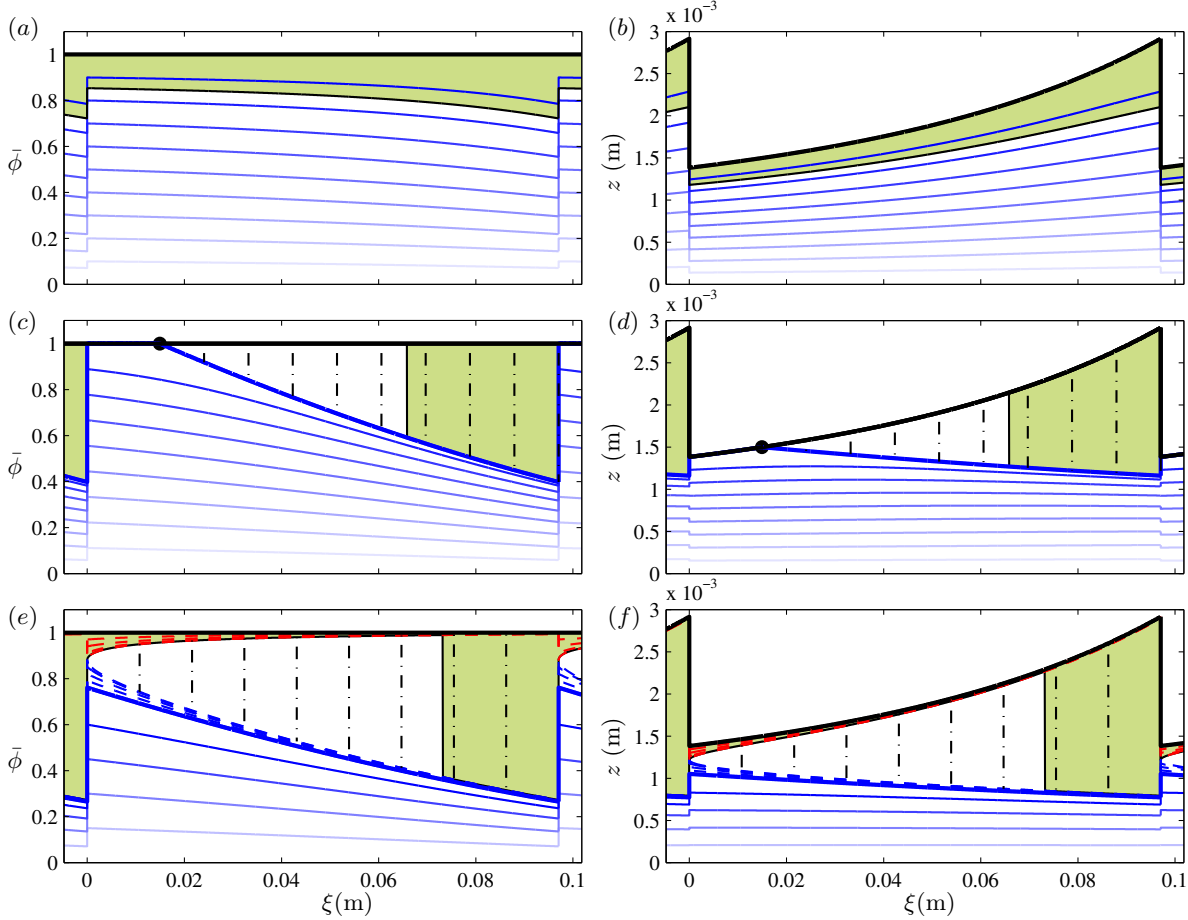


FIGURE 10: Permissible travelling wave solutions for the concentration profile $\bar{\phi}(\xi)$ (a, c, e) and corresponding interface height $\eta(\xi)$ (b, d, f) in the three cases described in §5.1, §5.2 and §5.3. Solid black lines represent $\bar{\phi} = 1$ on the left hand plots and the flow thickness $z = h$ on the right hand plots, and solid blue lines represent the root $\bar{\phi}^{(1)}$ for $Q_2 < Q_1$. Bold blue lines on (c)–(f) show $\bar{\phi}^{(1)}$ when $Q_2 = Q_1$. On panels (c) and (d) the bifurcation point $h = h_b$ is present at $\xi = \xi_b$ and shown by a black marker, and possible shocks between $\bar{\phi}_s^- = 1$ and $\bar{\phi}_s^+ = Q_1/(Ah\bar{u})$ for $\xi > \xi_b$ are marked with dash-dotted black lines. On panels (e) and (f) the dashed lines show the roots $\bar{\phi}^{(1)}$ (blue) and $\bar{\phi}^{(2)}$ (red) for $Q_2 > Q_1$, and dash-dotted lines represent possible shock solutions between $\bar{\phi}_s^- = \bar{\phi}^{(2)}$ and $\bar{\phi}_s^+ = \bar{\phi}^{(1)}$ in the special case (5.21) when $Q_2 = Q_2^*$. The shaded green regions show specific solutions for the region occupied by large grains when the mean flux of small particles across one wave q^S is equal to that at the inflow q_0^S . All cases use the same bulk wave, calculated using $h^* = 2.05$ mm, $h^+ = 1.38$ mm and $\bar{\phi}_0 = 0.8$, but different shear parameters $A = 0.2$ for (a, b), $A = 0.6$ for (c, d) and $A = 0.9$ for (e, f).

there is a region where both $\bar{\phi}^{(1)}$ and $\bar{\phi}^{(2)}$ are valid, corresponding to where $Q_2 > Q_1$ (figure 9). However, for a particular choice of Q_2 in this region neither concentration profile remains real across the full thickness range, and hence these solutions are not permissible. The boundary case $Q_2 = Q_1$ is important because the two roots coalesce at $h = h_b$ and interchange through $\bar{\phi} = 1$. For $h > h_b$, (5.12) and (5.13) imply that $\bar{\phi}^{(1)} < 1$ and $\bar{\phi}^{(2)} = 1$, meaning that both roots are permissible for the same choice of Q_2 . This raises the possibility of shock solutions transitioning between $\bar{\phi}^{(1)}$ and $\bar{\phi}^{(2)}$ at an internal point in the wave, where the thickness and velocity remain continuous. Such a solution would automatically satisfy the shock condition (5.16) but must also satisfy

the causality condition to ensure that sufficient information is propagated into the shock (see e.g. Ockendon *et al.* 2004). This is equivalent to the Lax entropy condition (Lax 1957), and can be formulated in terms of the characteristic lines of the transport equation (3.7)

$$\frac{dx}{dt} = \bar{u}(1 - G'(\bar{\phi})). \quad (5.17)$$

The causality condition requires that the characteristics on either side of an internal concentration shock must travel into it, i.e. $dx/dt > u_w$ for $\xi < \xi_s$ and $dx/dt < u_w$ for $\xi > \xi_s$, where $\xi_s \geq \xi_b$ is the assumed internal shock position. Substituting in for the two roots (5.3) and (5.4), and using (4.3), implies

$$\bar{u}(1 - G'(\bar{\phi}^{(1)})) = u_w - \frac{1}{h} \sqrt{(Ah\bar{u} + Q_1)^2 - 4Ah\bar{u}Q_2}, \quad (5.18)$$

$$\bar{u}(1 - G'(\bar{\phi}^{(2)})) = u_w + \frac{1}{h} \sqrt{(Ah\bar{u} + Q_1)^2 - 4Ah\bar{u}Q_2}, \quad (5.19)$$

and it necessarily follows that $\bar{\phi}_s^- = \bar{\phi}^{(2)}$ and $\bar{\phi}_s^+ = \bar{\phi}^{(1)}$, where $\bar{\phi}_s^\pm$ are the values of $\bar{\phi}$ on either side of the internal shock. Furthermore, the causality condition should also be applied at the wave end points, where there are also shocks in h and \bar{u} . In this case one of the concentration characteristics (5.17) must travel into the shock and another travel out, because there are already three of the bulk characteristics travelling in and one travelling out (see e.g. Viroulet *et al.* 2017). Choosing $\bar{\phi}^- = \bar{\phi}^{(1)}$ and $\bar{\phi}^+ = \bar{\phi}^{(2)}$ at the end points satisfies this requirement, and, due to the two roots swapping over at the bifurcation point, is also consistent with the internal shock values. ‘Full internal shock’ solutions can therefore be constructed as

$$\bar{\phi}(\xi) = \begin{cases} 1 & \text{for } \xi \leq \xi_s, \\ \frac{Q_1}{Ah(\xi)\bar{u}(\xi)} & \text{for } \xi > \xi_s, \end{cases} \quad (5.20)$$

where ‘full’ refers to the fact that the backward side of the shock fully consists of small particles. Figure 10(c) and (d) shows some example solutions of this type, with different possible shock positions ξ_s indicated with dash-dotted lines. Note that there is again a region with a higher concentration of large particles towards the wavefront, as seen in the ‘continuous’ concentration profiles and experimental results. However, the pure small particle region $\bar{\phi} = 1$ behind the wavefront is qualitatively different. This will prevent transport of large particles backwards through the wave, which was determined to be the dominant mechanism from the tracer particle experiments. This

shock regime represents large particles travelling downslope with the wave itself and is indicative of a breaking size-segregation wave in a non-depth-averaged framework (Thornton & Gray 2008; Gray & Ancey 2009; Johnson *et al.* 2012; Gajjar *et al.* 2016), where large particles are continuously segregated, sheared and recirculated inside the crest of the wave.

5.3. Case 3: $h > h_b$ everywhere

Finally, consider the case where $h > h_b$ at all points along the wave profile, meaning all surface particles travel faster than the waves. Continuous solutions can again be constructed by picking a thickness h_p and concentration $\bar{\phi}_p$, using (5.2) to calculate Q_2 , and then substituting into the root (5.3). Note that Q_2 is only less than Q_1 if $\bar{\phi}_p < Q_1/(Ah_p\bar{u}(h_p))$ at this point. Specifying $\bar{\phi}_p \geq Q_1/(Ah_p\bar{u}(h_p))$ places the solution on a branch where $Q_2 \geq Q_1$, and figure 9 shows that both $\bar{\phi}^{(1)}$ and $\bar{\phi}^{(2)}$ are valid at the specified location. However, they may become complex if the discriminant (5.5) is zero, which occurs when $Ah\bar{u} = D^+$. To avoid such a point lying on the wave profile one can specify the concentration at the minimum wave thickness h^+ . In this case $Q_2 \geq Q_1$ can be determined by picking the forward concentration $\bar{\phi}^+$ in the range $Q_1/(Ah^+\bar{u}(h^+)) \leq \bar{\phi}^+ \leq 1$, and both roots (5.3) and (5.4) are then real, valid solutions throughout the entire wave. These are shown as dashed lines in figure 10(e) and (f).

Since there are two permissible concentration profiles for the same value of Q_2 , it should also be investigated whether internal shock solutions connecting the two, similar to those described in §5.2, are possible in this case. The causality condition again implies that an internal shock should have $\bar{\phi}_s^- = \bar{\phi}^{(2)}$ and $\bar{\phi}_s^+ = \bar{\phi}^{(1)}$, and the end-point shock have $\bar{\phi}^- = \bar{\phi}^{(1)}$ and $\bar{\phi}^+ = \bar{\phi}^{(2)}$. It is only possible to satisfy both criteria if the concentration can switch between the two roots without becoming discontinuous. Previously, the bifurcation point $h = h_b$ provided the means to achieve this, but such a point is not present in these wave profiles. However, there is precisely one pair of solutions that do coalesce at the point $h = h^+$ where the discriminant $D(h^+) = 0$, and this allows for the desired interchange. From (5.3) and (5.4) the concentration at this point is $\bar{\phi}^+ = (1 + Q_1/(Ah^+\bar{u}^+))/2$ and, substituting into (5.2), the corresponding

value of Q_2 is

$$Q_2 = Q_2^* \equiv \frac{Ah^+\bar{u}^+}{4} \left(1 + \frac{Q_1}{Ah^+\bar{u}^+} \right)^2. \quad (5.21)$$

One can therefore construct solutions of the form

$$\bar{\phi}(\xi) = \begin{cases} \bar{\phi}^{(2)} < 1 & \text{for } \xi \leq \xi_s, \\ \bar{\phi}^{(1)} < 1 & \text{for } \xi > \xi_s, \end{cases} \quad (5.22)$$

which have an internal shock at position $\xi_s \in [0, \Lambda]$, where the profiles $\bar{\phi}^{(1)}$ and $\bar{\phi}^{(2)}$ are calculated by substituting (5.21) into (5.3) and (5.4). These are referred to as ‘partial internal shock’ solutions because the backward side of the wave is only partially saturated with small particles ($\bar{\phi}_s^- < 1$), in contrast to §5.2 where $\bar{\phi}_s^- = 1$. Figure 10(e) and (f) shows some example solutions of this type, with different possible shock positions ξ_s being indicated with dash-dotted lines. As before, the concentration of large particles is significantly higher towards the wavefront, but some large grains are present at all points in the wave.

5.4. Relation to inflow conditions

For a given bulk wave profile, figure 10 illustrates the families of possible travelling-wave solutions for the concentration $\bar{\phi}$. To understand which of these profiles are likely to form downstream in chute-flow experiments, the flux of small particles can be considered in an analogous way to using the total flux for the bulk in §4.2. Assuming the waves form from a steady uniform flow of thickness h_0 , velocity \bar{u}_0 and mean concentration $\bar{\phi}_0$, the inflow has constant small particle flux $q_0^S = h_0\bar{u}_0\bar{\phi}_0 - h_0\bar{u}_0G(\bar{\phi}_0)$. The average flux across one travelling wave is

$$q^S = \frac{1}{\Lambda} \int_0^\Lambda h\bar{u}\bar{\phi} - h\bar{u}G(\bar{\phi}) \, d\xi, \quad (5.23)$$

and the waves that will be realised are those for which $q^S = q_0^S$. For the continuous concentration profiles, such as those shown on figure 10(a) and (b), the profile with the correct mean small particle flux can be found by iteratively choosing Q_2 . This profile is indicated on figure 10(a) and (b) by the interface between the large green region and the underlying white small particle region. The same approach can also be applied when internal shock solutions are possible (either full or partial, figure 10c–f), providing the desired small particle flux is sufficiently low. For higher values of q_0^S , however, concentration profiles require internal shocks in order to incorporate enough

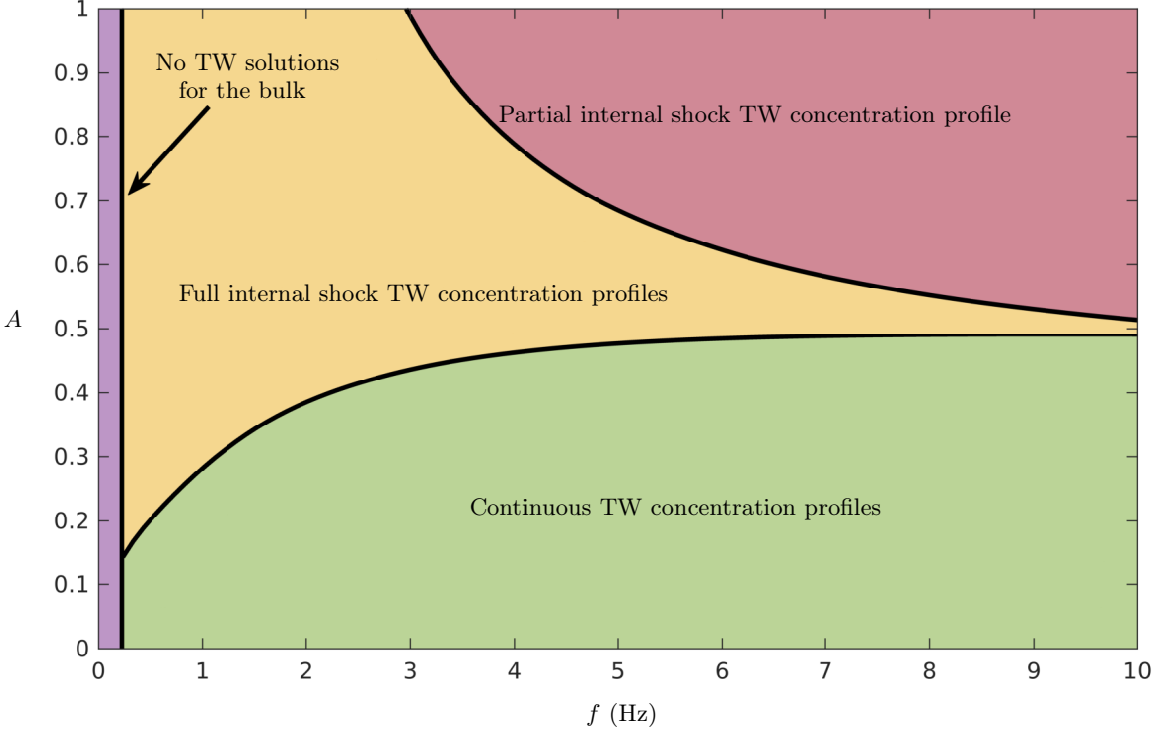


FIGURE 11: Phase diagram showing the different classes of inviscid travelling wave (TW) solutions that theoretically form from a steady uniform inflow of thickness $h_0 = 2$ mm and mean concentration $\bar{\phi}_0 = 0.8$, depending on the perturbation frequency f and effective shear parameter A . Boundaries are calculated by matching both the mean total flux q and small-particle flux q^S to the inflow values, q_0 and q_0^S respectively.

small particles. In this case the correct profile is selected by iteratively choosing the shock position ξ_s so that $q^S = q_0^S$ (indicated by the interface between the large particle green region and the underlying white small particle region in figure 10c–f). In the third regime (figure 10e and f), even higher small particle fluxes may require choosing the second concentration root (5.4) across the whole wave, with appropriate iterative choice of Q_2 . This would result in an alternative type of continuous solution with higher concentrations of small particles at the wavefront, in disagreement with the experimental results and other theoretical solutions.

The three different cases in figure 10 are all computed using the same bulk profile and varying the effective shear parameter A , which controls the relative position of the bifurcation point through (5.14). The continuous solutions in case 1 correspond to low shear regimes and, for higher shear, full internal shock solutions become possible (case 2). If the degree of shear becomes even higher then these full internal shock solutions disappear but alternative partial internal shock solutions may occur (case 3). Now, figure 7 shows that each inflow condition $(h_0, \bar{\phi}_0)$ gives rise to a one-parameter family of bulk waves with the same mean flux q_0 as the inflow, and figure 11 applies the

concentration flux matching approach described above to each wave in this family. Here, the bulk profiles are parameterised by their frequency f , which can be related to the wavespeeds and wavelengths of figure 8 using $f = u_w/\Lambda$, with smaller-amplitude, slower, shorter waves corresponding to higher frequencies. The phase diagram figure 11 shows the different classes of solution that would form from a given steady uniform inflow, depending on f and the shear parameter A . Below a minimum frequency no travelling-wave solutions are possible for the bulk, but above this frequency the bulk waves may be augmented with any of the continuous concentration profiles, full internal shock concentration profiles or partial internal shock solutions for the concentration. Note that travelling-wave solutions for $\bar{\phi}$ are unique for a given bulk profile.

6. Time-dependent numerical simulations

The full system of Partial Differential Equations (PDEs) (3.7), (3.9) and (3.10) is now solved numerically using the shock-capturing central scheme of Kurganov & Tadmor (2000), whose semi-discrete formulation is combined with a Runge-Kutta-Chebyshev adaptive time stepper (Medovikov 1998) and weighted essentially non-oscillatory (WENO) flux limiter (detailed in Noelle 2000). Similar numerical methods have been employed for related systems of conservation laws governing granular flows, for example monodisperse roll waves (Razis *et al.* 2014), erosion–deposition waves (Edwards & Gray 2015) and flow over variable basal topography (Viroulet *et al.* 2017), as well as segregation-induced finger formation in bidisperse flows (Baker *et al.* 2016*b*).

To simulate bidisperse roll waves in an inclined chute, a numerical domain $0 \leq x \leq 5$ m is discretised over 50 000 grid points, and initial conditions

$$h(x, 0) = h_0, \quad \bar{u}(x, 0) = \bar{u}_0, \quad \bar{\phi}(x, 0) = \bar{\phi}_0, \quad (6.1)$$

representing steady uniform flow are enforced along its length. Note that these conditions do not capture the initial front propagation down the empty chute, but have the advantage of avoiding the degeneracy of the system as $h \rightarrow 0$. The variables at the inflow of the chute are set to be

$$h(0, t) = h_0 + \delta h_1(t), \quad \bar{u}(0, t) = \bar{u}_0, \quad \bar{\phi}(0, t) = \bar{\phi}_0, \quad (6.2)$$

which constitute the same steady uniform flow as the initial conditions but with a time-dependent perturbation to the flow thickness, designed to trigger the roll wave

instability. All simulations are carried out with the same perturbation magnitude $\delta = h_0/100$, but different forms of the function $h_1(t)$ are subsequently employed. The numerics are computed using the viscous form of the momentum equation (3.10) with $\nu = 0.001\text{m}^3/2\text{s}^{-1}$.

6.1. Periodic inflow perturbation

The inflow perturbation is initially taken to be a sinusoidal function of the form $h_1(t) = \sin(2\pi ft)$, where $f = 2$ Hz is the perturbation frequency. This periodicity is motivated by the desire to produce well-defined, regular waves that can be directly related to the ODE travelling-wave solutions derived in §4 and §5.

Figure 12 shows the results of two numerical simulations at time $t = 20$ s, each computed with steady uniform thickness $h_0 = 2$ mm and concentration $\bar{\phi}_0 = 0.8$. The resulting thickness profiles are thus identical, and the bulk waves grow as they move downslope before their amplitudes eventually saturate (as shown in movies 3 and 4), forming a periodic train of steady travelling waves. Differences in the interface profiles $\eta(x, t)$ arise due to different shear parameters A being used in the two cases, with figure 12(a) showing a low shear value ($A = 0.1$) where the interface largely follows the wave. This corresponds to the ‘continuous’ concentration profiles described in §5. Figure 12(b), on the other hand, shows a higher shear value ($A = 0.5$) which leads to the formation of the second class of solutions with full internal concentration shocks. Numerical simulations have also been carried out in the third regime where $h > h_b$ everywhere, leading to concentration profiles with partial internal shocks, but these are omitted here for brevity.

These simulations suggest that all classes of travelling-wave solutions predicted by the inviscid ODE are stable and manifest themselves in the full system of viscous PDEs. Figures 12(c) and 12(d) extends this idea further by calculating the ODE solutions that have mean total flux $q = q_0$ and small particle flux $q^S = q_0^S$, and overlaying the profiles on the final downstream wave extracted from the PDE solutions. There is excellent agreement for both the thickness and concentration profiles in both regimes, indicating that solutions of the viscous PDEs are well approximated by inviscid travelling waves. Further comparisons between the inviscid and viscous solutions are described in the Appendix A.

To further investigate the kinematics of these two classes of solution, a tracer region

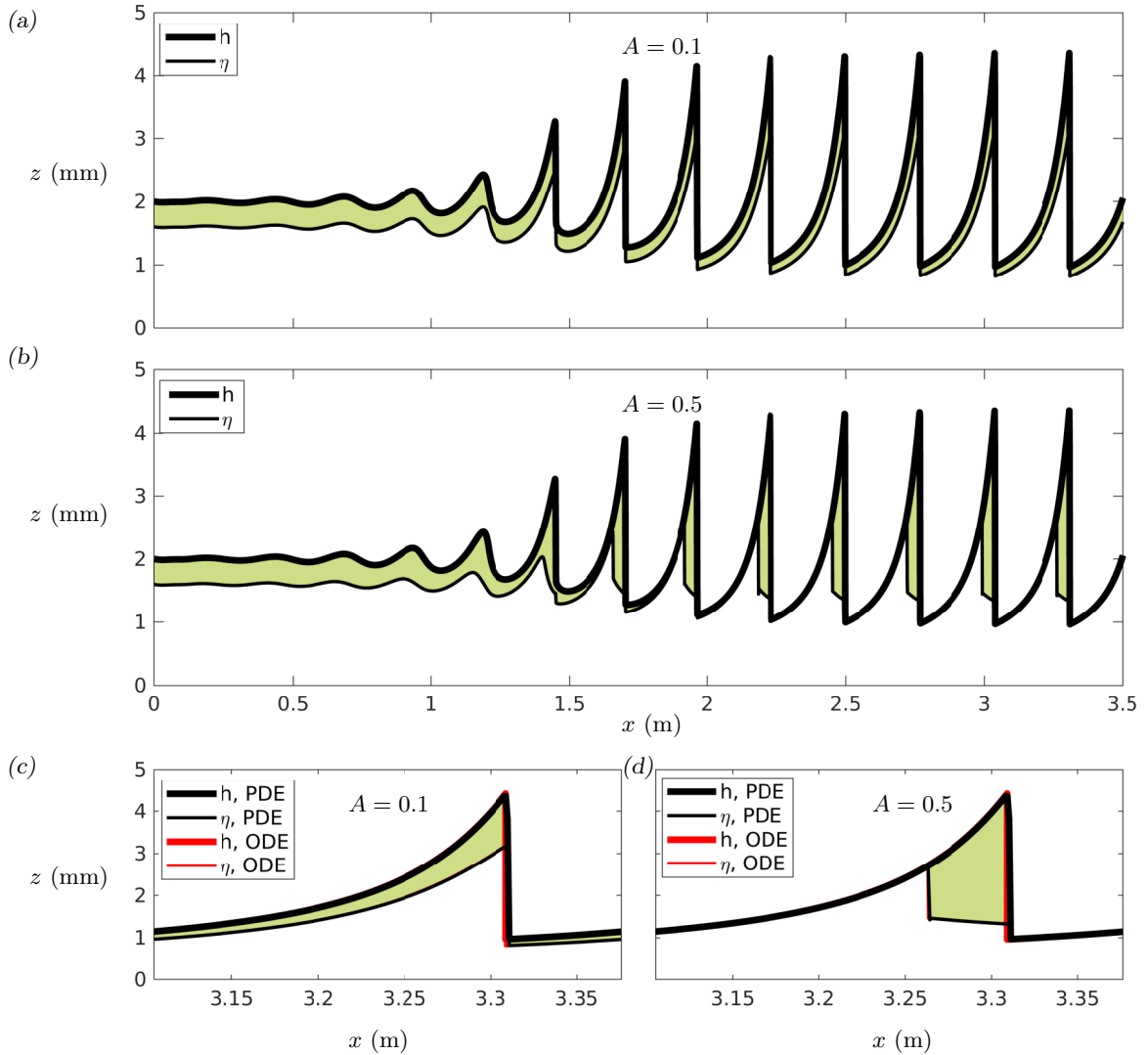


FIGURE 12: Numerical simulations showing the thickness h (thick solid lines) and interface η (thin solid lines) profiles at time $t = 20$ s for flows beginning from $h_0 = 2$ mm and $\bar{\phi}_0 = 0.8$, subject to a periodic inflow perturbation of frequency $f = 2$ Hz. The green shaded region therefore corresponds to the region with large grains and the white region underneath it to small grains. The shear parameter in (a) is $A = 0.1$ and in (b) is $A = 0.5$. (c) and (d) show close-ups of the final wave extracted from the PDE solutions (black lines), with the predictions from the inviscid ODE solutions superimposed on top (red lines). Supplementary movies 3 and 4 are available online showing the time evolution of both states.

of large red particles is now introduced into the simulations, which is designed to mimic the experimental approach of §2. To achieve this, the mass and momentum balance and transport equations, (3.9), (3.10) and (3.7) are solved as above until $t = 20$ s, allowing a well-developed periodic wavetrain to form. The final thickness, velocity and concentration profiles are then taken as initial conditions for a second set of simulations, where the same equations are solved for h , \bar{u} and $\bar{\phi}$ (with identical inflow perturbation) but an additional transport equation is solved for a new variable, say $\bar{\phi}_R$. This represents the relative amount of large red tracer particles, and is governed

by the same transport equation (3.7) but with initial and inflow conditions

$$\bar{\phi}_R(x, 0) = \begin{cases} \bar{\phi}(x, 0) & \text{if } x_0 < x < x_1, \\ 1 & \text{otherwise,} \end{cases} \quad (6.3)$$

$$\bar{\phi}_R(0, t) = 1, \quad (6.4)$$

where x_0 and x_1 are the up- and downslope limits of the tracer region. For a sufficiently narrow range (x_0, x_1) , solving for $\bar{\phi}_R$ thus represents the evolving concentration of a (large particle rich) red tracer region, whose boundary is determined by the interface $\eta_R = h\bar{\phi}_R$. Note that this approach works because the transport equation is decoupled from the bulk, meaning that it can be solved without altering the overall wave properties.

It is also insightful to study the paths of individual tracer particles on the surface of the flow, whose downslope position is determined by

$$\frac{dx}{dt} = u_s, \quad (6.5)$$

where the surface velocity $u_s(x, t)$ is calculated by substituting $z = h$ into the shear profile (3.5). Figure 13 and supplementary movies 5 and 6 show the results of these tracer region/particle simulations for the two different shear regimes. In the low shear case ($A = 0.1$, figure 13a,c,e,g and movie 5) the waves always travel faster than the tracer region, consequently catching up and then passing through the red shaded section. A compression/dilation concertina effect is also apparent, with the tracer region quickly being compressed as the wavefront initially passes through and then slowly dilating as it retreats relative to the leeward side of the wave. This is confirmed by the trajectories of surface particles starting at the lateral boundaries of the tracer region x_0 and x_1 . These stay a finite distance apart from each other, but the distance decreases/increases during the wave cycle.

The kinematics of the high shear regime ($A = 0.5$, figure 13b,d,f,h and movie 6) are completely different. In this case a red tracer region starting just behind the wavefront initially travels faster than the waves and is sheared to the front. It then proceeds to travel at precisely the wavespeed, meaning the tracer region remains at the front of the waves for all time. Tracer particles starting from x_0 and x_1 are both sheared to

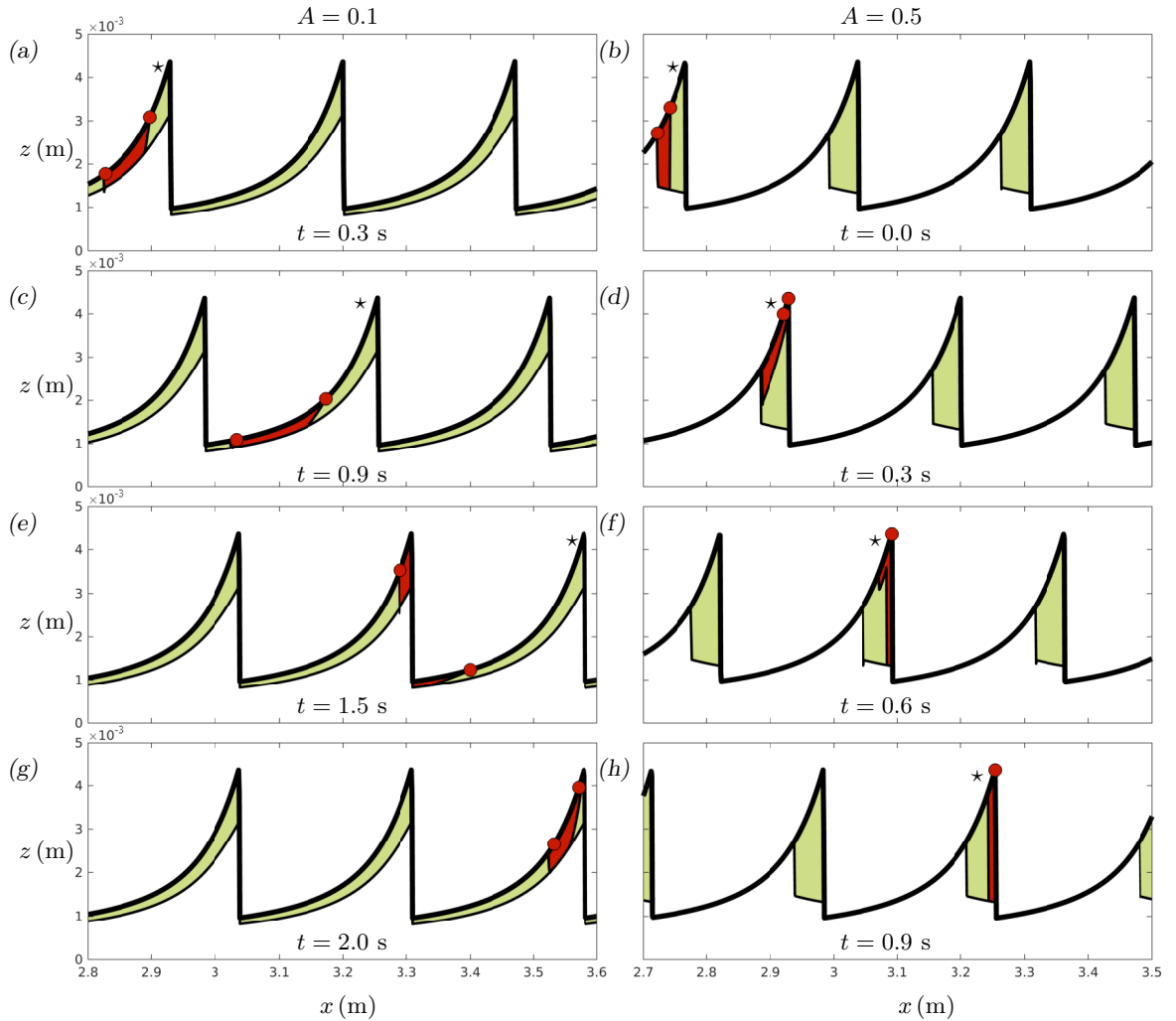


FIGURE 13: Numerical simulations showing the internal kinematics of the two classes of waves described in figure 12, corresponding to $A = 0.1$ (a,c,e,g) and $A = 0.5$ (b,d,f,h). The thick solid lines shows the flow thickness h . The green shading indicates large particles, the red shading shows the large red tracer particles and the white region underneath contains small particles. The interfaces between these regions determine the large/small interface η and the tracer interface η_R . Also shown with red dots are individual surface tracer grains, whose downslope position is calculated using (6.5). Times are given relative to the introduction of the tracer region/particles, and \star symbols track a single reference wavefront. Supplementary movies 5 and 6 show an additional representation of the internal kinematics and are available online.

the peak of the wave (where the velocity is fastest) and then continue to move as one and with the travelling wave.

6.2. Random inflow perturbation

Experimentally, the red tracer particles dropped on top of the flow travel slower than the waves and exhibit a concertina effect (figure 3), suggesting that the low shear regime is physically appropriate here. Although there is no current experimental evidence for large particles travelling with the wave crests, or faster than the wave crests, it is anticipated that these regimes could exist in more highly sheared flows. Even for the low shear regime, the periodic inflow perturbations described in §6.1

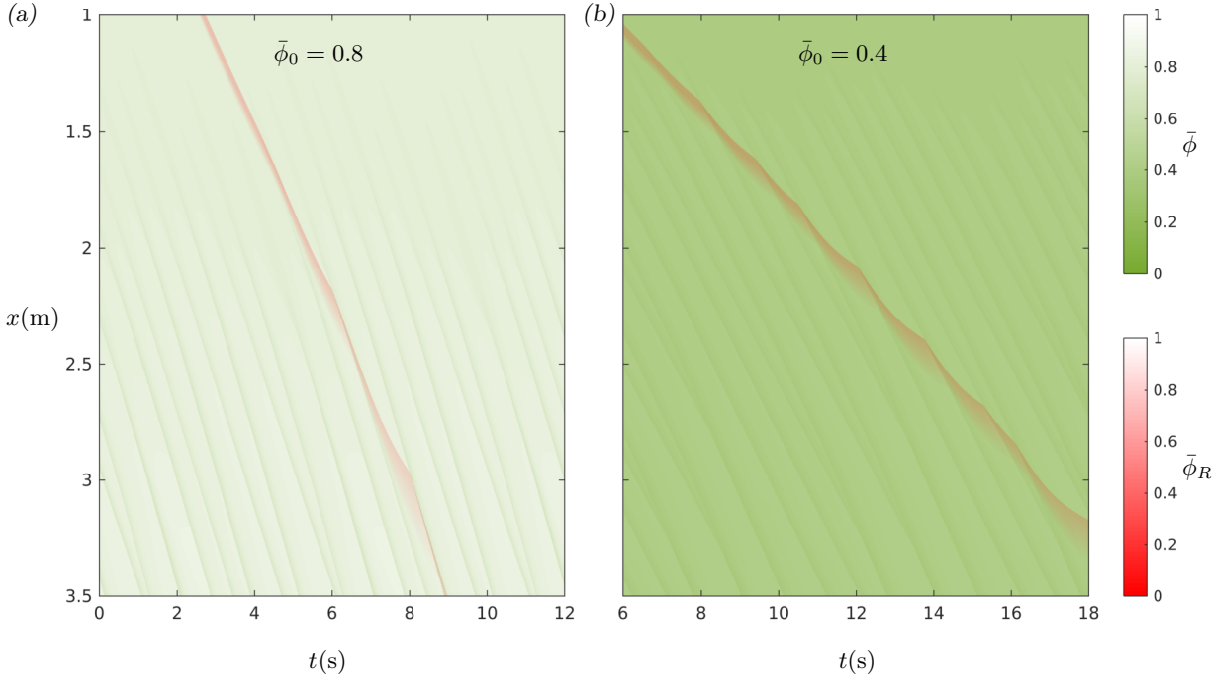


FIGURE 14: Aerial space-time plots of chute-flow simulations subject to a pseudo-random inflow perturbation, showing a downstream portion of the chute $1 < x < 3.5$ m. The green colour shows the evolution of the regular depth-averaged concentration $\bar{\phi}$, and red colour represents the concentration $\bar{\phi}_R$ of the tracer region. Mean inflow concentrations are (a) $\bar{\phi}_0 = 0.8$ and (b) $\bar{\phi}_0 = 0.4$. Both sets of simulations are conducted using shear parameter $A = 0.1$. Supplementary movies 7 and 8 show an additional representation of the internal kinematics and are available online.

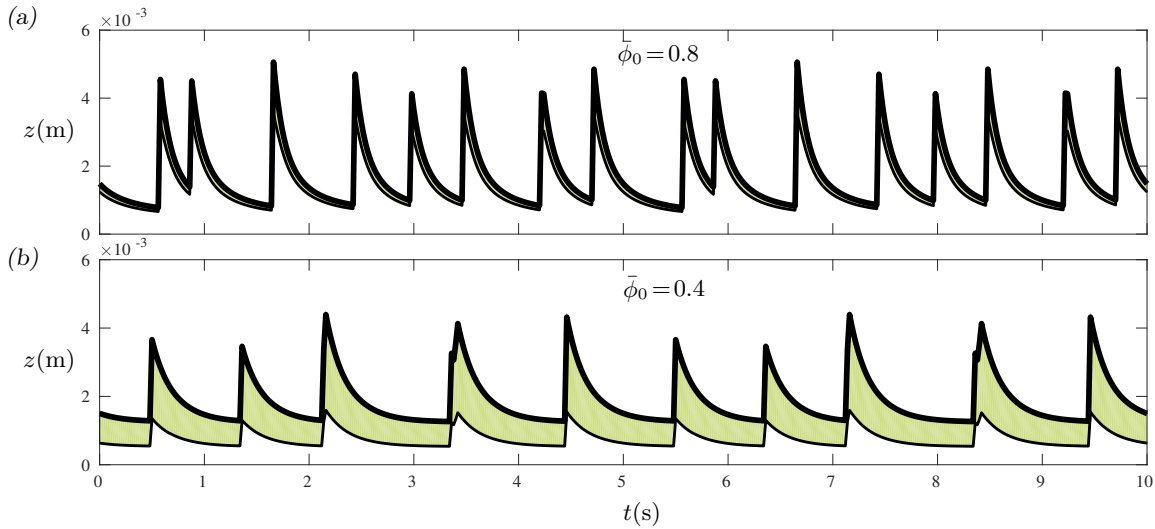


FIGURE 15: Internal space-time plots corresponding to the random-inflow numerical simulations of figure 14 at downslope position $x = 3.25$ m. The thick solid lines represent the flow thickness h , the green shading shows the large particle region and the white shaded region beneath is occupied by small particles. The interface η lies at the transition between these green and white regions. Mean inflow concentrations are (a) $\bar{\phi}_0 = 0.8$ and (b) $\bar{\phi}_0 = 0.4$.

represent an idealised version of the experiments, which do not form regular wavetrains. To model more realistic flows simulations are now carried out using a pseudo-random inflow perturbation $h_1(t)$ consisting of a random sum of Fourier modes and coefficients.

The regular equations are again solved until $t = 20$ s, before introducing a tracer region near the inflow and tracking its evolution.

Supplementary movies 7 and 8 show the resulting wave and interface profiles, computed using shear parameter $A = 0.1$, inflow thickness $h_0 = 2$ mm and inflow concentrations $\bar{\phi}_0 = 0.8$ and $\bar{\phi}_0 = 0.4$ corresponding to the two experimental mixtures. The same data are represented as an aerial space-time plot in figure 14 and internal space-time plot in figure 15, which are analogous to the experimental results (figures 3 and 4 respectively). For both mixtures, the random inflow perturbation leads to the development of different waves with varying wavespeeds and amplitudes, some of which merge and coarsen along the length of the chute. From figure 14 it is apparent that large green particles become concentrated at the wave fronts in both cases, but that the waves travel slower in the mixture with more large particles (figure 14b), consistent with experimental observations. Figure 15 shows that the computed amplitudes are also typically slightly smaller at the end of the chute $x = 3.25$ m for $\bar{\phi}_0 = 0.4$, again in qualitative agreement with experiments. There is, however, still some work necessary to obtain full quantitative agreement, since the amplitude of the computed waves in figure 15(b) is higher than those in the experiments in figure 4(b). There are a number of plausible reasons for this discrepancy. The most likely is that the choice of (i) inflow conditions, (ii) basal friction parameters and (iii) imposed perturbations are not exactly the same as the experiments, resulting in faster growth rates and hence bigger computed waves by the outflow. Certainly, the experimental waves appear still to be growing by the end of the chute, while the computed waves are already quite well developed. There may also be a direct feedback of the local particle size distribution on the bulk flow, which would necessitate fully coupled simulations.

Figure 14 and supplementary movies 7 and 8 show that the red tracer region behaves similarly in both cases, moving slower than the waves and experiencing the previously described concertina effect. Note that the time scales are different for the different mixtures in figure 14 because the bulk flow is slower for $\bar{\phi}_0 = 0.4$, meaning that the tracer region gets advected downslope more slowly.

7. Conclusions

This paper presents small-scale experiments in which a mass of bidisperse granular material consisting of large green and small white spherical glass ballotini (200 – 250 μm and 75 – 150 μm diameter, respectively) is released from a hopper and flows down a chute. As the initially homogenous mixture flows over the rough bed, the large particles rise to the free surface due to size segregation. Since the flow is faster near the free surface, the large particles are preferentially transported to the flow front, where a growing region of large particles forms. Upstream of this flow head is a breaking size-segregation wave (Thornton & Gray 2008; Gray & Ancey 2009; Johnson *et al.* 2012), a continuously segregating mixture of large and small grains, which connects the flow head to the inversely graded flow further upstream. The breaking wave ensures that large particles that are over-run by the advancing front are re-segregated upwards into the faster moving layers allowing the large-rich frontal region to grow in size. Small perturbations to the inversely graded upstream flow grow as they travel downslope, eventually developing into fully formed roll waves that travel faster than the bulk flow. These waves have approximately constant velocity (figure 2), although waves exist with a range of wavespeeds, leading to merging events as faster waves engulf slower moving ones. The inversely graded flow, large particle flow head, internal breaking size-segregation wave, and roll waves are directly observed through internal visualisation of the experimental flows (figure 4).

This basic roll wave instability mechanism and subsequent coarsening dynamics are understood for monodisperse flows (Forterre & Pouliquen 2003; Gray & Edwards 2014; Edwards & Gray 2015; Razis *et al.* 2014). In bidisperse flows, there are higher proportions of large particles at the wave fronts compared to the rest of the flow, which consequently form dark green bands in figure 2. Large red tracer particles seeded onto the flow surface travel more slowly than the waves and pass through the wave crests (figure 3), indicating that the increased large particle concentration at the wave fronts is not caused by large particles becoming trapped and accumulating in the wave crests.

Instead, it is caused by spatial variations in the large particle flux in a frame moving with the waves. This results in the layer of large particles on the surface of the flow being compressed in the streamwise direction near the wave crest, and consequently thickening this layer. This compression and thickening is less pronounced

in the small particle layer at the base of the flow, meaning that the depth integrated concentration of large particles is increased in the wave crests. This mechanism is observed experimentally; as a wavefront catches up with a region of red tracer particles, these tracers become compressed in the streamwise direction, before dilating after the wave has passed (figure 3).

The formation of bidisperse roll waves and increased concentration of large particles at roll wave crests are predicted by a depth-averaged model for the flow that combines particle size segregation (Gray & Kokelaar 2010a,b) with bulk mass and momentum balance equations (Gray & Edwards 2014). Motivated by the experimental observations of constant wavespeeds, inviscid travelling-wave solutions are constructed for the bulk thickness and velocity profiles by switching to a moving reference frame. Equating the mean flux of material across one wave with that at the inflow, the model predicts that a given steady uniform flow can develop into a family of different steadily travelling waves, each with different wavespeeds, amplitudes and wavelengths (figure 7). Fixing any one of these properties determines a unique bulk wave profile. Larger-amplitude waves are predicted to travel faster and have longer wavelength (figure 8), which is in agreement with experimental observations of larger-amplitude waves travelling faster than (and consequently merging with) smaller waves. For a given thickness of inflow, mixtures with higher proportions of small particles are predicted to produce waves that travel faster and reach higher amplitudes (figure 8), again consistent with experimental measurements (figure 2).

This agreement occurs despite the fact that frictional differences between large and small particles are accounted for in the model using a basal friction law that depends only on the mean composition of the mixture. The agreement suggests that any increase in the local basal friction caused by increased large particle concentration at wave crests is not central to the formation of roll waves. This is despite such segregation-mobility feedback playing an essential role in other bidisperse flows such as segregation-induced finger formation (Pouliquen *et al.* 1997; Woodhouse *et al.* 2012; Baker *et al.* 2016b). A natural extension to our modelling would be to account for this feedback, by using the local depth-averaged concentration $\bar{\phi}(x, t)$ in our friction law (3.13)–(3.16). This coupling adds significant mathematical complexity to the model (since the flow dynamics now depends on the predicted concentration profiles throughout the wave),

but is simple to implement in numerical codes, and is likely necessary for quantitative prediction of the dynamics, as well as the kinematics, of bidisperse roll waves.

Having obtained these bulk travelling-wave profiles, travelling-wave solutions can then be constructed for the relative concentration of particles throughout a wave. Three distinct classes of solution are found which all have higher concentrations of large particles towards the front but have key qualitative differences (figure 10). The first ‘continuous’ class of solution has an effective interface between layers of large and small particles that mostly follows the thickness profile, whereas the second ‘full internal shock’ solutions have a region of pure small particles at the rear of the wave transitioning rapidly to a coarser-rich zone at the front across a shock. The third ‘partial internal shock’ solutions are similar to case 2, except that some large particles are present at all points along the wave. By matching the average flux of small particles across a wave to the inflow conditions, one can predict the types of solution that may develop in chute-flow experiments (figure 11). It is found that the continuous concentration profiles typically correspond to low amounts of shear in the flow, the full internal shock solutions occur at higher degrees of shear and the partial internal shock solutions appear for the highest shear values.

Fully time-dependent numerical simulations confirm the existence and stability of the different types of concentration profile solutions (figure 12 and movies 3 and 4), which spontaneously form by perturbing a steady uniform inflow by a known frequency and allowing these perturbations to grow into a well-defined wavetrain. The resulting waves agree extremely well with the theoretical travelling waves, both in terms of the bulk and concentration profiles. The kinematics are also investigated numerically by simulating the evolution of a region of tracer particles, as well as individual grains (figures 13 and 14 and movies 5–8). In the low shear continuous regime, it can be seen that the particles move backwards relative to oncoming waves, and the tracer region dilates and compresses in the same concertina effect observed in the experiments. The kinematics are very different in the higher shear partial and full internal shock regimes, where surface tracer particles either move faster than the waves or move with the velocity of the wavefronts. At the moment there is no experimental evidence of this type of behaviour, but it may well occur in highly sheared geophysical flows.

Irrespective of which type of kinematics dominates, hazardous geophysical mass

flows spontaneously develop waves that move significantly faster than depth-averaged flow, have wave peak heights that are significantly higher than an equivalent steady uniform flow and have high concentrations of large particles at their wave crests. All of these factors strongly enhance the impact pressures that such flows can exert on structures in their path, making these flows significantly more destructive than current design criteria may allow for. It is therefore anticipated that modelling roll waves and surges in hazard assessments will become much more important in future.

This research was supported by NERC grants NE/E003206/1 and NE/K003011/1 as well as EPSRC grants EP/I019189/1, EP/K00428X/1 and EP/M022447/1. J.M.N.T.G. is a Royal Society Wolfson Research Merit Award holder (WM150058) and an EPSRC Established Career Fellow (EP/M022447/1). J.L.B. would also like to acknowledge support from a NERC doctoral training award and the University of Sydney HPC service. F.M.R. acknowledges financial support from CNPq, Conselho Nacional de Desenvolvimento Científico e Tecnológico – Brazil. All research data supporting this publication are directly available within this publication.

Appendix A. Construction of viscous travelling-wave solutions

This appendix explains how to construct viscous travelling-wave solutions for the bulk thickness and velocity field, and compares to the analogous inviscid case of §4. As before, switching to a moving reference frame and seeking steady travelling-wave solutions, the bulk mass and momentum balance equations (3.9) and (3.10) reduce to

$$\frac{d}{d\xi}(h(\bar{u} - u_w)) = 0, \quad (\text{A } 1)$$

$$\frac{d}{d\xi}(h\bar{u}(\bar{u} - u_w)) + \frac{d}{d\xi} \left(\frac{1}{2}gh^2 \cos \zeta \right) = gh \cos \zeta (\tan \zeta - \mu_b) + \frac{d}{d\xi} \left(\nu h^{3/2} \frac{d\bar{u}}{d\xi} \right). \quad (\text{A } 2)$$

Equation (A 1) can be integrated directly to give

$$h(u_w - \bar{u}) = Q_1, \quad (\text{A } 3)$$

for constant Q_1 , and substituting (A 3) into (A 2) leads to the second-order ODE

$$\frac{d^2 h}{d\xi^2} = \frac{1}{2h} \left(\frac{dh}{d\xi} \right)^2 + \frac{gh^{3/2} \cos \zeta}{\nu Q_1} \left[\left(1 - \frac{Q_1^2}{gh^3 \cos \zeta} \right) \frac{dh}{d\xi} - \tan \zeta + \mu_b(h) \right], \quad (\text{A } 4)$$

with

$$\mu_b(h) = \mu_1 + \frac{(\mu_2 - \mu_1)(hu_w - Q_1)}{\gamma h^{5/2} + hu_w - Q_1}. \quad (\text{A } 5)$$

Introducing $n = dh/d\xi$, allows this to be written as a first-order system

$$\frac{dh}{d\xi} = n, \quad (\text{A } 6)$$

$$\frac{dn}{d\xi} = \frac{1}{2h}n^2 + \frac{gh^{3/2}\cos\zeta}{\nu Q_1} \left[\left(1 - \frac{Q_1^2}{gh^3\cos\zeta} \right) n - \tan\zeta + \mu_b(h) \right], \quad (\text{A } 7)$$

with unknown parameters u_w and Q_1 . Gray & Edwards (2014) used (A 3) to relate Q_1 to u_w by assuming that each wave must go through the equilibrium point $h = h_0$, $\bar{u} = \bar{u}_0$. They then constructed periodic roll wave solutions as limit cycles in (h, n) -space around this fixed point by solving an initial value problem (IVP) and extracting the final periodic orbit. Gray & Edwards (2014) found that subtly different values of u_w gave rise to waves with drastically different wavelengths and amplitudes. This approach may be considered as the viscous analogue to the basic solution procedure of §4.1, with the main difference being that the resulting families of waves no longer travel at exactly the same speed as each other. A slightly different approach is adopted here. The viscous travelling-wave solutions are instead directly related to their parent steady uniform flow, in a similar way to the inviscid case explained in §4.2. To achieve this, it is useful to define

$$m(\xi) = \frac{1}{\Lambda} \int_0^\xi h(\xi') \bar{u}(\xi') d\xi', \quad (\text{A } 8)$$

where Λ is the wavelength of one wave. Note that $m(\Lambda) = q$, with the mean flux q being given by (4.24), and hence the waves that form from a steady uniform inflow (h_0, \bar{u}_0) are those for which $m(\Lambda) = q_0$. Equation (A 8) can also be written as a first-order ODE (using (A 3))

$$\frac{dm}{d\xi} = \frac{h}{\Lambda} \left(u_w - \frac{Q_1}{h} \right), \quad (\text{A } 9)$$

and the problem can now be reduced to a Boundary Value Problem (BVP) by solving (A 6), (A 7) and (A 9) subject to the boundary conditions

$$h(0) = h(\Lambda), \quad n(0) = n(\Lambda) = 0, \quad m(0) = 0, \quad m(\Lambda) = q_0. \quad (\text{A } 10)$$

For a given wavelength Λ these five conditions allow the two unknown parameters u_w and Q_1 to be found in conjunction with the three dependent variables h , n and m , providing a suitable initial guess is chosen. Here, such a guess is provided using the solution procedure of Gray & Edwards (2014) to find a limit cycle solution, which does not necessarily have the correct average flux or wavelength. The BVP is then solved iteratively, until the solution does have the correct mean flux, using *bvp4c* in

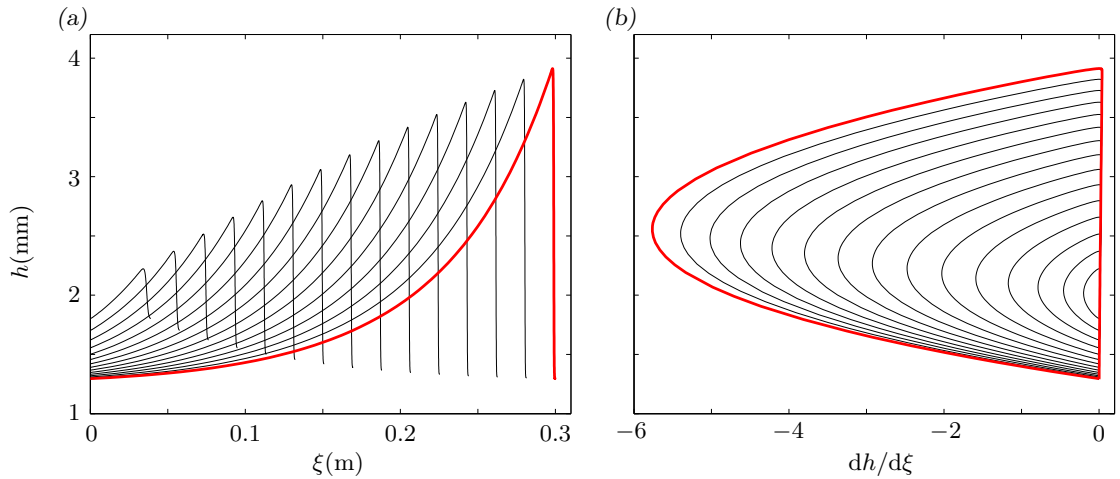


FIGURE 16: An example family of viscous roll wave solution using a BVP solver in (a) the physical plane (ξ, h) and (b) the phase plane (n, h) . Black lines represent previous iterations used to construct the final wave of wavelength 0.3 m (red). The inflow thickness and mean concentration are $h_0 = 0.002$ m and $\bar{\phi}_0 = 0.4$ respectively.

Matlab with the previous solution as an initial guess. At each stage the wavelength is gradually adjusted until it is equal to the required Λ . Figure 16 shows example wave profiles constructed with this method, with all (black) solutions having the same average flux and the final (red) wave having the desired wavelength.

These viscous travelling-wave solutions can also be directly compared to the inviscid ones constructed in §4.2. Setting the steady uniform inflow thickness h_0 and mean concentration $\bar{\phi}_0$ leads to a constant upstream flux q_0 given by equation (4.23). From this inflow flux, a family of inviscid roll waves can be found, each of them having a different amplitude and velocity but all with the same flux as q_0 (illustrated on figure 7). The wavelength of each of these inviscid waves can then be matched by the BVP procedure described above to get the corresponding viscous solution. Figure 17a) shows a comparison between inviscid and viscous travelling waves for the same inflow flux ($h_0 = 0.002$ m and $\bar{\phi}_0 = 0.4$). The viscous solution is almost identical to the inviscid one and a close-up view is actually needed to see any influence of the viscosity on the wave properties. In figure 17b), a zoom of the last wave shows the difference between both solutions. As expected, the viscosity smooths the shape of the wave and leads to a less sharp shock, but the differences are otherwise minimal.

REFERENCES

- BAKER, J. L., BARKER, T. & GRAY, J. M. N. T. 2016a A two-dimensional depth-averaged $\mu(I)$ -rheology for dense granular avalanches. *J. Fluid Mech.* **787**, 367–395.

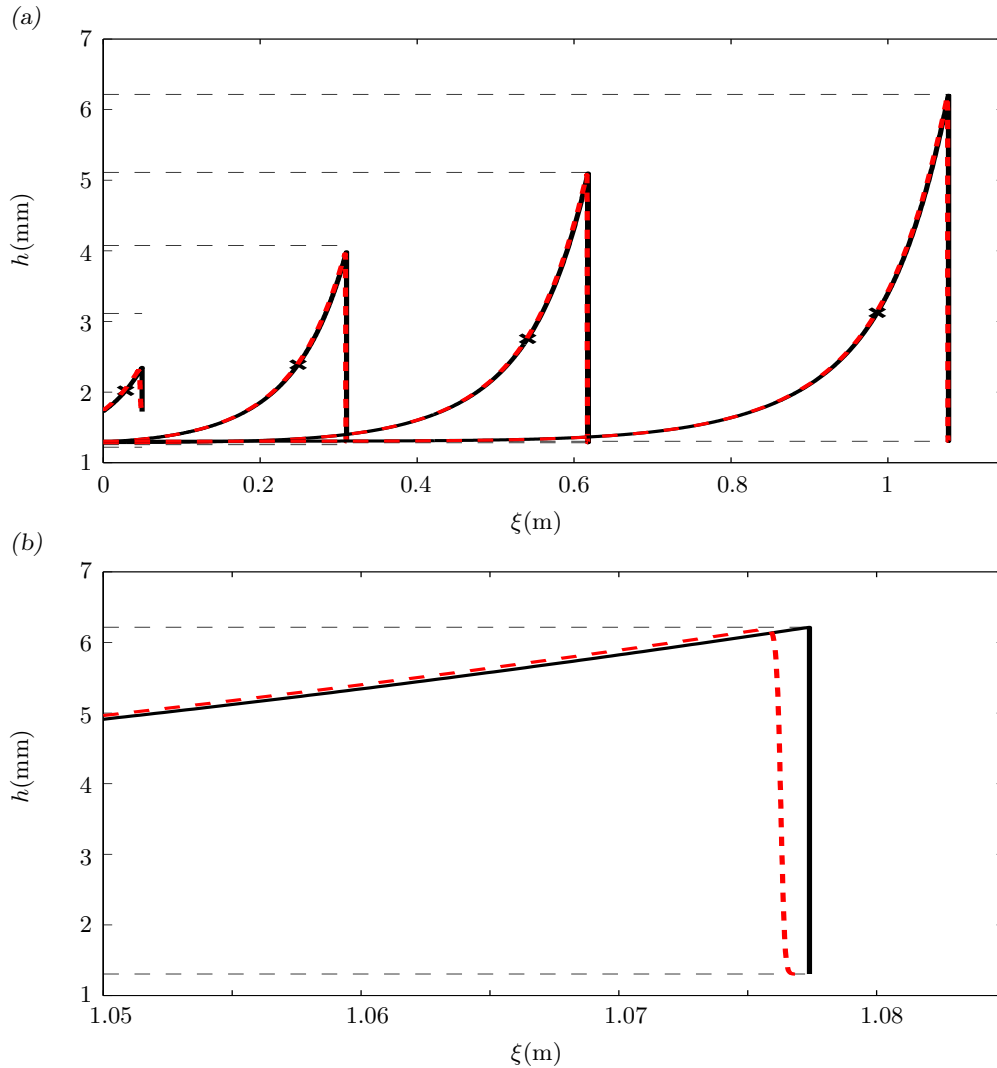


FIGURE 17: a) Comparison between inviscid (solid black lines) and viscous solutions (red dashed lines) of a family of roll wave solutions resulting from a steady uniform inflow thickness $h_0 = 2$ mm and mean concentration $\bar{\phi}_0 = 0.4$. The dashed black lines represent the theoretical absolute minimum and maximum thickness obtained from the inviscid solution. b) close-up of the largest wave showing the differences between both solutions.

BAKER, J. L., JOHNSON, C. G. & GRAY, J. M. N. T. 2016*b* Segregation-induced finger formation in granular free-surface flows. *J. Fluid Mech.* **809**, 168–212.

BALMFORTH, N. J. & LIU, J. 2004 Roll waves in mud. *J. Fluid Mech.* **519**, 33–54.

BALMFORTH, N. J. & MANDRE, S. 2004 Dynamics of roll waves. *J. Fluid Mech.* **514**, 1–33.

BARKER, T. & GRAY, J. M. N. T. 2017 Partial regularisation of the incompressible $\mu(I)$ -rheology for granular flow. *J. Fluid Mech.* **828**, 5–32.

BARKER, T., SCHAEFFER, D. G., BOHORQUEZ, P. & GRAY, J. M. N. T. 2015 Well-posed and ill-posed behaviour of the $\mu(I)$ -rheology for granular flow. *J. Fluid Mech.* **779**, 794–818.

BRIDGWATER, J., FOO, W. & STEPHENS, D. 1985 Particle mixing and segregation in failure zones - theory and experiment. *Powder Technol.* **41**, 147–158.

CHADWICK, P. 1976 *Continuum Mechanics. Concise theory and problems*. George Allen & Unwin.

- CHANG, H. C., DEMEKHIN, E. A., KALAJDIN, E. N. & YE, Y. 1996 Coarsening dynamics of falling-film solitary waves. *Phys. Rev. E* **54**, 1467.
- DOLGUNIN, V. N. & UKOLOV, A. A. 1995 Segregation modelling of particle rapid gravity flow. *Powder Technol.* **83**, 95–103.
- DRESSLER, R. F. 1949 Mathematical solution of the problem of roll-waves in clined open channels. *Comm. Pure Appl. Math.* **2**, 149–194.
- EDWARDS, A. N. & GRAY, J. M. N. T. 2015 Erosion–deposition waves in shallow granular free-surface flows. *J. Fluid Mech.* **762**, 35–67.
- FAN, Y., SCHLICK, C. P., UMBANHOWAR, P., OTTINO, J. M. & LUEPTOW, R. 2014 Modelling size segregation of granular materials: the roles of segregation, advection and diffusion. *J. Fluid Mech.* **741**, 252–279.
- FÉLIX, G. & THOMAS, N. 2004 Relation between dry granular flow regimes and morphology of deposits: formation of levées in pyroclastic deposits. *Earth Planet. Sci. Lett.* **221**, 197–213.
- FORTERRE, Y. 2006 Kapiza waves as a test for three-dimensional granular flow rheology. *J. Fluid Mech.* **563**, 123–132.
- FORTERRE, Y. & POULIQUEN, O. 2003 Long-surface-wave instability in dense granular flows. *J. Fluid Mech.* **486**, 21–50.
- GAJJAR, P. & GRAY, J. M. N. T. 2014 Asymmetric flux models for particle-size segregation in granular avalanches. *J. Fluid Mech.* **757**, 297–329.
- GAJJAR, P., VAN DER VAART, K., THORNTON, A. R., JOHNSON, C. G., ANCEY, C. & GRAY, J. M. N. T. 2016 Asymmetric breaking size-segregation waves in dense granular free-surface. *J. Fluid Mech.* **794**, 460–505.
- GDR MIDI 2004 On dense granular flows. *Eur. Phys. J. E* **14** (4), 341–65.
- GOUJON, C., THOMAS, N. & DALLOZ-DUBRUJEAUD, B. 2003 Monodisperse dry granular flows on inclined planes: Role of roughness. *Eur. Phys. J. E* **11**, 147–157.
- GRAY, J. M. N. T. 2018 Particle segregation in dense granular flows. *Ann. Rev. Fluid Mech.* **50**, 407–433.
- GRAY, J. M. N. T. & ANCEY, C. 2009 Segregation, recirculation and deposition of coarse particles near two-dimensional avalanche fronts. *J. Fluid Mech.* **629**, 387–423.
- GRAY, J. M. N. T. & ANCEY, C. 2011 Multi-component particle size-segregation in shallow granular avalanches. *J. Fluid Mech.* **678**, 535–588.
- GRAY, J. M. N. T. & CHUGUNOV, V. A. 2006 Particle-size segregation and diffusive remixing in shallow granular avalanches. *J. Fluid Mech.* **569**, 365–398.
- GRAY, J. M. N. T. & EDWARDS, A. N. 2014 A depth-averaged $\mu(I)$ -rheology for shallow granular free-surface flows. *J. Fluid Mech.* **755**, 503–534.
- GRAY, J. M. N. T. & KOKELAAR, B. P. 2010a Large particle segregation, transport and accumulation in granular free-surface flows. *J. Fluid Mech.* **652**, 105–137.
- GRAY, J. M. N. T. & KOKELAAR, B. P. 2010b Large particle segregation, transport and accumulation in granular free-surface flows – Erratum. *J. Fluid Mech.* **657**, 539.

- GRAY, J. M. N. T. & THORNTON, A. R. 2005 A theory for particle size segregation in shallow granular free-surface flows. *Proc. Roy. Soc. A* **461**, 1447–1473.
- HILL, K. M. & TAN, D. S. 2014 Segregation in dense sheared flows: gravity, temperature gradients, and stress partitioning. *J. Fluid Mech.* **756**, 54–88.
- HOGG, A. J. & PRITCHARD, D. 2004 The effects of hydraulic resistance on dam-break and other shallow inertial flows. *J. Fluid Mech.* **501**, 179–212.
- HU, K. H., CUI, P. & ZHANG, J. Q. 2012 Characteristics of damage to buildings by debris flows on 7 august 2010 in zhouqu, western china. *Nat. Hazards Earth Syst. Sci.* **12**, 2209–2217.
- JEFFREYS, H. 1925 The flow of water down in an inclined channel of rectangular cross-section. *Philos. Mag.* **49**, 793–807.
- JENKINS, S. F., PHILLIPS, J. C., PRICE, R., FELOY, K., BAXTER, P. J., HADMOKO, H. S. & DE BELIZAL, E. 2015 Developing building-damage scales for lahars: application to merapi volcano, indonesia. *Nat. Hazards Earth Syst. Sci.* p. 77:75.
- JING, L., KWOK, C. Y. & LEUNG, Y. F. 2017 Micromechanical origin of particle size segregation. *Phys. Rev. Lett.* **118**, 118001.
- JOHNSON, C. G., KOKELAAR, B. P., IVERSON, R. M., LOGAN, M., LAHUSEN, R. G. & GRAY, J. M. N. T. 2012 Grain-size segregation and levee formation in geophysical mass flows. *J. Geophys. Res.* **117**, F01032.
- JOP, P., FORTERRE, Y. & POULIQUEN, O. 2005 Crucial role of sidewalls in granular surface flows: consequences for the rheology. *J. Fluid Mech.* **541**, 167–192.
- JOP, P., FORTERRE, Y. & POULIQUEN, O. 2006 A constitutive relation for dense granular flows. *Nature* **44**, 727–730.
- KÖHLER, A., MCELWAIN, J. N., SOVILLA, B., ASH, M. & BRENNAN, P. 2016 The dynamics of surges in the 3 February 2015 avalanches in Vallée de la Sionne. *J. Geophys. Res. Earth Surf.* **121**, 2192–2210.
- KOKELAAR, B., GRAHAM, R., GRAY, J. & VALLANCE, J. 2014 Fine-grained linings of leveed channels facilitate runout of granular flows. *Earth Planet. Sci. Lett.* **385** (0), 172 – 180.
- KURGANOV, A. & TADMOR, E. 2000 New high-resolution central schemes for nonlinear conservation laws and convection-diffusion equations. *J. Comput. Phys.* **160** (1), 241–282.
- LAX, P. D. 1957 Hyperbolic systems of conservation laws 2. *Comm. Pure & Appl. Math.* **10** (4), 537–566.
- LI, J., JIANMO, J. Y., BI, C. & LUO, D. 1983 The main features of the mudflow in Jiang-Jia Ravine. *Z. Geomorphol.* **27**, 325–341.
- MARKS, B., ROGNON, P. & EINAV, I. 2012 Grainsize dynamics of polydisperse granular segregation down inclined planes. *J. Fluid Mech.* **690**, 499–511.
- MCARDELL, B. W., ZANUTTIGH, B., LAMBERTI, A. & RICKENMANN, D. 2003 Systematic comparison of debris flow laws at the Illgraben torrent, Switzerland. In *Debris-flow hazards mitigation: Mechanics, prediction and assessment: proceedings of the third international conference on Debris-flow hazards mitigation, Davos, Switzerland, September 10-12, 2003* (ed. D. Rickenmann & C. L. Chen), pp. 647–658. Millpress.

- MEDOVIKOV, A. 1998 High order explicit methods for parabolic equations. *BIT* **38** (2), 372–390.
- MIDDLETON, G. V. 1970 Experimental studies related to problems of flysch sedimentation. In *Flysch Sedimentology in North America* (ed. J. Lajoie), pp. 253–272. Business and Economics Science Ltd, Toronto.
- NEEDHAM, D. J. & MERKIN, J. H. 1984 On roll waves down an open inclined channel. *Proc. Roy. Soc. Lond. A* **394**, 258–278.
- NOËLLE, S. 2000 The MoT-ICE: A new high-resolution wave-propagation algorithm for multidimensional systems of conservation laws based on fey’s method of transport. *J. Comput. Phys.* **164** (2), 283–334.
- OCKENDON, J. R., HOWISON, S., LACEY, A. & MOVCHAN, A. 2004 *Applied Partial Differential Equations (revised edition)*. Oxford University Press.
- POULIQUEN, O. 1999a Scaling laws in granular flows down rough inclined planes. *Phys. Fluids* **11** (3), 542–548.
- POULIQUEN, O., DELOUR, J. & SAVAGE, S. B. 1997 Fingering in granular flows. *Nature* **386**, 816–817.
- POULIQUEN, O. & FORTERRE, Y. 2002 Friction law for dense granular flows: application to the motion of a mass down a rough inclined plane. *J. Fluid Mech.* **453**, 133–151.
- POULIQUEN, O. & VALLANCE, J. W. 1999 Segregation induced instabilities of granular fronts. *Chaos* **9** (3), 621–630.
- RAZIS, D., EDWARDS, A., GRAY, J. & VAN DER WEELE, K. 2014 Arrested coarsening of granular roll waves. *Phys. Fluids* **26**, 297–329.
- ROGNON, P. G., ROUX, J. N., NAAIM, M. & CHEVOIR, F. 2007 Dense flows of bidisperse assemblies of disks down an inclined plane. *Phys. Fluids* **19**, 058101.
- SAINGIER, G., DEBOEUF, S. & LAGRÉE, P.-Y. 2016 On the front shape of an inertial granular flow down a rough incline. *Phys. Fluids* **28**, 053302.
- SAVAGE, S. B. 1979 Gravity flow of cohesionless granular-materials in chutes and channels. *J. Fluid Mech.* **92**, 53–96.
- SAVAGE, S. B. & HUTTER, K. 1989 The motion of a finite mass of granular material down a rough incline. *J. Fluid Mech.* **199**, 177–215.
- SAVAGE, S. B. & LUN, C. K. K. 1988 Particle size segregation in inclined chute flow of dry cohesionless granular solids. *J. Fluid Mech.* **189**, 311–335.
- SCHLICK, C. P., FAN, Y., UMBANHOWAR, P. B., OTTINO, J. M. & LUEPTOW, R. M. 2015 Granular segregation in circular tumblers: theoretical model and scaling laws. *J. Fluid Mech.* **765**, 632–652.
- STARON, L. & PHILLIPS, J. C. 2015 Stress partition and microstructure in size-segregating granular flows. *Phys. Rev. E* **92**, 022210.
- THORNTON, A. R. & GRAY, J. M. N. T. 2008 Breaking size-segregation waves and particle recirculation in granular avalanches. *J. Fluid Mech.* **596**, 261–284.
- VAN DER VAART, K., GAJJAR, P., EPELY-CHAUVIN, G., ANDREINI, N., GRAY, J. M. N. T. & ANCEY, C. 2015 Underlying asymmetry within particle size segregation. *Phys. Rev. Lett.* **114**, 238001.
- VIROULET, S., BAKER, J. L., EDWARDS, A. N., JOHNSON, C. G., GJALTEMA, C., CLAVEL, P. & GRAY,

J. M. N. T. 2017 Multiple solutions for granular flow over a smooth two-dimensional bump. *J. Fluid Mech.* **815**, 77–116.

WOODHOUSE, M. J., THORNTON, A. R., JOHNSON, C. G., KOKELAAR, B. P. & GRAY, J. M. N. T. 2012 Segregation-induced fingering instabilities in granular free-surface flows. *J. Fluid Mech.* **709**, 543–580.

ZANUTTIGH, B. & LAMBERTI, A. 2007 Instability and surge development in debris flows. *Rev. Geophys.* **45**, RG3006.

6 | Conclusion

This thesis has investigated two distinct physical processes observed in dense granular flows through a combination of small-scale experiments, theory and numerical simulations. The first part of the thesis, linked to chapters 3 and 4, is dedicated to investigating flows in which the granular material self-channelises by spontaneously forming static levees that confine a fluid-like motion. The second part, related to chapter 5, presents an analysis of the kinematics of bidisperse granular roll waves, and investigates the different possible flow regimes, depending on particle concentration and bulk properties. To conclude, we highlight the main outcomes of each chapter and seize on the opportunity to emphasise the limitations of each of the models and discuss the possible avenues of future work.

In *Self-channelisation and levee formation in monodisperse granular flows*, a depth-averaged viscous theory is used to show that two ingredients are crucial to quantitatively predict the self-channelisation process. On one hand, frictional hysteresis, which is incorporated into the model via a non-monotonic friction law, is responsible for allowing the coexistence of static and moving layers. Due to the hysteretic nature, when the granular material flowing down the channel gets to the front, is advected to the sides and slows down, friction transitions to a velocity-decreasing behaviour and the material eventually comes to rest, forming the lateral static levees. Depth-averaged viscous stresses have the important function of creating a cross-slope velocity profile that connects static and fast-moving regions seamlessly through a shear-band-like structure, and provides the selection mechanism for the equilibrium state. The theory shows that, for a given inclination angle, there is a well-defined stress balance which governs the steady state for the *moving channel*, where gravity and basal friction are balanced by a depth-averaged lateral viscous stress. By seeking steady uniaxial solutions, which are invariant in the downslope direction, the model predicts that the thickness profile is

uniform across the fluid-like channel, and the motion is purely downstream, i.e. there is no depth-averaged lateral velocity. Thus, the steady-state force balance boils down to a second-order ordinary differential equation for the velocity profile across the moving channel, which has two unknown parameters: The constant thickness of the channel and the position of the levees, i.e. the width of the moving region. Assuming that the levee-channel boundaries are subjected to no-slip and no velocity gradient conditions and using the integral constraint, which relates the constant inflow mass flux to the flux across the channel, the boundary value problem admits solutions that goes from zero velocity at the levee-channel boundary to a maximum at the centre of the channel. This contrasts with the classic shallow-water inviscid approach, which predicts a constant speed everywhere across the channel and the steady state is degenerate. It is worth mentioning that in order to close the system of equations, it was crucial to assume that the lateral stress vanishes at the channel-levee interface ($d\bar{u}/dy = 0$ at the boundaries). Although we have not tested in our experiments, this assumption is supported by experimental measurements (Takagi *et al.*, 2011), discrete particle simulations, where the shear-rate appears to vanish adjacent to fully rough walls (Silbert *et al.*, 2003), and also assumed in non-local continuum modelling of granular flows down inclines (Kamrin & Henann, 2015).

The viscous theory predicts that solutions exist only for a range of thicknesses narrower than the hysteretic band, i.e. the region of existence is not limited by h_* and h_{start} . Instead, for thickness above a threshold $H_{max} < h_{start}$, the model predicts that friction lies in the velocity-decreasing regime everywhere in the channel and, hence, steady solutions become unstable. On the other extreme, the system undergoes a homoclinic bifurcation at a thickness $H_{min} > h_*$, below which no symmetric steady uniaxial solutions can be constructed, defining the lower bound of the existence region. It is interesting that the upper bound H_{max} is associated with a minimum mass flux Q_{min} , whereas the thickness goes to H_{min} when $Q_M \rightarrow \infty$.

Our steady-state predictions are compared against experimental data for flows of spherical glass beads (Félix & Thomas, 2004) and also angular sand particles (Takagi *et al.*, 2011). The results obtained directly from the depth-integrated model, such as how the width and height of the moving channel vary with the inflow mass flux, are in good quantitative agreement with experiments. However, when we try to reconstruct

the surface velocity from depth-averaged fields it is required to use an exponential shear profile to best represent the experimental data, which is different from the Bagnold velocity profile that comes out naturally from the $\mu(I)$ -rheology and was used in the depth-averaging process. The internal structure of a self-channelised flow in terms of what is exactly the depth of the moving layer is still an open question, which may be revealed with the development of novel dynamic X-ray techniques capable of accessing flow fields without affecting the flow (e.g. Baker *et al.*, 2018). Another interesting fact is that, due to frictional hysteresis as well as the multivalued nature of the static friction, there are infinitely many solutions for a levee profile able to sustain a self-channelised flow at a given angle and mass flux. In order to estimate the width of the static levees we assume that all the points in the solid margins are on the brink of yielding to compute the minimum levee profile able to support the traction of the fluidised flow.

Regarding the steady-state predictions, one limitation of the model relates to the constant thickness of the moving channel. In experiments, non-uniform free surface profiles are observed, specially for narrow channels, in which thickness gradients generally coincides with regions where the velocity profile is also non-uniform (Félix & Thomas, 2004; Takagi *et al.*, 2011). As said before, this change in the free-surface profile might stem from second normal stress difference (McElwaine *et al.*, 2012) and/or compressibility effects (Barker *et al.*, 2017; Heyman *et al.*, 2017; Schaeffer *et al.*, 2019), which are not straightforward to implement in a depth-averaged framework.

Time-dependent simulations were performed to investigate the evolution to the equilibrium state, and the process of levee formation. Our transient solutions corroborate the steady-state force balance, showing that a slow lateral creep process increases the width set by the front until it asymptotically converges to the velocity profile anticipated by the steady-state theory. This indicates that the width of self-channelised flows is not completely set by the dynamics at the flow head. Cyclic changes in the mass flux long after the initial front has passed also show that the width of the moving channel always converges to the steady-state profile associated with the corresponding mass flux, which shows the selection of a well-defined equilibrium state independent of history. By decreasing the inflow flux we show that below a critical mass flux the system transitions from a steadily travelling front to an unsteady regime, where the

front comes to a halt and a depositing wave is sent backwards, bringing all the material to rest. Due to the constant injection rate, a pile of material builds up near the source, which fails triggering an avalanche that propagates through the existing deposit, and stops not long after it reaches the empty rough base. This process eventually becomes periodic with the pulses being triggered at a well-defined period. The theory qualitatively agrees with the experiments of Takagi *et al.* (2011), but the period of the waves is over-predicted. There are possible explanations for this quantitative disagreement. First, the period of the waves is strongly related to the failure process of the static pile near the source, where it is not so obvious that the shallowness assumption should still hold. Another possibility is that at the solid-liquid phase transition variations in the volume fraction may start playing a more important role, which is not accounted for in our model.

The work presented in this chapter opens up avenues for future investigation. In the domain of monodisperse flows the steady-state solution here obtained can be used as the base state to perform a two-dimensional stability analysis, which may be useful to reveal the physics of the very small wavelength instability, which is almost always observed for sand particles. Another natural extension of this study would be to use the same approach to investigate self-channelisation in bidisperse flows. At first, the problem could be tackled with the simpler “effectively monodisperse” rheology, similar to the one presented in chapter 5, which would imply that the steady-state force balance would still hold, but now with the basal friction law being a function of the depth-averaged concentration. It is anticipated that for slope angles, where steady uniform flows are not possible for the larger and more frictional particles, segregation-mobility feedback may lead to more complex patterns, even for high flow rates. The steady-state results could be a way of computing a maximum concentration of more frictional grains, which still leads to an equilibrium situation with a single leveed channel. Moreover, the time-dependent solution can be easily expanded to account for gravity-driven segregation, which would allow more complicated pattern formation, such as constant changes in the path of a leveed channel, normally termed avulsions (de Haas *et al.*, 2018), which are very often observed on deposit fans of debris flows.

In *Granular fingering on a cone* we investigate another manifestation of frictional

hysteresis that leads to monodisperse self-channelisation, but this time for a flow down a rough cone. It is important to note that, at the time of writing, this project is still work in progress. Due to the conical geometry, the granular material, which is injected onto the cone with constant volume flux, thins as it propagates down, generating a decelerating flow front. The flow is initially governed by a velocity-strengthening basal friction, but as the material progresses downstream, it eventually transitions to the velocity-decreasing part of the friction curve, which is unstable, destabilising the flow and generating the self-channelised fingers. The onset of the instability is studied experimentally by using digital image processing to compute the critical radial position downstream the cone at which the material undergoes a solid-liquid phase transition, and the first levees start to form. Moreover, the number of fully developed fingers able to reach the bottom of the conical surface is measured. Experiments were performed for a range of inflow volume fluxes in order to investigate how the critical radius and the number of fully developed fingers vary with the injection rate. A depth-averaged avalanche model was used to model the initial axisymmetric spreading and predict the critical radial position. Crucially, the model incorporates frictional hysteresis via a non-monotonic basal friction law, in which the transition from velocity-strengthening to velocity-weakening defines when the flow becomes unstable. It is interesting that the theory predicts that the velocity-decreasing friction becomes active not at the front, but just behind the flow head, where the Froude number reaches a global minimum. This suggests that the source of the instability does not stem from the frontal interface. Another intriguing fact is the offset in the $r_{crit}(Q)$ function, which is not predicted by just using steady-state mass conservation arguments that lead to a purely linear relation, where the critical radius goes to zero when the flux vanishes. In order to recover this offset, time-dependent axisymmetric simulations had to be performed, suggesting that the offset is given by the length of the granular front, which is not taken into account in steady solutions.

In order to infer the number of fully developed fingers far downstream the cone, we apply the theory developed in chapter 3. We assume that far downstream the cone azimuthal curvature terms can be neglected and a flow over the cone is, at leading order, the same as a flow over a flat plane. At the splitting point, it is assumed that the interface breaks into the number of fingers, such that the perimeter of the

circular interface is equally divided by identical leveed channels, whose morphology is characterised by a central channel bounded by two static levees. The self-channelised solution presented in chapter 3 provides the relation between the volume flux and the width of the central fluidised channel, and the minimum levee profile is used to estimate the width of each levee. Moreover, in the long-time limit the inflow volume flux at the gate is also equally shared between the fingers. Thus, the number of fully developed fingers is found when both assumptions are satisfied at the same time. The theory is compared against experimental observations for the number of fingers as a function of the flux, and although the theoretical curve suggests a slightly steeper gradient, both curves display a very similar linear trend. The spreading and slowing features of the granular flow over the cone may provide a good test for rheological models, aiming to incorporate and better understand the transition to the velocity-decreasing friction.

Viscous and inviscid steady axisymmetric solutions should be compared in order to properly understand the role of the depth-averaged viscous stresses on the initial axisymmetric spreading. Steady axisymmetric solutions should be computed to predict the radial position at which the velocity-decreasing friction becomes active, which would allow us to have a more clear conclusion on the origin of the offset in the $r_{crit}(Q)$ function. The analysis presented here is appropriate for the initial radial spreading and it seems reasonable to assume the self-channelised morphology to compute the number of fully developed fingers. However, we lose information about the transition region between these two extreme states. Two-dimensional depth-averaged simulations in the “pac-man domain” (see figure 6 of chapter 4) would be a significant step forward to understand the full dynamical process.

Finally, in *The kinematics of bidisperse granular roll waves*, small-scale experiments with two sizes of spherical glass particles are performed to investigate the kinematics of bidisperse roll waves. From the experiments, we observe that waves propagate faster and also have larger amplitudes for higher concentrations of small particles. Experiments also show a larger concentration of large particles at the wave crests, which interestingly is not due to accumulation of individual larger grains at the wave front. Instead, tracer particles placed at the surface of the flow indicate that surface large particles move slower than the wave peak, and, hence, have an effective backwards motion relative to the wave, but, on the other hand, when they get to the rear they

start moving faster than the wave, creating a forward relative motion. As a result, this creates a *concertina* effect that increases the concentration of larger grains just behind the wave crest. A depth-averaged approach is used to investigate the effects of particle-size segregation on the kinematics of the waves. Since roll waves develop for fast flows, in this chapter only the dynamic velocity-strengthening part of the friction law is used. In order to keep the mathematical simplicity, the bidisperse material is treated as effectively monodisperse, where the rheological parameters are weighted by the concentration of each species of particles. As a result, travelling-wave solutions can be constructed for the bulk flow and these are then used to compute solutions for the concentration profile. For the bulk flow, we first consider an inviscid depth-averaged momentum balance, in which the thickness profile of the waves is determined by a first-order differential equation and jump conditions are used to construct periodic wavetrains. The inviscid ODE has a critical point, where its numerator and denominator vanish, which allows the computation of maximum and minimum thicknesses for a roll wave, as well as how the wavespeed, wavelength and amplitude of the waves relate for different depth-averaged concentrations. Travelling-wave solutions are also constructed for the concentration by prescribing a velocity profile from the steady solutions for the bulk. We find that there are three different flow regimes depending on the relative speed between surface particles and the wave, where surface particles can move slower than the waves everywhere, anywhere or just in some regions. The different regimes are associated with the amount of shear through the avalanche depth. In experiments, however, we only observe the regime where all surface particles always move slower than wave crests, which results in the concertina effect mentioned above.

We compute time-dependent solutions using the viscous set of conservation laws, which shows that all the classes of solutions found in the inviscid travelling-wave ODE are indeed observed in the time-dependent system of viscous equations. Simulations are performed with tracers to investigate transient kinematics of the different classes of solutions. The same concertina effect is observed numerically in the low shear regime, whereas for high shear, particles firstly move faster than the waves but get trapped when they get to the wave front and move precisely with the wavespeed thereafter. In order to mimic the experimental situation, simulations are carried with random inflow perturbations, which show that waves develop with different wavespeeds and

amplitudes, and, hence, simulations also display coarsening dynamics, with the waves merging due to their different speeds, similarly to what is seen in the experiments.

As mentioned during the thesis, when the bidisperse material is treated as effectively monodisperse the model does not correspond to reality, where local accumulation of a given species affects the granular rheology locally. Therefore, a way of improving the quantitative agreement between theory and experiments would be to perform time-dependent simulations of the fully coupled system of equations. The basal friction law is then a function of the local concentration, which is allowed to change in space and time, in similar way to what is done by Baker *et al.* (2016b) to model segregation-induced finger formation. An interesting feature less explored in this paper is the presence of white bands near the rigid glass sidewalls (see figure 1 of chapter 5). This is an indication that even under effect of gravity, small particles (white ones here) are able to remain at the surface near the walls, suggesting that there is a competition between segregation processes, with gravity-driven segregation being dominant in the centre and some other mechanism takes over near the boundaries. One possible explanation would be to consider shear-induced segregation (Fan & Hill, 2011). It is also possible that longitudinal vortices are forming in dipole configuration or even in wider chains, depending on the confining distance (Brodu *et al.*, 2013). Therefore, another possible explanation for the fine linings at the margins of the chute is the presence of large amplitude vortices in near-wall regions and weaker convection rolls towards the centre of the flow. As a result, near the margins the lateral motion of grains would be dominated by circulation, whilst in the centre diffusion governs the segregation pattern. Preliminary time-dependent simulations of the inviscid depth-averaged segregation equation in a unit cell show that the existence of circulating stream functions in the cross slope direction might explain lateral segregation of a initially vertically segregated mixture. Moreover, the existence of two regimes, which have not yet been found experimentally motivates more experiments to be performed in order to reveal in which scenario these regimes may occur.

Bibliography

- ABRAMOWITZ, M. & STEGUN, I. 1970 *Handbook of Mathematical Functions*, 9th edn., p. 3.3.7. Dover.
- AHN, H., BRENNEN, C. E. & SABERSKY, R. H. 1991 Measurements of velocity, velocity fluctuation, density, and stresses in chute flows of granular materials. *J. Applied Mech.* **58** (3), 792–803.
- ANDREOTTI, B., FORTERRE, Y. & POULIQUEN, O. 2013 *Granular media: between fluid and solid*. Cambridge University Press.
- ARANSON, I. S. & TSIMRING, L. S. 2001 Continuum description of avalanches in granular media. *Phys. Rev. E* **64** (2), 020301.
- ARANSON, I. S. & TSIMRING, L. S. 2002 Continuum theory of partially fluidized granular flows. *Phys. Rev. E* **65** (6), 061303.
- BAGNOLD, R. A. 1954 Experiments on gravity-free dispersion of large solid spheres in a newtonian fluid under shear. *Proc. Roy. Soc. Lond. A* **225**, 49–63.
- BAKER, J., GUILLARD, F., MARKS, B. & EINAV, I. 2018 X-ray rheography uncovers planar granular flows despite non-planar walls. *Nat. Commun.* **9** (1), 5119.
- BAKER, J. L., BARKER, T. & GRAY, J. M. N. T. 2016a A two-dimensional depth-averaged $\mu(I)$ -rheology for dense granular avalanches. *J. Fluid. Mech.* **787**, 367–395.
- BAKER, J. L., JOHNSON, C. G. & GRAY, J. M. N. T. 2016b Segregation-induced finger formation in granular free-surface flows. *J. Fluid. Mech.* **809**, 168–212.
- BARALE, L. 2015 Footstep-triggered grain flows on the lee side of a desert sand dune (Erg Chebbi, Morocco). *Int. J. Earth Sci.* **104** (8), 2213.

- BARAN, O., ERTAŞ, D., HALSEY, T. C., GREST, G. S. & LECHMAN, J. B. 2006 Velocity correlations in dense gravity-driven granular chute flow. *Phys. Rev. E* **74** (5), 051302.
- BARBOLINI, M., DOMAAS, U., FAUG, T., GAUER, P., HÁKONARDÓTTIR, K. M., HARBITZ, C. B., ISSLER, D., JÓHANNESSEN, T., LIED, K., NAAIM, M., NAAIM-BOUVET, F. & RAMMER, L. 2009 *EUR 23339 – The design of avalanche protection dams – Recent practical and theoretical developments*. European Commission.
- BARKER, T., SCHAEFFER, D. G., BOHÓRQUEZ, P. & GRAY, J. M. N. T. 2015 Well-posed and ill-posed behaviour of the $\mu(I)$ -rheology for granular flows. *J. Fluid. Mech.* **779**, 794–818.
- BARKER, T., SCHAEFFER, D. G., SHEARER, M. & GRAY, J. M. N. T. 2017 Well-posed continuum equations for granular flow with compressibility and $\mu(I)$ -rheology. *Proc. R. Soc. A* **473** (2201), 20160846.
- BARTELT, P., GLOVER, J., FEISTL, T., BÜHLER, Y. & BUSER, O. 2012 Formation of levees and en-echelon shear planes during snow avalanche run-out. *J. Glaciol.* **58**, 980–992.
- BATCHELOR, G. K. 1967 *An Introduction to Fluid Dynamics*. Cambridge University Press.
- BATES, L. 1997 *User guide to segregation*. Marlow: British Material Handling Board.
- BATES, L. 2006 Bulk solids characterisation-the need for industrial education in bulk technology. *Bulk Solids Handling* **26** (7), 464–475.
- BAUMBERGER, T., HESLOT, F. & PERRIN, B. 1994 Crossover from creep to inertial motion in friction dynamics. *Nature* **367** (6463), 544.
- BAXTER, J., TÜZÜN, U., HEYES, D., HAYATI, I. & FREDLUND, P. 1998 Stratification in poured granular heaps. *Nature* **391**, 136.
- BÖRZSÖNYI, T. & ECKE, R. E. 2006 Rapid granular flows on a rough incline: Phase diagram, gas transition, and effects of air drag. *Phys. Rev. E* **74** (6), 061301.

- BOUCHUT, F. & WESTDICKENBERG, M. 2004 Gravity driven shallow water models for arbitrary topography. *Comm. Math. Sci* **2**, 359–389.
- BRIDGWATER, J. 1976 Fundamental powder mixing mechanisms. *Powder Technol.* **15**, 215–236.
- BRIDGWATER, J., FOO, W. & STEPHENS, D. 1985 Particle mixing and segregation in failure zones - theory and experiment. *Powder Technol.* **41**, 147–158.
- BRODU, N, RICHARD, P & DELANNAY, R 2013 Shallow granular flows down flat frictional channels: Steady flows and longitudinal vortices. *Phys. Rev. E* **87**, 022202.
- CALDER, E. S., SPARKS, R. S. J. & GARDEWEG, M. C. 2000 Erosion, transport and segregation of pumice and lithic clasts in pyroclastic flows inferred from ignimbrite at lascar volcano, chile. *J. Volcan. Geotherm. Res.* **104**, 201–235.
- CARRIGY, M. A. 1970 Experiments on the angles of repose of granular materials 1. *Sedimentology* **14** (3-4), 147–158.
- CHADWICK, P. 1976 *Continuum Mechanics. Concise theory and problems*. George Allen & Unwin.
- CRASSOUS, J., METAYER, J-F., RICHARD, P. & LAROCHE, C. 2008 Experimental study of a creeping granular flow at very low velocity. *J. Stat. Mech.: Theory Exp* **2008** (03), P03009.
- DA CRUZ, F., EMAM, S., PROCHNOW, M., ROUX, J. N. & CHEVOIR, F. 2005 Rheophysics of dense granular materials: Discrete simulation of plane shear flows. *Phys. Rev. E* **72** (2).
- CUI, X. & GRAY, J. M. N. T. 2013 Gravity-driven granular free-surface flow around a circular cylinder. *J. Fluid Mech.* **720**, 314–337.
- CUI, X., GRAY, J. M. N. T. & JÓHANNESSON, T. 2007 Deflecting dams and the formation of oblique shocks in snow avalanches at flateyri, Iceland. *J. Geophys. Res.* **112**, F04012.
- DAERR, A. 2001 Dynamical equilibrium of avalanches on a rough plane. *Phys. Fluids* **13**, 2115–2124.

- DAERR, A. & DOUADY, S. 1999 Two types of avalanche behaviour in granular media. *Nature* **399**, 241–243.
- DEBOEUF, S., LAJEUNESSE, E., DAUCHOT, O. & ANDREOTTI, B. 2006 Flow rule, self channelization, and levees in unconfined granular flows. *Phys. Rev. Lett.* **97**, 158303.
- DEGIULI, E. & WYART, M. 2017 Friction law and hysteresis in granular materials. *Proc. Nat. Acad. Scien.* **114** (35), 9284–9289.
- DENISSEN, I. F. C., WEINHART, T., TE VOORTWIS, A., LUDING, S., GRAY, J. M. N. T. & THORNTON, A. R. 2019 Bulbous head formation in bidisperse shallow granular flow over an inclined plane. *J. Fluid Mech.* **866**, 263–297.
- DENLINGER, R. P. & IVERSON, R. M. 2001 Flow of variably fluidized granular masses across three-dimensional terrain 2. numerical predictions and experimental tests. *J. Geophys. Res.* **106** (B1), 553–566.
- DOLGUNIN, V. N. & UKOLOV, A. A. 1995 Segregation modelling of particle rapid gravity flow. *Powder Technol.* **83**, 95–103.
- DOYLE, E. E., HOGG, A. J. & MADER, H. 2011 A two-layer approach to modelling the transformation of dilute pyroclastic currents into dense pyroclastic flows. *Proc. Roy. Soc. A* **467** (2129), 1348–1371.
- DRUCKER, D. C. & PRAGER, W. 1952 Soil mechanics and plastic analysis or limit design. *Quart. Appl. Math* **10** (2), 157–165.
- DURAN, J. 1997 *Sables, poudres et grains*. Eyrolles.
- ECKERSTORFER, M. & CHRISTIANSEN, H. H. 2012 Meteorology, topography and snowpack conditions causing two extreme mid-winter slush and wet slab avalanche periods in high arctic maritime svalbard. *Permaf. Periglac. Process.* **23** (1), 15–25.
- EDWARDS, A. N. & GRAY, J. M. N. T. 2015 Erosion-deposition waves in shallow granular free-surface flows. *J. Fluid Mech.* **762**, 35–67.

- EDWARDS, A. N., RUSSELL, A. S., JOHNSON, C. G. & GRAY, J. M. N. T. 2019 Frictional hysteresis and particle deposition in granular free-surface flows. *J. Fluid Mech.* **875**, 1058–1095.
- EDWARDS, A. N., VIROULET, S., KOKELAAR, B. P. & GRAY, J. M. N. T. 2017 Formation of levees, troughs and elevated channels by avalanches on erodible slopes. *J. Fluid Mech.* **823**, 278–315.
- EHRICHS, E. E., JAEGER, H. M., KARCZMAR, G. S., KNIGHT, J. B., KUPERMAN, V. Y. & NAGEL, S. R. 1995 Granular convection observed by magnetic-resonance-imaging. *Science* **267**, 1632–1634.
- FAN, Y. & HILL, K. M. 2011 Theory for shear-induced segregation of dense granular mixtures. *New J. Phys.* **13** (9), 095009.
- FÉLIX, G. & THOMAS, N. 2004 Relation between dry granular flow regimes and morphology of deposits: formation of levées in pyroclastic deposits. *Earth Planet. Sci. Lett.* **221**, 197–213.
- FLAVOR, FARM 2017 How the Montana state grain lab ensures top-quality grains, legumes and more.
- FORTERRE, Y. 2006 Kapiza waves as a test for three-dimensional granular flow rheology. *J. Fluid Mech.* **563**, 123–132.
- FORTERRE, Y. & POULIQUEN, O. 2003 Long-surface-wave instability dense granular flows. *J. Fluid Mech.* **486**, 21–50.
- FORTERRE, Y. & POULIQUEN, O. 2008 Flows of dense granular media. *Ann. Rev. Fluid Mech.* **40**, 1–24.
- GAJJAR, P. & GRAY, J. M. N. T. 2014 Asymmetric flux models for particle-size segregation in granular avalanches. *J. Fluid Mech.* **757**, 297–329.
- GAJJAR, P., VAN DER VAART, K., THORNTON, A. R., JOHNSON, C. G., ANCEY, C. & GRAY, J. M. N. T. 2016 Asymmetric breaking size-segregation waves in dense granular free-surface flows. *J. Fluid Mech.* **794**, 460–505.

- GDR-MiDi 2004 On dense granular flows. *Eur. Phys. J. E* **14**, 341–365.
- GOLICK, L. A. & DANIELS, K. E. 2009 Mixing and segregation rates in sheared granular materials. *Phys. Rev. E* **80** (4), 042301.
- GOUJON, C., DALLOZ-DUBRUJEAUD, B. & THOMAS, N. 2007 Bidisperse granular avalanches on inclined planes: A rich variety of behaviours. *Eur. Phys. J. E* **23**, 199–215.
- GRASSELLI, Y. & HERRMANN, H. J. 1997 On the angles of dry granular heaps. *Physica A* **246**, 301–312.
- GRAY, J. M. N. T. 1999 Loss of hyperbolicity and ill-posedness of the viscous-plastic sea ice rheology in uniaxial divergent flow. *J. Phys. Oceanog.* **29** (11), 2920–2929.
- GRAY, J. M. N. T. 2001 Granular flow in partially filled slowly rotating drums. *J. Fluid Mech.* **441**, 1–29.
- GRAY, J. M. N. T. 2018 Particle segregation in dense granular flows. *Ann. Rev. Fluid Mech.* **50**, 407–433.
- GRAY, J. M. N. T. & ANCEY, C. 2009 Segregation, recirculation and deposition of coarse particles near two-dimensional avalanche fronts. *J. Fluid Mech.* **629**, 387–423.
- GRAY, J. M. N. T. & ANCEY, C. 2011 Multi-component particle size-segregation in shallow granular avalanches. *J. Fluid Mech.* **678**, 535–588.
- GRAY, J. M. N. T. & ANCEY, C. 2015 Particle-size and particle-density segregation in granular avalanches. *J. Fluid Mech.* **779**, 622–668.
- GRAY, J. M. N. T. & CHUGUNOV, V. A. 2006 Particle-size segregation and diffusive remixing in shallow granular avalanches. *J. Fluid Mech.* **569**, 365–398.
- GRAY, J. M. N. T. & CUI, X. 2007 Weak, strong and detached oblique shocks in gravity driven granular free-surface flows. *J. Fluid Mech.* **579**, 113–136.
- GRAY, J. M. N. T. & EDWARDS, A. N. 2014 A depth-averaged $\mu(I)$ -rheology for shallow granular free-surface flows. *J. Fluid Mech.* **755**, 503–544.

- GRAY, J. M. N. T., GAJJAR, P. & KOKELAAR, P. 2015 Particle-size segregation in dense granular avalanches. *C. R. Phys.* **16** (1), 73–85.
- GRAY, J. M. N. T. & HUTTER, K. 1997 Pattern formation in granular avalanches. *Continuum Mech. & Thermodyn.* **9**, 341–345.
- GRAY, J. M. N. T. & KOKELAAR, B. P. 2010a Large particle segregation, transport and accumulation in granular free-surface flows. *J. Fluid Mech.* **652**, 105–137.
- GRAY, J. M. N. T. & KOKELAAR, B. P. 2010b Erratum large particle segregation, transport and accumulation in granular free-surface flows – erratum. *J. Fluid Mech.* **657**, 539.
- GRAY, J. M. N. T., SHEARER, M. & THORNTON, A. R. 2006 Time-dependent solutions for particle-size segregation in shallow granular avalanches. *Proc. Roy. Soc. A* **462**, 947–972.
- GRAY, J. M. N. T., TAI, Y. C. & NOELLE, S. 2003 Shock waves, dead-zones and particle-free regions in rapid granular free-surface flows. *J. Fluid Mech.* **491**, 161–181.
- GRAY, J. M. N. T. & THORNTON, A. R. 2005 A theory for particle size segregation in shallow granular free-surface flows. *Proc. Roy. Soc. A* **461**, 1447–1473.
- GRAY, J. M. N. T., WIELAND, M. & HUTTER, K. 1999 Gravity-driven free surface flow of granular avalanches over complex basal topography. *Proc. Roy. Soc. Lond. A* **455** (1985), 1841–1874.
- GREVE, R. & HUTTER, K. 1993 Motion of a granular avalanche in a convex and concave curved chute: experiments and theoretical predictions. *Phil. Trans. R. Soc. Lond. A* **342**, 573–600.
- GRIGORIAN, S. S., EGLIT, M. E. & IAKIMOV, I. L. 1967 New statement and solution of the problem of the motion of snow avalanche. *Snow, Avalanches & Glaciers. Tr. Vysokogornogo Geofizich Inst* **12**, 104–113.

- DE HAAS, T., DENSMORE, A. L., STOFFEL, M., SUWA, H., IMAIZUMI, F., BALLESTEROS-CÁNOVAS, J. A. & WASKLEWICZ, T. 2018 Avulsions and the spatio-temporal evolution of debris-flow fans. *Earth-Sci. Rev.* **177**, 53–75.
- HÁKONARDÓTTIR, K. M. & HOGG, A. J. 2005 Oblique shocks in rapid granular flows. *Phys. Fluids* **17**, 0077101.
- HESLOT, F., BAUMBERGER, T., PERRIN, B., CAROLI, B. & CAROLI, C. 1994 Creep, stick-slip, and dry-friction dynamics: Experiments and a heuristic model. *Phys. Rev. E* **49** (6), 4973.
- HEYMAN, J., DELANNAY, R., TABUTEAU, H & VALANCE, A 2017 Compressibility regularizes the $\mu(I)$ -rheology for dense granular flows. *J. Fluid Mech.* **830**, 553–568.
- HUNG, C-Y, STARK, C. P. & CAPART, H. 2016 Granular flow regimes in rotating drums from depth-integrated theory. *Phys. Rev. E* **93** (3), 030902.
- HUNGR, O. & MORGENSTERN, N. R. 1984 Experiments on the flow behaviour of granular materials at high velocity in an open channel. *Géotechnique* **34** (3), 405–413.
- IORDANOFF, I. & KHONSARI, M. M. 2004 Granular lubrication: toward an understanding of the transition between kinetic and quasi-fluid regime. *J. Tribol.* **126** (1), 137–145.
- IVERSON, R. M. 1997 The physics of debris-flows. *Rev. Geophys.* **35**, 245–296.
- IVERSON, R. M. & DENLINGER, R. P. 2001 Flow of variably fluidized granular masses across three-dimensional terrain 1. Coulomb mixture theory. *J. Geophys. Res.* **106** (B1), 553–566.
- JAEGER, H. M. & NAGEL, S. R. 1992 Physics of the granular state. *Science* **255** (5051), 1523–1531.
- JAEGER, H. M., NAGEL, S. R. & BEHRINGER, R. P. 1996 Granular solids, liquids, and gases. *Rev. Mod. Phys.* **68** (4), 1259.
- JENKINS, J. T. & YOON, D. & 2001 Segregation in binary mixtures under gravity. *Phys. Rev. Lett.* **88** (19), 194301–4.

- JING, L., KWOK, C. Y. & LEUNG, Y. F. 2017 Micromechanical origin of particle size segregation. *Phys. Rev. Lett.* **118** (11), 118001.
- JOHANSON, J. R. 1978 Particle segregation ... and what to do about it. *Chem. Eng.* pp. 183–188.
- JOHNSON, C. G., KOKELAAR, B. P., IVERSON, R. M., LOGAN, M., LAHUSEN, R. G. & GRAY, J. M. N. T. 2012 Grain-size segregation and levee formation in geophysical mass flows. *J. Geophys. Res.* **117**, F01032.
- JOP, P., FORTERRE, Y. & POULIQUEN, O. 2005 Crucial role of sidewalls in granular surface flows: consequences for the rheology. *J. Fluid Mech.* **541**, 167–192.
- JOP, P., FORTERRE, Y. & POULIQUEN, O. 2006 A constitutive relation for dense granular flows. *Nature* **44**, 727–730.
- KAMRIN, K. & BAZANT, M. Z. 2007 Stochastic flow rule for granular materials. *Phys. Rev. E* **75** (4), 041301.
- KAMRIN, K. & HENANN, D. L. 2015 Nonlocal modeling of granular flows down inclines. *Soft Matter* **11** (1), 179–185.
- KOKELAAR, B. P., BAHIA, R. S., JOY, K. H., VIROULET, S & GRAY, J. M. N. T. 2017 Granular avalanches on the moon: Mass-wasting conditions, processes and features. *J. Geophys. Res.: Planets* **122**, 1893–1925.
- KOKELAAR, B. P., GRAHAM, R. L., GRAY, J. M. N. T. & VALLANCE, J. W. 2014 Fine-grained linings of leveed channels facilitate runout of granular flows. *Earth Planet. Sci. Lett.* **385**, 172–180.
- KOMATSU, T. S., INAGAKI, S., NAKAGAWA, N. & NASUNO, S. 2001 Creep motion in a granular pile exhibiting steady surface flow. *Phys. Rev. Lett.* **86**, 1757–1760.
- KUO, C.Y., TAI, Y. C., BOUCHUT, F., MANGENEY, A., PELANTI, M., CHEN, R.F. & CHANG, K.J. 2009 Simulation of Tsaoiling landslide, Taiwan, based on Saint Venant equations over general topography. *Engng. Geol.* **104** (3-4), 181–189.

- LAGRÉE, P.-Y., STARON, L. & POPINET, S. 2011 The granular column collapse as a continuum: validity of a two-dimensional navier-stokes model with a $\mu(I)$ -rheology. *J. Fluid Mech.* **686**, 378–408.
- LINARES-GUERRERO, E., GOUJON, C. & ZENIT, R. 2007 Increased mobility of bidisperse granular avalanches. *J. Fluid Mech.* **593**, 475–504.
- LUCA, I., HUTTER, K., TAI, Y. C. & KUO, C. Y. 2009 A hierarchy of avalanche models on arbitrary topography. *Acta Mech.* **205**, 121–149.
- LUEPTOW, R. M., DENG, Z., XIAO, H. & UMBANHOWAR, P. B. 2017 Modeling segregation in modulated granular flow. In *EPJ Web of Conferences*, , vol. 140, p. 03018. EDP Sciences.
- MANGENEY-CASTELNAU, A., VILOTTE, J. P., BRISTEAU, M. O., PERTHAME, B., BOUCHUT, F., SIMEONI, C. & YERNENI, S. 2003 Numerical modeling of avalanches based on Saint-Venant equations using a kinetic scheme. *J. Geophys. Res.* **108**, 2527.
- MCCELWAINE, J. N., TAKAGI, D. & HUPPERT, H. E. 2012 Surface curvature of steady granular flows. *Granular Matter* **14** (2), 229–234.
- MIDDLETON, G. V. 1970 Experimental studies related to problems of flysch sedimentation. In *Flysch Sedimentology in North America* (ed. J. Lajoie), pp. 253–272. Toronto: Business and Economics Science Ltd.
- MONLLAR, VIAJES 2011 Festival internacional de esculturas en arena, Algarve (Portugal).
- MULLIN, T. 2000 Coarsening of self-organized clusters in binary mixtures of particles. *Phys. Rev. Lett.* **84**, 4741–4744.
- PATTON, J. S., BRENNEN, C. E. & SABERSKY, R. H. 1987 Shear flows of rapidly flowing granular materials. *J. Applied Mech.* **54** (4), 801–805.
- PITMAN, E. B., NICHITA, C. C., PATRA, A., BAUER, A., SHERIDAN, M. & BURSIK, M. 2003 Computing granular avalanches and landslides. *Phys. Fluids* **15** (12), 3638–3646.

- POULIQUEN, O. 1999a Scaling laws in granular flows down rough inclined planes. *Phys. Fluids* **11** (3), 542–548.
- POULIQUEN, O. 1999b On the shape of granular fronts down rough inclined planes. *Phys. Fluids* **11** (7), 1956–1958.
- POULIQUEN, O., DELOUR, J. & SAVAGE, S. B. 1997 Fingering in granular flows. *Nature* **386**, 816–817.
- POULIQUEN, O. & FORTERRE, Y. 2002 Friction law for dense granular flows: application to the motion of a mass down a rough inclined plane. *J. Fluid Mech.* **453**, 133–151.
- POULIQUEN, O. & RENAUT, N. 1996 Onset of granular flows on an inclined rough surface: dilatancy effects. *J. Phys. II France* **6**, 923–935.
- POULIQUEN, O. & VALLANCE, J. W. 1999 Segregation induced instabilities of granular fronts. *Chaos* **9** (3), 621–630.
- PUDASAINI, S. P. & HUTTER, K. 2003 Rapid shear flows of dry granular masses down curved and twisted channels. *J. Fluid Mech.* **495**, 193–208.
- ROCHA, F. M., JOHNSON, C. G. & GRAY, J. M. N. T. 2019 Self-channelisation and levee formation in monodisperse granular flows. *J. Fluid Mech.* **876**, 591–641.
- ROGNON, P. G., ROUX, J. N., NAAIM, M. & CHEVOIR, F. 2007 Dense flows of bidisperse assemblies of disks down an inclined plane. *Phys. Fluids* **19**, 058101.
- RUSSELL, A. S., JOHNSON, C. G., EDWARDS, A. N., VIROULET, S., ROCHA, F. M. & GRAY, J. M. N. T. 2019 Retrogressive failure of a static granular layer on an inclined plane. *J. Fluid Mech.* **869**, 313–340.
- DE SAINT-VENANT, A. J.-C. 1871 Théorie du mouvement non-permanent des eaux, avec application aux crues des rivières et à l'introduction des marées dans leur lit. *CR Acad. Sci. Paris* **73** (147-154), 5.
- SAVAGE, S. B. & HUTTER, K. 1989 The motion of a finite mass of granular material down a rough incline. *J. Fluid Mech.* **199**, 177–215.

- SAVAGE, S. B. & HUTTER, K. 1991 The dynamics of avalanches of granular materials from initiation to run-out. I. analysis. *Acta Mech.* **86**, 201–223.
- SAVAGE, S. B. & LUN, C. K. K. 1988 Particle size segregation in inclined chute flow of dry cohesionless granular solids. *J. Fluid Mech.* **189**, 311–335.
- SCHAEFFER, D. G. 1987 Instability in the evolution equations describing incompressible granular flow. *J. Differ. Equations* **66** (1), 19–50.
- SCHAEFFER, D. G., BARKER, T., TSUJI, D., GREMAUD, P., SHEARER, M. & GRAY, J. M. N. T. 2019 Constitutive relations for compressible granular flow in the inertial regime. *J. Fluid Mech.* **874**, 926–951.
- SCHRÖTER, M., ULRICH, S., KREFT, J., SWIFT, J. B. & SWINNEY, H. L. 2006 Mechanisms in the size segregation of a binary granular mixture. *Phys. Rev. E* **74** (1), 011307.
- SCHULZE, D. 2008 *Powders and Bulk Solids*. Springer Berlin Heidelberg, 10.1007/978-3-540-73768-1.
- SCOTT, A. M. & BRIDGWATER, J. 1975 Interparticle percolation: A fundamental solids mixing mechanism. *Industrial & Engineering Chemistry Fundamentals* **14** (1), 22–27, arXiv: <http://pubs.acs.org/doi/pdf/10.1021/i160053a004>.
- SHARP, R. P. & NOBLES, L. H. 1953 Mudflow of 1941 at Wrightwood, Southern California. *Geol. Soc. America Bull.* **66**, 1489–1498.
- SHEARER, M., GRAY, J. M. N. T. & THORNTON, A. R. 2008 Stable solutions of a scalar conservation law for particle-size segregation in dense granular avalanches. *Eur. J. App. Math.* **19**, 61–86.
- SHEPHERD, G., TERRADELLAS, E., BAKLANOV, A., KANG, U., SPRIGG, W., NICKOVIC, S., BOLOORANI, A. D., AL-DOUSARI, A., BASART, S., BENEDETTI, A., SEALY, A., TONG, D., ZHANG, X., SHUMAKE-GUILLEMOT, J., ZHANG, K., KNIPPERTZ, P., MOHAMMED, A. A. A., AL-DABBAS, M., CHENG, L., OTANI, S., WANG, F., ZHANG, C., RYOO, S. B. & JOOWAN, C. 2016 Global assessment of sand and dust storms .

- SILBERT, L. E., ERTAŞ, D., GREY, G. S., HALSEY, T. C., LEVINE, D. & PLIMPTON, S. J. 2001 Granular flow down an inclined plane: Bagnold scaling and rheology. *Phys. Rev. E* **64**, 051302.
- SILBERT, L. E., LANDRY, J. W. & GREY, G. S. 2003 Granular flow down a rough inclined plane: transition between thin and thick piles. *Phys. Fluids* **15**, 1–10.
- STARON, L., LAGRÉE, P.-Y. & POPINET, S. 2012 The granular silo as a continuum plastic flow: The hour-glass vs the clepsydra. *Phys. Fluids* **24**, 103301.
- STARON, L., LAGRÉE, P.-Y. & POPINET, S. 2014 Continuum simulation of the discharge of the granular silo. *Eur. Phys. J. E* **37** (1), 5.
- TAI, Y. C., NOELLE, S., GRAY, J. M. N. T. & HUTTER, K. 2002 Shock-capturing and front-tracking methods for granular avalanches. *J. Comput. Phys.* **175**, 269–301.
- TAKAGI, D., MCELWAIN, J. N. & HUPPERT, H. E. 2011 Shallow granular flows. *Phys. Rev. E* **83** (3), 031306.
- THOMAS, N. 2000 Reverse and intermediate segregation of large beads in dry granular media. *Phys. Rev. E* **62** (1), 961.
- TUNUGUNTLA, D. R., BOKHOVE, O. & THORNTON, A. R. 2014 A mixture theory for size and density segregation in shallow granular free-surface flows. *J. Fluid Mech.* **749**, 99–112.
- VAN DER VAART, K., GAJJAR, P., EPELY-CHAUVIN, G., ANDREINI, N., GRAY, J. M. N. T. & ANCEY, C. 2015 Underlying asymmetry within particle size segregation. *Phys. Rev. Lett.* **114** (23), 238001.
- VALLANCE, J. W. 2000 Lahars. In *Encyclopedia of Volcanoes* (ed. H. Sigurdsson), pp. 601–616. Academic.
- VIROULET, S., BAKER, J. L., ROCHA, F. M., JOHNSON, C. G., KOKELAAR, B. P. & GRAY, J. M. N. T. 2018 The kinematics of bidisperse granular roll waves. *J. Fluid Mech.* **848**, 836–875.

- VREMAN, A. W., AL-TARAZI, M., KUIPERS, J. A. M., SINT, M. VAN & BOKHOVE, O. 2007 Supercritical shallow granular flow through a contraction: experiment, theory and simulation. *J. Fluid Mech.* **578**, 233–269.
- WIELAND, M., GRAY, J. M. N. T. & HUTTER, K. 1999 Channelised free surface flow of cohesionless granular avalanches in a chute with shallow lateral curvature. *J. Fluid Mech.* **392**, 73–100.
- WOODHOUSE, M. J., THORNTON, A. R., JOHNSON, C. G., KOKELAAR, B. P. & GRAY, J. M. N. T. 2012 Segregation-induced fingering instabilities in granular free-surface flows. *J. Fluid Mech.* **709**, 543–580.
- ZURIGUEL, I., GRAY, J. M. N. T., PEIXINHO, J. & MULLIN, T. 2006 Pattern selection by a granular wave in a rotating drum. *Phys. Rev. E* **73**, 061302.